To the Graduate Council:

I am submitting herewith a dissertation written by David Wayne Pruitt entitled "Potassium and Sulfur Interactions in Hydrocarbon Flames. An Application to the CFFF Secondary Combustor." I have examined the final copy of this dissertation for form and content and recommend that it be accepted in partial fulfillment of the requirements for the degree of Doctor of Philosophy, with a major in Mechanical Engineering.

Roy J. Schulz

Roy Schulz, Major Professor

We have read this dissertation
and recommend its acceptance:

Frank G. Collins

Frank Collins

Gary Flandro

Gary Flandro

Atul Sheth

Atul Sheth

Accepted for the Council:

Associate Vice Chancellor and
Dean of the Graduate School

Potassium and Sulfur Interactions in Hydrocarbon Flames.

An Application to the CFFF Secondary Combustor

A Dissertation

Presented for the

Doctor of Philosophy

Degree

The University of Tennessee, Knoxville

David Wayne Pruitt

May 2000

Acknowledgements

I am thankful to many people who have supported this work. My sincere thanks for the patience of my major professor, Dr. Roy Schulz, cannot be overstated. The other members of my committee, Drs. Collins, Flandro, Sheth, and Winkleman also deserve my appreciation, particularly Dr. Winkleman. If not for him, the experiments would not have been completed.

I am indebted to many colleagues for support, encouragement, example, and education. Drs. James Drakes and Robert Hiers, III were always available for discussion. It has been a privilege to be able to work with them over these past years. I am sure that I have received much more than I have given. I am grateful to Dr. Keith Schofield, who was kind enough to rummage through old files to provide important information that helped this work along. Dr. Paul Marshall provided important information on the HOSO molecule prior to publication that proved to be critical. Both graciously gave their insights and time during my visit to their campuses. Mr. Karl Kneile was (and continues to be) available for discussion on any topic. Specifically, Karl guided me through matters of data reduction and error analysis. I thank Mr. Jim Hornkohl at UTSI for providing me with the OD spectrum that answered so many questions. I would like to thank Ms. Bonnie McBride who provided the PAC91 code for computing thermodynamic properties and Ms. Fran Rupley who provide the CHEMKIN computer programs. The review team at Arnold Engineering Development

Center (Danny Brown, James Drakes, Doug Garrard, and Robert Heirs, III) suffered through one very long and late draft with many valuable comments and suggestions, tenderly offered. Finally, I would like to thank Ms. Martha Simmons, who said a prayer for me.

It is no exaggeration to say that this dissertation would not have been completed without the assistance of Dr. Virgil Smith who drives the Sverdrup Technology, Inc. Advanced Education Program. I am very grateful to Dr. Smith and honored to be a recipient of the scholarship award. I am also thankful to the U.S. Air Force for allowing me to pursue this degree program while employed at AEDC.

I finally thank my family. Their patience has been the greatest of all.

Abstract

Potassium concentration and OH concentration measurements were made in the post flame gases of methane/oxygen/nitrogen flames seeded with potassium. Sulfur was added to some of the flames. These concentration measurements were used to investigate the finite rate chemistry of potassium and sulfur at high temperature. A new potassium oxidation mechanism has been developed herein based on this data for flames with no added sulfur. This mechanism is a modification and extension of the model discussed by Slack, et al [20] and Hynes, et al [18]. Potassium 'catalytically' consumes flame radical, like OH, primarily through two termolecular reactions:

$$K + O_2 + M \Leftrightarrow KO_2 + M \qquad (1)$$

$$K + OH + M \Leftrightarrow KOH + M \qquad (2)$$

and a handful of bimolecular reactions, most importantly

$$KO_2 + O \Leftrightarrow KO + O_2 \qquad (6)$$

$$KOH + H \Leftrightarrow K + H_2O \qquad (16)$$

$$KO + H_2O \Leftrightarrow KOH + OH \qquad (17).$$

The catalytic cycle includes the channel $K \Rightarrow KOH \Rightarrow K$ via reactions (2) and (16) and the alternate path; $K \Rightarrow KO_2 \Rightarrow KO \Rightarrow KOH \Rightarrow K$ via reactions (1), (6), (17), and (16). The latter path is particularly important in fuel-lean flames.

In flames with added sulfur, it was found that the post flame chemistry was still governed by reactions (1), (2), (6), (16) and (17). However, reactions of the flame radicals with sulfur compounds

$$H + SO_2 + M \Leftrightarrow HOSO + M \qquad (34)$$

$$H + HOSO \Leftrightarrow H_2 + SO_2 \qquad (36)$$

$$OH + HOSO \Leftrightarrow H_2O + SO_2 \qquad (37)$$

perturbed the potassium species in the post flame. Reactions between potassium and sulfur species are required to explain the concentration data in the fuel-rich flames investigated. The reactions

$$K + SO_2 + M \Leftrightarrow KSO_2 + M \qquad (48)$$

$$KSO_2 + OH \Leftrightarrow KOH + SO_2 \qquad (53)$$

Are analogs of reactions (34) and (37). These reactions open an alternate channel between K and KOH through KSO_2 in fuel-rich flames. The potassium/sulfur reaction mechanism develop herein was applied in a simple model the MHD combustion system and adequately explained the ignition behavior in question.

Table of Contents

Section	Page
1. Introduction and Research Summary	1
2. Background	6
2.1. CFFF Background	6
2.1.1. CFFF Description	6
2.1.2. Secondary Combustor	9
2.1.3. Secondary Combustor Anomaly	11
2.2. Background Chemistry	19
2.2.1. Alkali-Metal Chemistry	19
2.2.2. Sulfur Chemistry	24
2.2.3. Alkali-Metal/Sulfur Coupling	27
2.3. Secondary Combustor Chemistry	28
3. Experiment Apparatus and Sample Data	30
3.1. Introduction to the Experimental Program	30
3.2. Apparatus	36
3.2.1. Burner Design	36
3.2.2. Flowmeters	39
3.2.3. Nebulizer	43
3.3. Absorption Measurements	46
3.3.1. Theory	46
3.3.2. Potassium Absorption Measurement	53
3.3.2.1. Experimental Setup	53

3.3.2.2. Sample Data Reduction 57
3.3.2.3. Error Analysis 63
3.3.3. OH Absorption Measurement 65
3.3.3.1. Experimental Setup 65
3.3.3.2. Sample Data Reduction 69
3.3.3.3. Error Analysis 75
3.4. Temperature Measurement 77
3.4.1. Theory 77
3.4.2. Experimental Setup 80
3.4.3. Sample Data Reduction 80
3.4.4. Error Analysis 82
4. Experimental Results 85
4.1. Experiment Matrix 85
4.2. Temperature Profiles 85
4.3. Potassium and OH Decay Profiles 90
5. Kinetic Analysis 95
5.1. CHEMKIN Description 96
5.2. Review of Alkali-Metal Kinetics 103
5.3. Flame Modeling - Flames without Sulfur 116
5.3.1. Species Thermodynamics Properties 116
5.3.2. Transport Properties 124
5.3.3. Hydrocarbon Combustion Mechanism 125
5.3.4. Modeling Results - Flames without Sulfur 127

5.4. Review of Sulfur Kinetics 147

5.5. Flame Modeling - Flames with Sulfur 158

5.5.1. Thermodynamics of K/S Compounds 158

5.5.2. Transport Properties 175

5.5.3. Modeling Results - Flames with Sulfur 177

6. Secondary Combustor Modeling 197

6.1. Approach 197

6.2. LSENS Description 199

6.3. Plug Flow Model Results 201

7. Final Conclusions 220

References 223

Appendices 238

Appendix A 239

Appendix B 243

Appendix C 257

Appendix D 276

Appendix E 290

Appendix F 295

Appendix G 307

Vita 311

List of Table

Table **Page**

Table 2-1 Eastern coal composition 12

Table 2-2 Western coal composition 12

Table 2-3 LMF5-I experiment summary T_{SCI} = 1640 °F 14

Table 2-4 LMF5-I experiment summary T_{SCI} = 1920 °F 14

Table 2-5 LMF5-I experiment summary T_{SCI} = 2140 °F 15

Table 2-6 LMF5-J experiment summary 15

Table 3.1 Summary of flowmeters 41

Table 3-2 Electronic states for potassium 62

Table 3-3 Error components for potassium absorption data 64

Table 3-4 Parameters used in OH absorption data reduction 72

Table 3-5 Parameters for the calculation of the rotational partition function 74

Table 3-6 Parameters for the electronic partition function 75

Table 3-7 Error components for OH absorption data 76

Table 3-8 Optical parameters for modified line reversal temperature measurement 79

Table 3-9 Error components for temperature measurement 83

Table 4-1 Flame Matrix 86

Table 5-1 Slack's potassium oxidation mechanism 113

Table 5-2 Summary of spectroscopic parameters for KO 118

Table **Page**

Table 5-3 Summary of geometry determinations for KO_2 120

Table 5-4 Summary of vibrational mode determinations for KO_2 120

Table 5-5 Inputs for the calculation of transport properties for K/O/H species 125

Table 5-6 Simplified hydrocarbon combustion mechanism 128

Table 5-7 Reactions initially proposed for potassium oxidation 130

Table 5-8 Final potassium oxidation mechanism 132

Table 5-9 Vibrational frequencies for HOSO and HSO_2 156

Table 5-10 Sulfur oxidation and radical recombination mechanism 159

Table 5-11 Summary of KS molecular and thermodynamic properties 161

Table 5-12 Electronic configurations of atoms 163

Table 5-13 Determination of C from Herzberg's Correlation 163

Table 5-14 Summary of the parameters used to estimate KS_2 thermodynamic properties 166

Table 5-15 Comparison of force constants for hydroxides 168

Table 5-16 Summary of KSH thermodynamic properties and the parameters used to estimate them 173

Table 5-17 Summary of KOS thermodynamic properties and the parameters used to estimate them 174

Table 5-18 Summary of KSO_2 thermodynamic properties and the parameters used to estimate them 176

Table **Page**

Table 5-19 Transport properties for K/O/S/H species 178

Table 5-20 Reactions proposed for potassium/sulfur interactions 179

Table 5-21 Final Potassium/Sulfur interaction mechanism 181

Table A-1 Summary of reactions used in kinetic calculations 239

Table B-1 Calibration data for N_2 flowmeter 245

Table B-2 Calibration data for O_2 flowmeter 246

Table B-3 Calibration data for CH_4 flowmeter 247

Table B-4 Calibration data for H_2S flowmeter 248

Table B-5 Nebulizer calibration results 255

Table C-1 Uncertainty parameters for integrated absorption - potassium 259

Table C-2 Estimated component errors 264

Table C-3 Uncertainty parameters for integrated absorption - OH 269

Table C-4 Error components for OH absorption data 270

Table C-5 Brightness temperature statistics 272

Table C-6 Error components for MLR optical train 273

Table C-7 Estimated component errors 274

Table F-1 Curve fit coefficients for KO 295

Table F-2 Curve fit coefficients for KO_2 295

Table F-3 Curve fit coefficients for KOH 296

Table F-4 Curve fit coefficients for KS 296

Table F-5 Curve fit coefficients for KS_2 296

Table **Page**

Table F-6 Curve fit coefficients for KSH 296

Table F-7 Curve fit coefficients for KOS 297

Table F-8 Curve fit coefficients for KSO_2 297

Table F-9 Curve fit coefficients for HOSO 297

Table F-10 Thermodynamic properties for KO 298

Table F-11 Thermodynamic properties for KO_2 299

Table F-12 Thermodynamic properties for KOH 300

Table F-13 Thermodynamic properties for KS 301

Table F-14 Thermodynamic properties for KS_2 302

Table F-15 Thermodynamic properties for KSH 303

Table F-16 Thermodynamic properties for KOS 304

Table F-17 Thermodynamic properties for KSO_2 305

Table F-18 Thermodynamic properties for HOSO 306

List of Figures

Figure **Page**

Figure 2.1 Coal-Fired Flow Facility (CFFF) 7

Figure 2-2 Secondary combustor drawing 10

Figure 2-3 Secondary combustor temperature rise (From Table 2-3) 17

Figure 2-4 Secondary combustor temperature rise (From Table 2-4) 17

Figure 2-5 Secondary combustor temperature rise (From Table 2-5) 18

Figure 2-6 Secondary combustor temperature rise (From Table 2-6) 18

Figure 2-7 Sodium oxidation chemistry proposed by Hynes, et al 23

Figure 3-1 Experiment schematic 31

Figure 3-2 Tube pattern at burner surface. 38

Figure 3-3 Exploded view of burner 40

Figure 3-4 Assembled burner 41

Figure 3-5 The Burgerner nebulizer 44

Figure 3-6 Nebulizer body assembly 45

Figure 3-7 Schematic of nebulizer system 46

Figure 3-8. Schematic of absorption measurement (After Alkemade) 47

Figure 3-9 Layout for potassium absorption measurement 53

Figure 3-10 Current-to-voltage converter for PMT output 55

Figure 3-11 Spatial resolution of potassium absorption measurement 57

Figure 3-12 Spectrally correlated source scans (fuel-lean flame, 1.0 mm) 60

Figure **Page**

Figure 3-13 Spectrally correlated absorption scans (fuel-lean flame, 1.0 mm) 60

Figure 3-14 Potassium absorption sample data (fuel-lean flame, 1.0 mm) 61

Figure 3-15 Instrumentation layout for OH absorption measurement 66

Figure 3-16 Spatial resolution for OH absorption measurement 68

Figure 3-17 Correlated $\bar{I}_{\nu,0}$ scans 70

Figure 3-18 Correlated $\bar{I}_{\nu}$ (absorption) scans 70

Figure 3-19 OH absorption profile (fuel-lean flame, 1.0 mm) 71

Figure 3-20 Dimensions required for modified line reversal temperature measurement 79

Figure 3-21 Modified line reversal temperature measurement setup 81

Figure 3-22. Typical modified line reversal results (fuel-lean flame, 1.0 mm) 82

Figure 4-1 Comparison of the temperature 87

Figure 4-2 Comparison of the calculated equilibrium adiabatic flame temperatures with measured temperature 89

Figure 4-3 Potassium decay profiles: No sulfur and 1% H_2S (0.75% for ϕ=1.3) 91

Figure 4-4 OH decay profiles: No sulfur and 1% H_2S (0.75% for ϕ=1.3) 93

Figure 5-1 Geometry of the flame problem 97

Figure 5-2 Sodium oxidation cycle proposed by Hynes, et al [18] 108

Figure 5-3 Summary of rate determinations for K + O_2 + N_2 115

Figure **Page**

Figure 5-4 Summary of rate determinations for K + OH + M 115

Figure 5-5 KO_2 geometry and vibration compared to KO and O^-_2 121

Figure 5-6 Display of KO_2 dissociation energy determinations 123

Figure 5-7 Comparison of experimental and calculated species profiles in the fuel-lean (ϕ=0.85) flame, no sulfur 134

Figure 5-8 Comparison of experimental and calculated species profiles in the stoichiometric (ϕ=1.0) flame, no sulfur 135

Figure 5-9 Comparison of experimental and calculated species profiles in the fuel-rich (ϕ=1.2) flame, no sulfur 136

Figure 5-10 Comparison of experimental and calculated species profiles in the fuel-rich (ϕ=1.3) flame, no sulfur 137

Figure 5-11 Calculated distribution of potassium species in fuel-lean (ϕ=0.85) and fuel-rich (ϕ=1.2) flames 138

Figure 5-12 Potassium oxidation cycle 140

Figure 5-13 Production rates for potassium species in each reaction - fuel-lean (ϕ=0.85) flames 141

Figure 5-14 Sensitivity coefficients for potassium reactions - fuel-lean (ϕ=0.85) flame 142

Figure 5-15 Production rates for potassium species in each reaction - fuel-lean (ϕ=0.85) flame 144

Figure **Page**

Figure 5-16 Sensitivity coefficients for potassium reactions - fuel-rich (ϕ=1.2) flame 145

Figure 5-17 HOSO and HSO_2 geometries [87] 156

Figure 5-18 Reaction rates for H + SO_2 + M 157

Figure 5-19 Correlation for M-SH bond energy 170

Figure 5-20 Na-S-O bond comparisons 173

Figure 5-21 K-S-O bond comparisons (determined by analogy with NaSO) 174

Figure 5-22 Comparison of KSO_2 and K_2SO_4 176

Figure 5-23 Model results for the lean flame (ϕ=0.85) – 1% added H_2S 183

Figure 5-24 Model results for the stoichiometric flame – 1% added H_2S 184

Figure 5-25 Model results for the rich (ϕ=1.2) flame – 1% added H_2S 185

Figure 5-26 Model results for the rich (ϕ=1.3) flame – 0.75% added H_2S 186

Figure 5-27 Calculated distribution of potassium species in the fuel-lean (ϕ=0.85) and fuel-rich (ϕ=1.2) flame – 1% H_2S added 188

Figure 5-28 Production rates for potassium reactions - fuel-lean (ϕ=0.85) flame, 1% added H_2S 190

Figure 5-29 Production rates for potassium reactions - fuel-rich (ϕ=1.2) flame, 1% added H_2S 191

Figure 5-30 Normalized sensitivity coefficients for potassium reactions - fuel-lean (ϕ=0.85) flame, 1% added H_2S 193

Figure **Page**

Figure 5-31 Normalized sensitivity coefficients for potassium reactions - fuel-rich (ϕ=1.2) flame, 1% added H_2S 194

Figure 5-32 Potassium kinetics modified by sulfur 195

Figure 6-1 Primary combustor inflow schematic 204

Figure 6-2 Equilibrium distribution of sulfur species with temperature in Eastern coal, K_2/S = 1.0 206

Figure 6-3 Equilibrium distribution of sulfur species with temperature in Western coal, K_2/S = 4.0 206

Figure 6-4 Equilibrium distribution of potassium species with temperature in Eastern coal, K_2/S = 1.0 207

Figure 6-5 Equilibrium distribution of potassium species with temperature in Western coal, K_2/S = 4.0 207

Figure 6-6 Equilibrium of shift of sulfur from H_2S to KSH, Eastern coal, $T_{Primary}$ = 1200 K 208

Figure 6-7 Equilibrium of shift of sulfur from H_2S to KSH, Western coal, $T_{Primary}$ = 1200 K 208

Figure 6-8 Ignition temperature histories for Eastern coal, $T_{Primary}$ = 1150 K 210

Figure 6-9 Ignition temperature histories for Western coal, $T_{Primary}$ = 1150 K 211

Figure 6-10 Ignition of the secondary combustor, Eastern coal K_2S = 1.0 213

Figure **Page**

Figure 6-10 Ignition of the secondary combustor, Western coal K_2S = 4.0 _____ 213

Figure 6-12 Detail of ignition temperature history for Eastern coal _____ 215

Figure 6-13 Detail of ignition temperature history for Western coal _____ 215

Figure 6-14 Production rates for K/S/H/O and S/H/O reactions Prior to ignition. Eastern coal with $T_{Primary}$ = 1150 K _____ 216

Figure 6-15 Modification to the mechanism for H_2S oxidation _____ 218

Figure B-1 Flowmeter calibration schematic _____ 244

Figure B-2 N_2 calibration results _____ 252

Figure B-3 O_2 calibration results _____ 252

Figure B-4 CH_4 calibration results _____ 253

Figure B-5 H_2S calibration results _____ 253

Figure B-6 Nebulizer calibration system _____ 254

Figure C-1 Signal statisitics for potassium absorption measurement _____ 263

Figure C-2 Histogram for potassium absorption measurement _____ 263

Figure C-3 Signal statistics for OH absorption measurement _____ 268

Figure C-4 Histogram for OH absorption measurement _____ 268

Figure C-5 Estimate of $\delta\eta$ _____ 269

Figure D-1 Schematic of absorption measurement (After Alkemade [41]) _____ 276

Figure D-2 Emission feature in $\bar{I}_{\nu,0}$ scan of deuterium lamp _____ 280

Figure D-3 Normalized scan of Hg emission line (312.567 nm) to determine slit function shape _____ 281

Figure **Page**

Figure D-4 Theoretical and convolved absorption profiles 282

Figure D-5 $\bar{I}_{\nu,0}$ correction procedure 284

Figure D-6 Examples of OH absorption data correction procedure 285

Figure D-7 Maximum correction for limited spectral scan 287

Figure D-8 Slit function corrected for scattered light 288

Figure D-9 Minimum correction for limited spectral scan 288

Figure E-1 Results of brightness temperature calibration 291

1.0 Introduction and Research Summary

Because of the pervasiveness of alkali metals in organic fuels, the high-temperature chemistry of alkali-metal compounds has been the subject of research for 50 years. This branch of research is extended by the work recorded here. The extension concerns the interaction of an alkali metal – potassium – with sulfur in a high temperature combustion environment. The research was motivated by problems encountered with the use of potassium to "seed" the combustion gases of a coal-fired Magnetohydrodynamic (MHD) channel [1].

The coal-fired MHD power generation system, developed at the University of Tennessee Space Institute (UTSI) under contract with the U.S. Department of Energy (DOE), burned potassium-seeded coal with oxygen-enriched air to produce a plasma. The plasma was expanded to a high velocity. In a MHD power generation system, the plasma would pass through an applied magnetic field (not present in the UTSI facility) and induce a direct electrical current. The generated current would be used for commercial electrical power generation. A conventional steam-based power generation system was located downstream of the MHD channel. The fuel-rich gas that flowed from the MHD channel was re-burned with injected air to provide thermal energy for steam power generation.

The Coal-Fired Flow Facility (CFFF) at UTSI was developed as a 1/3-scale simulation of the conventional thermal energy recovery cycle required for an efficient MHD power generation system. The exhaust gases of the MHD channel

flowed into the radiant furnace, where thermal energy was extracted to boil cooling water for steam generation. The cooled gases flowed into a secondary combustor where atmospheric air was injected to burn the remaining fuel (CO and H_2) and release the remaining chemical energy. This energy was extracted from the flow by a conventional superheater heat exchanger.

During testing of the CFFF, it was discovered that the performance of the secondary combustor was sensitive to the level of potassium seeding of the primary fuel, pulverized coal. The secondary combustor performance was monitored during test operation of the CFFF channel by observing the levels of CO at the secondary combustor outlet and comparing that to the levels of CO at the inlet to the secondary combustor. During one such test, high CO levels at the secondary combustor outlet indicated that combustion was not occurring within the secondary combustor even though the temperature and stoichiometry of the gas indicated that combustion should take place. Further tests that established higher and lower potassium seed levels and fuel-rich gas temperatures quantified the extent to which the secondary combustor operation was sensitive to potassium seed levels.

The combustion problems occurred in tests conducted with 'Western' coal. No problems were noted in previous CFFF testing that was conducted with 'Eastern' coal. The Western coal generally was lower in sulfur content (<1% by mass) than Eastern coal (2-5% by mass). It was known from a cold flow mixing study [2]

that there were intense levels of turbulent mixing in the secondary combustor. Thus mixing was not thought to be the cause of the combustion anomaly. It was hypothesized that some interaction between the potassium and sulfur was occurring that affected the flammability of the secondary combustor mixture.

Alkali metals, sodium and potassium in particular, are known to possess flame-inhibiting properties (see, for example [3]). In addition, sulfur is known to suppress the flammability of combustible mixtures (see, for example, [4]). A design study for the secondary combustor was performed to address this problem [5]. The design study concluded that potassium and sulfur increased the time required to complete combustion in the secondary combustor. Lewis, et al [5] noted that their study was deficient in two ways. First, the thermodynamic properties of key compounds and the kinetic rates of key reactions were unknown. Thus, they were either estimated or ignored. Second, the existence of potassium-sulfur (K/S) containing compounds or the kinetics of their formation was not considered.

The present dissertation research reported here was defined in order to resolve these deficiencies in K/S kinetics by a combined experimental and analytical study of the high-temperature combustion of methane/oxygen/nitrogen mixtures containing potassium and sulfur. The results of this study have a direct impact on the design of combustion systems wherein both potassium and sulfur compounds will be encountered. This study was executed in four parts:

1. An experimental study of flames of methane/oxygen/nitrogen mixtures containing potassium and sulfur compounds was conducted.

2. A thorough review was made of the thermodynamics and kinetics of alkali metal and sulfur compounds. As a result of this review, a new potassium oxidation (K/O) mechanism was generated.

3. Thermodynamic properties of K/S compounds were generated together with the development of a kinetic mechanism to describe the formation and consumption of the K/S compounds.

4. The results of the study of the K/S mechanism were applied to explain the observed secondary combustor performance.

In the flames studied in part 1, potassium and OH concentration decay profiles were measured using absorption spectroscopy, and temperature was measured using potassium line reversal. Eight premixed $CH_4/O_2/N_2$ flames seeded with potassium were studied. Sulfur in the form of H_2S was added to four of the flames. In all cases, addition of sulfur decreased the quantity of free potassium and OH in the flame.

The conclusion of the analysis of the flame data and the literature review (parts 2 and 3) is that the coupling between potassium and sulfur is weak, although many K/S compounds are formed. In fuel-lean flames, the addition of sulfur causes a pronounced decrease in the flame radical (OH, H, O) population. This effect is the primary influence on the potassium species distribution. However in fuel-rich flames, the presence of K/S species (particularly KSO_2) opens an alternate channel in the K/O oxidation mechanism. This channel, in addition to the perturbation of the flame radicals by the added sulfur, is responsible for the decrease of free potassium observed in rich flames.

In a simple model of the CFFF secondary combustor (part 4), the K/S mechanism reproduced the behavior observed in the CFFF test with Western coal. The ignition of the CO/H_2 mixture is suppressed for high levels of potassium seeding and low temperatures. However, if the gas temperature is high enough, the mixture will ignite even for very high potassium levels, as was observed. Calculations for Eastern coal produced similar results. The difficulties encountered with Western coal in the CFFF were not due to K/S interactions. Instead, the flame stability is now attributed to differences in the secondary combustor inlet temperatures. Eastern coal temperatures were about 200° F higher than that obtained with Western coal for the same stoichiometry. Thus, lower secondary combustor inlet temperature in the case of the LMF5 series of tests is thought primarily responsible for the observed behavior.

2.0 Background

The background material needed for this work is discussed in two parts of this section. In the first part, the Coal-Fired Flow Facility (CFFF) and the secondary combustor anomaly are discussed. A brief overview of the pertinent alkali metal and sulfur chemistry is given in the second part.

2.1 CFFF Background

2.1.1 CFFF Description

The CFFF was constructed on the University of Tennessee Space Institute campus as part of a program to investigate the performance and durability of the downstream components of a MHD (Magnetohydrodynamic) commercial power generation system. The overall facility is shown in Figure 2-1 (reproduced from [6]). The facility operation and program objectives are documented in reference [7].

Primary combustion in the CFFF occurred in the vitiation heater (A) and the main combustor (B). The combustor pressure was nominally 90 psia. Fuel oil and air were burned under fuel-lean conditions in the vitiation heater to raise the temperature of the main combustor air. Oxygen was added to the vitiation heater exhaust and mixed with pulverized coal in the main combustor. The coal and oxygen burned in the main combustor under fuel-rich conditions. The nominal temperature in the primary combustor for these conditions was 2900 K.

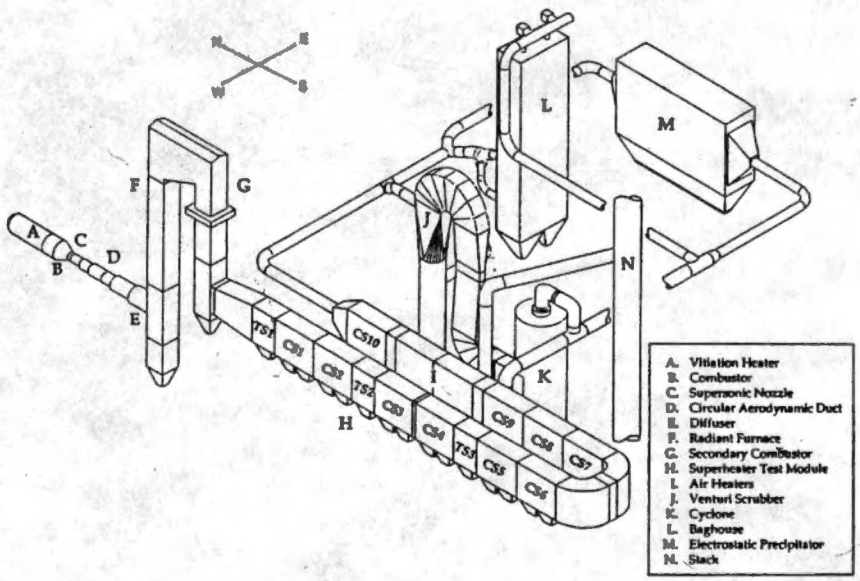

Figure 2-1 Coal-Fired Flow Facility (CFFF) [6].

However, ionization of the coal combustion products at this temperature did not provide the electrical conductivity required for the MHD process. The addition of an alkali metal salt to the pulverized coal provided a source of easily ionizable alkali metal atoms in sufficient quantity to provide the required electrical conductivity. The primary combustor was operated fuel-rich to reduce the formation of alkali oxides and hydroxides, and to greatly reduce the production of nitrogen oxides. Potassium carbonate (K_2CO_3) was used as the seed compound for all testing at the CFFF. Potassium seed was added to achieve the required plasma conductivity, nominally potassium made up 1% of the total mass.

Following combustion, the high-pressure combustion products were expanded supersonically (C) through the simulated MHD channel (D). The high velocity, conductive stream would normally flow through the magnetic field surrounding the MHD channel, but this was not present in the CFFF. The MHD channel was replaced by a 'channel simulator' duct that reduced the flow enthalpy properly by heat losses. Total pressure losses were achieved by shock-boundary layer aerodynamics. After the channel simulator, the stream was decelerated through a step-diffuser (E) to low speed and a slightly sub-atmospheric pressure at the entrance to the radiant furnace (F). The radiant furnace performed two functions: heat extraction and slag rejection. The water-cooled walls of the radiant furnace served as a boiler to produce steam for power generation. As the gas cooled in the furnace, various slag components condensed and fell to the slag trap below the furnace. The gases entered the radiant furnace at about 2000 K and left the furnace at between 1400 K and 1100 K.

The secondary combustor (G) followed the radiant furnace. The primary combustor exhaust gas was fuel-rich, as previously explained. Thus, further combustion of the exhaust gas and heat extraction was possible. This was accomplished in the secondary combustor. Heated air was added to the exhaust gas so that the resulting mixture was slightly fuel-lean. The temperature of the mixture was such that the CO/H_2 mixture should spontaneously ignite. The combustion proceeds along the duct before reaching the final heat extraction section of the CFFF (H). The superheater test module section of the CFFF

extracted the heat from the fully oxidized gas to achieve nominal steam plant conditions for steam turbines. Following the superheater were the emissions control devices (J-M). These components are not considered in this work and will not be discussed further.

2.1.2 Secondary Combustor

Secondary combustor operation, including flame stability characteristics, was the original motivation for this investigation and will now be described in greater detail. The secondary combustor is shown in detail in Figure 2-2 (reproduced from [8]). The design of the combustor is described in detail in [8]. The combustor was a refractory-lined water-cooled duct. The entrance to the combustor was a four-foot square duct. Following the entrance, two opposite walls of the duct formed a convergence (~25°). A row of air injection holes was located near the throat of this convergence, across each of the converging walls. These holes injected heated air into the combustor at an angle of 60° relative to the duct centerline.

Secondary combustor inlet and outlet temperature and outlet CO concentration were routinely monitored to ensure that an accumulation of a combustible mixture would not occur in the superheaters. The inlet concentration of CO was nominally 10% (by mole) with the specific level depending on primary combustor

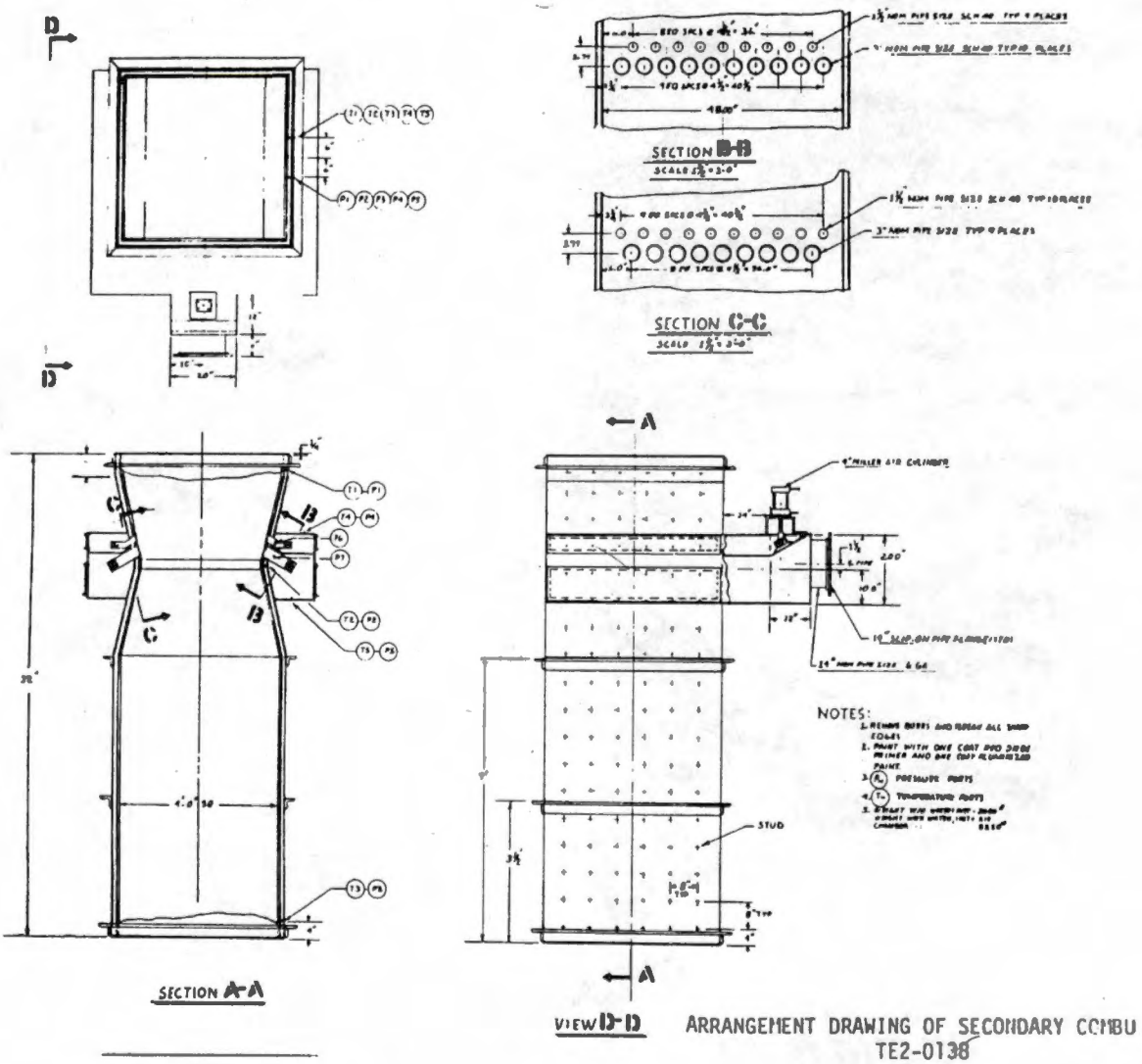

Figure 2-2 Secondary combustor drawing [8].

stoichiometry. The secondary combustor was said to be operating properly when the CO outlet concentration was less than about 1000 ppm (dry basis).

2.1.3 Secondary Combustor Anomaly

Proof-of-Concept testing at the CFFF was conducted in two major test series, identified as LMF4 [9] and LMF5 [10] (LMF means Low Mass Flow). Test series LMF4 was conducted using Eastern coal. Test series LMF5 was conducted using Western coal. The objectives of the individual test series were to determine the operational characteristics and performance of the CFFF. Several performance differences between the tests were identified that may be directly related to the coal composition. The operation of the secondary combustor is a particular example.

The constituents of coal vary significantly depending on the conditions under which the coal was initially formed. Thus coal composition can depend on the geographic location of a mine and on the location of the coal within a specific mine. Testing at the CFFF used coal from two geographic regions. For this work, coal obtained from various mines in the state of Illinois is referred to as Eastern coal, whereas coal obtained from various mines in the state of Montana is referred to as Western coal. Differences in constituents of Eastern and Western coals include carbon/hydrogen (C/H) ratio, sulfur content, reactivity (oxygen content) and inorganic content (ash) (Tables 2-1 and 2-2, respectively.)

Table 2-1 Eastern coal composition [11].

Constituent	Mass Percentage[1]
C	0.7984
H	0.0546
N	0.0167
S	0.0312
O	0.0991

[1]Does not include moisture (3%) or ash (10.2%)

Table 2-2 Western coal composition [12].

Constituent	Mass Percentage[1]
C	0.7412
H	0.0504
N	0.0122
S	0.0079
O	0.1883

[1]Does not include moisture (6.3%) or ash (10.5%)

Prior to the LMF5 series of tests in the CFFF, the secondary combustor had operated reliably. A review of LMF4 test logs uncovered no record of anomalous secondary combustor operation for the LMF4 series of tests. However, the secondary combustor did not ignite at the nominal test point during LMF5-E [1]. During LMF5-E, prior to the introduction of coal-flow (fuel oil combustion only), the secondary combustor inlet temperature was about 1510° F (1095 K). At this condition, the outlet CO concentration was less than 1000 ppm. When coal flow (and seed flow) was established, the secondary combustor inlet temperature was about 1700° F (1200 K) but, the outlet CO concentration was greater than 10,000 ppm. This problem was noted again during test LMF5-H. These observations prompted additional experiments to determine the ignition characteristics of the

secondary combustor as a function of temperature and potassium concentration. These experiments were conducted during tests LMF5-I and LMF5-J.

The CFFF was configured differently for the LMF5 series of test in that the potassium carbonate seed was delivered as an aqueous solution while K_2CO_3 was delivered as a solid along with the pulverized coal during LMF4. This configuration allowed for simple variation of the potassium concentration. Changing coal flow (with fixed stoichiometry) varied secondary combustor inlet temperature; increasing coal flow increased temperature, decreasing coal flow decreased temperature. The experiments were performed at fixed stoichiometry and fixed combustor inlet temperature while potassium concentration was increased in discrete steps until combustion in the secondary combustor was extinguished. This kind of experiment was not possible during LMF4.

Potassium content is parameterized as the K_2/S molar ratio. Since potassium will combine with sulfur dioxide (SO_2, a major pollutant) to produce the condensed-phase sulfate, K_2SO_4(c), effectively removing SO_2 from the gas phase, this parameterization was useful in MHD research and is used here. The results of the seed-flow variation experiments conducted during the LMF5-I and LMF5-J tests are shown in Tables 2-3 through 2-6. In these tables, the following symbols are used:

$\phi_{PRIMARY}$ = primary combustor stoichiometric ratio $\equiv (O_2)_{ACTUAL}/(O_2)_{STOICHIOMETRIC}$

$\phi_{OVERALL}$ = overall system stoichiometric ratio

Table 2-3 LMF5-I experiment summary T_{SCI} = 1640° F.

K_2/S Ratio	$\phi_{PRIMARY}$[1]	$\phi_{OVERALL}$[1]	T_{SCI} (°F)[2]	T_{SCO}(°F)[2]	ΔT_{SC} (°F)	$[CO]_{SCO}$[3]
0.00	0.911	1.013	1634	1817	183	948
1.48	0.913	1.020	1626	1810	184	1439
2.28	0.909	1.002	1627	1750	126	>10000

a. $\phi_{PRIMARY}$ = 0.91

K_2/S Ratio	$\phi_{PRIMARY}$[1]	$\phi_{OVERALL}$[1]	T_{SCI} (°F)[2]	T_{SCO}(°F)[2]	ΔT_{SC} (°F)	$[CO]_{SCO}$[3]
0.00	0.863	1.020	1639	1960	322	1607
1.47	0.863	1.018	1633	1946	313	3801
2.29	0.863	1.017	1636	1897	261	6959
3.35	0.870	1.028	1635	1620	-15	>10000

b. $\phi_{PRIMARY}$ = 0.86

K_2/S Ratio	$\phi_{PRIMARY}$[1]	$\phi_{OVERALL}$[1]	T_{SCI} (°F)[2]	T_{SCO}(°F)[2]	ΔT_{SC} (°F)	$[CO]_{SCO}$[3]
0.00	0.815	1.031	1654	2172	518	333
1.29	0.816	1.029	1640	2183	543	439
2.21	0.818	1.030	1656	2162	506	150
3.17	0.815	1.022	1644	2171	67	>10000

c. $\phi_{PRIMARY}$ = 0.82

[1] Based on system inputs
[2] Corrected for radiation losses
[3] Dry CO concentration

Table 2-4 LMF5-I experiment summary T_{SCI} = 1920° F.

K_2/S Ratio	$\phi_{PRIMARY}$[1]	$\phi_{OVERALL}$[1]	T_{SCI} (°F)[2]	T_{SCO}(°F)[2]	ΔT_{SC} (°F)	$[CO]_{SCO}$[3]
0.00	0.935	1.003	1944	1883	-61	1646
1.76	0.940	1.008	1939	1856	-83	1479
3.80	0.951	1.020	1937	1850	-88	887

a. $\phi_{PRIMARY}$ = 0.94

K_2/S Ratio	$\phi_{PRIMARY}$[1]	$\phi_{OVERALL}$[1]	T_{SCI} (°F)[2]	T_{SCO}(°F)[2]	ΔT_{SC} (°F)	$[CO]_{SCO}$[3]
0.00	0.893	1.029	1934	2090	156	511
1.37	0.887	1.020	1925	2090	165	1401
2.41	0.883	1.016	1917	2003	86	1585
3.38	0.880	1.010	1911	1986	65	507
4.47	0.897	1.030	1910	2038	128	537

b. $\phi_{PRIMARY}$ = 0.89

K_2/S Ratio	$\phi_{PRIMARY}$[1]	$\phi_{OVERALL}$[1]	T_{SCI} (°F)[2]	T_{SCO}(°F)[2]	ΔT_{SC} (°F)	$[CO]_{SCO}$[3]
0.00	0.833	1.020	1928	2305	376	782
1.62	0.820	1.006	1922	2320	397	561
3.38	0.829	1.013	1906	2268	363	651

c. $\phi_{PRIMARY}$ = 0.83

[1] Based on system inputs
[2] Corrected for radiation losses
[3] Dry CO concentration

Table 2-5 LMF5-I experiment summary T_{SCI} = 2140° F.

K_2/S Ratio	$\phi_{PRIMARY}$[1]	$\phi_{OVERALL}$[1]	T_{SCI} (°F)[2]	T_{SCO}(°F)[2]	ΔT_{SC} (°F)	$[CO]_{SCO}$[3]
0.00	0.924	1.061	2149	2336	187	417
1.40	0.917	1.041	2140	2332	192	635
3.29	0.922	1.046	2138	2328	191	324

a. $\phi_{PRIMARY}$ = 0.92

K_2/S Ratio	$\phi_{PRIMARY}$[1]	$\phi_{OVERALL}$[1]	T_{SCI} (°F)[2]	T_{SCO}(°F)[2]	ΔT_{SC} (°F)	$[CO]_{SCO}$[3]
0.00	0.868	1.068	2158	2515	358	276
1.56	0.861	1.059	2141	2519	378	92
3.26	0.864	1.057	2138	2485	348	118

b. $\phi_{PRIMARY}$ = 0.86

[1] Based on system inputs
[2] Corrected for radiation losses
[3] Dry CO concentration

Table 2-6 LMF5-J experiment summary.

K_2/S Ratio	$\phi_{PRIMARY}$[1]	$\phi_{OVERALL}$[1]	T_{SCI} (°F)[2]	T_{SCO}(°F)[2]	ΔT_{SC} (°F)	$[CO]_{SCO}$[3]
0.00	0.856	1.005	1684	1941	257	1684
1.26	0.859	1.019	1681	1924	243	1184
2.55	0.852	1.005	1683	1918	236	3554
3.66	0.858	1.001	1682	1697	14	>10,000
4.81	0.859	1.001	1683	1672	-10	>10,000

a. T_{SCI} = 1680° F

K_2/S Ratio	$\phi_{PRIMARY}$[1]	$\phi_{OVERALL}$[1]	T_{SCI} (°F)[2]	T_{SCO}(°F)[2]	ΔT_{SC} (°F)	$[CO]_{SCO}$[3]
2.59	0.816	1.033	1738	2053	315	35
3.72	0.808	1.020	1701	1770	69	>10,000
4.66	0.818	1.031	1707	1799	92	>10,000
4.63	0.819	1.032	1712	1891	178	672
5.03	0.820	1.031	1723	2048	325	16

b. T_{SCI} = 1700° F

K_2/S Ratio	$\phi_{PRIMARY}$[1]	$\phi_{OVERALL}$[1]	T_{SCI} (°F)[2]	T_{SCO}(°F)[2]	ΔT_{SC} (°F)	$[CO]_{SCO}$[3]
5.81	0.861	0.990	1758	1951	193	0

c. T_{SCI} = 1760° F

[1] Based on system inputs
[2] Corrected for radiation losses
[3] Dry CO concentration

T_{SCI} = Secondary combustor inlet temperature

T_{SCO} = Secondary combustor outlet temperature

$\Delta T_{SC} = T_{SCO} - T_{SCI}$

$[CO]_{SCO}$ = Secondary combustor outlet CO concentration

Additionally, they are shown graphically in Figures 2-3 through 2-6. It is clear that, for combustor inlet temperatures below about 1700° F (1200 K) and K_2/S above about 3, combustion did not occur. However, at higher temperatures and lower values of K_2/S, combustion was robust.

Because no difficulties of this type were experienced during the LMF4 test series, it was reasoned that a possible cause of this problem was the use of Western coal. Sulfur content is distinctly different between Eastern and Western coals. Typically, Eastern coals contain 2% to 5% (by weight) sulfur, while Western coals contain less than 1% sulfur. Specific values for the LMF4-R test and the LMF5-H test are shown in the previous tables. It was hypothesized that the high sulfur content of the Eastern coal used during LMF4 "tied up" the potassium in stable K/S compounds so that free potassium was not able to participate in the "catalytic" radical consumption cycle known to inhibit combustion (described in Section 2.2.1). For the low-sulfur Western coal used in LMF5, more free potassium could be available for flame inhibition. Testing this hypothesis is the objective of this work.

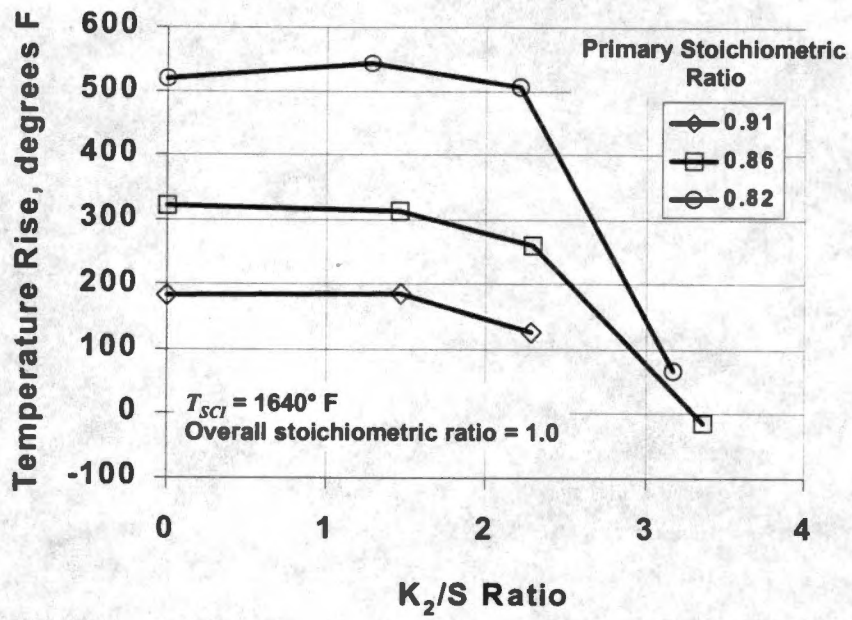

Figure 2-3 Secondary combustor temperature rise (From Table 2-3).

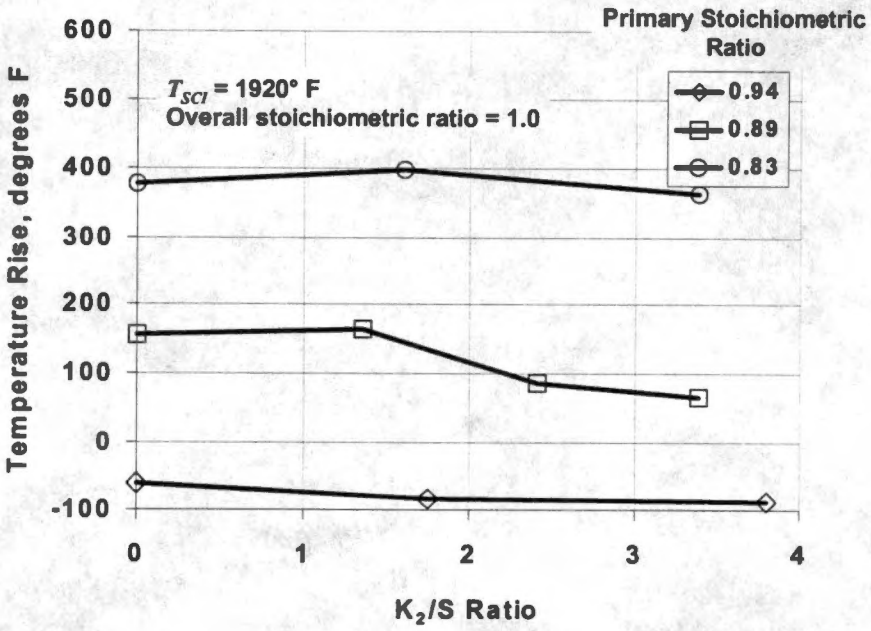

Figure 2-4 Secondary combustor temperature rise (From Table 2-4).

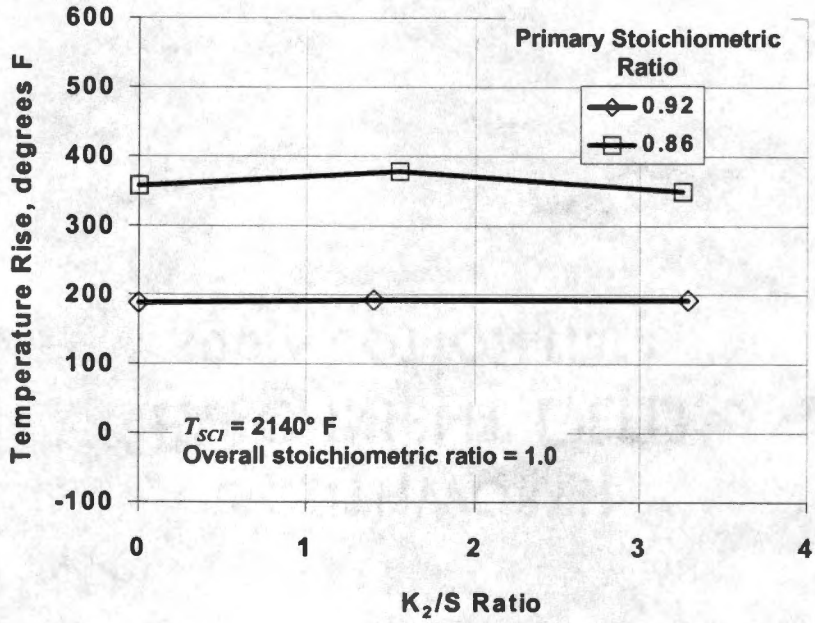

Figure 2-5 Secondary combustor temperature rise (From Table 2-5).

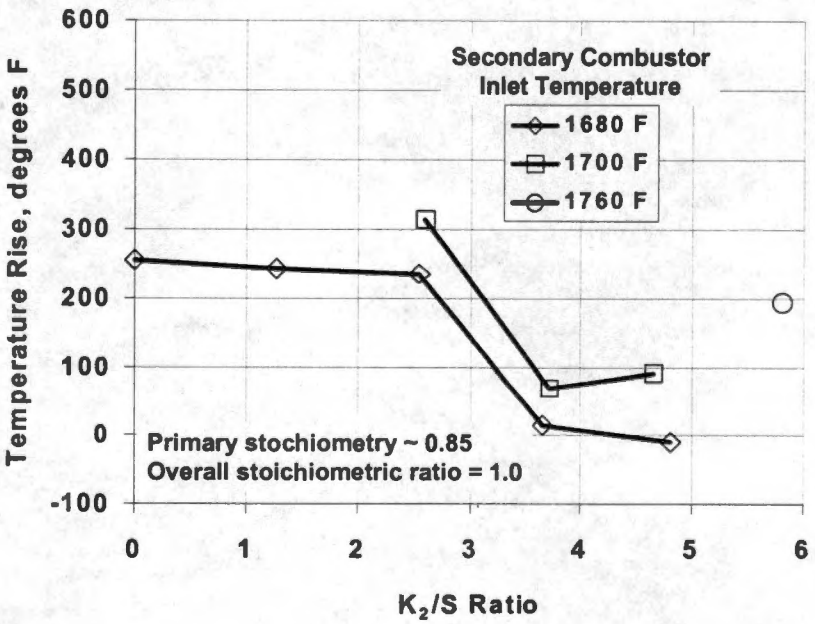

Figure 2-6 Secondary combustor temperature rise (From Table 2-6).

The next section gives an overview of the prior state of knowledge of the chemistry of alkali metals and sulfur in combustion.

2.2 Background Chemistry

Alkali metal chemistry and sulfur chemistry have been extensively investigated. In this section, a brief review of the literature content is given. More detailed reviews are given in Section 5. (Note – reaction numbers are given by the ordering of reactions used in calculations described in Section 5. The complete K/S reaction mechanism is included in Appendix A.)

2.2.1 Alkali-Metal Chemistry

Alkali metals have long been known to inhibit the propagation of flames. Potassium and sodium have been used in the past for suppression of ignition of explosive mixtures in mines, rocket motor afterburning, muzzle flash, and have been used in dry powder fire extinguishers [3]. Friedman and Levy [3] investigated fuel-rich opposed-jet methane flames seeded with various alkali metal salts. In this early work, the objective was to determine if the alkali-metal interaction with gaseous species took place homogeneously or heterogeneously. Since the added salts were known to volatilize in the flame, any observed inhibition would be attributed to a homogeneous interaction. They observed that KOH was a slightly more effective inhibitor than any of the salts. They reasoned that the inhibition mechanism must include KOH in simple bimolecular

processes. They correctly identified a major path for consumption of flame radicals:

$$KOH + H \Rightarrow K + H_2O \qquad (16)$$

$$KOH + OH \Rightarrow KO + H_2O \qquad (17).$$

Their reasoning showed that these bimolecular processes must be fast compared to the only viable three-body process involving K and OH that they knew of, namely:

$$K + OH + M \Rightarrow KOH + M \qquad (2).$$

James and Sugden [13] investigated the addition of alkali metals to fuel-rich flames to infer the populations of certain flame radicals. They concluded that reactions (16) and (17) are equilibrated in high-temperature flames. (That is, the relative species concentrations of K, OH, KOH, KO, and H_2O were related by the equilibrium constants at the flame temperature.)

Kaskan [14] investigated the conclusions of Freidman and Levy [3] and James and Sugden [13] by observing the behavior of potassium in very fuel-lean hydrogen/oxygen flames and found that he was forced to discard the assumption that reactions (16) and (17) were equilibrated. He proposed the three-body reaction:

$$K + O_2 + M \Rightarrow KO_2 + M \qquad (1)$$

to explain his data. Later Carabetta and Kaskan [15] investigated potassium and sodium in low-pressure hydrogen/oxygen flames to verify the three-body nature of the potassium concentration decay. However, lack of confidence in the

structure and stability of the KO_2 molecule prevented proper rate determinations for this reaction.

Jensen et al [16] sought to quantify the mechanism for flame inhibition put forward by Freidman and Levy [3]. They acquired new data for potassium and sodium decay in fuel-rich hydrogen/oxygen flames. They explained their potassium data via the cycle:

$$K + OH + M \Rightarrow KOH + M \quad (2)$$

$$KOH + H \Rightarrow K + H_2O \quad (16)$$

and noted that this cycle was, in a sense, catalytic: KOH consumes H via reaction (16) and is latter recycled back to KOH via reaction (2). In a latter reference, Jensen [17] analyzed Kaskan's [14] results and reported that this mechanism could also be invoked to explain the Kaskan's data, assuming that the superoxide (KO_2) bond energy was low enough, thereby closing the alternate path (reaction (1)) for K consumption.

Up to Jensen's investigation [17], the investigations of alkali metal kinetics had primarily concerned fuel-rich flames at high temperature. Only the limited data of Kaskan ([14,15]) considered fuel-lean, cooler flames. Hynes, Steinberg and Schofield [18] investigated sodium oxidation in a large number of atmospheric pressure fuel-lean hydrogen/oxygen flames at various temperatures. They constructed a complex network of simple bimolecular reactions and reasonable three-body reactions involving the species Na, NaO, NaO_2, and NaOH. They fit

their data by varying the bond dissociation energy, D_0(Na-O_2), and the rates of each of the reactions in their network. They found that a 17-step mechanism could be used to explain their data (Figure 2.7), with five reactions controlling the network (here, the 'a' in the reaction number indicates the sodium analog of the equivalent potassium reaction),

$$Na + O_2 + M \Rightarrow NaO_2 + M \qquad (1a)$$

$$NaO_2 + H \Rightarrow NaO + OH \qquad (11a)$$

$$NaO + H_2 \Rightarrow NaOH + H \qquad (13a)$$

$$NaOH + H \Rightarrow Na + H_2O \qquad (16a)$$

$$Na + OH + M \Rightarrow NaOH + M \qquad (2a)$$

They set D_0(Na-O_2) at 48 kcal/mole, in agreement with Jensen [17]. However, in subsequent analysis ([19]), they modified their kinetic analysis and found that the best fit required D_0(Na-O_2) be raised to 58 kcal/mole.

Similar work was performed by Slack, et al ([20]) for potassium addition to methane/oxygen/nitrogen/argon flames. Their findings were in agreement with those of Hynes, et al, [18] and the mechanism selected was:

$$K + O_2 + M \Rightarrow KO_2 + M \qquad (1)$$

$$KO_2 + H \Rightarrow KO + OH \qquad (11)$$

$$KO + H_2 \Rightarrow KOH + H \qquad (13)$$

$$KOH + H \Rightarrow K + H_2O \qquad (16)$$

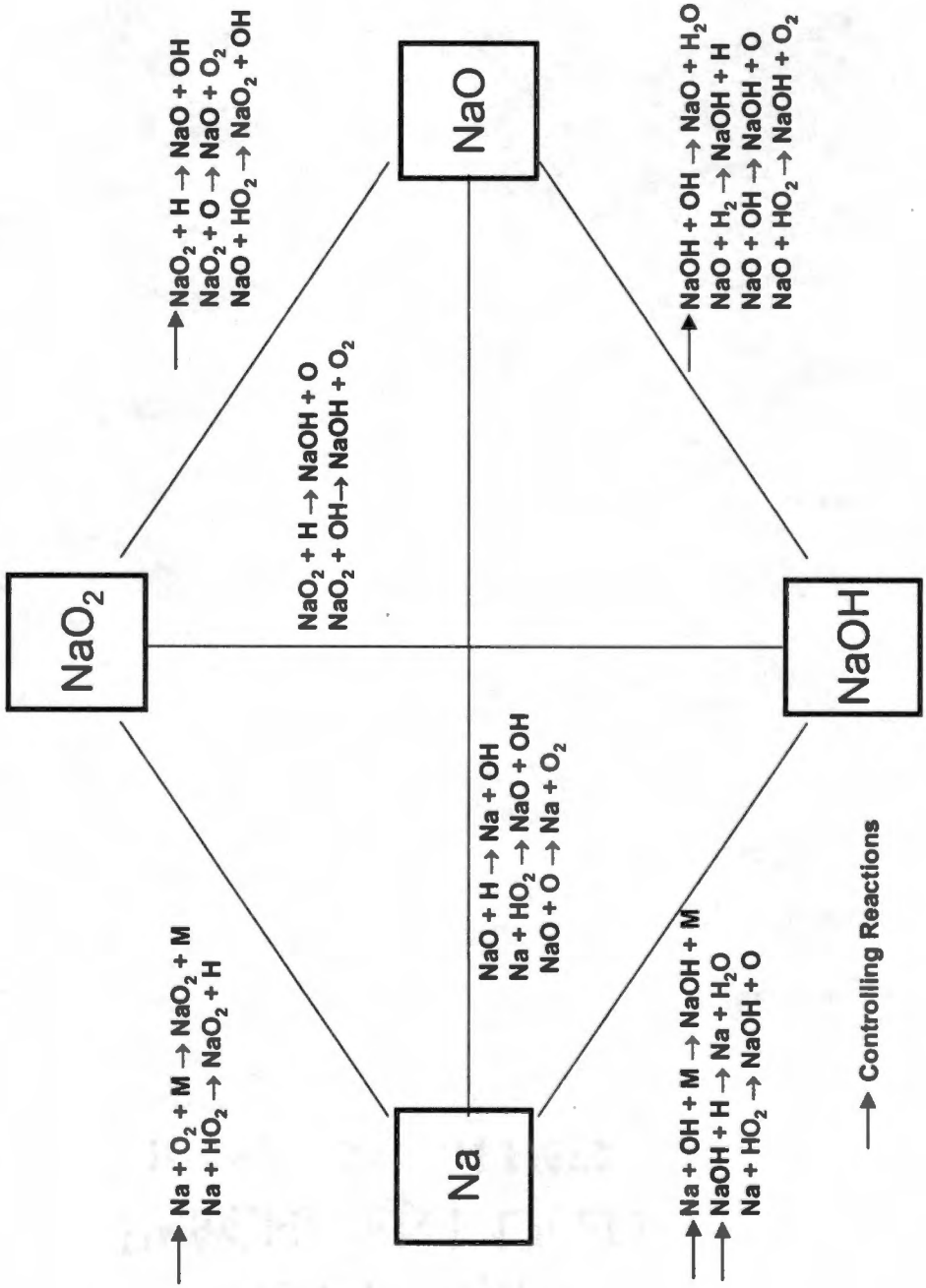

Figure 2-7 Sodium oxidation chemistry proposed by Hynes, et al [18].

$$K + OH + M \Rightarrow KOH + M \quad (2)$$

This mechanism and the corresponding reaction rates and thermodynamics will be discussed in more detail in Section 5. There, specific changes will be made based on a detailed review of this and other literature.

2.2.2 Sulfur Chemistry

In an effort to understand the nature of the termolecular recombination reactions in the post-flame gases of H_2/O_2 flames, McAndrew and Wheeler [21] added CO_2, N_2, and SO_2 to C_3H_8/O_2 flames. It was observed that the presence of SO_2 increased the decay rate of H atoms by a factor of 20. A very general explanation of this phenomenon was postulated. However specific mechanistic details were not provided.

Webster and Walsh [4] first investigated sulfur chemistry at high temperatures in connection with the inhibition of H_2/O_2 explosions. They found that addition of sulfur dioxide, SO_2, changed the second explosion limit of H_2/O_2 mixtures and proposed that this effect was due to the consumption of hydrogen atoms by the reaction

$$H + SO_2 + M \Rightarrow HSO_2 + M \quad (34)$$

Fenimore and Jones [22] investigated the recombination of flame radicals in H_2/O_2 flames and assigned a rate to reaction (34) and proposed the following steps to complete a catalytic cycle:

$$H + HSO_2 \Rightarrow H_2 + SO_2 \quad (36)$$

$$OH + HSO_2 \Rightarrow H_2O + SO_2 \qquad (37)$$

Their results were somewhat speculative because of uncertainties in the bond energy and structure of the product (HOSO v. HSO_2). Kallend [23], Halstead and Jenkins [24], Durie, et al [25], and Kallend [26] further investigated this catalytic cycle. This mechanism is currently generally accepted as the predominant source of radical recombination in sulfur bearing flames. However many kinetic details remain uncertain.

Muller, et al [27] made detailed measurements of sulfur species and flame radicals in fuel-rich H_2/O_2 flames with up to 2% H_2S added. They sought to verify the various H/S/O equilibrium assumptions put forth by Fenimore and Jones [22]. Their data confirmed the equilibrium suggested by the prior authors. Most importantly, they assembled a relatively complete H/S/O mechanism that has served as the starting point for further work.

Kramlich, et al [28] investigated sulfur addition in a jet-stirred reactor burning H_2/O_2 and CH_4/O_2 under fuel-rich and fuel-lean conditions. Their observations indicated that SO_2 was the dominant sulfur species in all conditions (fuel-rich or fuel-lean). This concurred with previous analyses ([23]-[27]). In the fuel-rich H_2/O_2 flames, the alternate sulfur product was H_2S. In the fuel-rich CH_4/O_2 flames, sampling measurements indicated that CS_2 and COS were preferred over H_2S. However, kinetic analysis showed that these species were formed in the sample probe, presumably due to reaction on the probe walls.

Smith, et al [29], Tseregounis and Smith [30], and Wendt, Wooten and Corley [31], each investigated radical recombination in flames bearing sulfur in an effort to unravel the chemistry of fuel-bound nitrogen. In each case, the sulfur oxidation mechanism of Muller [27] was further updated. Most recently, Zachariah and Smith [32] extensively revised the Muller mechanism during their investigation of low-pressure H_2/O_2 flames with SO_2 added. They generated sulfur species profiles using their updated mechanism in a reacting flow model and compared the theory to the experimental data with good results. They did not measure flame radicals in their experiment and were therefore not able to test the modeling of flame radical decay predicted by the model, and therefore could not establish the rates of reactions (34), (36), and (37).

Pauwels et al [33] investigated stoichiometric methanol/oxygen/nitrogen flames seeded with H_2S. They measured temperature, [OH], [O], [H], and major flame species. They developed a "reduced" version of Zachariah's [32] sulfur-catalyzed radical recombination mechanism and applied it to their data using a laminar flame model. They were not able to reproduce the flame radical decay they observed in their sulfur bearing flames. The complete Zachariah mechanism was also unable to reproduce the observed behavior.

Glarborg, et al [34] investigated the impact of SO_2 on CO oxidation in a flow reactor. As part of the investigation, they developed an extensive H/S/O

mechanism. The mechanism appeared to improve the modeling of the CO-oxidation and SO_3/SO_2 chemistry. However, many of the additional reaction rates were determined theoretically with little experimental foundation.

The sulfur-catalyzed radical recombination aspects of sulfur chemistry are important to the problem at hand. The basic mechanism proposed by Fenimore and Jones [22] remains intact. The rates and thermodynamics of these reactions remain uncertain. A full discussion of the recommended sulfur mechanism is given in Section 5.4.

2.2.3 Alkali-Metal/Sulfur Coupling

The possibility of the formation of compounds of alkali metals and sulfur species has been investigated by a few authors, usually in connection with the formation of suflates and corrosion. Fenimore [35] added SO_2 and Na to fuel-lean H_2/O_2 flames and observed the decrease in Na atoms in the post flame gases. He felt that his data could be explained by the reaction

$$NaOH + SO_2 \Rightarrow NaSO_2 + OH \qquad (53a).$$

Durie [36] performed further experiments in fuel-rich and fuel-lean C_3H_8/Air flames, monitoring Na and H atom decays in the post-flame gases. He described the reactions

$$NaOH + S \Rightarrow NaS + OH \qquad (56a)$$

$$NaOH + SO_3 \Rightarrow NaSO_3 + OH \qquad (No\ K\ Analog).$$

However, the justification of these processes was highly approximate and speculative.

Schofield and Steinberg [37] measured OH and Na in several fuel-rich and fuel-ean H_2/O_2 flames. They constructed a large network of reactions involving many Na/S species and fit their data by adjusting the thermodynamics and rates of each of these reactions in a manner very similar to that employed in their work with Na/O kinetics (Hynes, et al, [18]). They found that $NaSO_2$ was the most significant Na/S species in fuel-lean flames and that NaOS was the most significant Na/S in fuel-rich flames. However, no Na/S species was present in quantities greater than about 1/10 [Na] or [NaOH] in any flames. Nevertheless, the Na/S kinetics were required to account for the observed Na decay.

2.3 Secondary Combustor Chemistry

Li [6] examined the equilibrium chemistry of the entire CFFF flow train, including K/S species (KS, K_2SO_4(g), K_2SO_4(c)). The study [6] discussed calculations for Eastern coal. Regarding the secondary combustor, the study concluded that, in the flow entering the secondary combustor, potassium is predominantly in the form of KOH and sulfur is in the form of H_2S. After the secondary combustor, both potassium and sulfur are bound together as K_2SO_4. This study did not address the complete temperature and species concentration history or mechanism of the potassium-sulfur compound formation throughout the entire

secondary combustor. Rather, the results focus on equilibrium distribution of potassium and sulfur species in the secondary combustor.

Lewis, et al performed kinetic calculations for the secondary combustor, before the secondary combustor was fully designed [5]. The conclusion of these calculations was that both potassium and sulfur acted to inhibit the consumption of CO and H_2 in the secondary combustor. In fact, sulfur was stated to have the more significant impact on flame inhibition. Lewis, et al [5], did not include finite rate interaction of K and S species. Further, in light of recent (including this work) determinations of rate constants and thermodynamics for K and S chemistry, the conclusions of this reference should be reinvestigated.

Before the present study, there had been no determination of a mechanism for the finite rate chemistry of potassium and sulfur. In order to assess the impact of K/S chemistry on the operation of the secondary combustor, K/S species thermodynamics, reaction mechanism and reaction rates needed to be determined. This is the focus of the work reported here. The results of experiments conducted to determine K/S kinetics, analysis of the data, and the application to the ignition problem of the secondary combustor are described in each of the following sections of this dissertation.

3.0 Experiment Apparatus and Sample Data

3.1 Introduction to the Experimental Program

The goal of this experiment and analysis is to produce and verify a kinetic reaction mechanism to describe the kinetic interaction of potassium and sulfur in a low-pressure combustion system. The post-flame burned gas of a laminar, premixed flame over a flat flame burner is a convenient environment for investigation of the kinetic aspects of combustion chemistry. Here, flame radicals are perturbed from equilibrium levels at the flame front and relax toward equilibrium as recombination proceeds. Observing this mixture as it approaches chemical equilibrium can reveal subtle changes in the path along which the mixture proceeds toward equilibrium. Since the flow is laminar and nearly isothermal, a one-dimensional analysis of these changes is possible.

In the present research, atmospheric pressure flat flames of mixtures of methane, nitrogen and oxygen were established over a burner constructed of bundled hypodermic tubing. A schematic of the experiment is shown in Figure 3-1. All flames had potassium added to the premixed gases (in the form of a nebulized solution of K_2CO_3 and H_2O). Some of the flames had sulfur added in the form of H_2S. Eight flames were monitored in pairs: four without sulfur and four with sulfur. The added potassium species was not high enough in concentration to significantly perturb the flame radicals. Gas flows were metered and controlled through calibrated rotometers. The potassium carbonate solution was metered through a calibrated nebulizer.

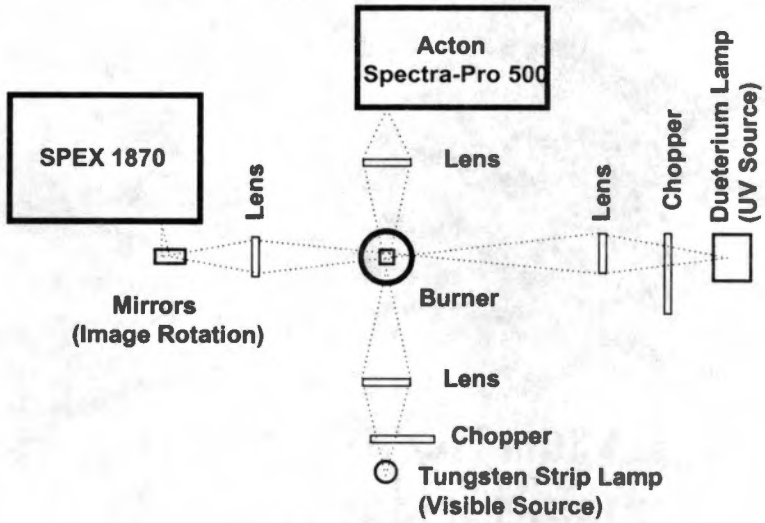

Figure 3-1 Experiment schematic.

OH concentration and K concentration were measured using absorption spectroscopy. Temperature was measured using the potassium line reversal technique. The OH measurement employed a deuterium lamp to create a stable UV source that was absorbed by the $P_1(5)$ rotational transition in the $OH(X^2\Sigma^+ - A^2\Pi)$ (v',v"=0,0) vibrational band. The potassium absorption measurement used a tungsten strip lamp to create a stable visible source for $K(^2S_{1/2}-^2P_{1/2})$ absorption. The line reversal temperature measurement also used the tungsten strip lamp source. [OH], [K], and temperature was measured at several locations above the burner surface, ranging from 0.5 mm to 10 mm above the burner. The flame front was established within 0.5 mm above the burner surface.

The kinetic interaction of potassium and sulfur involves several species that are transient and present in small quantities. These species are not easily detectable using available techniques; thus, it was not feasible to monitor all of the important and relevant species in these experiments. This situation is often encountered in studies of combustion kinetics and requires resources and methods beyond the scope of the present research effort. To overcome this deficiency, careful experiment design and judicious use of models was required. For these experiments, the added potassium was limited so that the flame radicals were essentially unperturbed, as determined by observing OH absorption with and without added potassium. For flames without sulfur, kinetic models show that the potassium tracks the flame radicals ([13]-[20]), predominantly through reactions like those suggested by Slack [20]:

$$K + O_2 + M \Rightarrow KO_2 + M \quad (1)$$

$$KO_2 + H \Rightarrow KO + OH \quad (11)$$

$$KO + H_2 \Rightarrow KOH + H \quad (13)$$

$$KOH + H \Rightarrow K + H_2O \quad (16)$$

$$K + OH + M \Rightarrow KOH + M \quad (2)$$

Sulfur has two effects on the flame radical species profiles. First, the sulfur will accelerate the decay of flame radicals (OH, O, H) ([21]-[34]), predominantly through the reactions:

$$H + SO_2 + M \Rightarrow HSO_2 + M \quad (34)$$

$$H + HSO_2 \Rightarrow H_2 + SO_2 \quad (36)$$

$$OH + HSO_2 \Rightarrow H_2O + SO_2 \qquad (37)$$

Second, the sulfur will interact with the alkali metal species, combining to produce species that did not exist in the non-sulfur bearing flames ([35]-[37]). For sulfur bearing flames, the fate of potassium will depend on the perturbed flame radicals and the extent to which potassium and sulfur combine.

The combustion of hydrocarbons, particularly saturated alkanes like methane, is well understood. The rates of the important chain-branching, chain-propagating and chain-terminating reactions have been measured or otherwise determined so that the system is well-determined [38]. It is known that the flame radicals (H, O, OH, CO) are tightly linked through fast bimolecular reactions. In fact, these radicals seem to be in equilibrium with each other (and CO_2, H_2, O_2, H_2O) at the flame temperature [39]. Thus, if the concentration of OH and the flame temperature are monitored, the flame radical system is determined.

The reactions describing the evolution of potassium and sulfur species are not of the same stature as those describing methane combustion. While the detailed picture of the kinetic chemistry is well established for hydrocarbon-air flames without sulfur, the reaction rates of individual reactions in the potassium oxidation mechanism are uncertain. However, by monitoring the decay of free potassium concentration in a flame, the distribution of potassium species and the kinetic flux between these species can be inferred. In fact, that is how the alkali-metal oxidation process was deduced [18]. Thus by measuring [OH] and [K] in the

flame, two strongly inter-related species in the kinetic chemistry of these flames is established. For flames with added sulfur, the two effects – radical scavenging by sulfur and K-S species production – can be separated to the extent that the sulfur radical scavenging mechanism in the model can account for the radical decay profiles. The mechanism of sulfur radical scavenging has been established (reactions (34)-(37), [23]-[26],[32]), however the thermodynamics of the species involved and the rates of the reactions are uncertain.

In this study, measurements of the initial mixture composition (fuel, oxidizer, additives), flame temperature profile, OH number density and K number density were used in conjunction with a detailed flame model to infer the values of the other species thought to be involved in the K/S interactions. This procedure followed a "brute force" method of sensitivity analysis. In the brute force method, reaction rate coefficients of selected reaction steps are varied one at a time around an expected value. As these rates are varied, the computed and measured profiles are compared. By considering the quality of the comparison, the reaction rate sensitivity coefficients, and the "kinetic flux" of species through the mechanism, the reaction rates in the mechanism can be adjusted or fine-tuned so that the comparison is improved. Sensitivity coefficitions are defined as:

$$S_{ij} = \frac{A_i}{Y_j^{Max}} \frac{\partial Y_j}{\partial A_i} \qquad (3.1)$$

where

Y_j = *j-th* species mass fraction, with $Y^{max}{}_j$ as the maximum mass fraction for the *j-th* species

A_i = *i-th* reaction pre-exponential factor

Thus, the sensitivity coefficient is the normalized influence coefficient of the j-th species to the *i-th* reaction. If S_{ij} is positive, then an increase of Ai would increase Y_j. The so-called kinetic flux is defined as the time rate of change of the *j-th* species in the *i-th* reaction:

$$\frac{dc_j}{dt} = -k_i c_j c_k \qquad (3.2)$$

where k_i is the rate constant for the *i-th* reaction and c_j and c_k are the concentrations of the reactant species in the *i-th* reaction. Note that the expression for the reverse process results in the production of the *j-th* species. When the comparison is deemed satisfactory, one has a tentative mechanism that must be tested by comparison to other experimental results and in practical use.

The construction, calibration and operation of each of the experimental components are described in the following sections. The analysis of the resulting data is described in sections 4 and 5.

3.2 Apparatus

3.2.1 Burner Design

Premixed flames are flames for which the fuel and oxidizer are mixed together prior to combustion. The mixture is passed though a burner apparatus and ignited upon exiting. A flame-front is stabilized on the burner through heat-release to the burner. The resulting flow of hot gases is a non-equilibrium mixture of combustion products at a nearly constant temperature. For flame chemistry research, burner-stabilized, laminar flat flames to which an aqueous solution can be added are needed. Padley and Sugden [40] first described burners of this type. Their burner was a cylindrical construction that provided separate cavities for the premixed fuel and oxidizer and an inert shield gas. The premixed fuel and oxidizer were fed to a central, cylindrical bundle of hypodermic tubes. The inert shield gases were fed to a separate bundle of hypodermic tubes. This construction allowed various atomized additives to be fed to the central core of tubes along with the premixed gases. The resulting flame front is actually composed of several small premixed flames (one for each hypodermic tube) which are slightly concave toward the burner surface. Additionally, the small diameter of the hypodermic tubes maintains a laminar character within the tube.

A Padley and Sugden burner was designed and constructed for these experiments. In this case, the tube bundle was constructed as a rectangular array rather than a circular array. The central tube bundle was constructed from

regular hexagonally-packed group of 0.04 in ID (0.0625 in OD) stainless steel tubes six inches long. The tube bundle for the inert gas shield was constructed of similar tubes three inches long. The inner tube bundle was composed of 281 tubes, resulting in an area of 2.4 cm by 2.7 cm. The inert gas shield tubes formed a strip around the central bundle approximately 0.6 cm wide.

The tubes of the central tube bundle and the outer tube bundle were fastened together using JB Weld™ epoxy. The central tube bundle was first assembled in a jig that allowed the tubes to be placed side to side, one at a time, until a row was completed. At the completion of a layer of tubes, a new layer was begun, the new tubes being placed between each of the tubes of the previous layer. Tubes were placed in this way until the entire central core was completed. The outer tube bundle was formed in a similar way. After one side of the outer tube bundle was completed (four layers of four tubes), the central core tube bundle was added. The remaining tubes of the outer bundle were then placed around the central tube bundle. The resulting tube bundle (Figure 3-2) was sealed by the epoxy so that no gases could flow into the interstitial volume within the tube bundle. The fabricated tube bundle was held in an autoclave at 250° C for three weeks in order to drive off volatile compounds in the tube bundle and cured epoxy.

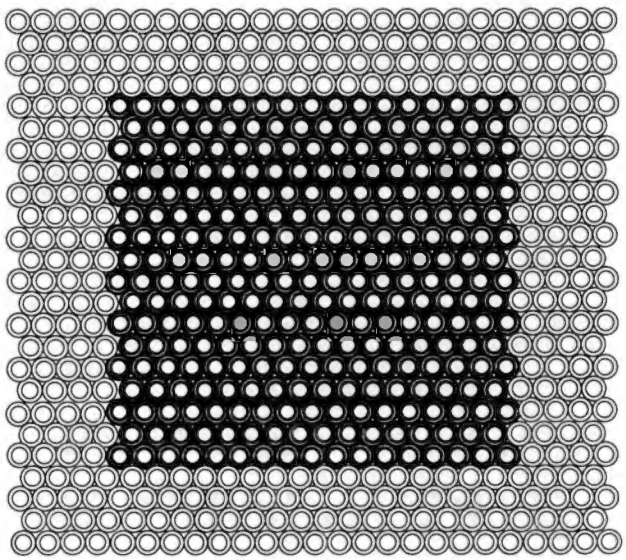

Figure 3-2 Tube pattern at burner surface. Heavy circles indicate reactant flow passages. Light circles indicate shield flow passages.

A burner housing was constructed to support the tube bundles and to form cavities for the premixed gases and the inert gas. The burner housing was fabricated from a six-inch diameter thick-walled aluminum pipe. The burner housing was formed in four sections. The sections were threaded together.

Between each threaded section a separator was placed to isolate the individual cavities. The upper separator divided the upper cavity and the inert gas cavity. The lower separator divided the inert gas cavity and the premixed reactant cavity. The separators included grooves machined for o-rings and rectangular openings

to accommodate the tube bundles. An exploded view of the burner components is shown in Figure 3-3.

Fittings were provided to add the reactant and inert gases. Perforated mixing rings provided a means of distributing the reactant gases inside the cavity. Figure 3-4 shows the assembled burner. The tube bundle was epoxied into the rectangular openings of the separators, the perforated rings were added and the tube sections were threaded together to compress the o-rings. Finally, potting the tube bundle into the burner cap and separators with epoxy sealed the tube bundle.

3.2.2 Flowmeters

The volume flowrate of the gases to the burner was metered using rotometers (Cole-Parmer). Rotometers were selected so that the gas flow requirements were near mid-range of the individual rotometers. The rotometers used for each of the gases are tabulated in Table 3-1. The nebulizer (described in the section 3.2.3) required a high-pressure (60-70 psig) driver gas. Nitrogen gas was used for this purpose; thus the N_2 flowmeter was operated at 60 psig throughout the experiment.

The flowmeters included precision valves that allowed the flow rate to be set precisely. The valves and flowmeter housings were made of aluminum for O_2,

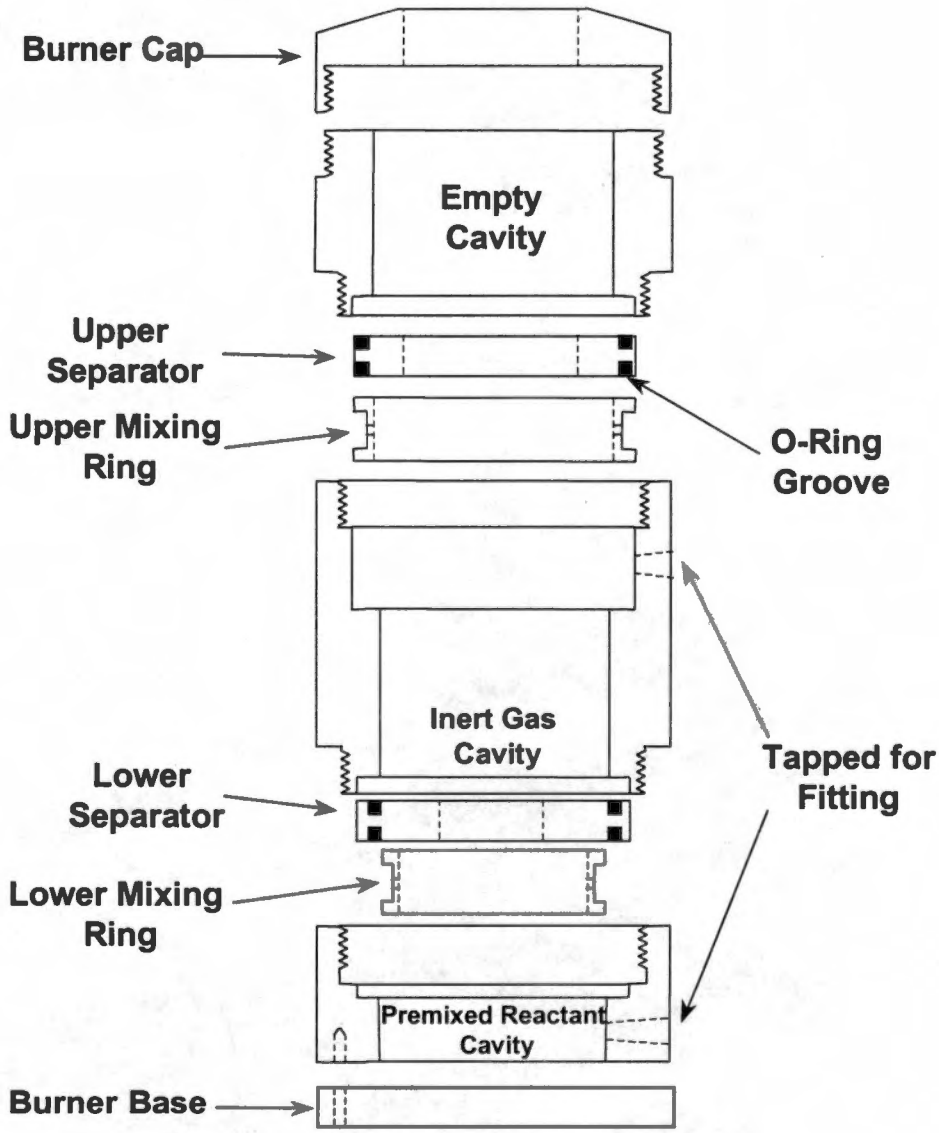

Figure 3-3 Exploded view of burner.

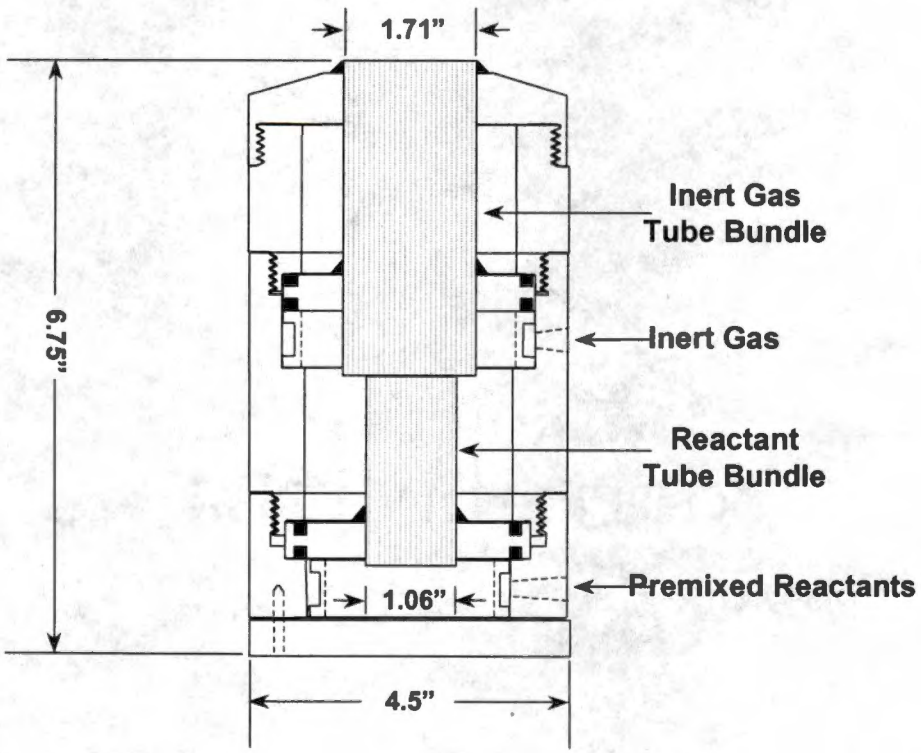

Figure 3-4 Assembled burner.

Table 3-1 Summary of flowmeters.

Gas	Flowmeter
Methane	0-830 (cc/min)
Oxygen	0-4500 (cc/min)
Nitrogen	0-4800 (cc/min)
Hydrogen Sulfide	0-140 (cc/min)

N_2, and CH_4. A stainless steel valve was used for H_2S. The rotometer floats were made of stainless steel for O_2, N_2, and H_2S. A Carboloy™ float was used for CH_4. The variable area flowtubes were 150 mm long, with graduations every millimeter.

The flowmeters were individually calibrated using a bubble flowmeter. The bubble flowmeter is a vertical glass tube of accurately graduated volume. To calibrate each of the rotometers, regulated gas (CH_4, O_2, or N_2) was supplied to the appropriate flowmeter. The gas leaving the flowmeter then passed through the bubble meter. The bubble meter provides a means of introducing a bubble solution into the gas stream, causing a thin film to form across the cross-section of the calibration section (the vertical tube) of the bubble meter. As the gas flows, the film propagates upward along the calibration section. The flow rate is determined by the time required for the film to sweep out the known volume of the calibration section. Calibration sections were available in three volume ranges to accommodate a wide range of flow rates.

Each of the rotometers was calibrated over the range of flowtube graduations of interest in 20 mm increments. The calibration at each graduation point was taken as the average of 10 or 30 samples of bubble transit time from the bubble meter. The set of the calibration points (scale position v. flowrate) for each flowmeter was fit using a second-order least squares fit. The flowmeters were then set according to these second-order equations.

For the CH_4, O_2, and N_2, this calibration gives an uncertainty in flowrate estimated to be +/-2% of the reading. It is not possible to flow H_2S through the bubble meter (based on safety considerations - H_2S is a toxic gas), so the H_2S meter was calibrated using N_2. The calibration was corrected by a function of the ratio of molecular weights of N_2 and H_2S. The resulting uncertainty was estimated to be +/-5% of the reading for the H_2S flowrate. The details of the flowmeter calibrations are included in Appendix B.

3.2.3 Nebulizer

A nebulizer was used to supply the aqueous solution of potassium carbonate to the burner in addition to the gaseous reactants. A Burgener™ Teflon nebulizer was selected for use in this experiment (Figure 3-5). The nebulizer was supplied by Technical Solutions unLimited, Mississaugua, Ontario, Canada. This nebulizer requires the liquid solution to be pumped into the nebulizer. High-pressure gas (in this case, 60 psig N_2) was supplied to the nebulizer and exited through a 0.004 in orifice at the nebulizer face. The high velocity gas stream nebulized the liquid stream. This nebulizer produced a stream of fine particles with almost no 'large' particles (particles that fall out of the gas stream). Throughout the experiment, the nebulizer performed well.

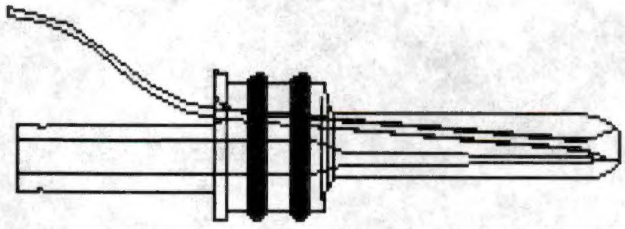

Figure 3-5 The Burgener nebulizer.

The nebulizer was calibrated using a modification to the trapping technique suggested by Alkemade [41]. The gas stream laden with solution particles was passed through a 0.1μm particle filter (Dalston BQ) over a long time period (about 1 minute). The difference between the mass of the filter prior to collecting particles and after collecting particles was taken to indicate the mass flow rate of the solution. The details of this calibration are included in Appendix B. The nebulizer was determined to deliver $2x10^{-4}$ to $3x10^{-4}$ gm/hr of solution.

A nebulizer body was constructed from a scavenged Perkin-Elmer atomic absorption system. The body assembly is shown in Figure 3-6. An adapter was made to accommodate the nebulizer. The transition piece connected through a Swagelock fitting, then to tubing that supplied the reactants to the burner. The adapter and the transition piece were made of Teflon.

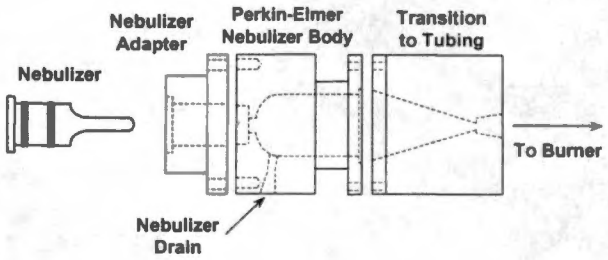

Figure 3-6 Nebulizer body assembly.

A schematic of the nebulizer flow system is shown in Figure 3-7. The nebulizer assembly was mounted at a small angle so that the large droplets that fell from the nebulized stream would collect around the drain and flow back to the reservoir. The drain tubing included a trap to prevent the nebulized stream from flowing out through the drain. Liquid was supplied to the nebulizer from peristaltic pump. A low flowrate pump head was used to provide liquid to the nebulizer. The pump provided more liquid than was required by the nebulizer, so a bypass valve and tubing were installed. The bypass valve was graduated so that valve settings could be repeated. The nebulizer was operated by first starting the gas flow with the bypass valve fully opened. The bypass valve was slowly closed to the nebulizer calibration position. This forced liquid into the nebulizer and the stream of fine droplets was formed.

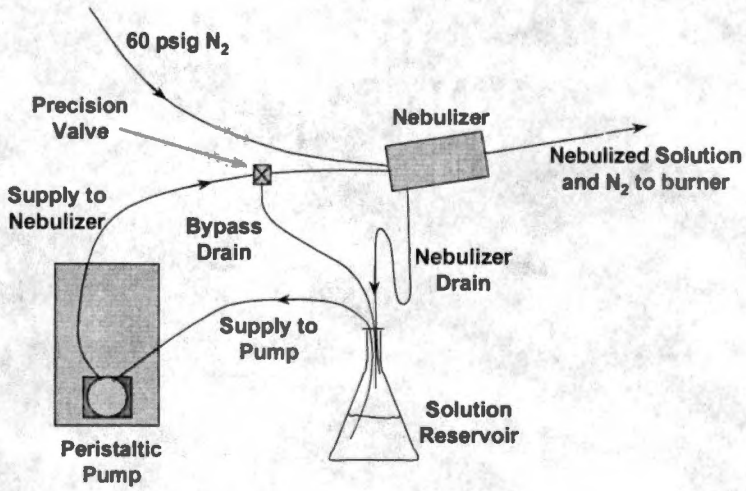

Figure 3-7 Schematic of nebulizer system.

3.3 Absorption Measurements

3.3.1 Theory

Densities of atomic and molecular species in gas mixtures can be inferred by measuring the absorption of light by the gas mixture. An absorption measurement is made by illuminating an absorbing medium with a beam of radiation at an energy (frequency) coincident with that of some appropriately chosen energy transition for an atom or molecule of interest. The situation is illustrated in Figure 3-8. The *general* development of the relationship between the measured absorption and species population is given in this section. Specific details for the potassium population measurement and the OH population

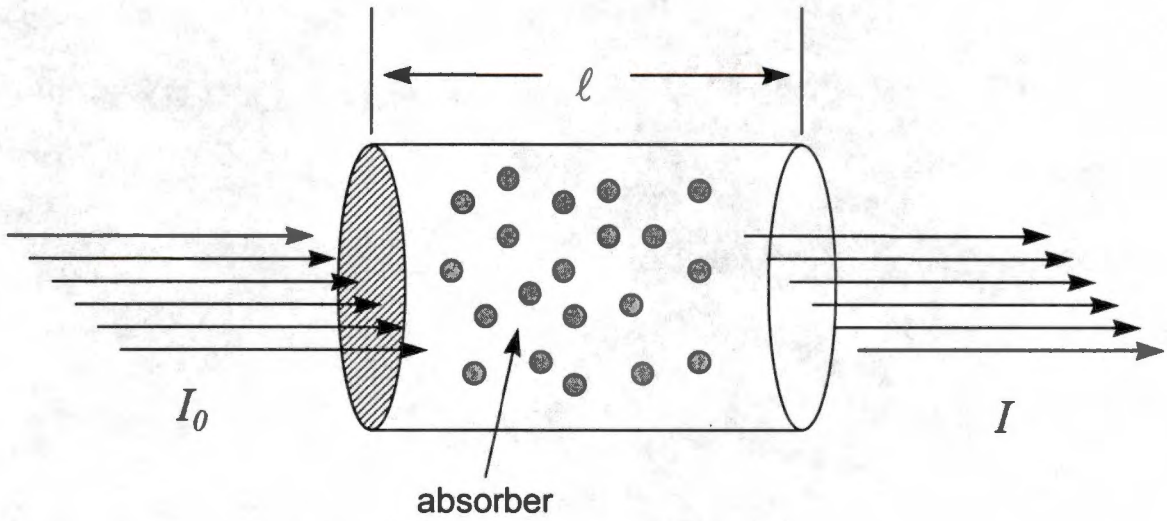

Figure 3-8. Schematic of absorption measurement (After Alkemade [41]).

measurement are given in Sections 3.3.2 and 3.3.3, respectively. This development closely follows that of Lucht, et al [42].

The quantities $I_{0,\nu}$ and I_ν represent the spectral radiation flux entering and leaving the absorption volume, respectively. Radiation-absorbing species in the volume will reduce the intensity I_ν below the incident intensity $I_{0,\nu}$. By considering an infinitesimal volume of absorbing gas, and defining the spectral absorption coefficient, κ_ν, the relationship between the percentage of radiation absorbed and the path length, `l` , through the uniform absorbing medium is found as follows:

$$I_{\nu,x+\Delta x} - I_{\nu,x} = -I_{\nu,x}\kappa_\nu \Delta x \qquad (3.3)$$

$$\lim_{\Delta x \to 0}\left(\frac{I_{\nu,x+\Delta x} - I_{\nu,x}}{I_{\nu,x}} = -\kappa_\nu \Delta x\right) \qquad (3.4)$$

$$\int_{I_\nu(x)=I_\nu(0)}^{I_\nu(x)=I_\nu(\ell)} \frac{dI_\nu}{I_\nu} = -\int_{x=0}^{x=\ell} \kappa_\nu dx \qquad (3.5)$$

$$\ln\left(\frac{I_\nu(\ell)}{I_\nu(0)}\right) = -\kappa_\nu \ell \qquad (3.6)$$

$$\frac{I_\nu(\ell)}{I_\nu(0)} = e^{-\kappa_\nu \ell} \qquad (3.7)$$

This expression is commonly known as Lambert-Beer's law and serves to relate the measured absorption to the number density of the absorbing species through the spectral absorption coefficient, $\kappa_\nu(n_p, T_{gas})$. The spectral transmission is defined as:

$$T(\nu) = \frac{I_\nu}{I_{\nu,0}} \qquad (3.8)$$

and the spectral absorption is:

$$A(\nu) = 1 - T(\nu) \qquad (3.9)$$

The total absorption is the quantity:

$$A = \int_{\nu-\Delta\nu}^{\nu+\Delta\nu} A(\nu)d\nu = \int_{\nu-\Delta\nu}^{\nu+\Delta\nu} (1 - e^{-\kappa_\nu \ell})d\nu \,. \qquad (3.10)$$

It is related, through the absorption coefficient, to the number density and is the quantity sought in the absorption measurement.

For the case at hand, continuum light sources were used for the absorption measurements. When the source radiation is observed with a spectrometer, the quantity, $\bar{I}_\nu$ is measured. $\bar{I}_\nu$ is the convolution of the instrument response and the incident radiation:

$$\bar{I}_\nu = \int_{\nu_1}^{\nu_2} I(\nu')g(\nu-\nu')d\nu' \qquad (3.11)$$

and $g(\nu-\nu')$ is the so-called 'slit function' that represents the modification of the incident radiation by the spectrometer. For good spectrometers, the slit function is approximately gaussian. The effect of the slit function is to disperse the incident radiation spectrally. Thus, a delta function is observed as a gaussian and other peaked functions are similarly dispersed. The quantity, $\bar{I}_{\nu,0}$ is the measured radiation without the absorbing medium.

In the experiments described here, the measured quantity is:

$$W = \int_{\nu-\Delta\nu}^{\nu+\Delta\nu} \left[1 - \frac{\int_{\nu_1}^{\nu_2} I_\nu(\nu')g(\nu-\nu')d\nu'}{\int_{\nu_1}^{\nu_2} I_{0,\nu}(\nu')g(\nu-\nu')d\nu'} \right] d\nu \qquad (3.12)$$

or

$$W = \int_{\nu-\Delta\nu}^{\nu+\Delta\nu} \left[1 - \frac{\bar{I}_\nu}{\bar{I}_{0,\nu}} \right] d\nu \qquad (3.13)$$

The measured absorption, W is nearly equal to A (equation 3.10) and can be used to determine atomic and molecular densities.

A expression for $\kappa_\nu(n_p, T_{gas})$ involves certain atomic or molecular properties. Alkamade [41] gives the expression for the spectral absorption coefficient as:

$$\kappa_\nu(n_p, T_{gas}) = \frac{\pi e^2}{m_e c^2} f_{pq} S(\nu) n_p \qquad (3.14)$$

where

e = electronic charge

m_e = electronic rest mass

c = speed of light

f_{pq} = oscillator strength

$S(\nu)$ = line shape

n_p = number density of pth (lower) state

The stated temperature dependence resides in the line shape, $S(\nu)$. Oscillator strength, f_{pq}, has been measured and reported in the literature for many transitions of interest. $S(\nu)$ accounts for all forms of spectral line broadening.

For these atmospheric pressure flames, it was assumed that the line shapes were dominated by collisional broadening. The Voigt profile was used to express $S(\nu)$ for combined doppler, collisional, and natural broadening. The Voigt profile is given by Lucht, et al [42] as

$$V(\xi,a) = \frac{a}{\pi}\int_{-\infty}^{+\infty}\frac{\exp(-y^2)dy}{a^2+(\xi-y)^2} \qquad (3.15)$$

In this expression, ξ, and y are parameters given by

$$y = \left(\frac{mc^2}{2kT}\right)^{1/2}\left(\frac{\nu' - \nu_0}{\nu_0}\right)$$

$$\xi = \left(\frac{mc^2}{2kT}\right)^{1/2}\left(\frac{\nu - \nu_0}{\nu_0}\right) \qquad (3.16)$$

$$\nu' = \nu_0\left(1 - \frac{u'}{c}\right)$$

where

m = particle mass

k = Boltzmann's constant

ν = frequency

ν_0 = line-center frequency

T = gas temperature

u' = relative velocity

ν' = doppler-shifted frequency

The parameter, a, is the ratio of doppler broadening to collisional and natural broadening:

$$a = \sqrt{\ln 2}\left(\frac{\Delta\nu_N + \Delta\nu_C}{\Delta\nu_D}\right) \qquad (3.17)$$

where

$\Delta\nu_N$ = natural (uncertainty) broadening

$\Delta\nu_D$ = doppler broadening

$\Delta\nu_C$ = collisional broadening

The parameter, a is a function of temperature and pressure and has been determined experimentally for different species. The Voigt profile was determined approximately using the subroutine reported given by Annino and Driver [43].

Finally, the line shape factor is given by:

$$S_\nu = \frac{2\sqrt{\ln 2}}{\sqrt{\pi}\Delta\omega_D} V(\xi, a) \qquad (3.18)$$

For specified conditions, equations 3.10, 3.14, and 3.18, together with the required physical constants were used to calculate the theoretical integrated absorption. The calculated absorption, A_{CALC}, was compared to the measured absorption, W to determine the population of the pth (lower) state, n_p. The procedure used starts with an estimate of n_p and calculates the absorption for the specified conditions - measured T_{gas} and path length `l`. Guesses at n_p were updated using a Newton iteration. The state density n_p was modified until A_{CALC} was nearly equal to W. The total population was determined assuming thermal equilibrium. Since the partition functions and notations for potassium and OH differ, the details for the total population determinations for each species are given separately in Sections 3.3.2 and 3.3.3.

3.3.2 Potassium Absorption Measurement

3.3.2.1 Experimental Setup

The setup for the potassium measurement is shown schematically in Figure 3-9. The setup was contained on the top of an optical workbench. A tungsten strip lamp provided the continuum radiation source for the absorption measurement. Continuum emission from the tungsten lamp was focussed on a spot at the center of the burner surface using an f=171.5 mm 2" diameter achromatic lens. An adjustable aperture was used to stop down the beam. The light was then gathered by an f=387 mm 2" achromatic lens and focussed on to the entrance slit of a spectrometer. Another adjustable aperture was place in the beam between the flame and the lens. The diameter of the aperture openings was set by the requirements of the modified line reversal temperature measurement, to

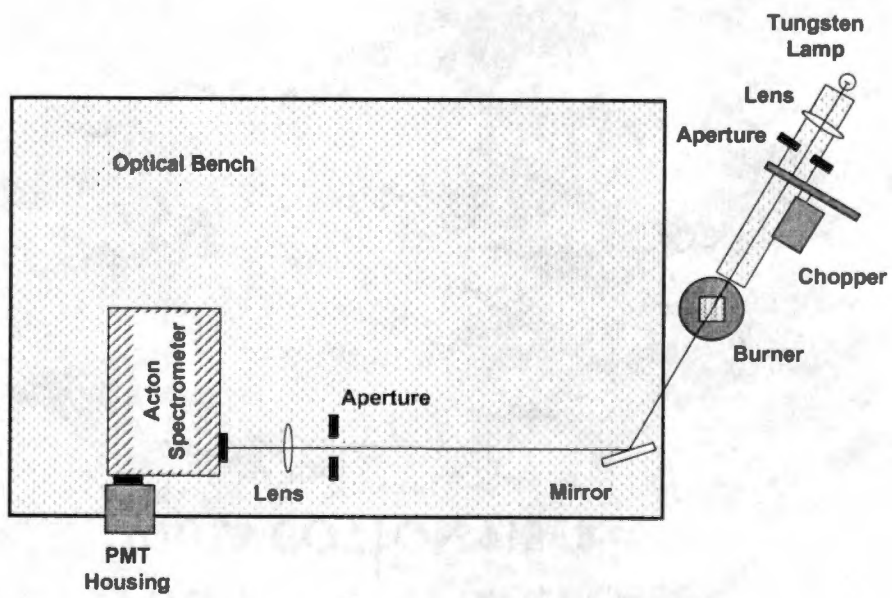

Figure 3-9 Layout for potassium absorption measurement.

be discussed in Section 3.3.4. Due to the arrangement of other instruments on the workbench, the line-of-sight from the tungsten strip lamp to the burner was not perpendicular to one of the straight sides of the burner. A 2" diameter elliptical mirror was used to redirect the light into the final lens and the spectrometer.

The lamp power supply was a Hewlett-Packard 6031-A System Power Supply. The power supply was operated in current-control mode so that the lamp power was fixed. The lamp was driven by a current of 12.51 amps. The power supply and lamp emissions were very stable.

During the absorption measurements, an optical chopper (Ithaco Model 383A, Optical Chopper; Ithaco Model 383B, Speed Control Unit) was placed in the beam on the lamp-side of the optical train. The lamp beam was modulated by the chopper wheel at 289 Hz.

An Acton spectrometer was used to measure the spectral absorption of the potassium atoms. The Acton SpectraPro-500 (Acton Research Corporation) is a 0.5-meter Czerny-Turner mount. The spectrometer included three user-selectable gratings. The grating for visible light (1200 lines/mm - holographic) was used during these experiments. Since the transitions being observed were well separated from other transitions, spectral resolution requirements were modest and the entrance and exit slit widths were set for optimal signal. Slit

widths of 50 μm were used for this experiment. A cooled-PMT (Photomultiplier Tube) housing (Products for Research Model TE177TOPF) was mounted on the exit slit flange. The PMT used was a Hamamatsu R955. The PMT was cooled to +5° C during the measurements. The PMT was energized using a Power Designs Model 3K10B, High Voltage Power Supply. A setting of –830 volts was used.

The current output of the PMT was converted to a voltage signal using an operational amplifier (OpAmp) as shown in Figure 3-10. The converted voltage output of the PMT was synchronously amplified using a lock-in amplifier (Stanford Research Systems Model SR510 or EG&G Princeton Applied Research Model 5104). The PMT output was used as the signal input to the lock-in amplifier and the reference signal from the chopper speed control unit

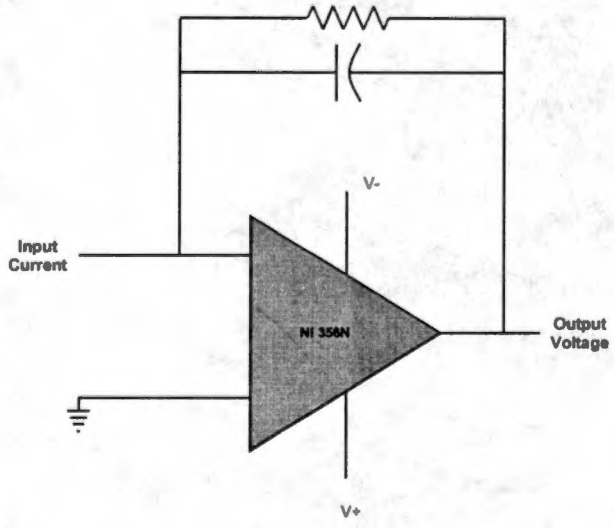

Figure 3-10 Current-to-voltage converter for PMT output.

was used as the frequency reference for the lock-in amplifier. Since a small capacitor was used in the OpAmp circuit, minimal signal conditioning (integration) was done on the signal fed to the lock-in amplifier. The low voltage (a few millivolts) signal from the OpAmp was amplified and smoothed by the lock-in amplifier. The sensitivity setting for the lock-in amplifier was 10 mV (10 mV input is amplified to full scale on the output, 10 volts). The first time constant (integrating filter applied to the input signal) was 300 ms and the second time constant (integrating filter applied to the output signal) was 100 ms.

Data were gathered using the National Instruments NI-NB-MIO-16 data acquisition card installed in an Apple Macintosh IIfx desktop computer. Data acquisition was controlled by a National Instruments LabView™ program. The data acquisition system was configured so that 1,000 samples of data were gathered over a 100 ms time period. The samples were averaged and the average recorded on the hard disk of the computer. Data were sampled in this way at every wavelength setting for a spectral scan. The signal-to-noise ratio (SNR) determined from measuring the unabsorbed light beam is approximately 200.

Spatial resolution for this measurement was achieved by placing a horizontal slit at the entrance of the spectrometer. The second lens essentially imaged this horizontally-oriented slit into the flame. The spatial resolution was verified by collecting data while the burner was translated from a low position (which did not block the beam) to a high position (which fully blocked the beam). The results

are shown in Figure 3-11. These results indicate that the beam intensity is reduced by one-half after the burner is translated about 0.2 mm. This resulted in an estimated spatial resolution of about 0.5 mm as shown in Figure 3-11. This procedure was used before each test to define both the spatial resolution and the relative position of the flame for various burner translations. When the beam power was reduced by one-half, the burner was defined to be in a zero-reference position.

3.3.2.2 Sample Data Reduction

Spectral absorption data were gathered at fixed vertical positions in the flame in a discrete step-and-dwell fashion. That is, the spectrometer grating was stepped to the desired wavelength where it would dwell for a specified period of time gathering and averaging data samples. As indicated previously, 1,000 samples

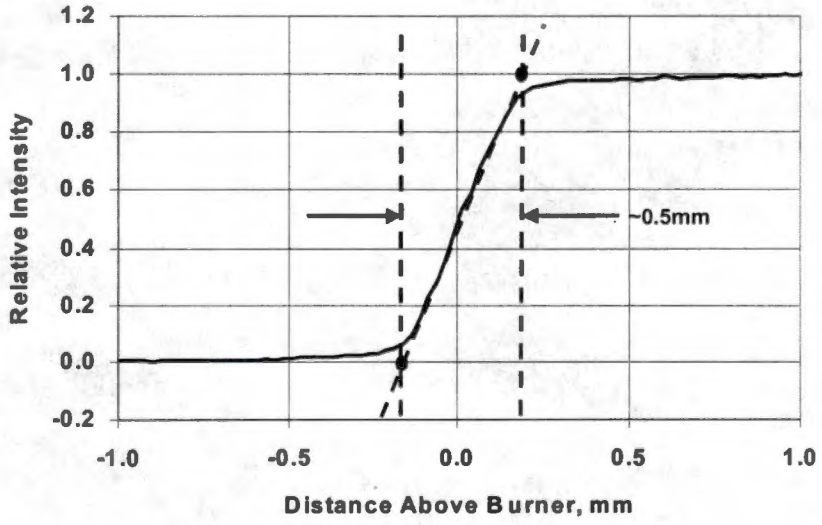

Figure 3-11 Spatial resolution of potassium absorption measurement.

gathered over a 100 ms period were averaged at each wavelength step. The potassium absorption was monitored at 766.49 nm, the $4s^2S_{1/2} - 4s^2P_{1/2}$ transition. For the absorption measurements, the scans were started at 766.20 nm and stepped in 0.01nm steps to 766.80 nm.

In order to construct an absorption line profile, the intensity of both the unabsorbed source and absorbed light beam must be measured. Three spectral scans of the source were made without the flame at the beginning of each experimental period, and then spectral absorption scans were collected with the flame present: three scans for each position above the burner. After all the absorption scans were collected, three post-experiment source scans were acquired.

The averages of the three absorption scans, $\bar{I}_\nu$ and the three pre-experiment source scans, $\bar{I}_{0,\nu}$ were computed to increase the signal-to-noise of the absorption data. The individual scans were correlated so that spectral structures (i.e. the absorption peak) were aligned. Correlation was required because of imprecision in the opto-mechanical linkage in the spectrometer. That is, the wavelength reading for the grating position is not a precise indicator of the position of the grating. The spectral structure observed in the absorption scans is precise. So, the individual scans were 'aligned' to this spectral structure. Correlation was performed by computing the correlation coefficient for pairs of spectral scans for various spectral alignments. The alignment that gave the

greatest correlation coefficient (typically about 0.95 or greater) was selected as the proper alignment. The results for typical sets of source and absorption scans are shown in Figures 3-12 and 3-13. Following correlation, the scans were averaged point-by-point. Since the wavelength increments were uniform and the correlation was performed on a point-by-point basis, no interpolation was required to compute the average.

Since $\bar{I}_{0,\nu}$ and $\bar{I}_{\nu}$ were not recorded simultaneously, the averaged $\bar{I}_{0,\nu}$ and $\bar{I}_{\nu}$ had to be spectrally correlated. This correlation was complicated because there was a strong spectral feature in the absorption scan but no feature in the source scan. Since the sets of $\bar{I}_{0,\nu}$ and $\bar{I}_{\nu}$ scans were individually nearly perfectly correlated without shifting, the average scans were not shifted prior to computing W. Error contributions from this procedure are negligible. An example of an absorption profile is shown in Figure 3-14.

The trapezoid rule was used to approximate the integral of equation 3.12 and computed the measured absorption, W, from the measured profile:

$$W = \sum_{1}^{n} (\nu_{i+1} - \nu_i) \frac{W_{i+1} + W_i}{2} \qquad (3.19)$$

where n is the number of samples in the scan. W_i is the component of the absorption from the ith point in the scan. The sampled wavelength (wavenumber) increments were used as recorded for the abscissa.

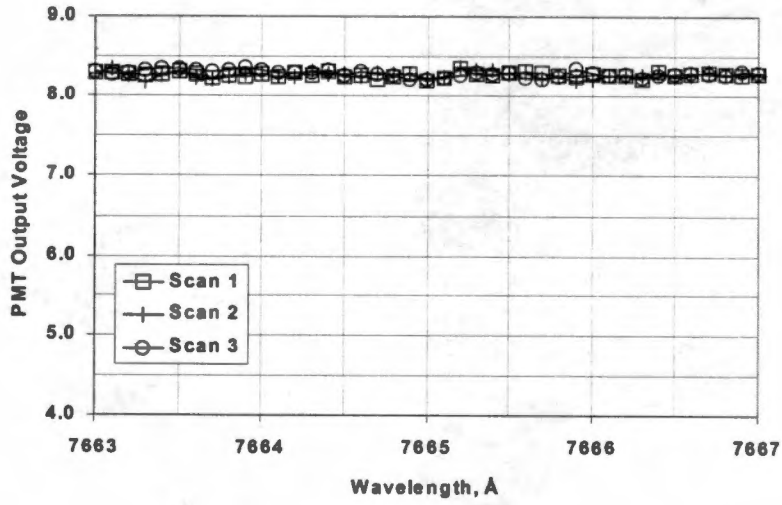

Figure 3-12 Spectrally correlated source scans (fuel-lean flame, 1.0 mm).

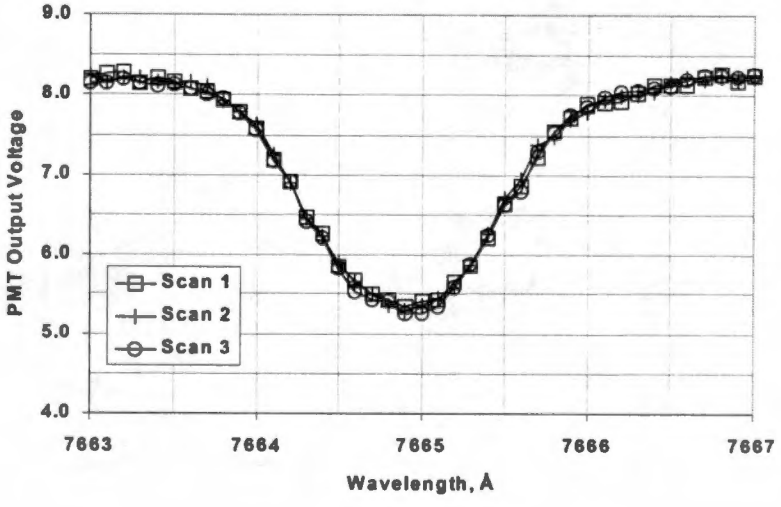

Figure 3-13 Spectrally correlated scans showing absorption (fuel-lean flame, 1.0 mm).

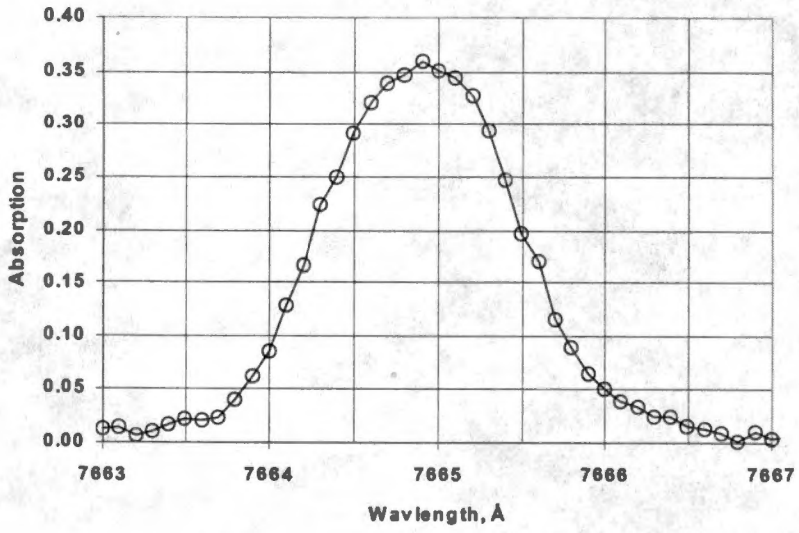

Figure 3-14 Potassium absorption sample data (fuel-lean flame,1.0 mm).

The lower-state number density was calculated from the measured absorption using the procedure outlined in Section 3.3.1. The path length was measured to be 2.77 cm. Temperature was taken from the line reversal measurement to be described in Section 3.4. The broadening parameter was taken from Alkemade et al [41]. In their review of the literature, the value of 1.1 was selected for the broadening parameter and was used here. The oscillator strength was taken to be 0.7 from Mavrodineanu and Boiteux [44]. For the sample absorption spectrum shown in Figure 3-14, the integrated absorption is 0.9025 cm^{-1}. The measured temperature was 1988 K. Using these inputs, the lower-state density was 2.65×10^{12} atoms/cm^3.

The total number density was calculated from the lower state density, n_p, and the partition function:

$$n_T = n_p \frac{\sum_{States} Q_i}{Q_p} \qquad (3.20)$$

where

n_T = total potassium number density

Q_p = lower state partition function term

Q_i = partition function term for i^{th} state

The partition function for the atom consists of only electronic terms. The terms included in the partition function and their degeneracies are summarized in the table taken from Mavrodineanu and Boiteux [44] (Table 3-2).

Table 3-2 Electronic states for potassium.

State	Wavelength[1] (nm)	Energy (cm^{-1})	Degeneracy
Ground State - $4s^2S_{1/2}$	-	0	2
$4p^2P_{1/2}$	769.99	12985	2
$4p^2P_{3/2}$	766.49	13043	4
$5p^2P_{1/2}$	404.72	24701	2
$5p^2P_{3/2}$	404.41	24720	4
$6p^2P_{1/2}$	344.74	28999	2
$6p^2P_{3/2}$	344.64	29008	4

[1]Wavelength for transition from ground state

The lower-state term is given by

$$Q_p = g_p e^{-E_p/kT} \qquad (3.21)$$

and the partition function is given by

$$Q = \sum_{States} g_i e^{-E_i/kT} . \qquad (3.22)$$

Using these data, the total number density for this example is found to be 2.69×10^{12} potassium atoms/cm^3.

3.3.2.3 Error Analysis

The potassium population is not directly measured; it is inferred from the measurement of integrated absorption, path length, temperature and a model relating the potassium population to these quantities, along with a variety of constants. Since the potassium population is related to these quantities in a non-linear way, the total measurement uncertainty must be propagated according to well-developed procedures (see for example [45]). Since the measured components are independent, the random measurement uncertainty is given by Rabinovich [45]

$$U_{Random} = \sqrt{\left(\frac{\partial n_p}{\partial T}\delta T\right)^2 + \left(\frac{\partial n_p}{\partial \ell}\delta \ell\right)^2 + \left(\frac{\partial n_p}{\partial W}\delta W\right)^2} . \qquad (3.23)$$

The influence coefficients are computed numerically using 1% perturbations to the model equation. The fixed error – or bias – is given by

$$U_{Fixed} = \left| \frac{\partial n_p}{\partial T_g} \delta T_g^{Bias} \right| \qquad (3.24)$$

The total uncertainty (the random error component and the fixed error – bias – component) is given by

$$U_{Total} = U_{Random} + U_{Fixed} \qquad (3.25)$$

The component errors are shown in Table 3-3. The details of the determination of the component errors are included in Appendix C. All error components are stated as 2σ-errors. The measured absorption uncertainty, δW, was estimated based on the statistics of the scans of the quantities $\bar{I}_\nu$ and $\bar{I}_{\nu,0}$. This uncertainty is very low because of the large number of points involved in the integration. The path length was measured using a steel scale with 1/32" markings. The error is assumed to be uniformly distributed across an interval of 1/32". The error in

Table 3-3 Error components for potassium absorption data.

Parameter	Random Uncertainty	Bias Uncertainty
Temperature, δT (K)	17	5
Path Length, δl (cm)	0.046	0.0
Integral Absorption, δW (cm^{-1})	0.009	0.0
Total Error, δn_p (atoms/cc)	3.4%	1.3%

temperature, δT_g, is discussed in Section 3.4. The error has a random component and a fixed component (bias). The random error (2σ) is 17 K and the bias error is 35 K (see Section 3.4). The combination of these errors yields a total uncertainty on the potassium number density of less 5% of the reading. A conservative quotation of 10% total error is used.

3.3.3 OH Absorption Measurement

3.3.3.1 Experimental Setup

The experimental setup is shown schematically in the Figure 3-15. As was the case for the potassium measurement, the setup was contained on an optical workbench. A deuterium lamp provided the continuum radiation needed for the absorption measurement. The emission from the lamp was focussed on a spot at the center of the burner surface using an f=250 mm 2" diameter quartz lens. An adjustable aperture was used to stop down the beam slightly to reduce aberrations and improve the beam focus. The light was then gathered by an f=250 mm 2" calcium fluoride lens and then focussed on the slit of a spectrometer. Another adjustable aperture was placed in the beam between the lens and the spectrometer. The source image was rotated 90° using a pair of mirrors so that the spatial resolution was set by the entrance slit of the spectrometer.

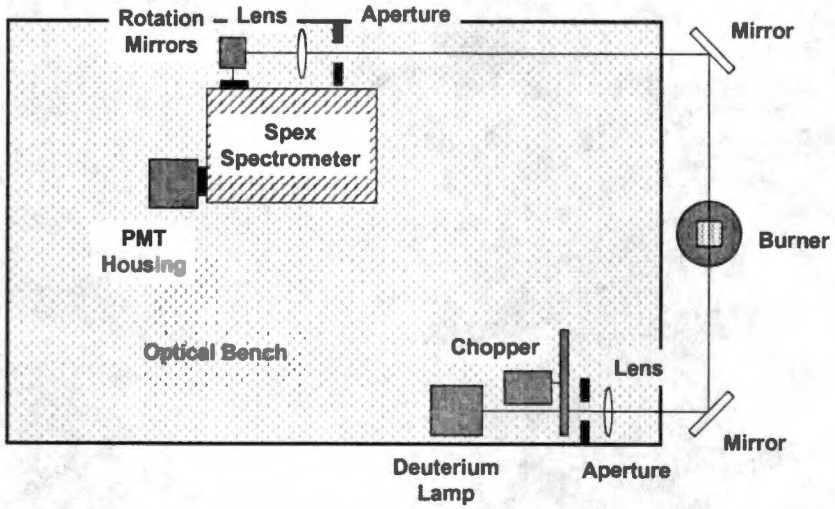

Figure 3-15 Instrumentation layout for OH absorption measurement.

The deuterium lamp assembly was manufactured by Oriel. The lamp power supply was Oriel model number 68840. During the absorption measurements, an optical chopper (Ithaco Model 383A, Optical Chopper; Ithaco Model 383B, Speed Control Unit) was placed in the beam on the lamp-side of the optical train. The lamp beam was chopped at 289 Hz.

The spectrometer used to measure the spectral absorption of the hydroxyl radical was a Spex 1870 (Spex Industries) 0.6-meter Czerny-Turner mount. The spectrometer was used with a 3600 lines/mm grating blazed at 300 nm. Since the OH rotational transitions being observed were closely spaced and there was the possibility of interference from sulfur compounds, high spectral resolution was required. Using entrance and exit slit widths of 10 μm, the instrument had a

spectral resolution of 0.01 nm as determined by scanning the Hg doublet at 254.6 nm. A cooled-PMT housing (Products for Research Model TE177TSRF) was mounted on the exit slit flange. The PMT used was a Hamamatsu R955. The PMT was cooled to -20°C during the measurements. The PMT was energized using a Stanford Research Industries, Model PS325, High Voltage Power Supply. A setting of –900 Volts was used.

The current output of the PMT was converted to a voltage signal using a operational amplifier (OpAmp) as shown in the Figure 3-10. As was the case with the potassium absorption measurement, minimal signal conditioning (integration) was used on the signal fed to the lock-in amplifier. The converted voltage output of the PMT was synchronously amplified using a lock-in amplifier (Stanford Research Systems Model SR510 or EG&G Princeton Applied Research Model 5104). The PMT output was used as the signal input to the lock-in amplifier and the reference signal from the chopper speed control unit was used as the frequency reference for the lock-in amplifier. The low voltage (a few millivolts) signal from the OpAmp was amplified and smoothed through the lock-in amplifier. The sensitivity setting for the lock-In amplifier was 10 mV (10 mV input is amplified to full scale on the output, 10 volts). The first time constant of the integrating filter applied to the input signal was one-second and the second time constant of the integrating filter applied to the output signal was 300 ms.

Data were gathered using the National Instruments NI-NB-MIO-16 data acquisition card installed in an Apple Macintosh IIfx. The data acquisition system was configured so that 10,000 samples of data gathered over a one-second time period were averaged and the average recorded on the hard disk of the computer. Data were sampled in this way at every wavelength step for a spectral scan. The signal-to-noise ratio (SNR) determined from monitoring the unabsorbed light beam was about 60.

The spatial resolution of the OH absorption measurement was determined in the same way as previously discussed for the potassium measurement. The results are shown in Figure 3-16. The spatial resolution for the measurement was approximately 0.5 mm.

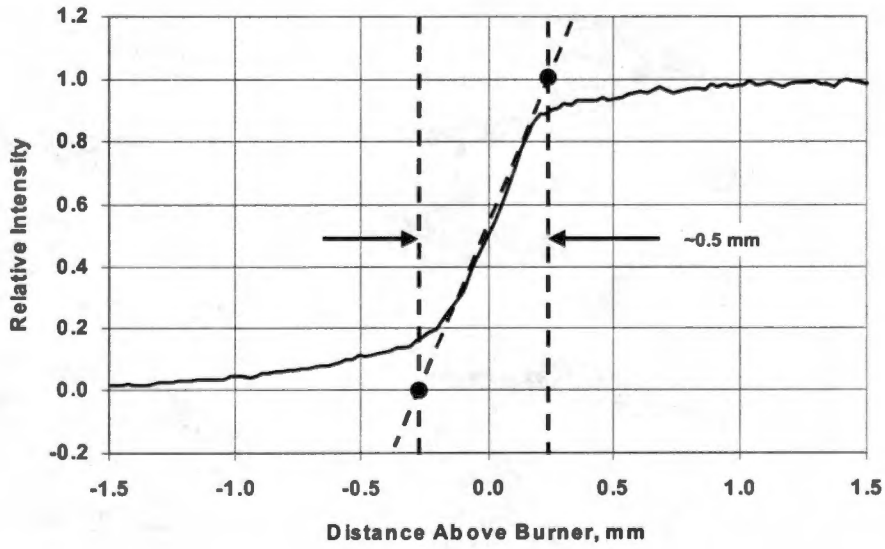

Figure 3-16 Spatial resolution for OH absorption measurement.

3.3.3.2 Sample Data Reduction

Spectral absorption data were gathered in a discrete step-and-dwell fashion. That is, the spectrometer grating was stepped to the desired wavelength where it would dwell for a specific period of time, gathering and averaging data samples. For the OH measurements, 10,000 samples gathered over a one-second period were averaged at each wavelength step. The OH absorption line surveyed was at 310.123 nm, which is the $P_1(5)$ rotational line of the $(X^2\Sigma^+–A^2\Pi)(v',v"=0,0)$ transition. For the absorption measurements, the scans were started at 310.09 nm and stepped in 0.001nm steps to 310.14 nm. Five source scans were made at the beginning of each test. After all the absorption scans were collected, five post-experiment source scans were acquired.

The absorption scans and the source scans were aligned in the same way as was done for the potassium absorption data. That is, the scans were spectrally aligned based on the maximum correlation coefficient. An emission feature was detected in the deuterium source that was used to spectrally align the absorption and source scans. The emission feature detected in the source scan was identified as the $Q_2(5)$ rotational transition of the OD(0-0) transition [46]. This feature is located at 310.122 nm, near the OH(0-0) $P_1(5)$ line observed in this experiment. More detail regarding the computation of OH line absorption is given in Appendix D. Typical examples of absorption scans are shown in Figures 3-17 and 3-18. An example of an absorption profile is shown in Figure 3-19.

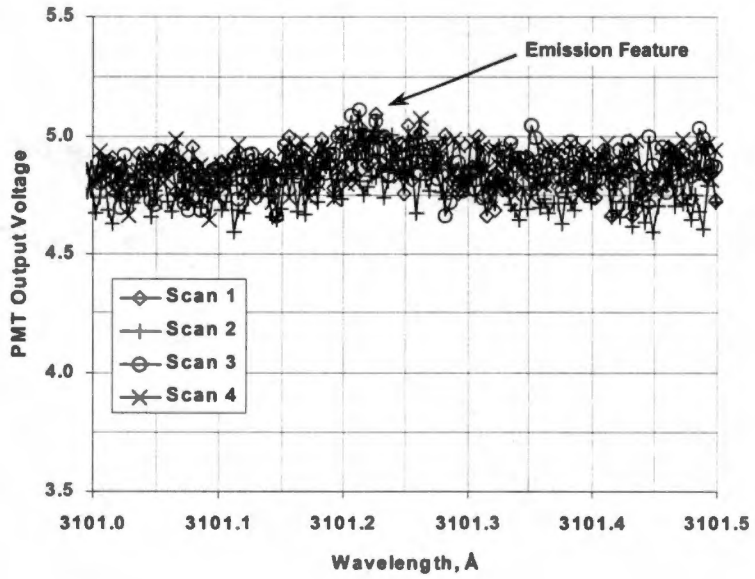

Figure 3-17 Correlated $\bar{I}_{\nu,0}$ (source) scans.

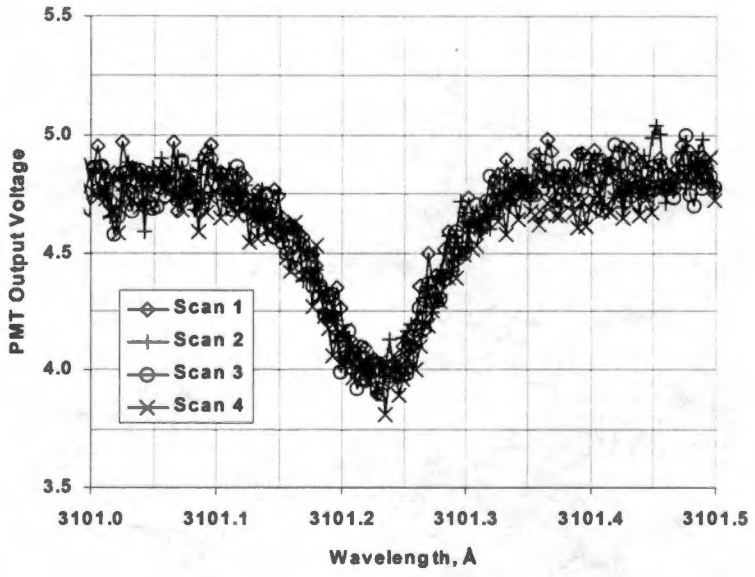

Figure 3-18 Correlated $\bar{I}_{\nu}$ (absorption) scans.

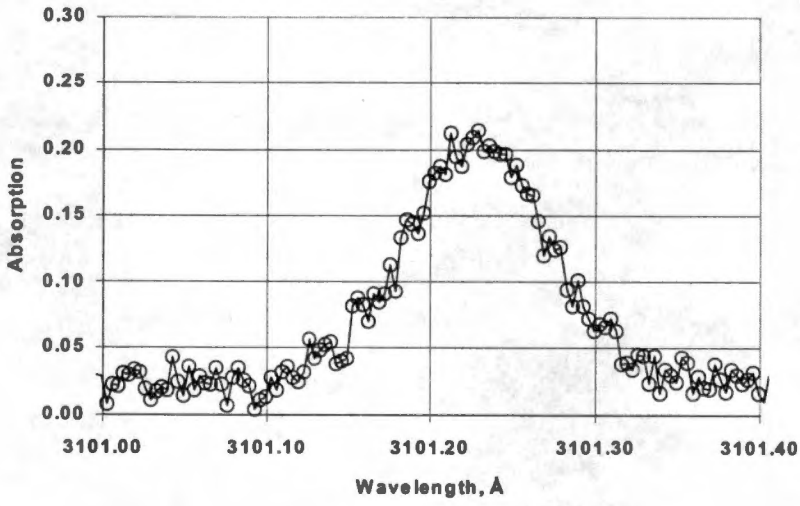

Figure 3-19 OH absorption profile (fuel-lean flame, 1.0mm).

The lower-state number density was calculated from the measured absorption using the procedure outlined in Section 3.3.1. The path length was measured to be 2.4 cm. Temperature was taken from a line reversal measurement (described in Section 3.4). The broadening parameter was taken from Cattolica [47] and Schmidt and Malte [48]. In their reduction of absorption data from similar hydrocarbon flames, they used a value ranging between 0.3 and 0.2. The value of 0.2 was used throughout these calculations. The band oscillator strength was calculated as described by Lucht [42]:

$$f_{pq} = f_{00} \frac{S_{pq} T_{pq}}{2p+1} \qquad (3.26)$$

where:

f_{00} = the band oscillator strength

p = lower state rotational quantum number

S_{pq} = line strength for the p→q rotational transition

T_{pq} = Learner's empirically determined correction for rotational-vibrational interactions

These parameters, shown in Table 3-4, are taken from Lucht [42].

For the sample absorption spectrum shown in Figure 3-19, the temperature was found to be 1988 K, the integrated absorption was 0.377 cm^{-1}. Using these inputs, the lower-state density was 6.09×10^{14} atoms/cm^3.

The total number density was calculated from the lower state density and the partition function:

$$n_T = n_p \frac{\sum_{States} Q_i}{Q_p} \qquad (3.27)$$

Table 3-4 Parameters used in OH absorption data reduction.

Parameter	Value
p	5.5
f_{00}	0.00098
S_{pq}	6.127
T_{pq}	0.986

where n_T = total number density

n_p = lower-state number density

Q_p = lower state partition function term

Q_i = partition function term for p^{th} state

The lower-state partition function includes energy contributions from rotation, vibration, and electronic states as follows

$$Q_p = (2p+1)e^{-\frac{hc}{kT}[T_e+G(v)+F(p)]} \qquad (3.28)$$

where

h = Planck's constant

T = temperature

T_e = electronic term energy

$G(v)$ = vibrational term energy, lower state vibrational quantum number v

$F(p)$ = rotational term energy, lower state rotational quantum number p

and the total partition function is given by

$$Q = Q_{elec}Q_{vib}Q_{rot} \qquad (3.29)$$

where

Q_{elec} = electronic partition function $\quad Q_{elec} = \sum_n g_e e^{-\frac{hc}{kT}T_e}$

Q_{vib} = vibration partition function $\quad Q_{vib} = \sum_v e^{-\frac{hc}{kT}G_v}$

Q_{rot} = rotational partition function $\quad Q_{rot} = \sum_p (2p+1)e^{-\frac{hc}{kT}F(p)}$

The rotational partition function term energies, $F(p)$, were taken from Lucht [42] and are tabulated in Table 3-5. The vibrational partition function term energies were calculated using the approximation

$$G(v) = \omega_e v - \omega_e x_e v^2 \qquad (3.30)$$

where

ω_e = oscillator frequency

$\omega_e x_e$ = anharmonic correction

For the electronic partition function, only the ground state and the first excited state contribute to the partition function. The parameters used are shown in Table 3-6. Using these parameters, the total number density was determined to be 2.46×10^{16} molecules/cm^3.

Table 3-5 Parameters for the calculation of the rotational partition function.

Rotational Quantum Number	Term Energy (cm^{-1})	Rotational Quantum Number	Term Energy (cm^{-1})	Rotational Quantum Number	Term Energy (cm^{-1})
1.5	0.0	11.5	2415.2	21.5	8165.7
2.5	83.8	12.5	2847.8	22.5	8901.1
3.5	202.1	13.5	3313.7	23.5	9662.1
4.5	355.6	14.5	3812.5	24.5	10447.8
5.5	544.1	15.5	4343.5	25.5	11256.9
6.5	768.1	16.5	4906.1	26.5	12088.5
7.5	1027.6	17.5	5499.1	27.5	12941.4
8.5	1322.3	18.5	6122.9	28.5	13814.3
9.5	1652.3	19.5	6775.7	29.5	14705.9
10.5	2016.4	20.5	7456.9	30.5	15615.1

Table 3-6 Parameters for the electronic partition function.

State	Degeneracy	Term Energy (cm^{-1})
$^2\Pi$	4	0
$^2\Sigma^+$	2	32682

3.3.3.3 Error Analysis

Random errors for the OH absorption data were assessed in the same way as those for the potassium absorption data. However, the uncertainty in the OH data is dominated by a potential bias error in the absorption measurement. The random error components of the population measurement are included in the following equation:

$$U_{Random} = \sqrt{\left(\frac{\partial n_p}{\partial T_g}\delta T_g\right)^2 + \left(\frac{\partial n_p}{\partial \ell}\delta \ell\right)^2 + \left(\frac{\partial n_p}{\partial W}\delta W\right)^2} \qquad (3.31)$$

The random component of the temperature error is discussed in Section 3-4. The path length was measured and is assumed to have error uniformly distributed over an interval of 1/32" (2σ=0.46 mm). The absorption error, δW, is derived from the component errors in $\bar{I}_\nu$ and $\bar{I}_{\nu,0}$. The actual error propagation involved is discussed in Appendix C. The random component of the absorption measurement error (2σ) was 0.011 cm^{-1}. As was the case for the potassium measurement, this error is small due to the large number of points involved in the spectral integration. The component errors are summarized in Table 3-7.

Table 3-7 Error components for OH absorption data.

Parameter	Random Uncertainty	Bias Uncertainty
Temperature, δT (K)	17	35
Path Length, δl (cm)	0.0046	0
Integral Absorption, δW (cm^{-1})	0.0114	0.025
Total Uncertainty	5.6%	12.0%

There are two sources of bias error in these measurements. The temperature measurements included a bias error due to the bias in the source temperature measurement. This error is discussed in Section 3.4. The integrated absorption error includes a bias error due to properties of the measuring instrument. These errors include:

1. $\bar{I}_{\nu,0}$ bias due to grating "ghosts"
2. $\bar{I}_{\nu,0}$ corrections due to presence of a spectral emission feature on the source lamp
3. Occlusion of the source lamp beam

These errors are discussed in Appendix C. The uncertainty that results from the bias error is

$$U_{Bias} = \left| \frac{\partial n_p}{\partial T_g} \delta T_g^{Bias} \right| + \left| \frac{\partial n_p}{\partial W} \delta W^{Bias} \right| \qquad (3.32)$$

The total error is then

$$U_{Total} = U_{Random} + U_{Bias} \qquad (3.33)$$

The total error is estimated to be less than 18% of the calculated number density. An error specification of 20% is made to be conservative.

3.4 Temperature Measurement

3.4.1 Theory

Flame gas temperature measurements were made using the Modified Line Reversal (MLR) technique described by Winkleman [49]. In the usual line reversal method, a broadband source is used to illuminate an absorbing/emitting medium. The temperature of the medium is equal to the source brightness temperature when radiance of the broadband source is just equal to the radiance of the medium, accounting for the optical elements. This point is found by changing the intensity of the source and detecting the radiance transmitted through the medium.

In MLR, the specific reversal point is not located. Temperature is determined directly from the flame radiation, source radiation and the combination of the two. MLR is well documented by Winkleman [49]. Only an outline of the relevant details is given here. Consideration of the details of radiative transfer along the optical path from the source, through the medium and optics, to the detector yield the following relationship between the source brightness temperature (T_s) and the absorbing/emitting medium temperature (T_g):

$$T_g = \left[1 - \frac{\lambda T_s}{hc} \ln\left(\frac{\eta_v R_f}{R_s + R_f - R_{s+f}}\right)\right]^{-1} T_s \qquad (3.34)$$

where

R_s = radiance due to the source

R_f = radiance due to the flame

R_{s+f} = radiance due to the source and flame combined

λ = Wavelength monitored by the detector

η_v = optical correction term

Note that this expression reduces to the usual line reversal expression if $R_s = R_{s+f}$ and if $\eta_v = 1$. The latter is only true for optically symmetric setups. For asymmetric setups, the correction factor η_v is determined by the setup geometry (see Section 3.4.3). For a focussed optical setup, the optics correction, $\eta_v = \eta_{foc}$, is given by

$$\eta_{foc} = \tau_s \left(\frac{p_1 - F_1}{F_1}\right)^2 \frac{r_{s_1}^2\left[r_{s_2}^2 + (p_2 - d_2)^2\right]}{r_{s_2}^2\left[r_{s_1}^2 + (p_1 - q_s)^2\right]} \qquad (3.35)$$

In this equation, the geometric parameters are defined in Figure 3-20. All of the parameters are tabulated in Table 3-8. The system used in the present study was designed according to the requirements stated by Winkleman [49] so that the measured irradiance for the source and the flame were related to the corresponding source or flame radiance by the same constant. That is

$$\frac{I_{source}}{R_{source}} = \frac{I_{flame}}{R_{flame}} = \frac{I_{source+flame}}{R_{source+flame}} \qquad (3.36)$$

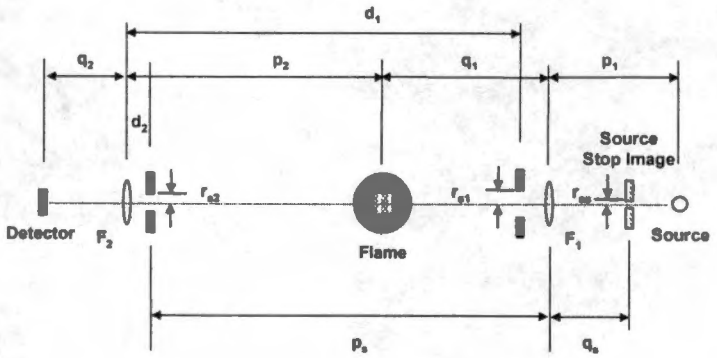

Figure 3-20 Dimensions required for modified line reversal temperature measurement.

Table 3-8 Optical parameters for modified line reversal temperature measurement.

Parameter	Value
F_1 (mm)	152.4
F_2 (mm)	387.4
p_1 (mm)	238.10
q_1 (mm)	523.9
p_2 (mm)	822.4
d_2 (mm)	31.8
r_{s_1} (mm)	12
r_{s_2} (mm)	4
p_s (mm)	1314.5
q_s (mm)	172.4
r_{s_s} (mm)	0.52
τ_s	0.97
η_{foc}	0.76

Additionally, the detector aperture must be set so that the aperture is fully lit. The condition is met by setting r_{s_1} large enough so that the fully lit image radius is larger than the detector aperture. Note that the detector aperture is set small (<0.5 mm) to get good spatial resolution in the flame. The source-optic transmissivity, τ_s, was measured directly as discussed in Appendix E.

3.4.2 Experimental Setup

The layout of the temperature measurement instrumentation is shown in Figure 3-21. This layout is the same as that used for the potassium absorption measurement, with the exclusion of the lock-in amplifier and chopper. The equipment used for the MLR measurement was identical to that used for the potassium absorption measurement, described in Section 3.3.2. The measurements were taken with the spectrometer entrance and exit slits widths set to 100 μm and the PMT voltage set to –800 volts.

3.4.3 Sample Data Reduction

The source brightness temperature is the apparent temperature of a black body that would produce the same radiance as observed from the source. The brightness temperature of the source, the tungsten strip lamp, was determined by direct measurement using an optical pyrometer. The optical pyrometer gave the brightness temperature at 653 nm. The brightness temperature of the lamp at 765 nm was estimated using the Planck function. A lamp current was chosen

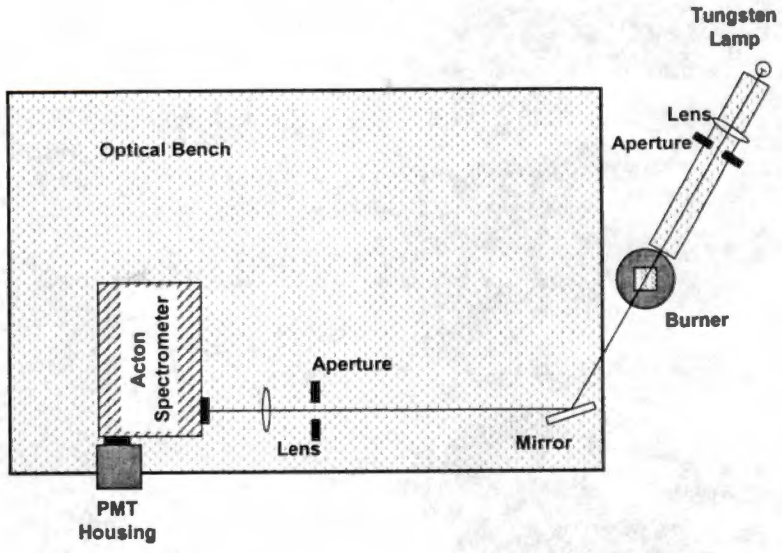

Figure 3-21 Modified line reversal temperature measurement setup.

so that the lamp brightness temperature was close to that expected from the flame. Potassium emission from the transition, $4s^2S_{1/2} - 4s^2P_{1/2}$ at 764.95 nm, was observed for the line reversal measurement. Details of this calibration and other elements of the MLR measurement are given in Appendix D.

The procedure for measuring the individual terms in the equation was similar to that used for measuring potassium absorption. The step-and-dwell data acquisition method was used to obtain flame radiation intensity at the wavelength centered at 764.95 nm. The wavelength scans were obtained in the interval 765.8 nm to 767.2 nm by stepping at 0.01 nm intervals. At each wavelength step, 1,000 samples were acquired and averaged. At each burner position, the source radiation, flame radiation, and combined source and flame radiation were spectrally scanned. Typical results are shown in Figure 3-22.

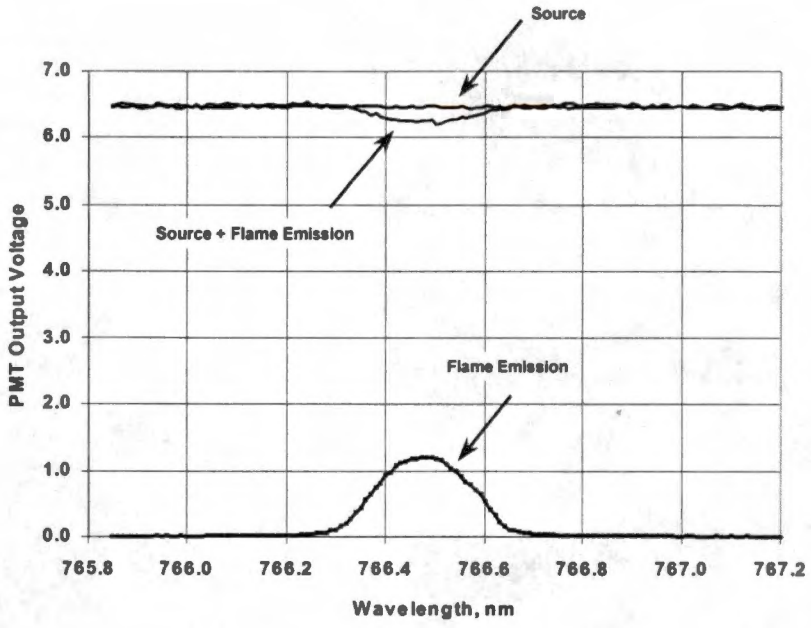

Figure 3-22. Typical modified line reversal results (fuel-lean flame, 1.0 mm).

The peak intensity of the emission (absorption) scan was used as the reference point for the temperature determination. The voltage at the reference point was assumed to be proportional to the radiance at that wavelength so that

$$\frac{V_f}{V_s + V_f - V_{s+f}} = \frac{R_f}{R_s + R_f - R_{s+f}} \qquad (3.37)$$

Temperature was calculated directly from these measurements.

3.4.4 Error Analysis

The gas temperature is not directly measured, but is inferred from other measurements based on a model (equation 3.32). Thus the error analysis must

propagate the component measurements errors consistently. The gas temperature, T_g, is a function of the lamp temperature, the flame radiance (irradiance) measurements and the geometric factors. The uncertainty due to random error is given by the following equation;

$$U_{Random} = \sqrt{\left(\frac{\partial T_g}{\partial T_s}\delta T_s\right)^2 + \left(\frac{\partial T_g}{\partial \eta_{foc}}\delta \eta_{foc}\right)^2 + \left(\frac{\partial T_g}{\partial R_s}\delta R_s\right)^2 + \left(\frac{\partial T_g}{\partial R_f}\delta R_f\right)^2 + \left(\frac{\partial T_g}{\partial R_{s+f}}\delta R_{s+f}\right)^2} \quad (3.38)$$

The estimated influence coefficients and component errors are tabulated in Table 3.9. The derivatives for the influence coefficients were calculated numerically by applying 1% perturbations to the line reversal model equation (equation 3.32).

Table 3-9 Error components for temperature measurement.

Parameter	Random Uncertainty (2σ)	Bias Uncertainty
Source Temperature, δT_s (K)	8	35
Optical Correction, $\delta \eta_{foc}$	0.05	0
Source Radiance, δR_s (volts)	0.004	0
Flame Radiance, δR_f (volts)	0.004	0
Total Radiance, δR_{s+f} (volts)	0.004	0
Total Uncertainty (K)	17	35

The errors in R_s, R_f, and R_{s+f}, were determined by statistical analysis of the measurements. In particular, the statistics for R_s were assumed to apply to each radiance measurement. This is a conservative estimate of the error for these components. The 2σ error for the radiance measurements corresponded to 0.004 volts in output signal. The optical factor, η_{foc} was also an inferred quantity, its value depending on the measurements in Table 3-8.

The brightness temperature was measured by an optical pyrometer (Leeds & Northrup Model 8632-C - described in Appendix E). The calibration of the lamp brightness temperature revealed a random error component (2σ) of about 8 K. However, there was also a possible bias error of about 35 K. When all these errors are accounted for in equation 3.36, the total uncertainty in the flame gas temperature is estimated to be 17 K random error with 35 K bias. Error components are summarized in Table 3-9.

4.0 Experimental Results

4.1 Experiment Matrix

Eight flames were observed in the course of the experimental program. The matrix of flame stoichiometries established is shown in Table 4-1. The flame stoichiometries span the range that supports stable flames. The N_2/O_2 ratio was less than that of air in order to increase the stability of the flames. The total volume flow rate was held constant at 12 slpm to match the gas inflow velocities used by Slack, et al [20] and Cattolica [47]. The post-flame gas temperatures of these flames were all about 2100K. For flames with sulfur added to the fuel, 1% H_2S (volume basis) was added. In the richest (ϕ=1.3) flame, 0.75% H_2S was added. The H_2S was added in such a way as to replace a comparable quantity of CH_4. In this way, the overall stoichiometry of the flame was preserved when sulfur was added. Additionally, the thermal impact of hydrogen sulfide fuel addition was minimized.

4.2 Temperature Profiles

The temperature profiles for each of the flames are shown in Figures 4-1a through 4-1d. The flame temperatures are compared to the equilibrium values as a function of stoichiometry in Figure 4-2a and b. The post-flame gas temperatures are generally below the equilibrium level due to heat-loss, for example, heat lost to the burner. The temperatures follow the trend expected with stoichiometry. These results compare well with the results of Slack, et al

Table 4-1 Flame Matrix[1].

Flame	$CH_4/O_2/N_2$	Temperature (K)	% H_2S
Fuel-Lean (ϕ = 0.85)	1.0/2.35/7.06	2100	0
Stoichiometric (ϕ = 1.0)	1.0/2.0/6.0	2100	0
Fuel-Rich (ϕ = 1.2)	1.0/1.67/5.01	2100	0
Rich (ϕ = 1.3)	1.0/1.54/4.62	2000	0
Fuel-Lean (ϕ = 0.85)	1.0/2.35/7.06	2100	1
Stoichiometric (ϕ = 1.0)	1.0/2.0/6.0	2100	1
Fuel-Rich (ϕ = 1.3)	1.0/1.67/5.01	2100	1
Fuel (ϕ = 1.3)	1.0/1.54/4.62	2000	0.75

[1] Equivalence ratio, $\phi \equiv$ (fuel-to-air molar ratio)$_{actual}$/(fuel-to-air molar ratio)$_{stoichiometric}$ - $\phi < 1$ implies fuel-lean mixture.

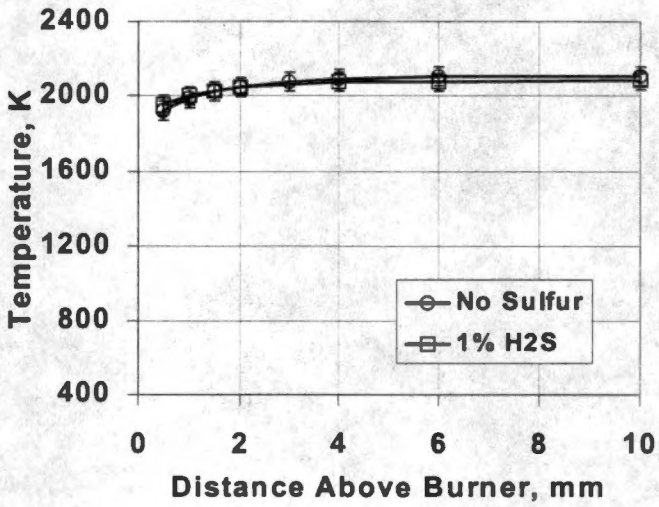

a Fuel-lean (ϕ = 0.85) flames with no sulfur and with 1% added H_2S.

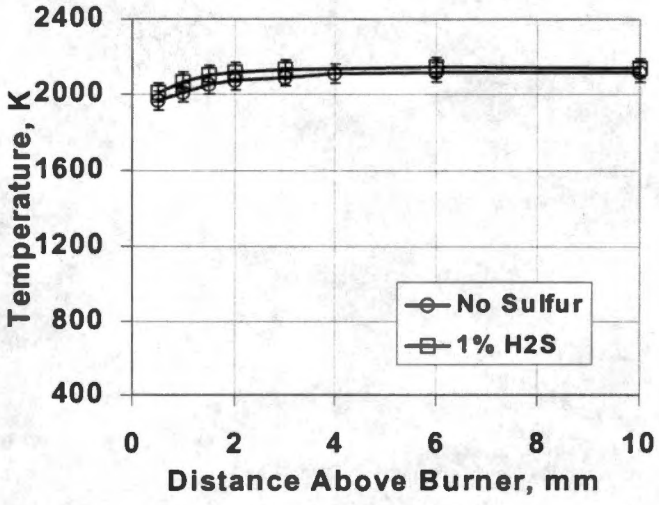

b Stoichiometric (ϕ = 1.0) flames with no sulfur and with 1% added H_2S.

Figure 4-1 Comparison of temperature profiles.

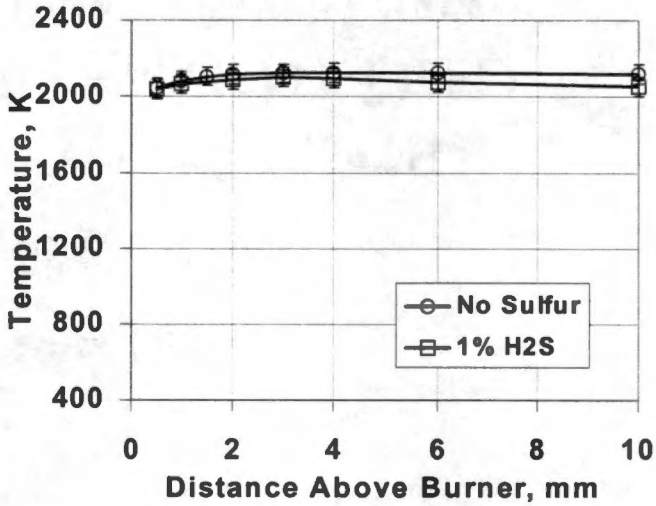

c Fuel-rich (ϕ = 1.2) flames with no sulfur and with 1% added H_2S.

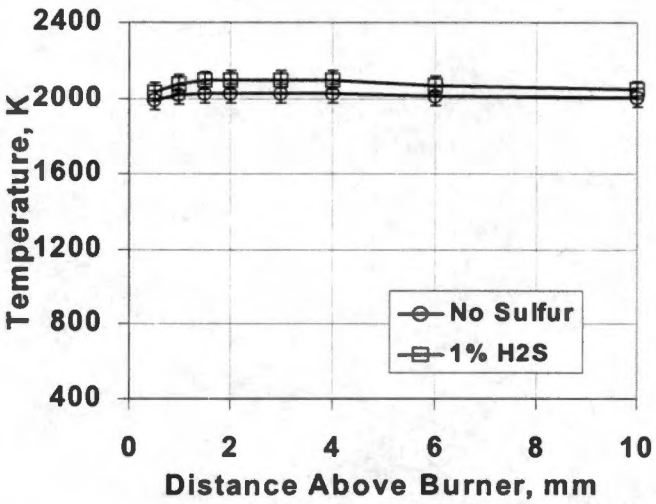

d Fuel-rich (ϕ = 1.3) flames with no sulfur and with 0.75% added H_2S.

Figure 4-1 (Continued)

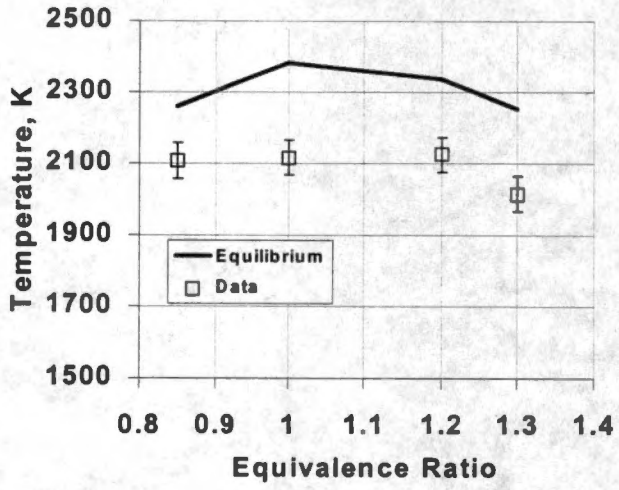

a Flames without sulfur.

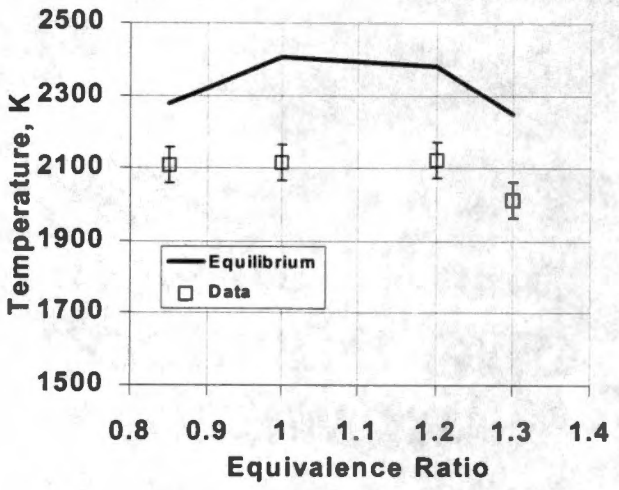

b Flames with added H_2S (1% for ϕ = 0.85,1.0,1.2, and 0.75% for ϕ = 1.3.

Figure 4-2 Comparison of the calculated equilibrium adiabatic flame temperatures with measured temperatures

[20] and Cattolica [47] who measured flame temperatures based on thermocouple and the OH rotational distribution measurements. In these flames, equilibrium calculations showed that the sulfur-bearing flame temperatures are slightly greater than the non-sulfur bearing flame temperatures for the first three flames. A large difference is not expected because the H_2S simply replaced a specified fraction of the CH_4. This minimized the thermal contribution of the H_2S. The experimental results show the opposite result. However, the temperature difference is smaller than the experimental error in the temperature measurement.

4.3 Potassium and OH Decay Profiles

These flames were observed to clarify the oxidation kinetics of potassium prior to investigating the potassium-sulfur interactions and to provide a basis for comparison with the sulfur-bearing flames. The potassium decay results are shown in Figure 4-3. Although the data were reduced to density units, the results are shown here in normalized form. Each point along the profile has been normalized to the value at the 0.5 mm point of the flame *without sulfur* (about $3x10^{12}$ atoms/cm^3). For example, the data for the fuel-lean flames with and without sulfur are normalized by the potassium density value at 0.5 mm from the fuel-lean flame with no sulfur. As previously noted, the nebulizer calibration is ot directly transferable to the burner due to unquantified losses within the burner. The potassium absorption measurement provided a calibration point that suggests that the nebulizer efficiency [41] was about 50%. However, no effort

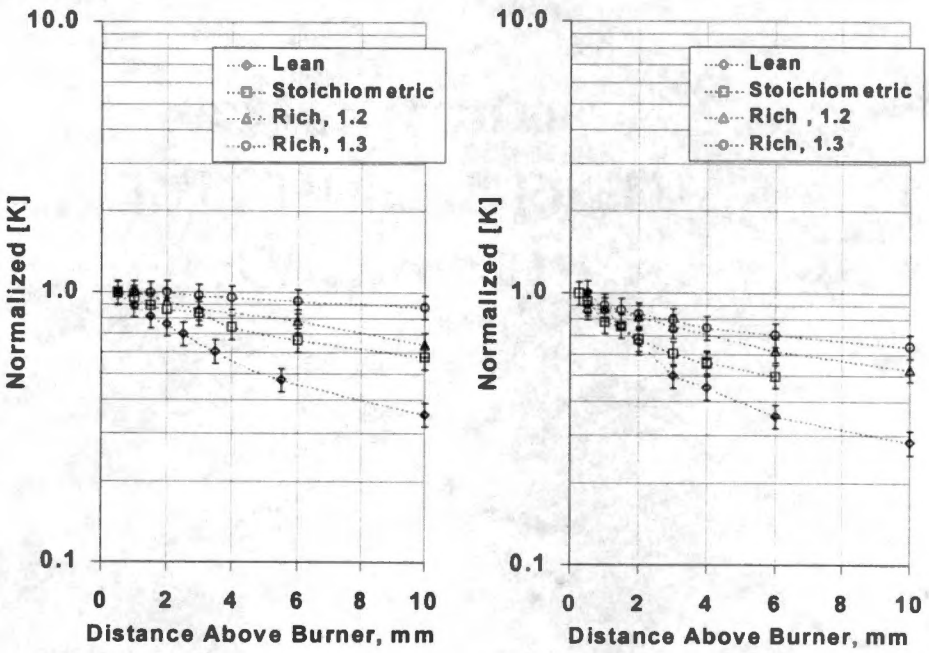

Figure 4-3 Potassium decay profiles: No sulfur and 1% H_2S (0.75% for $\phi = 1.3$).

was made to refine this estimate. Thus multiplication by an arbitrary constant is justified and the data can be presented in a normalized form without loss of relevant information. Due to oversight, the 10 mm point for the stoichiometric flame with 1% H_2S was not acquired.

Since the carbonate easily volatilizes, the potassium entered the flame as atomic potassium. In the fuel-lean and stoichiometric flames, the non-equilibrium OH population begins to combine with the free potassium to form KOH, so potassium is expected to be predominantly in the form of KOH. Additionally, potassium is cycled through KO_2 and KO via reactions with O_2, O, and OH towards KOH, as

discussed in Section 2. Hence the observed [K] decay is kinetically controlled. In the fuel-rich flames, [OH] is substantially reduced. Additionally, the H population is much increased and the potassium is shifted back towards unbound atoms through the reaction of KOH and H. Other investigators [14, 16, 18, 20] have observed these same trends for sodium and potassium. The data for flames without sulfur are in accord with the prior data.

The potassium data for the sulfur bearing flames are consistently below the potassium data for flames without sulfur. However, the data do not indicate a significant *acceleration* of the decay. The offset appears to be nearly constant along the flame axis. The offset is not sensitive to stoichiometry. The literature contains no data for potassium and sulfur in flames of any kind, so these data cannot be directly compared to any other source. However, there are data for sodium and sulfur in flames [37]. It is expected that sodium and potassium mechanisms will be similar so there is some merit in comparing the sodium results to the potassium results. The results of Schofield show similar trends. They present data from two relatively cool (~1800 K) flames - one fuel-rich and one fuel-lean. These data show that the sodium decay profiles of the sulfur-bearing flames are offset from the profiles of the flames without sulfur. The offset is similar to that of the flames observed in this work.

The OH decay results are shown in Figure 4-4. The OH data were recorded to track the changes in the radical pool as the flame gases approached equilibrium.

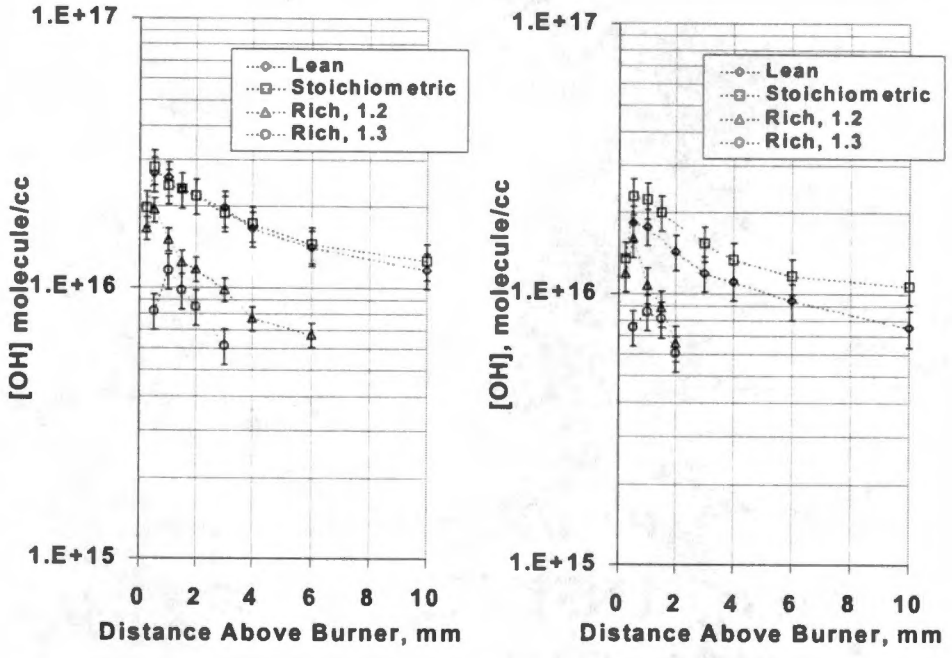

Figure 4-4 OH decay profiles: No sulfur and 1% H_2S (0.75% for $\phi = 1.3$).

These data are reported in density units. The OH population decayed below the minimum detectable level (about 5% peak absorption) before 10 mm in all four of the fuel-rich flames. The OH concentration is known to overshoot the equilibrium value at the beginning of the flame and then decay towards equilibrium. The equilibrium overshoot recorded here for flames without sulfur is in accord with that recorded by other investigators [20,47,50]. The OH levels are higher in the leaner flames, as expected.

The [OH] levels for the flames with sulfur are several percent below the levels for the flames without sulfur. Further, the OH decay is accelerated in the flames with

sulfur. This is due to the radical scavenging behavior of SO_2 in flames through reactions (34), (36), and (37). The data of the sulfur bearing flames cannot be directly compared to other literature sources because there are no other data for OH decay in methane flames with sulfur. However the data of Kallend [26] and Muller [27] for sulfur-bearing hydrogen flames show similar results.

5.0 Kinetic Analysis

At the beginning of this course of research, it was assumed that the potassium oxidation mechanism and the sulfur oxidation mechanism were established. In the early stages of modeling the flame data with the existing kinetic mechanism, it was determined that the potassium oxidation mechanism was inadequate, particularly for fuel-lean flames. A careful review of the literature concerning this subject revealed numerous errors and inconsistencies in the extant literature. In the case of the sulfur oxidation mechanism, it was determined that certain elements of sulfur chemistry were inadequate. In particular, the chemistry describing the radical scavenging behavior of sulfur – important for the main problem of the present research – was not established on a firm foundation. In both cases, the mechanisms are believed to be qualitatively correct; however, there are important details that remain unknown. Therefore, in presenting the details of the kinetic mechanism and thermodynamic data derived for this work, and the modeling comparisons, it is important to present a critical review of the literature.

This section concludes with a presentation of the modeling results compared to the data acquired in the present study. On the way to the conclusion, it is important to present a significant quantity of varied background material. This is done in five sections. First, the fundamentals of the flame model are presented. This model is used to generate all the results presented in this section. In the next two sections, the critical review of alkali-metal oxidation chemistry is

presented, followed by the development of a new potassium oxidation mechanism based on the data acquired in the sulfur-free flames. In the final two sections, sulfur chemistry is reviewed and a K/S interaction mechanism is developed and applied to calculate, through the flame model, the potassium and OH decay profiles for comparison to the data obtained in the sulfur-bearing flames. It is this mechanism that will be used to assess the impact of K/S coupling on the flammability of the secondary combustor mixtures.

5.1 CHEMKIN Description

The flow near the burner of a laminar, premixed flame can be idealized as a steady, one-dimensional, constant pressure, chemically reacting flow where reactants are passed to products through a thin flat flame. The situation is shown in Figure 5-1. Under these restrictions, the general flow equations are:

Mass Conservation: $\dot{M} = \rho u_z A$ (5.1)

Momentum Conservation: $\frac{u_z^2}{2} + \frac{P}{\rho} = const$ (5.2)

Energy Conservation: $\dot{M}\frac{dT}{dz} - \frac{1}{c_p}\frac{d}{dz}\left(\lambda A \frac{dT}{dz}\right) + \frac{A}{c_p}\sum_{k=1}^{K}\rho Y_k V_k c_{p,k}\frac{dT}{dz} + \frac{A}{c_p}\sum_{k=1}^{K}\dot{\omega}_k h_k W_k = 0$ (5.3)

Species Conservation: $\dot{M}\frac{dY_k}{dz} + \frac{d}{dz}\left(\rho A Y_k V_k\right) - A\dot{\omega}_k W_k = 0$ (5.4)

State Equation: $\rho = \frac{P\overline{W}}{RT}$ (5.5)

The symbols are defined as follows:

ρ – density

P – pressure

u_z – axial velocity

T – temperature

A – flow cross-sectional area

c_p, $c_{p,k}$ – mixture, species-k specific heat

Y_k – species-k mass fraction

V_k – species-k diffusion velocity

λ – gas thermal conductivity

h_k – species-k specific enthalpy

W_k – species-k molecular mass

ω_k – species-k production rate

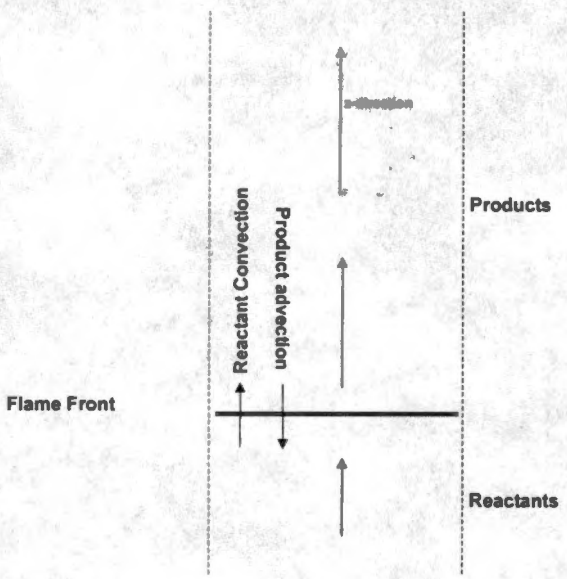

Figure 5-1 Geometry of the flame problem.

Note that the momentum equation reduces to this simple form when there are no strong axial velocity gradients. That is, when the flow velocity is very low. Since the gas is assumed to be calorically perfect, the energy equation can be written with temperature as the dependent variable. The inflow boundary conditions are specified temperature, T_{in}, and specified mass flux fractions:

$$\varepsilon_k = Y_k + \frac{\rho Y_k V_k A}{\dot{M}} \qquad (5.6)$$

At the outflow boundary, dependant variable gradients are set to zero.

The PREMIX computer program [51] is a model of this kind of flow based on these conservation equations. The PREMIX model is fully documented in reference [51]. Because temperature is often measured in experimental studies of premixed flames, PREMIX includes two options for solving the conservation equations. In one option, the energy equation is solved along with the mass and species conservation equations. In the other option, the temperature profile is prescribed and there is no need to solve the energy equation. Clearly this option is attractive because it reduces the required computations and the solution is constrained by the measured temperature, which should increase the model accuracy.

The conservation equations are solved by a finite-difference algorithm on a nonuniform grid. The algorithm includes grid refinement for regions of high spatial gradients and high curvature. The solution technique is a Newton

iteration with step-size damping and time-stepping as required. After the governing equations have been discretized, the collection of equations can be represented by a non-linear system of equations in the independent variables:

$\phi = (T_1, Y_{1,1},...,Y_{k,1}, M_1, ...T_J,Y_{1,J},...,Y_{k,J},M_J)$, 1 to k species, 1 to J grid points

The residual for the nth solution estimate is $F(\phi)$. The solution is obtained when $F(\phi) = 0$. A solution can be found using Newton's method, or

$$\phi^{(n+1)} = \phi^{(n)} - \left(\frac{\partial F}{\partial \phi}\right)^{-1}_{\phi^{(n)}} F(\phi^{(n)}) \qquad (5.7)$$

where the superscript (n) designates the nth solution estimate in the approach to the converged solution. The actual method applied in PREMIX is somewhat different to avoid computational excess. The method can be written as

$$\phi^{(n+1)} = \phi^{(n)} - \lambda^{(n)}\left(J^{(n)}\right)^{-1} F(\phi^{(n)}) \qquad (5.8)$$

Here, $\lambda^{(n)}$ is a damping parameter such that

$0 \le \lambda^{(n)} \le 1$

and

$$J^{(n)} = \left(\frac{\partial F}{\partial \phi}\right)_{\phi^{(n)}} = J^{(n-1)} \qquad (5.9)$$

that is, the Jacobian is inherited from the previous solution estimate. The Jacobian can be updated or the damping parameter reduced if the solution encounters numerical instabilities. If a solution is found, the grid is refined and a solution sought by the same method on the new grid. If no solution can be found via this method, the time derivative is added to the discretized equations and the

solution is time-marched at a user defined time step and number of steps. After time stepping, the solution by Newton iteration is tried again. When starting a new problem, the solution is first found on a coarse grid, then grid refinement takes place to a user-specified level. Convergence is not strongly sensitive to starting estimates. The PREMIX reference, [51] provides a procedure for creating starting estimates.

The thermodynamic and transport properties used in the program are provided as user input. The thermodynamic properties are stored as coefficients in temperature-dependant polynominal curve fits in the NASA format [52]. Seven coefficients are given for each species that simultaneously fit the specific heat c_P, the species enthalpy, H^0, and the species entropy S^0 as follows:

$$\frac{c_P}{R} = \sum_{n=1}^{5} a_n T^{(n-1)} \qquad (5.10)$$

$$\frac{H^0}{RT} = \sum_{n=1}^{5} \frac{a_n}{n} T^{(n-1)} + \frac{a_6}{T} \qquad (5.11)$$

$$\frac{S^0}{R} = a_1 \ln(T) + \sum_{n=2}^{5} \frac{a_n T^{(n-1)}}{n-1} + a_7 \qquad (5.12)$$

where R is the universal gas constant and T is the gas temperature. Additionally, the user supplies the molecular weight, atom count, and reference enthalpy for each species. The transport properties are computed from kinetic theory. The user provides the program the collision diameter, potential well depth, dipole moment, and polarizability for each species. The details of the calculations are given in [53].

The species source terms, ω_k, are computed from the individual reaction rates that create or destroy a particular species. The network of bimolecular reactions can be represented as

$$\sum_{k=1}^{K} \nu_{ki}' \chi_k \leftrightarrow \sum_{k=1}^{K} \nu_{ki}'' \chi_k \qquad (5.13)$$

where the ν_{ki}' and ν_{ki}'' are the stoichiometric coefficients of species k in reaction i for the reactant-side and product-side, respectively. The χ_k are the species names. Clearly, if a species is not involved as a reactant, $\nu_{ki} = 0$, and if it is not involved as a product, $\nu'_{ki} = 0$. The source terms are now

$$\dot{\omega}_k = \sum_{i=1}^{I} \nu_{ki} q_i \qquad (5.14)$$

where

$$\nu_{ki} = (\nu_{ki}'' - \nu_{ki}') \qquad (5.15)$$

and

$$q_i = k_{f_i} \prod_{k=1}^{K} [X_k]^{\nu_{ki}'} - k_{r_i} \prod_{k=1}^{K} [X_k]^{\nu_{ki}''} \qquad (5.16).$$

Here, the k_{f_i} and k_{r_i} are the forward and reverse reaction rates. The $[X_k]$ are the species mole fractions. For termolecular reactions, q_i is modified as follows

$$q_i = \left(\sum_{k=1}^{K} \alpha_{ki} X_k \right) \left(k_{f_i} \prod_{k=1}^{K} [X_k]^{\nu_{ki}'} - k_{r_i} \prod_{k=1}^{K} [X_k]^{\nu_{ki}''} \right) \qquad (5.17)$$

where the α_{ki} are relative third-body efficiencies.

The reaction mechanism is user-specified. Reactions can be specified as reversible with forward and reverse rates related through the equilibrium constant, or the forward and reverse reaction rates can be separately specified. Irreversible (one-way) reactions can also be specified. For bimolecular reactions, the reaction rate is generally specified in the generalized form,

$$k_{f_i} = A_i T^{\beta_i} e^{\frac{-E_{A,i}}{RT}} \qquad (5.18)$$

where A_i is the pre-exponential factor, β_i is the temperature exponent, and $E_{A,i}$ is the activation energy. When β_i is one-half, this is known as the Arrhenius form of the reaction rate. When microscopic reversibility is assumed, the reverse reaction rate is given by

$$k_{r_i} = \frac{k_{f_i}}{K_c} \qquad (5.19)$$

where K_c is the equilibrium constant (concentration units).

Termolecular reactions can also be given in the generalized Arrhenius form. However, pressure dependant reactions require an altemative formulation for the reaction rate. The Lindemann approach [54] has been used for all pressure dependant reactions in this work. The Lindemann approach requires Arrhenius expressions for the low- and high-pressure limits of the recombination reaction,

High-pressure: $k_0 = A_0 T^{\beta_0} e^{\frac{-E_{A,0}}{RT}}$ (5.20)

Low-pressure: $k_\infty = A_i T^{\beta_\infty} e^{\frac{-E_{A,\infty}}{RT}}$ (5.21)

For intermediate pressures, the rate is given by

$$k = k_\infty \left(\frac{P_r}{1+P_r} \right) F \qquad (5.22)$$

where

$$P_r = \frac{k_0[M]}{k_\infty} \qquad (5.23).$$

For the Lindemann form, F is one. However, Troe [55] has proposed expressions for F consistent with a higher order model, if such details is available and needed. Inputs for this form of F are included in the program.

PREMIX was used to model the flames produced in these experiments. Inputs for species concentrations were derived from the flowmeter calibrations and the nebulizer calibration. Using the measured temperatures for input to the program eliminated the energy equation. The reaction rates, thermodynamics and transport properties are described in the next sections.

5.2 Review of Alkali-Metal Kinetics

In Section 2.2.1, a summary of relevant potassium oxidation kinetics was given. The large number of scientific publications concerning the kinetics of alkali metals in high-temperature, reacting environments testifies that this subject has been more or less continuously investigated. Through the course of past investigations, the thermodynamics and kinetics have been disputed. In the initial modeling of the data acquired in the experimental phase of this work, the mechanism of Slack, et al [20] was used in the PREMIX model. Discrepancies in

the comparison between the model results and the data prompted a review of the basis of Slack's mechanism. This review revealed discrepancies in Slack's mechanism and several of the cited references. To the extent possible, these kinetic modeling discrepancies were eliminated, and good comparisons were obtained between the model results and the experimental data. In this section, the historical development of the potassium oxidation mechanism and reaction rates is considered in chronological order. Important rate determinations are summarized at the conclusion of this section.

Kaskan's experiments [14, 15] were the first premixed flame experiments to provide the details of flame radical and atomic potassium decay profiles. Fuel-lean flames of $H_2/O_2/N_2$ with added potassium or sodium (via nebulized aqueous solution) were stabilized on a flat flame burner. Absorption spectroscopy was used to monitor the decay of OH and K or Na above the burner. Each flame was established at a specific mixture ratio and temperature. After measurements were made in that flame, a small amount of O_2 was added and the decay observed again. In all cases, the alkali metal decay was accelerated by the addition of O_2. In the atmospheric and sub-atmospheric pressure flames, the decay of the alkali metal was first order in [K] (or [Na]), [O_2], and [M] in the initial regions of the flame decay profile. Furthermore, the equilibration of

$$KOH + H \Leftrightarrow K + H_2O \qquad (16)$$

as proposed by Friedman and Levy [3], was not well correlated to any of the data. Thus, in fuel-lean flames, results confirmed the pressure-dependant nature

of the potassium atom decay and suggested that a termolecular process involving an alkali-oxide governed the decay process. Kaskan [14,15] proposed that

$$K + O_2 + M \Leftrightarrow KO_2 + M \qquad (1)$$

was the only reasonable process, and assigned a rate on the order of 10^{-34} $cm^6/molecules^2/s$.

Jensen, et al performed experiments in fuel-rich flames of $H_2/O_2/N_2$ with added potassium [16], and sodium [56] to test the importance of the reactions:

$$KOH + H \Leftrightarrow K + H_2O \qquad (16)$$

and

$$K + OH + M \Leftrightarrow KOH + M \quad (2)$$

and the equivalent sodium reactions. Nine flames were observed at nearly constant temperature (~2100 K) and varying mixture ratio. Measurements of the alkali metal and H-atoms concentrations were made at several points above the burner. The kinetic fit of this data yielded

$$k_{16} = 1.8\text{x}10^{-11}e^{-1000/T}\ cm^3/molecule/s$$

and

$$k_2 = 1.5\text{x}10^{-27}T^{-1}\ cm^6/molecule^2/s.$$

He noted that the rate given for (2) was more than an order of magnitude greater than gas kinetic, but felt that this was justified as third body efficiencies greater than unity could account for the high rate.

Husain and Plane [57] investigated reaction (1) and the sodium analog [58] directly in flow tube experiments. They monitored the decay of alkali atom species concentrations by time-resolved absorption of potassium atoms (or Na atoms) generated by flash photolyzed KI (or NaI). The apparatus was operated at 753 K and 873 K and the bath gas was He, N_2, or CO_2. They fit their potassium data with the following form

$$k_1 = 1.7 \times 10^{-27} T^{-1} \text{ cm}^6/\text{molecule}^2/\text{s (M = N}_2\text{)},$$

where the T^{-1}-dependence was arbitrary. This was three orders-of-magnitude greater than estimated by Kaskan's rate [14].

After reviewing the experiments of Husain and Plane [57,58], Jensen [17] attempted to provide a consistent interpretation of the chemistry of his fuel-rich flames and Kaskan's [14] fuel-lean flames. Since k_{16} had been found to be competitive with k_2, he reasoned that the superoxides (superoxides are M-O_2 molecules, where M is an alkali metal) must be less stable than previously anticipated. He estimated the dissociation energy of KO_2 (D_0(K-O_2)) was no higher than about 41 kcal/mole, thus the recombination reaction (1) would not contribute to the decay observed in Kaskan's flame. This estimate of D_0(K-O_2) is indeed close to the currently accepted value (see Section 5.3.1), however, the agreement was fortuitous. Jensen concentrated on data from Kaskan's flame 3(a) and 3(b). However, there is an error in the publication of Kaskan's results, the decay rate labeled as "3(a)" is in fact flame "4(a)". The same error occurred for the flame labeled 3(b). (Note: in [14], flame 3(a) had an equivalence ratio and

temperature of 0.94 and 1580K, respectively; 4(a) had and equivalence ratio and temperature of 0.90 and 1720K, respectively.) Thus Jensen was analyzing a flame that was actually hotter and leaner than he thought. Given this error and the distance in time separating this data from recent observations, one can only conclude that Jensen's bond energy determination (D_0(K-O_2)) [17] be ignored. However, Jensen's determination of k_2 [16] remains valid.

Hynes, et al [18] investigated sodium decay in ten fuel-lean $H_2/O_2/N_2$ flames and temperatures ranging from 1600 K to 2400 K. [Na] and [OH] were measured by laser fluorescence. This work is of significance for understanding the flame chemistry of alkali metals in general. Noting the failure of the simple hypotheses of the previous twenty years, they reasoned that the Na/O chemistry (and alkali metal/oxygen chemistry in general) was more complex than the previous investigators had surmised. They proposed a complex network of reactions connecting Na, NaO, NaOH, and NaO_2 with the flame radicals (Figure 5-2). Measured rates were assigned to reactions for which there was data. They managed the large number of unknown reactions by assigning a rate corresponding to the O/H analog when possible and the gas kinetic rate with an adjustable coefficient when no analog existed. Further, D_0(Na-O_2) was a free parameter. They found that they could not support a high value for D_0(Na-O_2), as had been proposed by McEwan and Phillips [59]. They revised the value down to 40 kcal/mole, consistent with the value of Jensen. However, they did not feel they could support Jensen's rate for the sodium analog of (2) because it was so

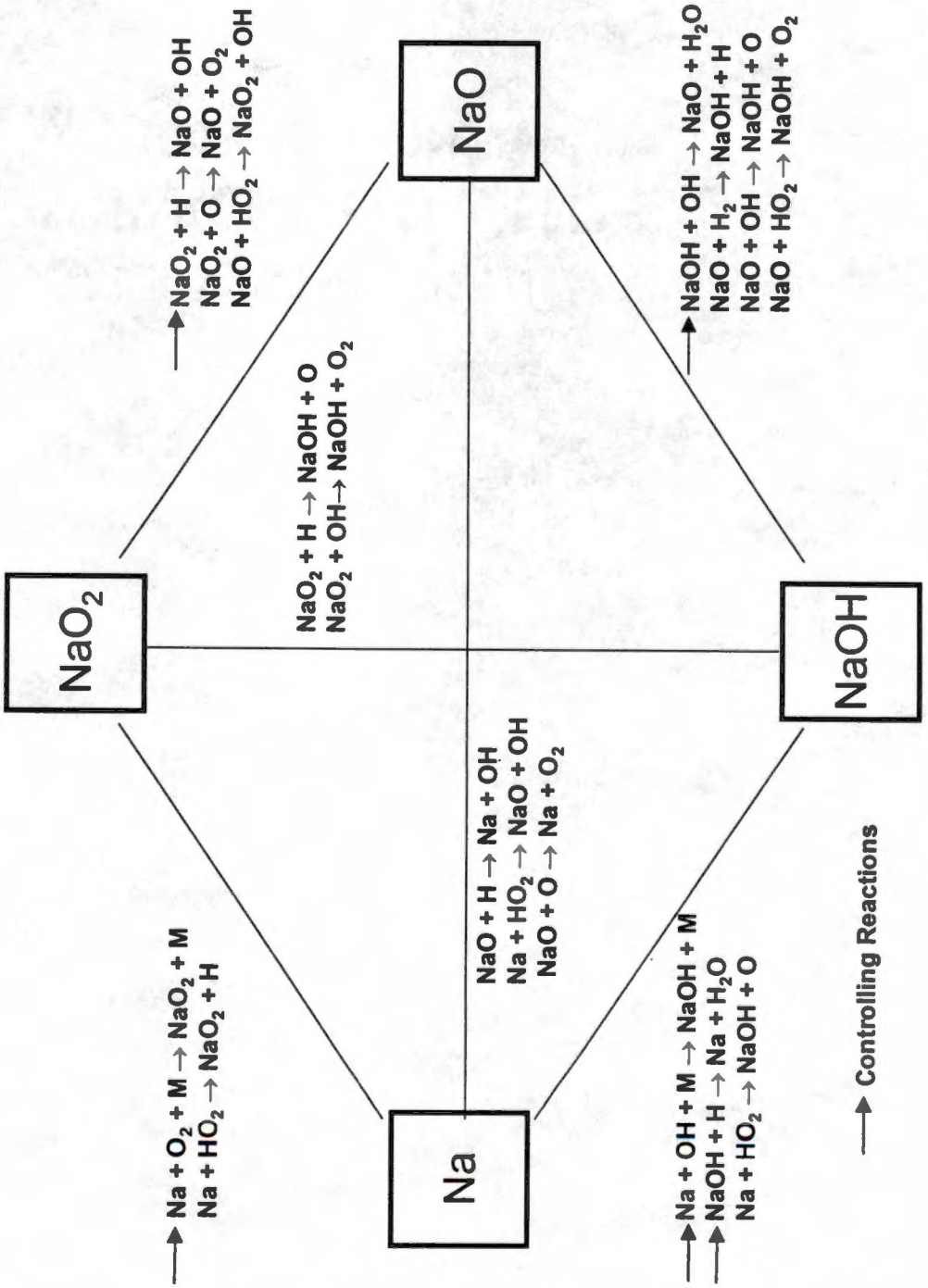

Figure 5-2 Sodium oxidation cycle proposed by Hynes, et al [18].

much faster than gas kinetic. They proposed a rate that was lower by two orders of magnitude. Finally, they abandoned the usual relationship between the forward and reverse rates for (1a). The forward rate was set to the value measured by Husain and Plane [58] while the reverse rate was set as required to match the data.

The flux of sodium through the network of Figure 5-2 follows two prominent paths. In fuel-rich flames, atomic sodium concentration decays only slightly. Thermodynamic calculations indicated that the only other sodium species would be NaOH. Thus the sodium analogs of reactions (2) and (16) provide the primary path between Na and NaOH. In fuel-lean flames, Na is predominantly found as NaOH at equilibrium. The decay of sodium observed in the flame experiments is due to the conversion of Na to NaOH. Hynes et al [18] found that the route Na $\Rightarrow$ NaO_2 $\Rightarrow$ NaO $\Rightarrow$ NaOH was very efficient. Additionally, the sodium analog of (1) accounted for a significant flux towards NaOH. The exchanges between Na and NaO and between NaOH and NaO_2 are relatively unimportant. The sodium species profiles measured in his flames could be modeled using the following four reactions:

$$NaOH + H \Leftrightarrow Na + H_2O \quad (16a)$$

$$Na + O_2 + M \Leftrightarrow NaO_2 + M \quad (1a)$$

$$NaO_2 + H \Leftrightarrow NaO + OH \quad (11a)$$

$$NaOH + OH \Leftrightarrow NaO + H_2O \quad (17a)$$

By now it was clear that the superoxides opened a new channel for the conversion of Na to NaOH, so that alkali-metal oxidation in general and by analogy potassium oxidation in particular – were sensitive to the rates for the two termolecular processes, (1) and (2).

Patrick and Golden [60] calculated the rates k_1 and k_2 using the methods outlined by Troe [55] to determine the rates for these two processes. For k_1, they determined a rate that was in reasonable agreement with measurement at T=530K [57]. For reaction (2), the rate determined was far below the rate specified by [16]. It should be noted that Patrick and Golden performed two sets of calculations for k_2: one assumed a linear geometry for KOH, and one assumed a bent K-O-H geometry (KOH is known to be linear, evidently, there was a last vestige of uncertainty about the geometry at the time of these calculations). The results for the bent geometry were in better accord with the data of [16], but still one order of magnitude lower. Later, Schofield [61] discovered minor errors in Patrick's and Golden's calculations [60]. It was revealed that the calculations for k_2 were in error (in the calculations for k_2, the bending frequency for the K-O-H bond was considered to be singly degenerate - but it should be doubly degenerate for the linear molecule.) Revised calculations were performed (but never published) and the new results [61] were in better accord with the rate specified by Jensen [16].

Husain, et al [62] measured k_2 with He as the third body. Potassium vapor was generated in a heat-pipe oven containing molten potassium. The potassium vapor was pumped into a heated stainless steel reactor. Water vapor in an excess of helium was admitted into the reactor as well. OH was generated by pulsed irradiation of the water vapor from a nitrogen-discharge flash lamp. The decay of [OH] due to reaction with the potassium vapor was observed via molecular resonance-fluorescence. The reactor temperature was 530 K. The measured rate was

$$k_2 = 8.8\text{x}10^{-31} \text{ cm}^6/\text{molecule}^2/\text{s (M=He)}.$$

This rate was extrapolated to combustion temperatures and composition using the Troe's methods [55] with approximations for the efficiencies for N_2, H_2, and H_2O relative to He. This estimate for 530 K was

$$k_2 \sim 4\text{x}10^{-30} \text{ cm}^6/\text{molecule}^2/\text{s (M=H}_2\text{, N}_2\text{, and H}_2\text{O)}.$$

Additionally, they provided an extrapolation of this rate to flame temperatures (500 K < T < 2100 K) using Troe's methods to obtain:

$$k_2 \sim 1.28\text{x}10^{-26}\, T^{1,28} \text{ cm}^6/\text{molecule}^2/\text{s (M=H}_2\text{, N}_2\text{, and H}_2\text{O)}.$$

Husain et al [63] acquired new data for k_1 with the third-body M = N_2 in flow tube experiments. They employed a new, refined apparatus in an attempt to acquire data over a wider temperature range than had been possible previously [57]. The goal of the experiment was to obtain data over a wide temperature range so that the temperature dependence of the rate could be extrapolate to combustion temperatures. They fit their data with

$$\ln(k_f) = -0.2558[\ln(T)]^2 + 1.361\ln(T) - 66.14 .$$

over the temperature range 200 to 2000 K. The temperature dependence of this rate is similar to that of Patrick and Golden [60], although their rate is somewhat higher.

Schofield and Steinberg [19] revisited their alkali metal oxidation data base (including unpublished lithium and potassium decay data). After reviewing the results of the lithium oxidation data, they discovered that the rapid decay of lithium in fuel-lean flames implied a stable superoxide. Further, they reassessed the relationship between the forward and reverse rates of (1) and concluded that they must be related through the equilibrium constant. From this analysis, they reported a value for D_0(Na-O_2) = 65 kcal/mole. No value was reported for KO_2, but it was stated that it should be close to the value for NaO_2. With their analysis, it was clear that the sodium oxidation cycle of Figure 5-2 was appropriate for each of the alkali metals, with species fluxes through each leg dependent on the relative stability of each of the species. Contrary to the proposed mechanism of Jensen [17], the path through the superoxide provides a potentially efficient route for the alkali metal to the hydroxide.

Slack et al [20] measured potassium and OH concentrations using laser absorption in three $CH_4/O_2/N_2$/Ar flames heavily seeded with potassium. Their goal was to clarify the mechanism for rocket motor afterburning suppression. In particular, they wanted to find out if potassium was a more effective flame

inhibitor than sodium. While few details were given, they reported investigating a network similar to that of Hynes, et al [18] and found five reactions were required to account for the observed decrease in OH molecules in their flames. Slack's mechanism [20] is given in Table 5-1. Slack found, in agreement with Hynes, et al [18], that the potassium species were connected through the network of Figure 5-2. The rate for reaction (1) was taken from Patrick and Golden [60]. The value of k_2 was established at 2000 K by best fit to the potassium and OH decay profiles. The temperature dependence for this rate was taken from the bent K-O-H structure calculations of [60]. While they noted that this temperature dependence fit their data and that of Husain's measurement with He as the third body [62], the KOH molecule is known to be a linear molecule. The temperature dependence based on the assumed bent molecular geometry is arbitrary.

Table 5-1 Slack's potassium oxidation mechanism [20]; $k = AT^n e^{-(E/RT)}$

Reaction	Number	*A*	*n*	*E*
$K + O_2 + M = KO_2 + M$ [1]	1	1.89×10^{-22}	-2.68	596.0
$K + OH + M = KOH + M$ [1]	2	1.90×10^{-25}	-2.00	0.0
$KOH + H = K + H_2O$ [2]	16	3.67×10^{-12}	0.5	0.0
$KO_2 + H = KO + OH$ [2]	11	3.67×10^{-12}	0.5	0.0
$KO + H_2O = KOH + OH$ [2]	17	9.88×10^{-13}	0.5	0.0

[1] - $cm^6/molecule^2/s$, [2] - $cm^3/molecule/s$

Plane, et al [64] measured k_1 in a flow tube reactor over a greater temperature range (250 – 1109 K). They flash photolyzed potassium acetate (CH_3OOCK) to produce free potassium atoms in a stream of O_2 and bath gas (N_2 or He). Potassium atoms were monitored by induced fluorescence spectroscopy. Diffusion-corrected potassium decay was used to infer k_1. Additionally, the bond dissociation energy, D_0(K-O_2) was inferred from this data. This determination is discussed in the Section 5.3.2. Extrapolations using the Troe's methods [55] were made, based on the measured rates, for two temperature ranges to obtain k_1 for two temperature ranges:

$$k_1 = 8.8\text{x}10^{-27}\ T^{1.23}\ \text{cm}^6/\text{molecule}^2/\text{s}\ (\text{M}=N_2,\ 140\ \text{K} < T < 240\ \text{K})$$

$$k_1 = 1.2\text{x}10^{-24}\ T^{1.96}\ \text{cm}^6/\text{molecule}^2/\text{s}\ (\text{M}=N_2,\ 1500\ \text{K} < T < 2000\ \text{K})$$

The high temperature extrapolation exhibits a lower temperature dependence than that of Husain, et al [57]. Plane explained that scavenging of potassium atoms by iodine in the flow tube reactions of [63] increased the observed decay of [K], causing the temperature dependence to be overestimated.

Rate determinations for the two important termolecular reactions (1) and (2) are summarized in Figures 5-3 (reaction 1) and 5-4 (reaction 2). For k_1, the flow tube data are in fair agreement. Divergence between the reaction rates occurs when the rates are extrapolated to combustion temperatures. If the rate determination of Husain, et al [57] is rejected because of the arbitrary temperature dependence, then the data and extrapolations are in fair agreement. Because of the experimental bias in the Husain's [63], the rate expression of [64] is preferred.

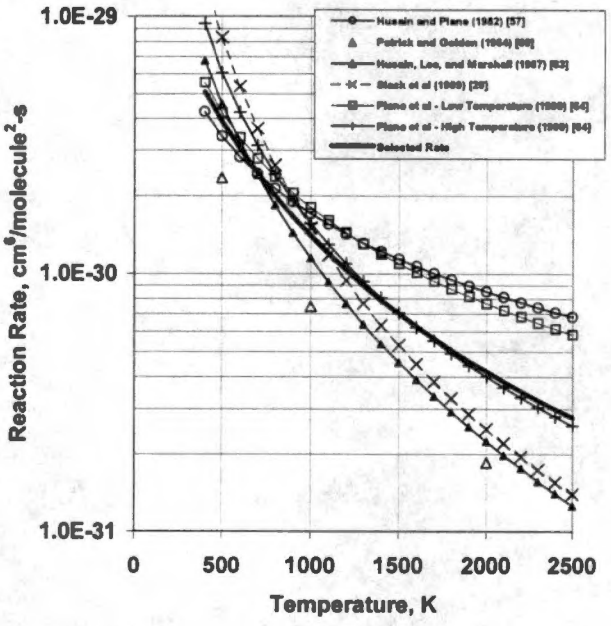

Figure 5-3 Summary of rate determinations for K + O_2 + N_2.

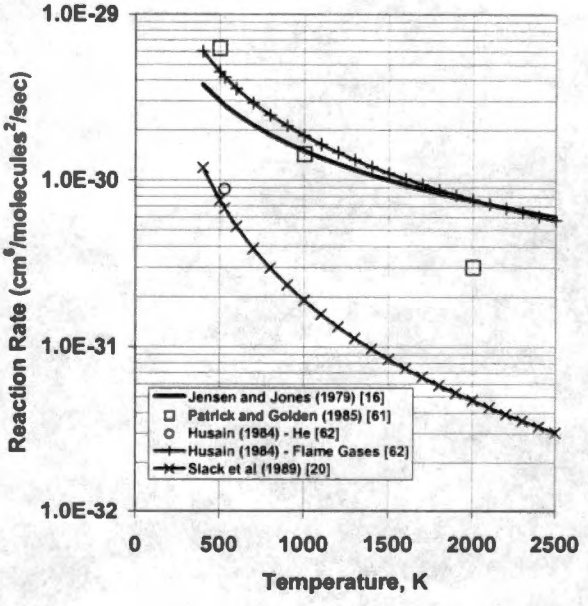

Figure 5-4 Summary of rate determinations for K + OH + M. Note: data from Patrick and Golden are the corrected, unpublished results.

The rate chosen for k_1 is indicated in Figure 5-3 by the heavy line. An Arrhenius form was fit to the low temperature and high temperature expressions of Plane [64], bridging the two expressions at intermediate temperatures. This yields the rate expression

$$k_1 = 2\text{x}10^{-24} T^{-2} e^{(-1500/RT)} \text{ cm}^6/\text{molecule}^2/\text{s}.$$

Four rate determinations for k_2 are shown in Figure 5-4. For this reaction, there is good agreement between the determinations of Jensen [16], the revised determinations of Patrick [61] and the determinations of Husain [62]. The determination of Slack [20] is rejected because it is based on the He data and does not account for flame gas composition. Additionally, the high-temperature determination is based on his flame data - the potassium decay in fuel-rich flames is not dependent on k_2, but on relative rates of k_2 and k_{16}. The rate of Husain [62] was employed in the calculations to be described.

5.3 Flame Modeling - Flames without Sulfur

5.3.1 Species Thermodynamic Properties

For C/H/O/N species, the thermodynamic properties from the CHEMKIN library [52] have been used. Only the K/O/H species properties are discussed in this section. Since the flames in this study contain a paucity of potassium atoms, no K_2 species were considered. The possible potassium species are KH, KO, KO_2, and KOH. KH can be neglected based on previous flame studies [20]. In the next section, the extant literature concerning the thermodynamic properties of

KO, KO_2, and KOH are reviewed. The PAC91 computer program [65] was used to compute thermodynamic properties and to compute curve fit coefficients in the form of equations 5.10 through 5.12. The rigid rotor-harmonic oscillator model was used to calculate the thermodynamic properties. The estimated thermodynamic properties of KS, KSO_2, KOS, KS_2, and KSH as well as H-O-S thermodynamic properties are presented in Section 5.5.1.

Diatomic Molecule KO

There are three experimental determinations of the dissociation energy for the KO molecule [66 - 68]. There are no experimental determinations of the spectroscopic constants of KO. References [69] and [70] provide summaries of spectroscopic constant estimates and theoretical determinations for KO. Lee, et al [71] conducted a thorough theoretical study of all the alkali oxides. A summary of the results of these studies is given in Table 5-2.

The spectroscopic constants from Lamoreaux, et al [69] were selected for this study. Schofield [72] selected the value of Lamoreaux, et al [69] for the dissociation energy. This value is within the error estimates for the other three experimental determinations. The values of Lamoreaux, et al [69] were selected here as well. However, the calculations of Lee, et al [71] indicate that the first excited state of KO is only 220 cm^{-1} above the ground state. The calculated value of D_0 for the A-state is 84.8 kcal/mole and the calculated values of D_0 for the ground state are significantly lower than the values inferred from measurements.

Table 5-2 Summary of spectroscopic parameters for KO.

Reference	r_e (Å)	ω_e (cm^{-1})	$\omega_e x_e$ (cm^{-1})	Electronic Degeneracy	D^0 (kcal/mole)	$\Delta_f H^0$ (kcal/mole)
[66]	-	-	-	-	65.97	
[67]	-	-	-	-	62.50	
[68]	-	-	-	-	62.27	
[69]	2.2	389	-	2	65.97	14.31
[70]	2.2	350	2.2	4	58.50	17.0
[71]	2.42	361	-	4	47.70	-
Selected	2.2	389	-	4	65.97	14.31

Thus it is probable that the measurements are 'contaminated' by the A-state of KO. The heat of formation, $\Delta_f H^0_{KO}$, was calculated from the bond dissociation energy using Hess's law, [73]. That is

$$\Delta_f H^0_{KO} = \Delta_f H^0_{O(v)} + \Delta_f H^0_{K(v)} - D_0(K-O) \qquad (5.24)$$

where $\Delta_f H^0$ for gaseous O and K ($\Delta_f H^0_{O(v)}$ and $\Delta_f H^0_{K(v)}$, respectively) were determined from tabulated data [70]. The resulting thermodynamic properties are tabulated in Appendix F.

Triatomic Molecule KO_2

Kaskan [14] first proposed KO_2 as an important intermediate in potassium oxidation. Since that time, the molecule has been investigated extensively by

several experimental and theoretical techniques. The equilibrium geometry, vibrational frequencies and electronic structure are now considered well established. However, the dissociation energy and heat of formation are disputed.

The initial determination of the KO_2 geometry by Andrews, et al [74,75] remains valid. Andrews was also able to determine two of the three vibrational modes. Additionally, Andrews determined that the molecule had C_{2v} symmetry and was predominately ionically bound. The geometry calculations by Partridge, et al [76] were consistent with the conclusions of Andrews. Trembaly, et al [77] provided an experimental determination of the asymmetric K-O stretch mode (not identified by Andrews) and confirmed the symmetric geometry, symmetric K-O stretch mode frequency, and O-K-O bending mode frequency of Andrews [74,75]. The calculations of geometry and vibrational frequencies by Lee, et al [78] additionally confirmed the conclusions of other investigators. However, they pointed out that the differences that do remain between the calculations of vibrational frequencies and the data are probably due to anharmonic vibrational properties of the molecule, which are not included in the models. The geometrical parameters for KO_2 are shown in Table 5-3. A summary of corresponding vibrational parameters is shown in Table 5-4. The experimentally determined geometry of Lee, at al was selected for this molecule. This geometry is close to that of Andrews. The theoretical geometry of Trembaly is suspect due to the use of a simplified potential function for the molecule. However, the

Table 5-3 Summary of geometry determinations for KO_2.

Reference	$r_{e,K-O}$ (Å)	$r_{e,O-O}$ (Å)	α (degrees)
[74]	2.28	1.33	33
[76]	2.415	1.346	-
[77]	2.10	1.33	37
[78]	2.410	1.341	32.3
Recommendation	2.410	1.341	32.3

Table 5-4 Summary of vibrational mode determinations for KO_2.

Reference	ν_1 (cm^{-1})	ν_2 (cm^{-1})	ν_3 (cm^{-1})
[74]	1097.7	307.5	-
[75]	1108	307.5	-
[77]	1108.9	306.98	304.3
[78]	1172.5	330.9	306.1
Recommendation	1108.9	306.98	304.3

experimentally determined vibrational frequencies of Trembaly were used. They have been measured directly and compare well to those measured by Andrews.

The ionic nature of the KO_2 molecule has significant implications for other K/S/O/H species. The KO_2 molecule is compared to the KO molecule and to the O_2^- anion in Figure 5-5. The K-O bond length is comparable in the two molecules, though the K-O bond is slightly longer in the KO_2 molecule. The measured O-O bond length in the two molecules is nearly identical. Finally, the O-O stretch frequency between the two molecules is nearly identical. These comparisons testify to the ionic nature of the bonds. The ionic nature of this molecule was exploited for the predictions of the K/S/O/H molecules.

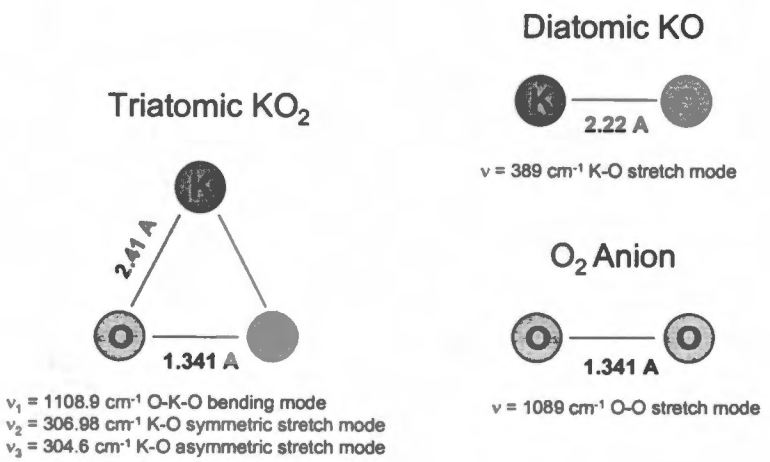

Figure 5-5 KO_2 geometry and vibration compared to KO and O^-_2.

A firm determination of the dissociation energy for KO_2 has been elusive. The current state of the literature is displayed in Figure 5-6. The data from Jensen [17] and Schofield [72] were obtained in flame studies. The data of Plane [64] were determined in a time-resolved kinetics study. The value of Partridge [76] was determined by an *ab initio* technique. Jensen's value must be rejected due to the error in the publications of Kaskan's data [14], as discussed in section 5.2. Schofield [61] has abandoned his value determined in his flame study [19]. The flame studies do not provide a sensitive means for determining bond dissociation energy in this instance. The required kinetic flux of potassium atoms through the $K \Rightarrow KO_2 \Rightarrow KO \Rightarrow KOH$ reaction steps can be achieved by either increasing the stability of KO_2 or increasing or decreasing one or more of the reaction rates taking KO_2 to KO and KOH. So it was left to reconcile Plane's experimental lower limit and the calculations of Partridge.

Plane's lower limit seems unequivocal, and is tentatively recommended. While this uncertainty does not diminish the understanding of alkali metal oxidation chemistry, it does limit the accuracy of rate determinations. The heat of formation was calculated from Hess's law as follows:

$$\Delta_f H^0_{KO_2(v)} = \Delta_f H^0_{O_2(v)} + \Delta_f H^0_{K(v)} - D_0(K - O_2) \qquad (5.25)$$

where $\Delta_f H^0$ for gaseous O_2 and K ($\Delta_f H^0{}_{O_2(v)}$ and $\Delta_f H^0{}_{K(v)}$, respectively) were determined from tabulated data [70]. The results are tabulated in Appendix F.

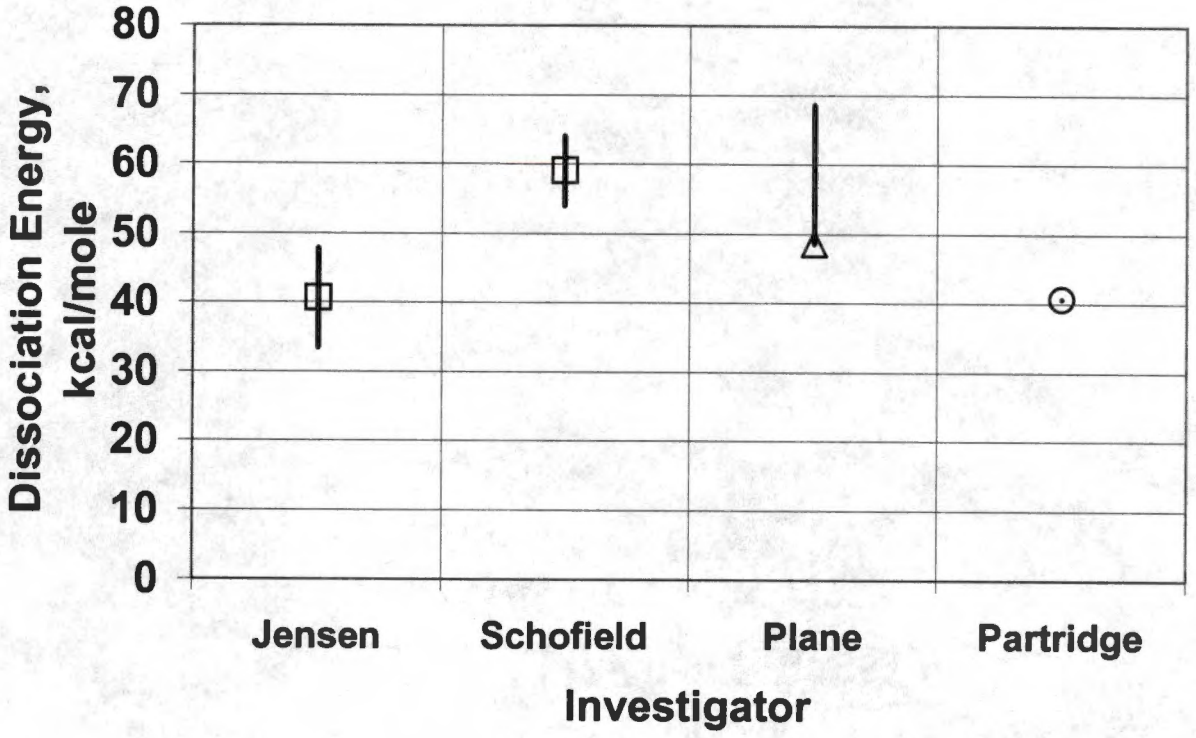

Figure 5-6 Display of KO_2 dissociation energy determinations. Note that Plane determined a lower limit (D_o > 48.5 kcal/mole). Squares are experimental determinations, triangle is experimental lower limit, circle is theoretical determination.

Triatomic Molecule KOH

Thermodynamic properties of all the alkali hydroxides were recently reviewed [79, 80]. KOH thermodynamic properties were derived from the summary of Gurvich, et al [80] and are shown in Appendix F.

5.3.2 Transport Properties

The required inputs to the PREMIX code [51] for calculation of transport properties are collision diameter, potential well depth, dipole moment, and polarizability for each of the molecular species involved in the calculation. Transport properties for the species K, KO, KO_2, and KOH were taken from Slack, et al [20] and are shown in Table 5-5. For the remaining species, the transport properties were taken from the CHEMKIN library [53]. In this work, a mixture-averaged diffusion coefficient, defined in reference [53], is employed. The diffusion model based on the mixture-averaged diffusion coefficient is much less sensitive to the details of the diffusion of the trace species of concern here. However this diffusion model is less accurate. For the atmospheric pressure flame, test calculations showed that the diffusion model is not critically important for the prediction of the post-flame species profiles.

Table 5-5 Inputs for the calculation of transport properties for K/O/H species.

Species	Collision Diameter σ(Å)	Well Depth ε/k_B (K)	Dipole Moment μ ($10^{-8}cm^{3/2}erg^{1/2}$)	Polarizability α(Å)
K	4.25	850	0	1
KO	3.812	383	0	1
KO_2	4.69	1213	0	1
KOH	4.52	1213	0	1

5.3.3 Hydrocarbon Combustion Mechanism

The combustion of methane provided the radical pool and bath gas for the experiments conducted in the present work. Thus, it was important for the model to calculate methane combustion accurately. The details of the combustion of saturated hydrocarbons have been extensively investigated for several years. This line of research has been so successful in this decade that mechanisms for the combustion of very high order hydrocarbons are being actively pursued.

Just after the flame front (~1 mm), methane is attacked by the flame radicals O, OH, H and rapidly consumed. The intermediate species CH_3, and CH_2O open important methane consumption branches. The methyl radical reacts with O to yield formaldehyde. The path though formaldehyde leads to HCO and CO. Of

course, H_2 is also created in large quantities as methane is consumed. In very fuel-rich flames, the concentration of CH_3 may be such that C_2-hydrocarbons may be found, generated through reactions such as $CH_3 + CH_3 = C_2H_5 + H$, leading eventually to other C_2-hydrocarbon fragments, such as acetylene, and to CO. The consumption of methane and the other hydrocarbon fragments occurs vary rapidly in the flame at atmospheric pressure.

After the initial flame sheet, the remaining fuel fragments are predominately CO and H_2. Therefore the primary task of the mechanism is to accurately compute the consumption of CO and H_2 in the post flame gases. The mechanism of Warnatz [81] provides such a mechanism. As presented [81], the mechanism was developed to describe the chemistry in very fuel-rich C_2H_2/O_2 flames. The mechanism composed by the Gas Research Institute (GRI) [82] is another example. This mechanism is composed and *adjusted* specifically for natural gas combustion. This mechanism has received extensive review and has been tested against many diverse data sets [82]. However, the authors of this mechanism strongly caution that since the mechanism was globally optimized, addition or deletion of reactions from this mechanism may have unwanted effects. In the present work, it was expected that the addition of sulfur-bearing compounds would significantly modify the radical profiles in both the pre- and post-flame chemistry. Thus, it was deemed unwise to use the GRI mechanism.

Two versions of the Warnatz mechanism [81] were employed in the present study. In early calculations, the complete mechanism [81] was used, updated with rates from [83]. A simplified mechanism was then extracted from this mechanism wherein all C_2-hydrocabon reactions were removed. For the flame conditions in the current experiments, no significant difference was noted in the flame radical profiles or major flame species. Thus, for computational efficiency, the simplified mechanism was used for all calculations in the present study. The simplified mechanism is shown in Table 5-6 and in Appendix A. Thermodynamic properties for all the species involved in the hydrocarbon mechanism were taken from the CHEMKIN thermodynamics library [52].

5.3.4 Modeling Results – Flames without Sulfur

Preliminary modeling of the flames described in Section 4 was based on the potassium kinetic mechanism of Slack, et al [20]. However, the comparison of the calculated results with the data was unsatisfactory, particularly for the fuel-lean flame. The experimental [OH] and [K] profiles of the fuel- flames were relatively well predicted, but the experimental [K] decay rate was significantly over-predicted in the fuel-lean flame. Because of this, the basis for Slack's potassium oxidation mechanism was reinvestigated, as discussed in Section 5.2. Given the number of discrepancies found in the literature, it was deemed necessary to redevelop the potassium oxidation mechanism based on the data gathered for this work. The procedure outlined by Hynes, et al [18] was used to generate a new potassium oxidation mechanism. That is, a reaction mechanism

Table 5.6 Simplified hydrocarbon combustion mechanism. Rate expressions are given in the form $k_i = A_i T^{\beta_i} e^{(-E_{a,i}/RT)}$. For bimolecular reactions, units are (cm^3/molecule/s). For termolecular reactions, units are (cm^6/$molecule^2$/s). The units for E_A are cal/mole.

Reaction	A	β	E_a
H+O2=>O+OH	9.76E+13	0.0	14851.0
O+OH=>H+O2	1.45E+13	0.0	701.0
H2+O=>H+OH	1.50E+07	2.0	7550.0
H+OH=>H2+O	6.70E+06	2.0	5570.0
H2+OH=>H2O+H	1.00E+08	1.6	3330.0
H2O+H=>H2+OH	4.60E+08	1.6	18560.0
OH+OH=>H2O+O	1.50E+09	1.1	0.0
H2O+O=>OH+OH	1.50E+10	1.1	17240.0
H+H+M=H2+M[1]	1.80E+18	-1.0	0.0
H+OH+M=H2O+M[1]	2.20E+22	-2.0	0.0
H+O2+M=HO2+M[1]	2.00E+18	-0.8	0.0
HO2+H=OH+OH	1.50E+14	0.0	1000.0
HO2+H=H2+O2	2.50E+13	0.0	690.0
HO2+O=OH+O2	2.00E+13	0.0	0.0
HO2+OH=H2O+O2	2.00E+13	0.0	0.0
CO+OH=CO2+H	6.32E+06	1.5	-497.0
CH3+H(+M)=CH4(+M)	6.00E+16	-1.0	0.0
Low Pressure[2]	8.00E+26	-3.0	0.0
CH4+H=>CH3+H2	2.20E+04	3.0	8740.0
CH3+H2=>CH4+H2	6.60E+02	3.0	7740.0
CH4+O=>CH3+OH	1.20E+07	2.1	7630.0
CH3+OH=>CH4+O	1.30E+05	2.1	4680.0
CH4+OH=>CH3+H2O	1.60E+06	2.1	2460.0
CH3=H2O=>CH4+OH	2.90E+05	2.1	16790.0
CH3+O=CH2O+H	8.43E+13	0.0	0.0
CH2O+H=HCO+H2	2.50E+13	0.0	3990.0
CH2O+O=HCO+OH	3.50E+13	0.0	3510.0
CH2O+OH=HCO+H2O	3.00E+13	0.0	1190.0
HCO+H=CO+H2	2.00E+14	0.0	0.0
HCO+O=CO+OH	3.00E+13	0.0	0.0
HCO+OH=CO+H2O	5.00E+13	0.0	0.0
HCO+O2=CO+HO2	3.00E+12	0.0	0.0
HCO+M=>CO+H+M[1]	1.57E+14	0.0	15760.0
H+CO+M=>HCO+M[1]	1.92E+14	0.0	735.0
CH2+H=CH+H2	4.00E+13	0.0	0.0
CH2+O=CO+H+H	5.00E+13	0.0	0.0
CH2+O2=CO2+H+H	1.30E+13	0.0	1500.0
CH+O=CO+H	4.00E+13	0.0	0.0
CH+O2=CO+OH	2.00E+13	0.0	0.0

[1] Third body efficiencies relative to N_2 are H_2 = 1.0, O_2 = 0.4, H_2O = 6.5, CO_2 = 1.5, CO = 0.75

[2] Lindemann form of the reaction rate for pressure-dependant reactions, see Gardiner [54].

was assembled, the various reaction rates were estimated, and the rate parameters were refined via the 'brute force' method of parameter estimation discussed in Section 3.1.

Reactions were considered between the potassium species (K, KO, KO_2, and KOH), the flame species (O, H, O_2, H_2, OH, HO_2, and H_2O) and the third-body species M. In order to capture every possible reactant combination, the algorithm of Indritz, et al [84] was modified and applied in the present study. After the first pass, 88 possible reactions were identified as relevant to the potassium oxidation kinetics. This list was further reduced by eliminating endothermic reactions and reactions that required more than two bonds to be broken and two to be formed. Twenty reactions remained. This list was further reduced by eliminating the reactions:

$$K + O + M \Leftrightarrow KO + M$$

$$KO + H + M \Leftrightarrow KOH + M$$

$$KO + O + M \Leftrightarrow KO_2 + M.$$

Each of these reactions paths is better served by simple bimolecular reactions that ought to be much faster. The final list included the same seventeen reactions identified by Hynes, et al [18] for sodium. These reactions are tabulated in Table 5-7.

For the important termolecular reactions (1) and (2), the rates identified in Section 5.2 were assigned and held fixed. The starting estimates for the rate

Table 5-7 Reactions initially proposed for potassium oxidation.

Number	Reaction	Rate Estimate
1	$K + O_2 + M = KO_2 + M$	Plane et al (1990) [64]
2	$K + OH + M = KOH + M$	Husain et al (1984) [62]
3	$K + HO_2 = KO_2 + H$	Gas Kinetic Model
4	$K + HO_2 = KOH + O$	$H + HO_2 = H_2O + O$
5	$KO_2 + H = KOH + O$	$H + HO_2 = H_2O + O$
6	$KO_2 + O = KO + O_2$	$HO_2 + O = OH + O_2$
7	$KO_2 + OH = KOH + O_2$	$HO_2 + OH = H_2O + O_2$
8	$KO + H = K + OH$	Gas Kinetic Model
9	$KO + O = K + O_2$	$OH + O = H + O_2$
10	$K + HO_2 = KO + H$	$H + HO_2 = OH + OH$
11	$KO_2 + H = KO + OH$	$HO_2 + H = OH + OH$
12	$KO + OH = KOH + O$	$OH + OH = H_2O + O$
13	$KO + H_2 = KOH + H$	$OH + H_2 = H_2O + H$
14	$KO + HO_2 = KO_2 + OH$	Gas Kinetic Model
15	$KO + HO_2 = KOH + O_2$	$OH + HO_2 = H_2O + O_2$
16	$KOH + H = K + H_2O$	Gas Kinetic Model
17	$KOH + OH = KO + H_2O$	Gas Kinetic Model

parameters of the remaining reactions were assigned based on the H/O analog of the K/O reaction, where possible. Otherwise, a hard-sphere gas kinetic collision frequency was used to estimate the rate. The expression for the hard-sphere collision frequency is well known and developed in references [85] and [86]. Frequency of collisions between two species A and B is given by

$$Z = \sqrt{\frac{8k_B T}{\pi \mu_{AB}}}\sigma \qquad (5.26)$$

where the parameters are defined as

Z = collision frequency

k_B = Boltzmann's constant

μ_{AB} = reduced mass $1/\mu_{AB}=(1/m_A + 1/m_B)$, m_A m_B - masses of particles A, B

σ = collision cross section: $\sigma = \pi(r_A + r_B)^2$

Molecular radii were taken from transport data (Section 5.3 and [53]). The gas kinetic collision frequency is a function of the square root of the translational temperature. Thus, reaction rates were specified as $k = AT^{0.5}$. This temperature dependence provides some measure of temperature extrapolation. Note that the parameters of the reaction rate constant expression (prexponential or steric factor$A$, temperature exponent β, and activation energy E_a) generated in this work are to be regarded as fit parameters rather than physical constants. However, there is no loss of physical relevance in this regard because the expression for the rate constant k generate physical values for k.

From the starting estimates, the rate parameters for these reactions were adjusted to get good simultaneous agreement with the potassium and hydroxyl decay profile data for each of the flames. The adjustments were guided by examining the goodness of fit (subjectively judged), species production through each reaction (known as kinetic flux: k_i[A][B] for the hypothetical reaction: A + B $\Rightarrow$ C +D), and the sensitivity coefficients after each adjustment. The final mechanism is shown in Table 5-8.

Table 5-8 Final potassium oxidation mechanism. Rate expressions are given in the form $k_i = A_i T^{\beta_i} e^{(-E_{a,i}/RT)}$. For bimolecular reactions, units are (cm^3/molecule/s). For termolecular reactions, units are (cm^6/$molecule^2$/s). E_A has units of cal/mole.

Number	Reaction	A	β	E_a
1	$K + O_2 + M = KO_2 + M$	7.25E+23	-2.00	712
2	$K + OH + M = KOH + M$	4.64E+21	-1.28	0
3	$K + HO_2 = KO_2 + H$	1.00E+10	0.5	0
4	$K + HO_2 = KOH + O$	6.13E+11	0.5	0
5	$KO_2 + H = KOH + O$	1.00E+11	0.5	0
6	$KO_2 + O = KO + O_2$	4.00E+11	0.5	0
7	$KO_2 + OH = KOH + O_2$	1.00E+11	0.5	0
8	$KO + H = K + OH$	6.40E+10	0.5	0
9	$KO + O = K + O_2$	4.22E+11	0.5	0
10	$K + HO_2 = KO + H$	9.66E+11	0.5	0
11	$KO_2 + H = KO + OH$	1.06E+11	0.5	0
12	$KO + OH = KOH + O$	8.21E+10	0.5	0
13	$KO + H_2 = KOH + H$	2.24E+12	0.5	0
14	$KO + HO_2 = KO_2 + OH$	8.02E+11	0.5	0
15	$KO + HO_2 = KOH + O_2$	8.02E+12	0.5	0
16	$KOH + H = K + H_2O$	1.00E+11	0.5	0
17	$KOH + OH = KO + H_2O$	2.02E+12	0.5	0

With this mechanism, the observed decay profiles from each of the flames are well reproduced. The comparisons are shown in Figures 5-7 through 5-10. The OH concentration profiles are well predicted for the fuel-lean flame (ϕ = 0.85), stoichiometric flame, and the fuel-rich flame (ϕ = 1.20), falling within the estimated error range of the experiments. For the richest flame (ϕ = 1.3), the [OH] decay rate is well predicted, but the level is under predicted. It is possible that the simplified hydrocarbon combustion mechanism is inadequate to describe the flame radical chemistry for very fuel-rich flames. Note that the measured potassium profiles were normalized by the potassium concentration taken at a point 1 mm above the burner and compared to normalized calculated profiles. The calculated profiles were normalized to the maximum value in the profile. In all cases, the model correctly calculated the observed trend and levels. For the stoichiometric and the fuel-rich (ϕ = 1.3) flame, the calculated potassium profiles slightly below the measure profiles.

The calculated distributions of other potassium species for the fuel-lean (ϕ = 0.85) and fuel-rich (ϕ = 1.2) flames are shown in Figure 5-11. In the fuel-lean flame, the bulk of the potassium is found bound to the hydroxyl radical, as expected. KO_2 and KO concentrations are an order of magnitude below that of K. In the fuel-rich flame, the potassium is essentially in the form of free atoms in the early stage of the flame. By the latter stages of the flame, the concentration of the hydroxide is nearly equal to that of the free atoms. The concentrations of KO_2 and KO are at least two orders of magnitude below that of the free atoms.

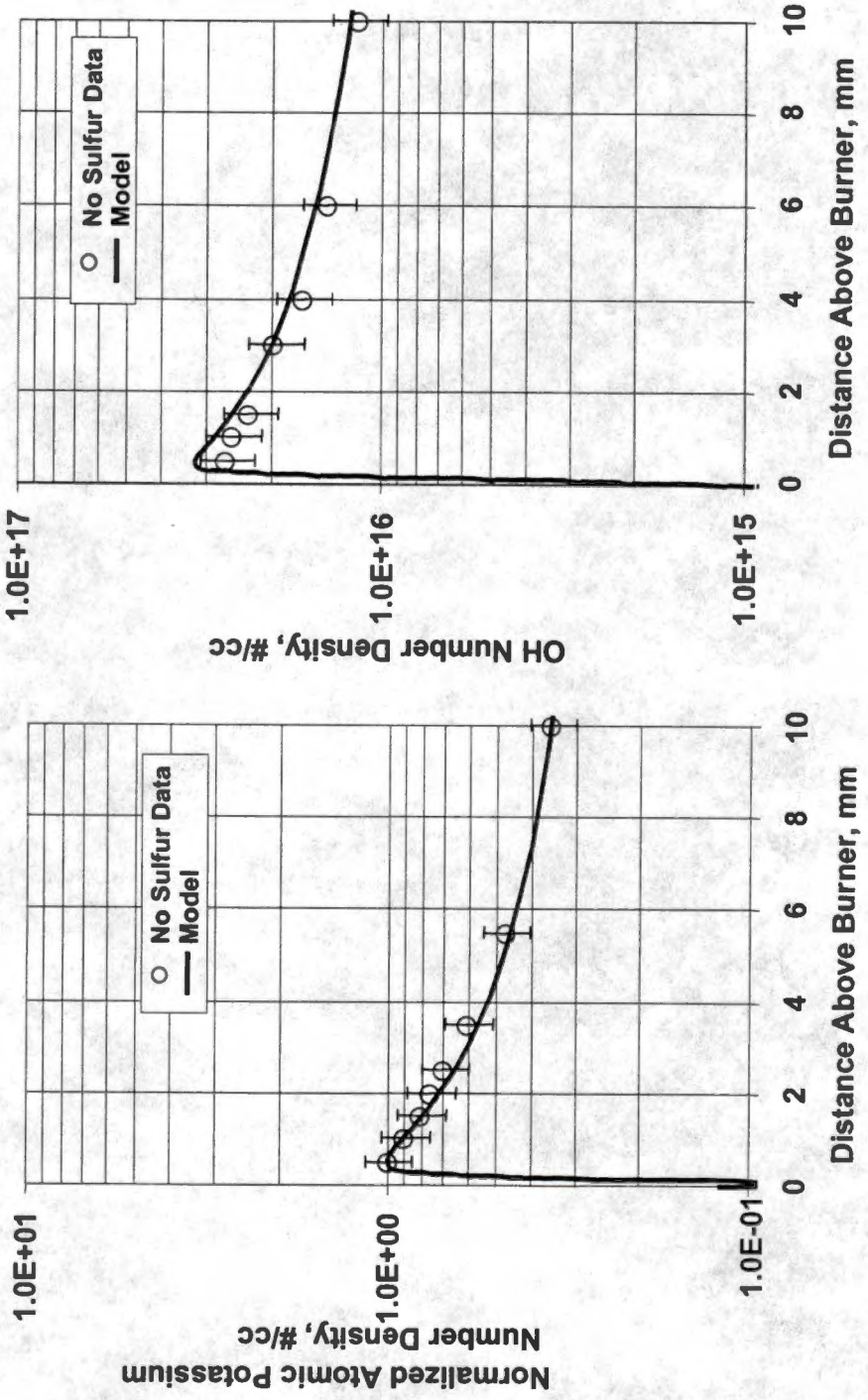

Figure 5-7 Comparison of experimental and calculated species profiles in the fuel-lean (ϕ=0.85) flame, no sulfur.

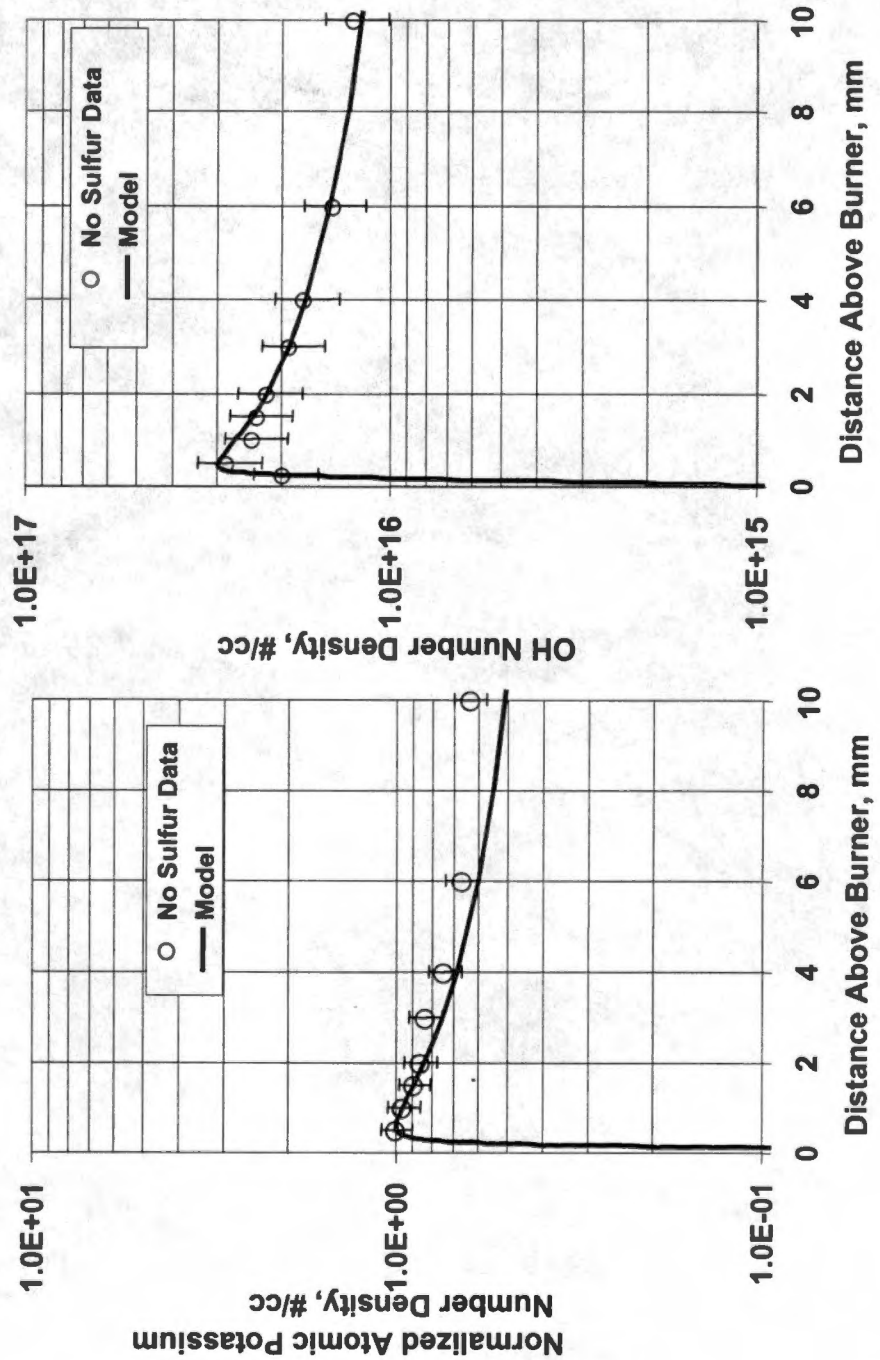

Figure 5-8 Comparison of experimental and calculated species profiles in the stoichiometric (ϕ=1.0) flame, no sulfur.

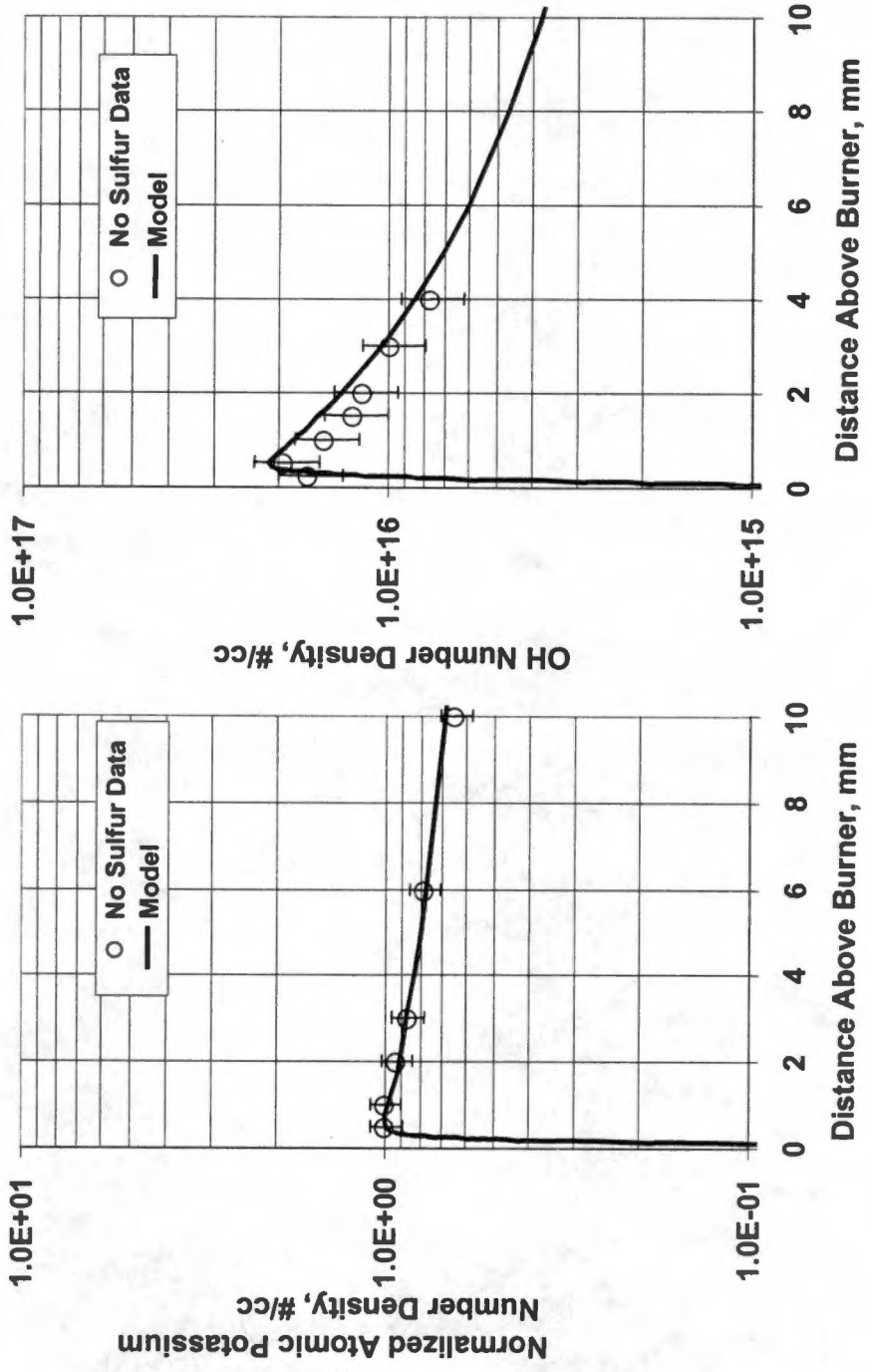

Figure 5-9 Comparison of experimental and calculated species profiles in the fuel-rich (ϕ=1.2) flame, no sulfur.

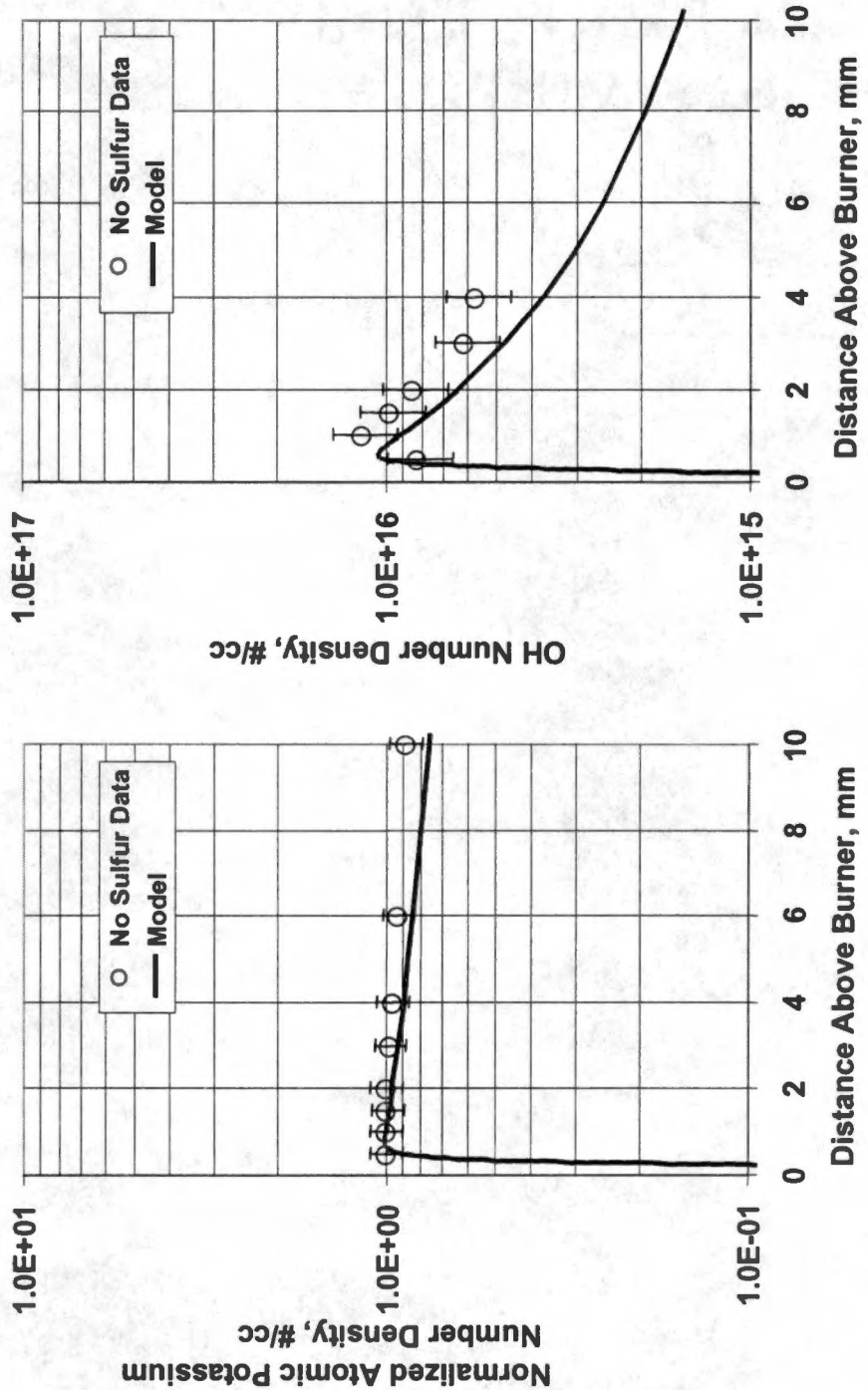

Figure 5-10 Comparison of experimental and calculated species profiles in the fuel-rich (ϕ=1.3) flame, no sulfur.

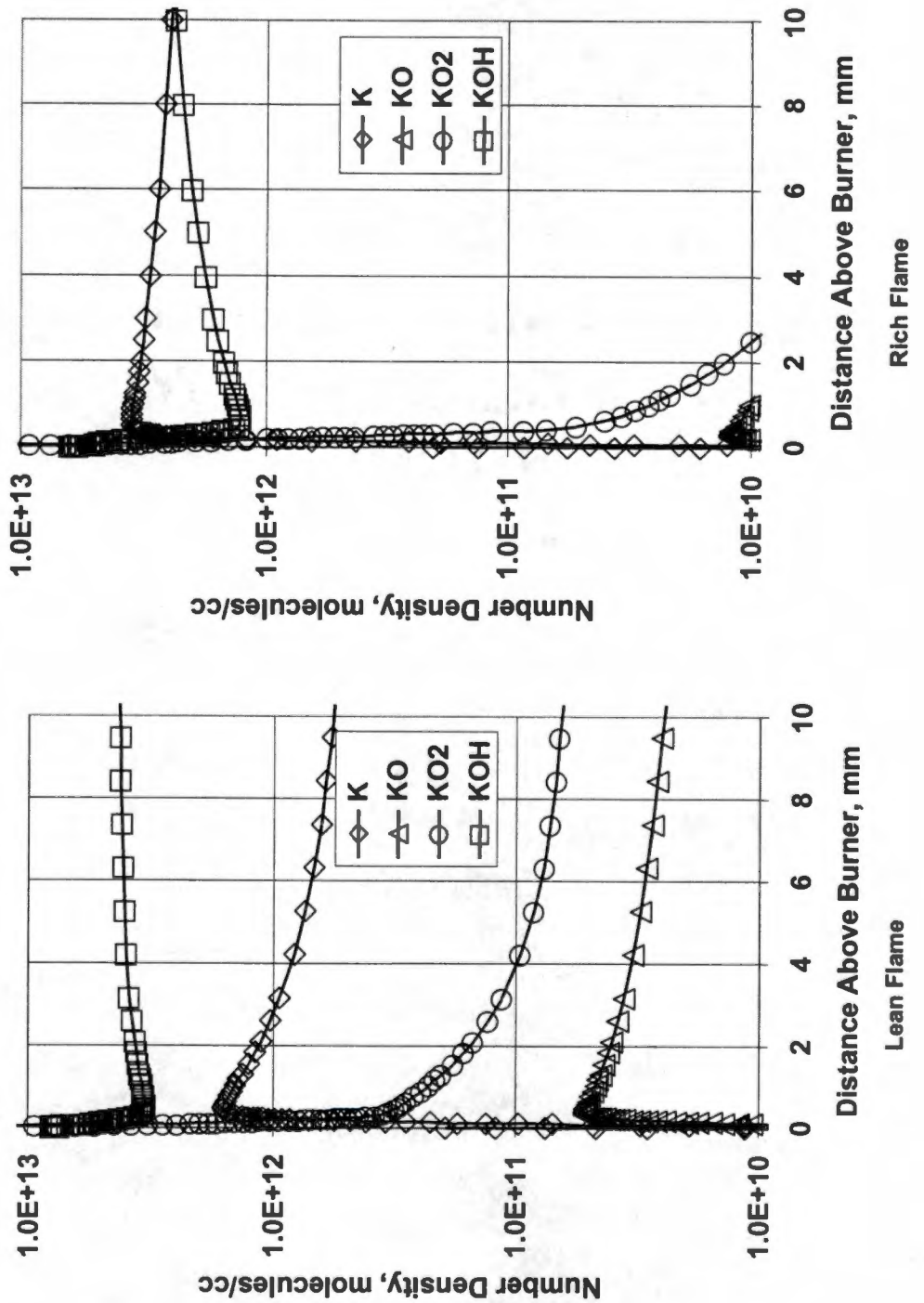

Figure 5-11 Calculated distribution of potassium species in fuel-lean (ϕ=0.85) and fuel-rich (ϕ=1.2) flames.

The reactions working within the mechanism are best interpreted through Figure 5-12, the potassium analog of the sodium oxidation cycle proposed by Hynes, et al [18] (see Figure 5-2). Species production rates and sensitivity coefficients for the fuel-lean flame (ϕ=0.85) are shown in Figures 5-13 and 5-14, respectively. Early in the flame (less than 2 mm above the burner) several reactions are active, as seen in Figure 5-13. Reaction (1):

$$K + O_2 + M \Leftrightarrow KO_2 + M \qquad (1)$$

consumes K atoms, pumping K into the upper channel ($K \Rightarrow KO_2$) of the cycle shown in Figure 5-12. The potassium atoms are then moved through reactions (6) and (11).

$$KO_2 + O \Leftrightarrow KO + O_2 \qquad (6)$$

$$KO_2 + H \Leftrightarrow KO + OH \qquad (11)$$

to KO. Reactions (5), (7) and (9) appear to be minor channels. There is a relatively large kinetic flux through reaction (17):

$$KOH + OH \Leftrightarrow KO + H_2O \qquad (17)$$

Reaction (17) is nearly in equilibrium, keeping KOH and KO tightly linked. Finally, K and KOH are directly linked through reactions (2) and (16):

$$K + OH + M \Leftrightarrow KOH + M \qquad (2)$$

$$KOH + H \Leftrightarrow K + H_2O \qquad (16)$$

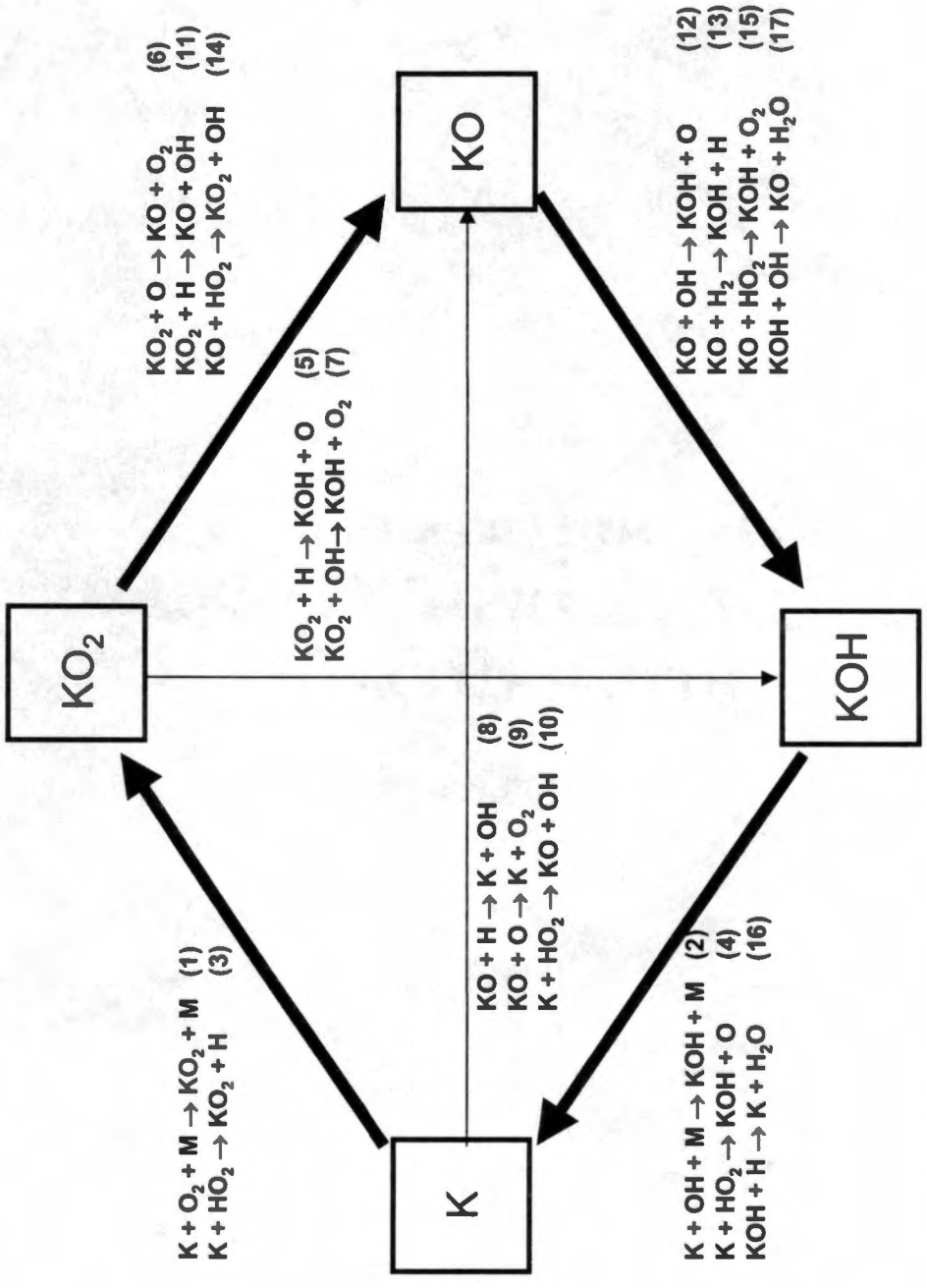

Figure 5-12 Potassium oxidation cycle.

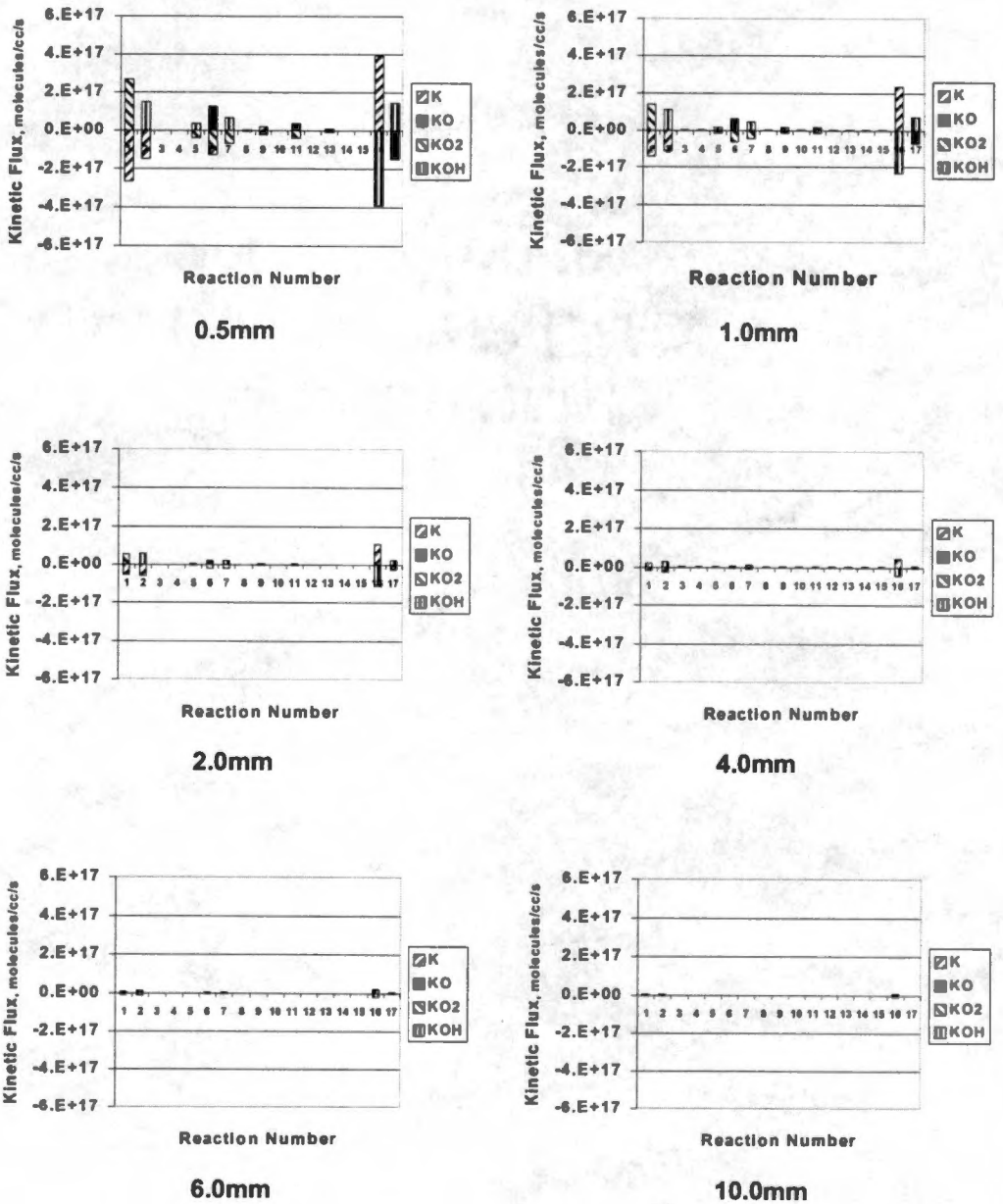

Figure 5-13 Production rates for potassium species in each reaction – fuel-lean (ϕ=0.85) flame.

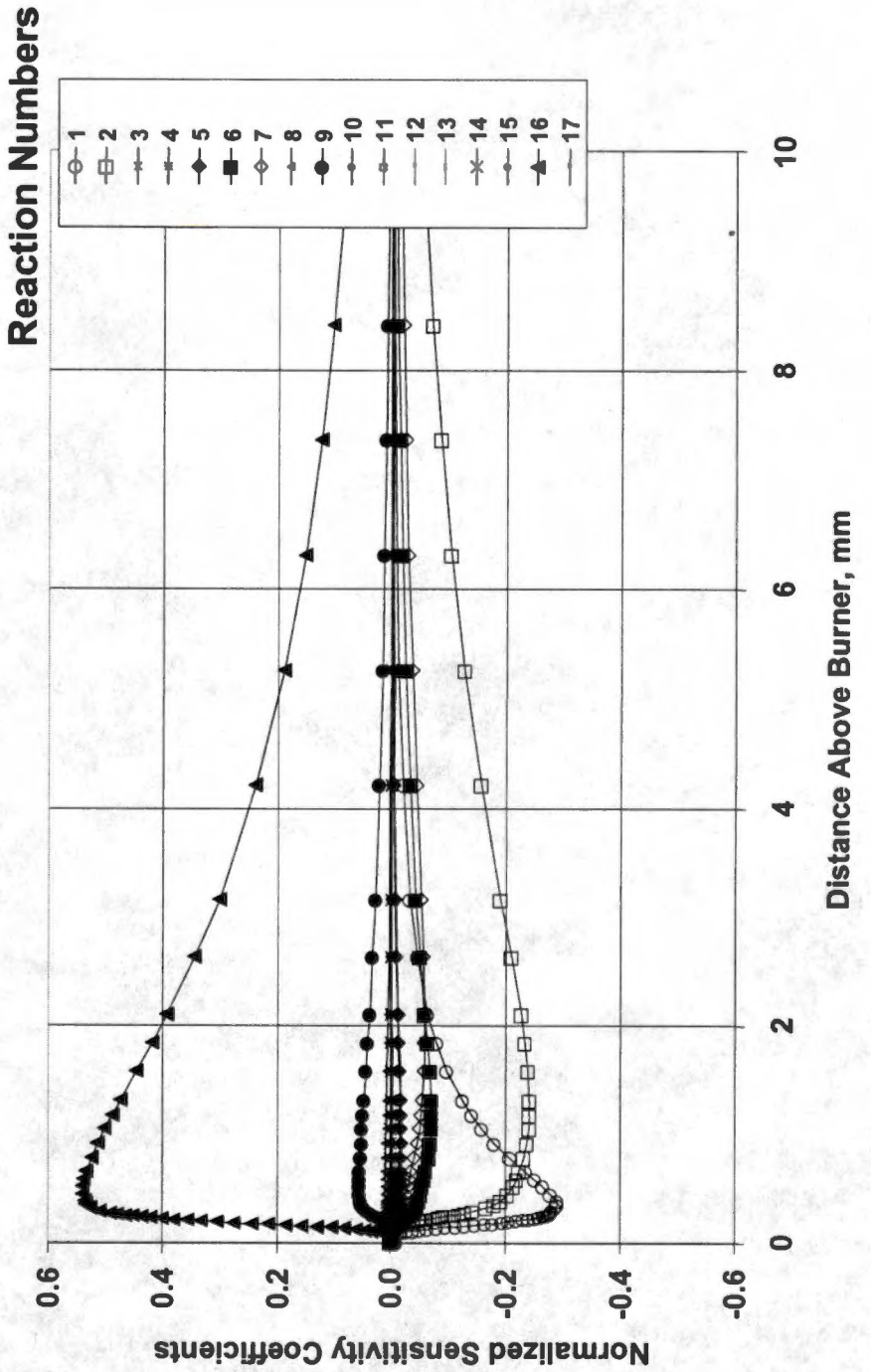

Figure 5-14 Sensitivity coefficients for potassium reactions – fuel-lean (ϕ=0.85) flame.

The balance between K and KOH is held by the flux through the upper channel ($K \Rightarrow KO_2 \Rightarrow KO \Rightarrow KOH$) of Figure 5-12 and the flux through the lower channel ($KOH \Rightarrow K$) of Figure 5-12. Even though KO_2 and KO are minor species, they clearly play a significant role in controlling the distribution of potassium atoms in the cycle in fuel-lean flames. The fluxes between KO_2 and KOH, and KO and K are relatively minor. The sensitivity coefficients for the fuel-lean flame (Figure 5-14) show that the potassium concentration is most sensitive to reactions (1), (2), (6), and (16). In fact, the overall mechanism can be simplified by eliminating all but these reactions and (17). Reaction (17) is also critical, but the flux through that channel will remain large with any reasonable reaction rate. Potassium concentration is most sensitive to reaction (16) and this rate controls the cycle. Overall, potassium is consumed and eventually converted to KOH. The importance of KO_2 and KO is to provide an alternate path for K to KOH.

Similar results are shown for the fuel-rich flame in Figures 5-15 and 5-16. As seen in Figure 5-15, the flux through the upper channel of Figure 5-12 is significantly diminished because of the lack of oxygen in the flame. The K/KOH balance is held by reactions (2) and (16), just as Jensen [16] had claimed. All other channels are minor. The sensitivity coefficients (Figure 5-16) confirm this. Beyond the flame sheet (above 0.5 mm) production through reactions (2) and (16) is nearly balanced. Now it is clear why Slack's flames [20], much like the fuel-rich flames observed in this study, are not particularly sensitive to the rate of

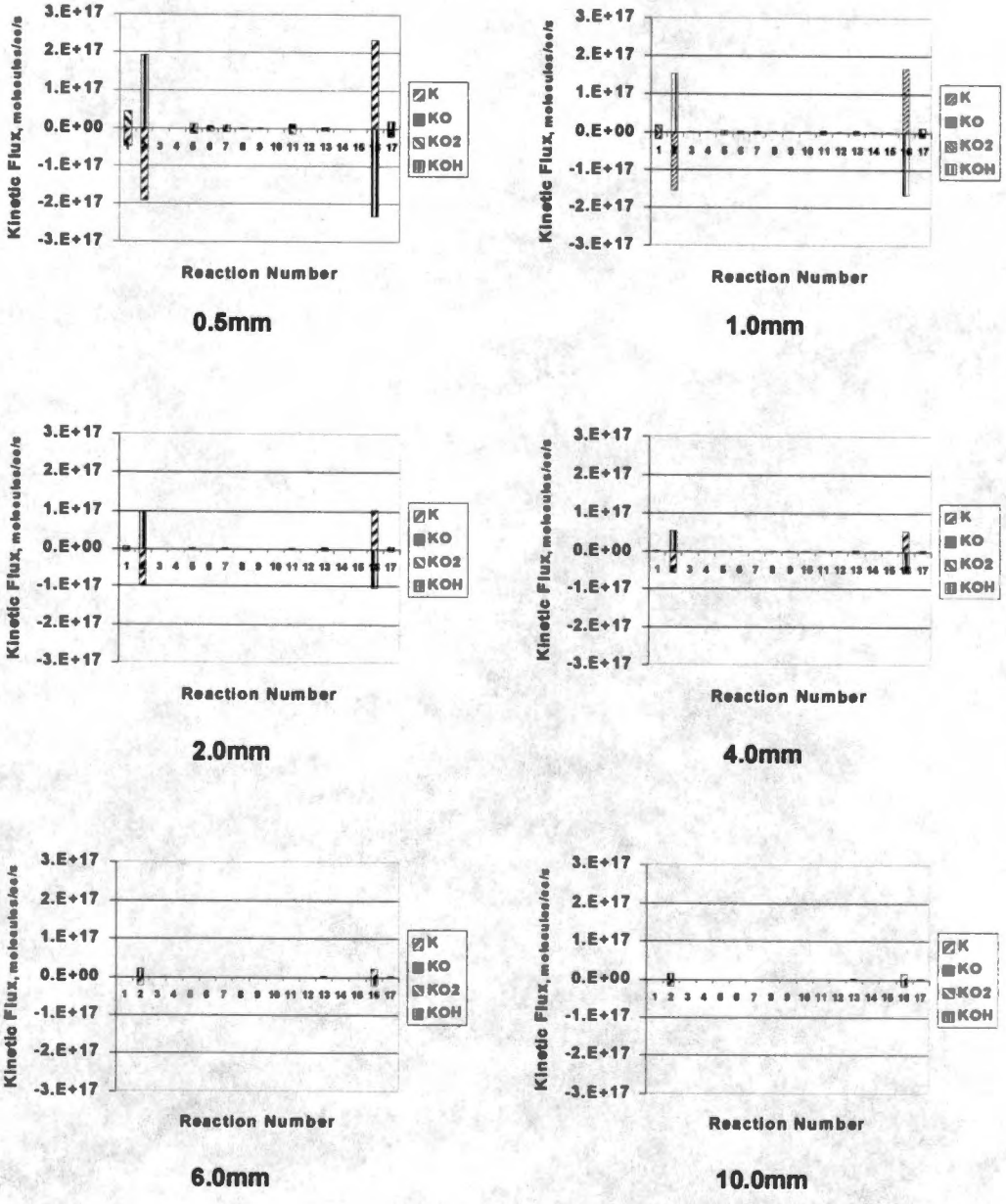

Figure 5-15 Production rates for potassium species in each reaction – fuel-rich (ϕ=1.2) flame.

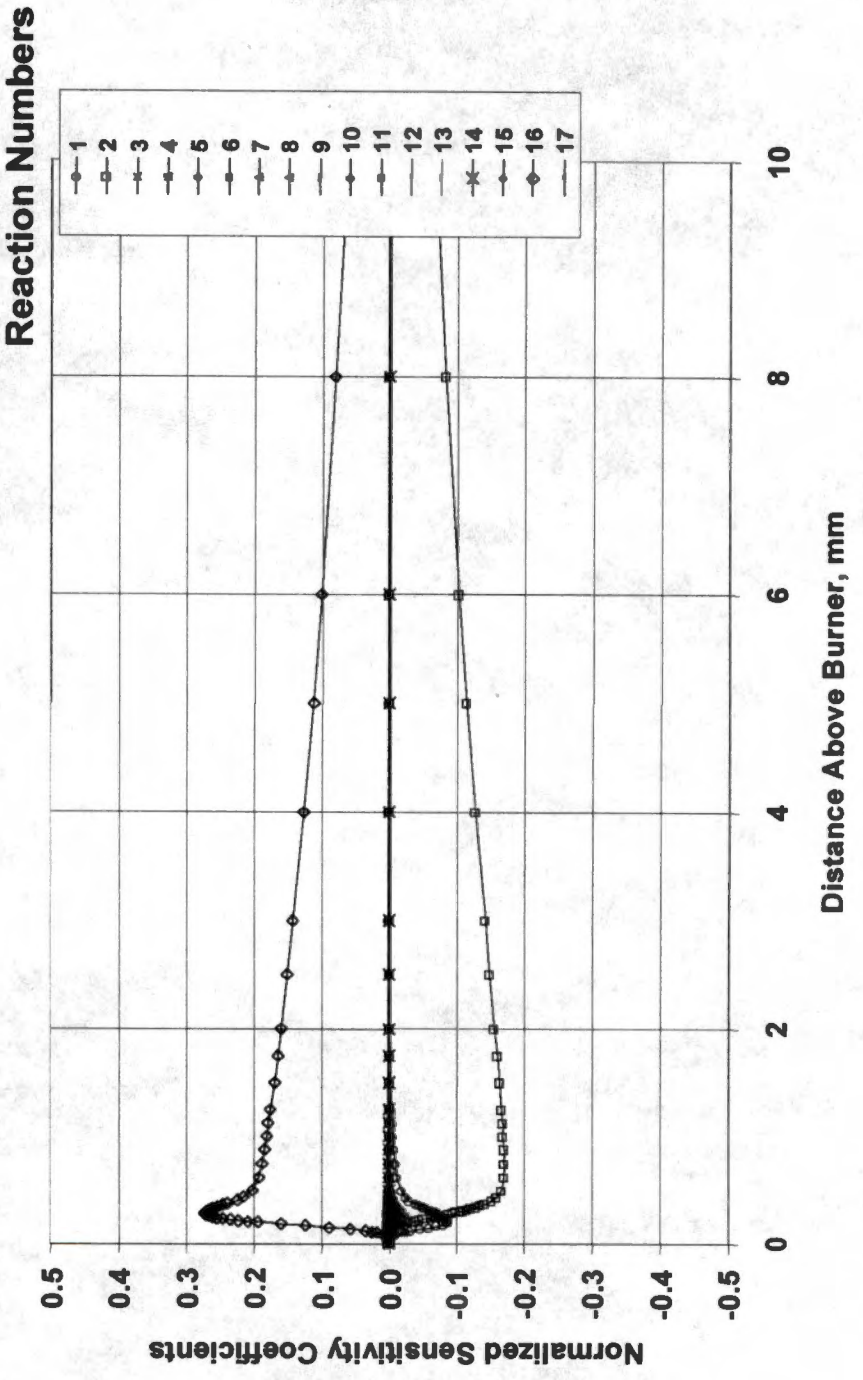

Figure 5-16 Sensitivity coefficients for potassium reactions – fuel-lean (ϕ=1.2) flame.

reaction (2), k_2. Reaction (2) serves the purpose of modulating the flux from KOH to K through reaction (16). If the rate for reaction (16) is adjusted, the rate of reaction (2) must be adjusted accordingly. Thus, if k_{16} is not known independently, k_2 cannot be uniquely determined.

While this model fits the data very well, the rates of many of the reactions remain uncertain, most importantly, reactions (1) and (2). There are extensive direct measurements for the rate of reaction (1). However, these measurements have not been made at combustion temperatures and the measurements have not yielded much information on the relative efficiencies of different third-body collision partners. Based on the measurements of Husain [54], one could expect CO_2 to be twice as efficient as N_2. The efficiency with H_2O as a third body is unknown. The rate derived from the measurements in N_2 is likely to be lower than the effective rate in flame gases. Measurements for reaction (2) are sparser. The only *published* theoretical work [60] is in error. The corrected (and unpublished [61]) analysis of reaction (2) shows a rate that is between the two flame determinations [16,20] of k_2. However, Slack's rate can be rejected in light of the analysis by Husain [62] and the insensitivity of these flame experiments to that rate. The brute force method has yielded the tentative mechanism in Table 5-7. This mechanism has performed well in the test against this data. Until such time as improved direct rate measurements or calculations are available, this mechanism is recommended for providing the engineering solutions required.

5.4 Review of Sulfur Kinetics

In Sections 5.2 and 5.3, potassium thermodynamics and oxidation chemistry were developed and the results of the flame model were compared to the experimental data gathered in the experiments of the present study. In this and the next section, a similar development of sulfur chemistry and thermodynamics, as well as K/S chemistry and thermodynamics will be presented. One aspect of sulfur chemistry of particular importance in the present work is the affect that sulfur compounds, and sulfur dioxide in particular, have on flame radicals. Another aspect of sulfur chemistry important for this work is the sulfur oxidation mechanism, needed to perform the flame computations. These topics are developed jointly in this section through a chronological review of the relevant literature. The sulfur oxidation mechanism is shown in Section 5-5 and in Appendix A.

McAndrew and Wheeler [21] were the first investigators to note the effects of SO_2 on flame radicals. In an effort to understand the mechanism for radical recombination in the post flame gases of H_2/O_2 flames, they added small amounts of different stable molecules (CO_2, SO_2, N_2) to premixed $C_3H_8/N_2/O_2$ flames and observed the changes in the spatial decay of H atoms. H atom populations were monitored by the lithium hydroxide method. They observed that even small added amounts of SO_2 greatly accelerated the decay of H atoms in the flame. The mechanism that they proposed to account for the observed interaction has never been accepted and will not be considered further.

Webster and Walsh [4] were the first to specifically investigate the effect of SO_2 on flame radicals. They added small amounts of SO_2 to H_2/O_2 mixtures and determined the change in the second explosion limit of the mixture. With small additions of SO_2 (<0.5%), the second explosion limit could be dramatically reduced, especially at low pressures. The pressure-dependence of the reduction showed that the explosion inhibition was due to direct H-atom removal by SO_2. Reaction (34) was proposed as the H-atom scavenging step:

$$H + SO_2 + M \Leftrightarrow HSO_2 + M \qquad (34).$$

They estimated the rate to be ~$4x10^{-32}$ $cm^6/molecule^2/s$. They were, however, unable to determine the fate of HSO_2. Additionally, the geometry and thermodynamic properties of HSO_2 were entirely speculative.

Fenimore and Jones [22] sampled SO_2, H_2S, H_2, and H_2O in the post flame gases above fuel-rich and -lean flat flames of H_2/O_2. They found notably that SO_2 was the predominant sulfur-bearing species in their fuel-rich flames. Additionally, they found that the rate of radical recombination in the flames with sulfur, determined from the rate of heat evolution in the post flame, was two times greater than for flames with no sulfur, implying the enhanced radical recombination noted by McAndrew and Wheeler [21]. Fenimore and Jones hypothesized that reaction (34), as proposed by Webster and Walsh [4], could account for the radical evolution if the rate were ~$2x10^{-31}$ $cm^6/molecule^2/s$, five times the rate specified by Webster and Walsh [4]. It was noted that differences in flame constituents and temperature probably account for the differences in

reaction rate The final significant development from the work of Fenimore and Jones [22] was the proposal of reactions to regenerate SO_2 molecules scavenged by reaction (34). Two reactions were proposed:

$$H + HSO_2 \Leftrightarrow H_2 + SO_2 \qquad (36)$$

$$OH + HSO_2 \Leftrightarrow H_2O + SO_2 \qquad (37)$$

However rates were not given for these reactions. In fuel-lean flames, reactions (43) followed by (44) were proposed to cause the observed increase in heat evolved with the addition of SO_2 to the flame.

$$SO_2 + O + M \Rightarrow SO_3 + M \qquad (43)$$

$$SO_3 + O \Rightarrow SO_2 + O_2 \qquad (44)$$

Kallend [23] explored the effect of SO_2 on the chemiluminescence of various emitters in H_2/O_2 flames. Prior investigators had noted that addition of SO_2 to flames increased the chemiluminescence of sodium D-lines at 589 nm, the potassium line at 766.5 nm, and the lithium line at 671 nm, while chemiluminescence from the cesium line at 455.5 nm, and the potassium line at 404 nm was markedly decreased. This affect was noted even for very small quantities of added SO_2, so, Kallend reasoned, the affect had to directly involve SO_2. As a special case of reaction (34) Kallend proposed

$$H + SO_2 + Na \Rightarrow HSO_2 + Na^*$$

If this process was to account for the observed chemiluminescence, then the dissociation energy of H-SO_2 (Kallend presumed an H-SO_2 bond) would have to be less than 60 kcal/mole. Kallend also measured [H] in his flames in which up to 1% SO_2 had been added. [H] was measured approximately by observing the

decay in sodium chemiluminescence along the flame axis. The rate k_{34} was determined to be ~4×10^{-32} $cm^6/molecule^2/s$, in agreement with the approximate determinations of Webster and Walsh [21] but lower than that of Fenimore and Jones [22].

Halstead and Jenkins [24] measured [H] decay in fuel-rich $H_2/O_2/N_2$ flames specifically to determine the reaction rates for reactions (34), (36), and (37). The concentration of H-atoms was measured using the lithium hydroxide method. Up to 1% SO_2 was added to the flames. They considered an additional termolecular process that had been proposed by Wheeler [87]:

$$OH + SO_2 + M \Rightarrow HOSO_2 + M$$

But they claimed that this reaction was unimportant in their flame because [OH] < [H].

Using the H-SO_2 bond energy estimated by Kallend, they fit their data with a simple kinetic model, and by using $k_{34}=3 \times 10^{-31}$ $cm^6/molecule^2/s$, they estimated k_{36} and k_{37} to be 5×10^{-12} $cm^3/molecule/s$ and $<8 \times 10^{-12}$ $cm^3/molecule/s$, respectively. At the conclusion of their work, they noted that the structure and thermodynamics of the HSO_2 (HOSO) molecule was uncertain, making these rate determinations uncertain.

Durie et al [25] extended the work of Halstead and Jenkins [24] by measuring [H] in fuel-rich $C_3H_8/O_2/N_2$ flames. They studied flames that had [H] > [OH] and [H]< [OH], allowing them to assess the importance of the reaction:

$$OH + SO_2 + M \Leftrightarrow HSO_2 + M$$

Again, [H] was measured using the lithium hydroxide method. Using simple kinetic models similar to those used by Halstead and Jenkins, Durie determined that reaction (35) could not be important in flames, even if [OH] > [H]. They provided estimates of k_{36} and k_{37} to be 2.6×10^{-12} cm^3/molecule/s and 7.6×10^{-12} cm^3/molecule/s, respectively, in good agreement with Halstead and Jenkins [24].

Kallend [26] collected new data for [H]-decay in fuel-rich $H_2/O_2/N_2$ flames seeded with SO_2. Post-flame gas temperatures ranged from 1660 K to 2100 K. H-atoms were measured using the lithium hydroxide method. In the analyses previously discussed, it had been assumed that the added SO_2 did not appreciably dissociate in the flame. Kallend developed a higher order model that included the affects of SO_2 dissociation but required numerical solution. He used his model to fit his new data and the data of Halstead and Jenkins [24] using $k_{34}=1.3 \times 10^{-32}$ cm^6/molecule^2/s, noting no temperature dependence across this range of temperatures.

Smith, et al [29] measured CO, O_2, CO_2, O and SO_3 in fuel-lean CO/O_2/Ar flames with added SO_2, using mass spectrometry. These flames are interesting because they contain only very small quantities of hydrogen, limiting the influence of reactions (34) through (37). They modeled their flames using a laminar flame model including coupled fluid dynamics and finite rate chemistry. As expected, reactions (43) and (44) dominated the O-atom species profile. They

found that the calculated O-atom consumption matched the data using the accepted value of k_{43}, adjusting the value of k_{44}. However, reactions (34), (36) and (37) had to be included to match the O-atom consumption.

The mechanistic conclusions of these early works remain standing. Flame radical consumption in the presence of sulfur proceeds via a mechanism of the form [30]

$$X + SO_2 + M \Rightarrow XSO_2 + M$$

$$XSO_2 + Y \Rightarrow XY + SO_2$$

where (X, Y = O, OH, H).

Which of these paths dominates the radical consumption in a combustion system is determined by the stoichiometry in the flame. Reactions (34), (36), and (37) dominate for fuel-rich flames, (43) and (44) are important in fuel-lean flames.

Muller, et al [27] provided the first assembled mechanism for the consumption of H_2S in flames. Their mechanism of 28 reactions involving S, HS, SO, SO_2, H_2S, HSO_2, and HSO_3 was used to analyze the data from fuel-rich $H_2/O_2/N_2$ flames with up to 2% H_2S added. In the experimental phase of their study, they acquired data for [OH], [SH], [S_2], [SO], and [SO_2] using laser fluorescence. They concluded that the reactions

$$H_2S + H \Leftrightarrow SH + H_2 \qquad (19)$$

$$OH + H_2S \Leftrightarrow H_2O + SH \qquad (21)$$

$$SH + SH \Leftrightarrow H2S + S \qquad (22)$$

$$SH + H \Leftrightarrow H_2 + S \qquad (23)$$

$$SH + O \Leftrightarrow SO + H \qquad (24)$$

$$SH + S \Leftrightarrow S_2 + H \qquad (26)$$

$$S + OH \Leftrightarrow SO + H \qquad (28)$$

$$SO + OH \Leftrightarrow SO_2 + H \qquad (32)$$

were responsible for the consumption of H_2S and formation of SO_2 in flames. Reactions (19), (21), (22), (23), and (26) interrelate reduced sulfur species. Reaction (32) related the major oxidized sulfur species. Reactions (24) and (28) provide the paths between reduced and oxidized sulfur species.

Zachariah and Smith [32] examined low-pressure fuel-rich H_2/O_2/Ar flames seeded with SO_2. They measured S, S_2, SO, SH, H_2S, SO, SO_2, H_2, O_2, and H_2O by mass spectrometry. They modeled the flame using a prior version of PREMIX [51]. Zachariah and Smith assembled a mechanism to describe the distribution of sulfur species that was based on the mechanism of Muller, et al [27]. Rates for the reactions relating the dominant species were updated and additional reactions were added to describe the influence of species HSO (HOS) and S_2O. The thermodynamic properties for these species and the rates for the reactions that involved them were estimated. The rates for reactions (34)-(36) were taken from Fenimore and Jones [22] and Halstead and Jenkins [24]. The model was able to reproduce the measured species profiles. However, the importance of the species HSO and S_2O on radical consumption could not be tested since flame radical measurements were not made.

Pauwels, et al [33] measured the major flame species and radicals in stoichiometric $CH_3OH/O_2/N_2$ flames seeded with H_2S. They compared the measured species profiles to the results of a numerical model for laminar flames. While the comparisons of measured and computed species profiles were adequate for the major flame hydrocarbon and sulfur species, the model was not able to account for the accelerated radical consumption caused by the sulfur addition.

The sulfur mechanism selected for use in the calculations presented here is a modification of the mechanism presented by Zachariah and Smith [32]. In early calculations made for the sulfur-bearing flames observed in this work, the PREMIX model could not account for the observed OH concentration decay, similar to the experience Pauwel, et al [33]. An examination of the sensitivity coefficients for the sulfur-containing reactions showed that

1. The OH radical decay profiles were most sensitive to reactions (34), (36) and (37).
2. The reactions involving HSO and S_2O did not influence the concentration profiles

The first modification to the overall sulfur mechanism was to remove the HSO and S_2O reactions. The next modification concerned reactions (34), (36), and (37) and the thermodynamics of HOSO (HSO_2).

The issues of the molecular geometries and bond energies of the HSO_2/HOSO adduct and the reaction H + SO_2 + M were thoroughly addressed theoretically in a series of articles by Marshall, et al [88-91]. They performed *ab initio* calculations to determine the stable geometries of the HOSO adducts. The initial modeling results [88] were updated [89,90]. The most stable geometry, HOSO, is shown in Figure 5-17a. A stable configuration with the H atom connected to the sulfur atom to form the HSO_2 adduct was also found. The HSO_2 geometry is shown in Figure 5-17b. The bond dissociation energy, $D^0(H\text{-}OSO)$ = 38.9 kcal/mole and heat of formation, $\Delta_f H^0_{HOSO}$ = -56.74 kcal/mole and for HSO_2, $D^0(H\text{-}SO_2)$ = 14.96 kcal/mole and $\Delta_f H^0_{HSO_2}$ = -32.29 kcal/mole. Calculated vibrational frequencies are shown in Table 5-9. The predicted bond strengths are significantly lower than those estimated by Kallend [23]. These values and geometry were used as input to PAC91 [65] to compute the thermodynamic properties for HOSO and HSO_2. For HOSO, a hindered rotor was included.

Goumri et al [91] used *ab initio* techniques to determine rate expressions for reactions (34). They determined that reaction (34) proceeds slowly at low temperatures due to the presence of an energy barrier, explaining why attempts to directly measure k_{34} [88] have not been successful. However, at higher temperatures, the reaction proceeds at a rate comparable to that of similar termolecular reactions. The rate determinations for this reaction are summarized in Figure 5-18. There is good agreement between the rates determined by Kallend [23], and Goumri [91], while the rate of Fenimore and Jones [22] is

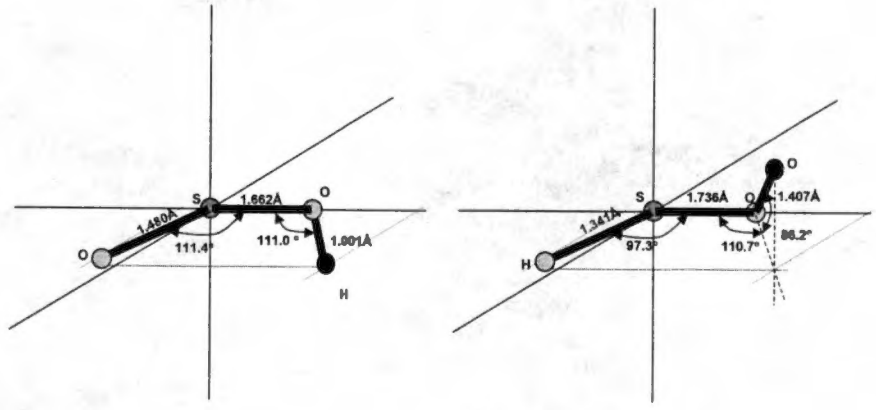

(a) HOSO (b) HSO_2

Figure 5-17 HOSO and HSO_2 geometries [87].

Table 5-9 Vibrational frequencies for HOSO and HSO_2 [90].

Mode	HOSO (cm^{-1})	Mode	HSO_2 (cm^{-1})
Torsion	200	Torsion	431
OSO bend	343	Deformation	810
SO stretch	764	OSO Symmetric Stretch	1065
HOS bend	1073	HSO bending	1128
SO stretch	1351	OSO Asymmetric Stretch	1600
OH stretch	3476	SH stretch	2269

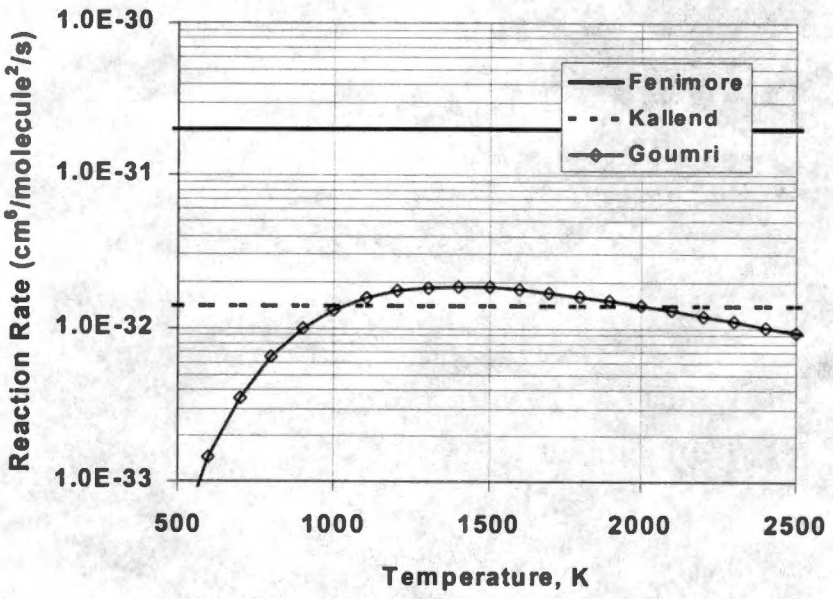

Figure 5-18 Reaction rates for H + SO_2 + M.

higher. Halstead and Jenkins [24] claimed that his data could be reconciled with the value of k_{34} determined by Fenimore and Jones [22]. The rate of Fenimore and Jones [22] was used in the mechanisms of Wendt, et al [31] and Zachariah and Smith [32]. The rates for (34), (36), and (37) from Fenimore and Jones [22] and Halstead and Jenkins [24] were used in this work. The basis for this choice will be discussed further in Section 5.5.2.

Zachariah and Smith's [32] mechanism did not include the oxidizing analog of (35)-(37), that is, it did not include reactions (43) and (44). A rate recommendation for reaction (43) [92] has been made for low temperature atmospheric chemistry [93]. The rate determined in an experimental and theoretical study of Astholtz, et al [93] of reaction (43) was used in this work.

Reaction (44) completes the fuel-lean catalytic cycle. The rate k_{42} was taken from Smith, et al [29]. The final mechanism for sulfur consumption adopted in this study, including catalyzed radical recombination, is shown in Table 5-10.

5.5 Flame Modeling - Flames with Sulfur

5.5.1 Thermodynamics of K/S Compounds

In order to construct a chemical mechanism to model the K/S interactions in flames, the thermochemical properties of K/S/O/H species must be known. The molecules of concern for this analysis are simple combinations of K, S, O, and H atoms. This grouping of atoms yield the molecules KS, KSH, KSO_2, KOS, and KS_2. Many of these species have not been experimentally observed. Thus details of their chemical bonds and structures are unknown. By employing simple theoretical techniques and constructing analogs with other molecules, the details of these molecules can be estimated.

The relative importance of each of these molecules depends primarily on the thermodynamic stability of the molecules. The analysis of the decay profiles in the post-flame gases cannot be expected to yield narrow estimates of the bond energies. When bond energies were unknown, they were estimated from the energies. When bond energies were unknown, they were estimated from the bonds of related or analogous molecules. As indicated by Partridge,et al [76] and Schofield and Steinberg [37], the bond energy for dissociation to ions ($MX \rightarrow M^+ + X^-$) correlates fairly well with the bond length. This is because these

Table 5-10 Sulfur oxidation and radical recombination mechanism. Rate expressions are given in the form $k_i = A_i T^{\beta_i} e^{(-E_{a,i}/RT)}$. (termolecular: cm^6/molecule^2/s, bimolecular: cm^2/molecule/s: cal/mole)

Number	Reaction	A	n	E
18	$H_2S+M=SH+H+M$	2.00E+14	0	76600
19	$H_2S+H=SH+H_2$	1.08E+13	0	2980
20	$H_2S+O=SH+OH$	4.36E+12	0	3322
21	$OH+H_2S=H_2O+SH$	1.39E+13	0	882.6
22	$SH+SH=H_2S+S$	1.00E+14	0	1430
23	$SH+H=H_2+S$	5.16E+14	0	2100
24	$SH+O=SO+H$	3.56E+14	0	642
25	$SH+O=S+OH$	6.31E+11	0.5	8060
26	$SH+S=S_2+H$	1.40E+13	0	478
27	$S+O_2=SO+O$	7.94E+10	0.5	0
28	$S+OH=SO+H$	7.20E+13	0	642
29	$S_2+O=SO+S$	6.30E+11	0.5	0
30	$S+S+M=S_2+M$	1.00E+18	-1	0
31	$SO+O_2=SO_2+O$	3.60E+11	0	5600
32	$SO+OH=SO_2+H$	1.80E+13	0	0
33	$SO+O+M=SO_2+M$	1.20E+22	-1.8	0
34	$H+SO_2+M=HOSO+M$	7.30E+16	0	0
35	$OH+SO+M=HOSO+M$	7.00E+16	0	0
36	$H+HOSO=SO_2+H_2$	4.00E+12	0	0
37	$OH+HOSO=SO_2+H_2O$	6.80E+13	0	1772
38	$O_2+HOSO=SO_2+HO_2$	1.00E+12	0	1000
39	$SO+SO=SO_2+S$	3.30E+11	0	2250
40	$H+SO_3=OH+SO_2$	1.81E+13	0	0
41	$S+SO_3=SO+SO_2$	1.20E+12	0	0
42	$SO+SO_3=SO_2+SO_2$	4.22E+12	0	0
43	$SO_2+O+M=SO_3+M$	3.99E+28	-4	5256
44	$O+SO_3=O_2+SO_2$	4.40E+11	0	6100

compounds are predominantly ionically bound. Bond distances and vibrational frequencies were estimated from the alkali and alkaline metal oxides and sulfides. As further computational or experimental work becomes available, the accuracy of these estimates can be assessed. The estimates discussed here must suffice for the present work.

The estimated geometries were used to calculate the moments of inertia for these molecules. Bond energies were used to calculate heats of formation. Electronic degeneracies were estimated from analogous molecules. These parameters along with vibrational frequencies, provided inputs to PAC91 [65] to calculate thermodynamic properties. The rigid rotor/harmonic oscillator approximation was used for all molecules.

Diatomic Molecule KS

Lewis, et al [5] estimated the K-S bond length by comparison to KCl, HCl, and HS. The vibrational frequency was estimated using an empirical relationship from Herzberg [94]. The K-S bond dissociation energy and heat of formation were estimated assuming a coulombic binding force [95]. Farber, et al [67] employed the results of Lewis to interpret vaporization data for K_2S. Partridge, et al [96] performed *ab initio* calculations for all alkali and alkaline metal-sulfur molecules. They quote the accuracy of their dissociation energy as +/-0.1 eV, or +/-2.3 kcal/mole. Their result is in reasonable accord with the bond energy estimated by Lewis, et al [5].

No direct experimental work is known to exist for KS. The dissociation energy from the *ab initio* calculations is close to the estimated value. The results from the *ab initio* calculation for bond distance and dissociation energy are recommended. The thermodynamic properties of KS are summarized in Table 5-11.

The correlation of Herzberg [94], combined with the bond length estimate of Partridge, et al [96], was used to estimate the vibrational frequency. According to Herzberg, the vibrational frequency of a diatomic molecule scales with bond length and the square root of the number of electrons in the outer shell of the bonding atomic species, according to:

$$r_e^3 \omega_e \sqrt{n} = C \qquad (5.27)$$

where, r_e is bond length, ω_e is vibrational frequency, n is the number of bonding electrons, and C is the correlation constant. To make this estimate, known data

Table 5-11 Summary of KS molecular and thermodynamic properties.

Reference	r_e (A)	ω_e (cm^{-1})	$\omega_e x_e$ (cm^{-1})	Electronic Degeneracy	D_O (kcal/mole)	$\Delta_f H^O$ (kcal/mole)
[5]	2.7	293	-	-	58.5	29
[67]	-	-	-	-	58.5	29
[96]	2.81	229	-	4	63.2	-
Recommendation	2.81	285	-	4	58.5	24

from the species CaS and CaCl were used to determine the correlation constant, C. The electron configurations of the atomic species required are given in Table 5-12.

The constant C was found to be ~14150 $Å^3$-cm^{-1}. Using the value of r_e = 2.81 Å, a value of ω_e = 285 cm^{-1} was derived. The values used for the various molecules are shown in Table 5-13. The resulting thermodynamic properties are tabulated in Appendix F.

Triatomic species KS_2

There are no determinations for KS_2. The geometry of the KS_2 molecule is assumed to be analogous to the geometry of the KO_2 molecule. The KO_2 molecule is triangular with C_{2v} symmetry. The geometry of KO_2 has been discussed in detail in Section 5.3.1. The molecule is ionically bound, K^+-O_2^-. The bond length, K-O, is 2.31 Å. The K-O bond length in KO_2 is close to the K-O bond length in diatomic KO (2.2 Å). The O-O bond length in KO_2 is 1.33 Å and compares well to the O-O bond length of the O_2^- anion (1.341Å). This situation was illustrated in Figure 5-5. A similar situation is assumed for KS_2. The S-S bond length is assumed to be equal to the S-S bond length in the S_2 anion. The S_2^- bond length has been determined experimentally [97] and computationally [98]. These two determinations are in reasonable agreement. The experimental determination from Moran, et al [97] was used here. The K-S bond length for KS_2 is assumed to have the same proportional increase over the K-S bond in the

Table 5-12 Electronic configurations of atoms.

Atom	Atomic Orbital
K	$[Ar]4s^1$
Ca	$[Ar]4s^2$
S	$[Ne]3s^23p^4$
Cl	$[Ne]3s^13p^5$

Table 5-13 Determination of C from Herzberg's Correlation.

Molecule	r_e (Å)	ω_e (cm^{-1})	n	C ($Å^3$-cm^{-1})
CaCl	2.439	369.8	7	14196
CaS	2.318	462.2	6	14101
KS	2.81	285	5	14150

diatomic molecule as is observed for the KO_2, KO pair. This assumption results in the following values; $r_{e,S\text{-}S}$ = 2.01 Å and $r_{e,K\text{-}S}$ = 2.90 Å.

The stretch mode frequency (S-S) is taken directly from the experimental determination Moran, et al [97] of the vibrational frequency of S^-_2. Thus, ν_1 = 570 cm^{-1}. Other vibrational frequencies were determined from Herzberg's valence force model [99] for triatomic C_{2V} symmetry. Herzberg's model requires the determination of two force constants, k_1 and k_δ; the force constant k_1 is the K-O

(or K-S) force constant and k_δ is the bending force constant. These are related to the frequencies via the following equations:

$$4\pi^2\left(\nu_1^2+\nu_2^2\right)=\left(1+\frac{2m_Y}{m_X}\cos^2(\alpha)\right)\frac{k_1}{m_Y}+\frac{2}{m_Y}\left(1+\frac{2m_Y}{m_X}\sin^2(\alpha)\right)\frac{k_\delta}{l^2} \tag{5.28}$$

$$16\pi^4\nu_1^2\nu_2^2=\left(1+\frac{2m_Y}{m_X}\right)\frac{k_1}{m_Y^2}\frac{k_\delta}{l^2} \tag{5.29}$$

and

$$4\pi^2\nu_3^2=\left(1+\frac{2m_Y}{m_X}\sin^2(\alpha)\right)\frac{k_1}{m_Y} \tag{5.30}$$

The force constants k_1 and k_δ were then estimated from data on KO and KO_2. Using the three equations above and the known frequencies of the KO_2 molecule, the force constants $k^{KO_2}{}_1$ and $k^{KO_2}{}_\delta$ were calculated. Force constants were derived from vibrational frequencies using:

$$k=\mu(2\pi\nu)^2 \tag{5.31}$$

where μ is the reduced mass:

$$\frac{1}{\mu}=\left(\frac{1}{m_1}+\frac{1}{m_2}\right) \tag{5.32}$$

and m_1 and m_2 were the masses of the bonded atoms. The force constant, k_1, is calculated from ν_3, and the force constant, k_δ, is calculated from ν_1, ν_2, and k_1. The force constants for the K-S stretch in the KS_2 molecule were estimated by comparing the KO_2 stretch mode to the KO stretch mode:

$$k_1^{KS_2} = k_1^{KS} \frac{k_1^{KO_2}}{k_1^{KO}} \qquad (5.33)$$

The resulting approximation of the K-S stretch mode force constant for KS_2 was 0.499 mdyne/Å. This compares to 0.807 mdyne/Å for KO_2. The bending force constant was related to the force constants for the S_2 and O_2 anions:

$$k_\delta^{KS_2} = k_\delta^{KO_2} \frac{k_{S_2^-}}{k_{O_2^-}} \qquad (5.34)$$

The resulting approximation of the S-K-S bending force constant was 2.01 mdyne/Å. This compares to 3.20 mdyne/Å for O-K-O.

The KS_2 frequencies were calculated using equations (5.28) through (5.30). The frequency ν_3 is calculated immediately from equation (5.30), while ν_1 and ν_2 require simultaneous solution of equations (5.28) and (5.29). The resulting vibrational frequencies are included in Table 5-14.

The heat of formation for KS_2 was determined assuming that the K-S_2 bond was purely ionic and the bond dissociation energy was estimated using the coulombic attractive potential. Estimates of the dissociation energy of the KO_2 molecule are bounded by the ionic assumption. The resulting dissociation energy and heat of formation for KS_2 are shown in Table 5-14.

Table 5-14 Summary of the parameters used to estimate KS_2 thermodynamic properties.

Parameter	Value	Parameter	Value
$r_{e,K\text{-}S}$ (Å)	2.90	α (degrees)	36.4°
$r_{e,S\text{-}S}$ (Å)	2.01	ν_1 (cm^{-1})	504
Electronic Degenerecy	2	ν_2 (cm^{-1})	241
D_0 (kcal/mole)	55.2	ν_3 (cm^{-1})	200
$\Delta_f H^0$ (kcal/mole)	-3.13		

Triatomic species KSH

There were no experimental determinations of the properties of KSH. The properties of this molecule were estimated by comparison to the linear molecule KOH [80]. It is expected that the KSH molecule will have the same geometry. The K-SH bond length is taken from the following rule [5]:

$$r_e(K\text{-}SH) = r_e(K\text{-}S) - r_e(K\text{-}O) + r_e(K\text{-}OH) \qquad (5.35)$$

The needed bond lengths are: $r_e(K\text{-}S)$ = 2.81Å, $r_e(K\text{-}O)$ = 2.2 Å, from this work and $r_e(K\text{-}OH)$ = 2.212 Å from reference [80]. The resulting K-SH bond length is $r_e(K\text{-}SH)$ = 2.8 Å. The KS-H bond length is taken from the bond length of the SH^- anion (1.343Å, [100]). Note that the bond length KO-H (0.912Å) and the bond length of OH^- (0.963Å, [70]) compare well.

Vibrational frequencies were derived using the valence-force model of Herzberg (equations II-198, II-199, II-200; [101]). In this model, there are assumed to be forces that act along bonds and a force that maintains the angle between bonds. Thus for KSH there will be three force constants, $k_{K\text{-}SH}$, $k_{KS\text{-}H}$, and k_δ, where k_δ is the force constant that preserves the K-S-H angle. The force constant $k_{KS\text{-}H}$ is related to the vibrational frequency of SH^-. The force constant $k_{K\text{-}SH}$ is related to the vibrational frequency of the KS molecule. The force constants thus derived were:

$k_{K\text{-}SH}$=17.62 mdyne/A

$k_{KS\text{-}H}$=4.044 mdyne/A

The force constant k_δ was inferred from inspection of the properties of the alkali-hydroxides. Comparing k_δ (Table 5-15) from the known bending-mode vibration frequencies of the alkali-hydroxides, one finds only small variation. The average value of k_δ from the alkali hydroxides was used for the KSH molecule.

The valence force model from Herzberg [101] relates the stretch frequencies to the force constants $k_{K\text{-}SH}$ and $k_{KS\text{-}H}$ as follows:

$$4\pi^2\left(\nu_1^2+\nu_3^2\right)=k_1\left(\frac{1}{m_X}+\frac{1}{m_Y}\right)+k_2\left(\frac{1}{m_Y}+\frac{1}{m_Z}\right) \qquad (5.36)$$

and

$$16\pi^4\nu_1^2\nu_3^2=\left(\frac{m_X+m_Y+m_Z}{m_Xm_Ym_Z}\right)k_1k_2 \qquad (5.37)$$

Table 5-15 Comparison of force constants for hydroxides.

Hydroxide	Vibrational Frequency (cm^{-1})	Force Constant, k_δ (mdyne/Å)
LiOH	362.0	6.42E-13
NaOH	337.0	5.82E-13
KOH	300.0	4.12E-13
RbOH	309.0	4.40E-13
CsOH	306.0	4.39E-13
	Average	5.03E-13
	Variance(%)	20.3

where k_1 and k_2 are $k_{K\text{-}SH}$ and $k_{KS\text{-}H}$, respectively. X, Y, and Z represent K, S and H atoms, respectively. Equations (5.36) and (5.37) were solved simultaneously to yield ν_1 and ν_3. This solution was found to be:

$$\nu_1 = 241\text{cm}^{-1}$$

$$\nu_3 = 2650\ \text{cm}^{-1}$$

The bending mode frequency was calculated directly from

$$\nu_2^2 = \frac{1}{4\pi^2 \ell_1^2 \ell_2^2}\left[\frac{\ell_1^2}{m_Z} + \frac{\ell_2^1}{m_X} + \frac{(\ell_1 + \ell_2)^2}{m_Y}\right] k_\delta \qquad (5.38)$$

The value obtained for ν_2 was 199 cm^{-1}. These results compare well with estimates for NaSH made by Schofield and Steinberg [37].

The dissociation energy estimate was made from comparison of data from the alkali fluorides, hydroxides, and chlorides. This correlation is shown in Figure 5-19. In this figure, dissociation energies of alkali metals (Li, Na, K, Rb, Cs) in ionically bound compounds such as hydroxides, fluorides and chlorides [70] are plotted vs. the corresponding bond distance reciprocals. The hydroxides and fluorides correlate well on a semi-log plot. The curve for the chlorides is shifted to lower dissociation energies relative to the hydroxides. For reference, the binding energy for a coulombic potential (e^2/r) is also shown. Evidently, repulsive forces are at work for the closely held pairs and a coulombic potential is approached as the bond distance grows.

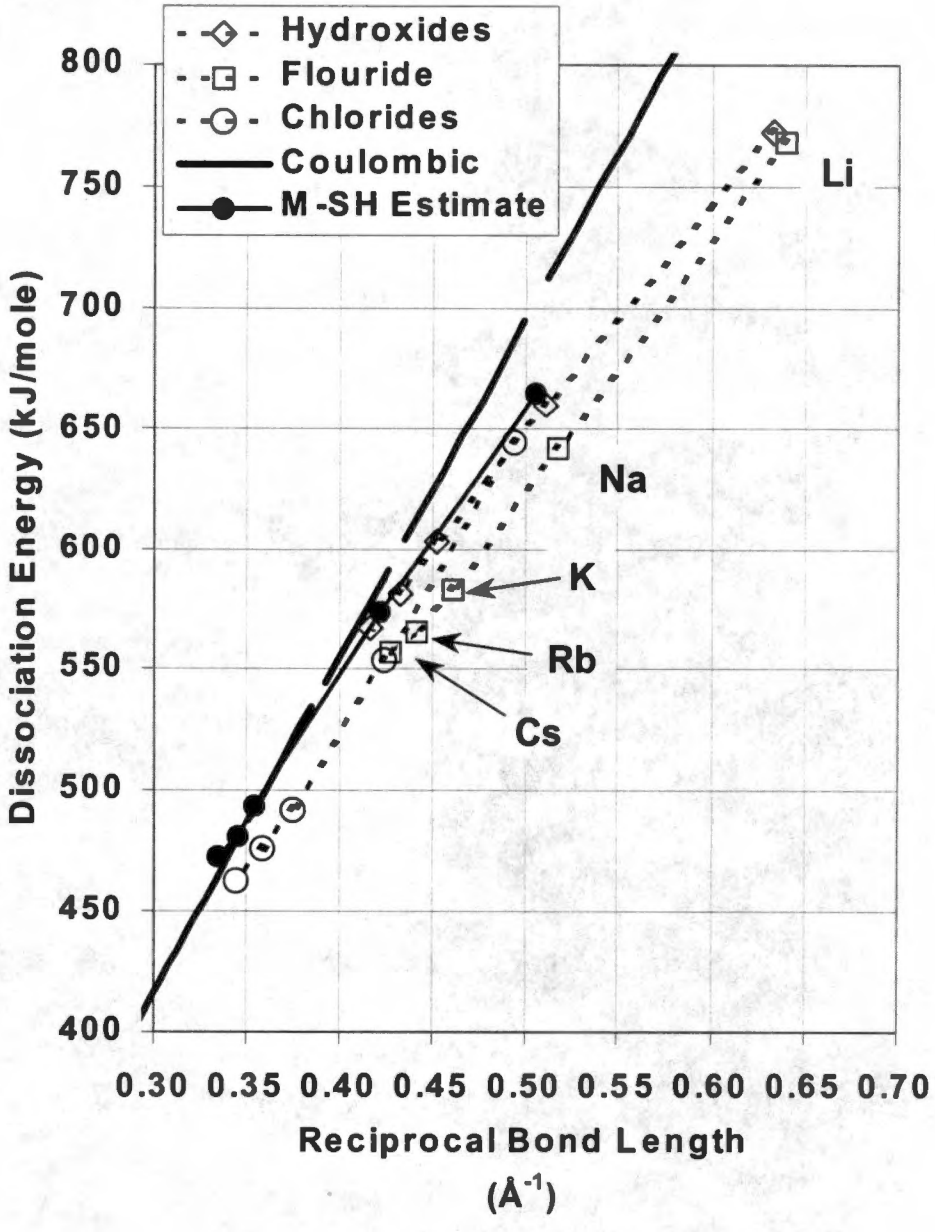

Figure 5-19 Correlation for M-SH bond energy.

To estimate the dissociation energy for KSH, the KCl/KSH pair was assumed to be analogous to the KF/KOH pair. The bond energy for dissociation to ions was estimated as

$$D_{0,K-SH}^{IONS} = \left[\frac{D_{0,K-OH}^{IONS}\Big|_{Measured}}{D_{0,K-OH}^{IONS}\Big|_{F/OH_comparison}} \right] D_{0,K-SH}^{IONS}\Big|_{Cl/SH_comparison} \qquad (5.39)$$

The K-OH dissociation energy was related to the K-F dissociation energy by

$$D_{0,K-OH}^{IONS}\Big|_{F/OH_comparison} = \frac{D_{0,K-F}^{IONS} - D_{0,Rb-F}^{IONS}}{r_e^{K-F} - r_e^{Rb-F}} \left(r_e^{K-OH} - r_e^{Rb-F} \right) + D_{0,Rb-F}^{IONS} \qquad (5.40)$$

and the K-SH dissociation energy was related to the K-Cl dissociation energy by

$$D_{0,K-SH}^{IONS}\Big|_{Cl/OH_comparison} = \frac{D_{0,K-Cl}^{IONS} - D_{0,Rb-Cl}^{IONS}}{r_e^{K-Cl} - r_e^{Rb-Cl}} \left(r_e^{K-SH} - r_e^{Rb-Cl} \right) + D_{0,Rb-Cl}^{IONS} \qquad (5.41).$$

The results are shown for all of the alkali-SH compounds (M-SH) in Figure 5-19.

As bond distance increases, the dissociation energy approaches the coulombic limit. The estimated dissociation energies for Rb and Cs slightly exceed the coulombic limit, suggesting that this technique over-estimates the dissociation energy.

The K-SH dissociation energy for dissociation to atoms is needed to estimate the heat of formation for KSH. The dissociation energy to atoms was estimated from

$$D_{0,K-SH}^{ATOM} = D_{0,K-SH}^{IONS} - I.P.\big|_K + E.A.\big|_{SH} \qquad (5.42)$$

where $I.P.|_K$ is the ionization potential of K and $E.A.|_{SH}$ is the electron affinity of SH [70]. Finally, the heat of formation of KSH, $\Delta_f H^0|_{KSH}$ is computed from Hess's law:

$$\Delta_f H^0\big|_{KSH} = \Delta_f H^0\big|_{K(v)} + \Delta_f H^0\big|_{SH(v)} - D^{ATOMS}_{0,K-SH} \qquad (5.43).$$

Properties for KSH are summarized in Table 5-16.

Triatomic species KOS

There are no determinations of the properties of the KOS molecule. The *ab inito* calculations of Jin and Schaefer [102] for NaOS provided the only guidance for the geometry and vibrational characteristics of this molecule. The calculated geometry of the NaOS adduct can be compared to the geometries of NaO_2, NaS_2, NaO, and NaS [37]. From Figure 5-20, it is seen that the Na-O bond length and the O-S bond length compare to the Na-O bond length in NaO_2 and the S-O bond length of SO^- [103]. The same was assumed for the K-O and O-S bonds of KOS. Additionally, a bent configuration was assumed, with the K-O-S angle of 90 degrees. The assumed molecular geometry for KOS is compared to the other molecules in Figure 5-21. The vibrational frequencies are simply taken from SO^- [103] and KO_2 tabulated in Table 5-8.

The heat of formation for KOS was determined assuming that the K-OS bond was purely ionic and the bond dissociation energy was calculated using a Coulombic attractive potential. The resulting dissociation energy and heat of formation are shown in Table 5-17.

Table 5-16 Summary of KSH thermodynamic properties and the parameters used to estimate them.

Parameter	Value	Parameter	Value
$r_{e,K\text{-}S}$ (Å)	2.82	α (degrees)	180°
$r_{e,S\text{-}H}$ (Å)	1.34	ν_1 (cm^{-1})	241
Electronic Degenerecy	1	ν_2 (cm^{-1})	199
D_0 (kcal/mole)	71.5	ν_3 (cm^{-1})	2650
$\Delta_f H^0$ (kcal/mole)	-17.2		

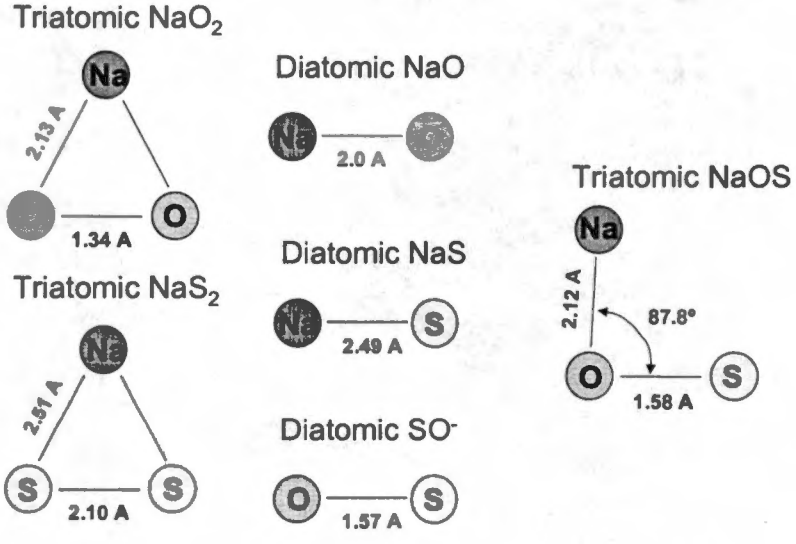

Figure 5-20 Na-S-O bond comparisons.

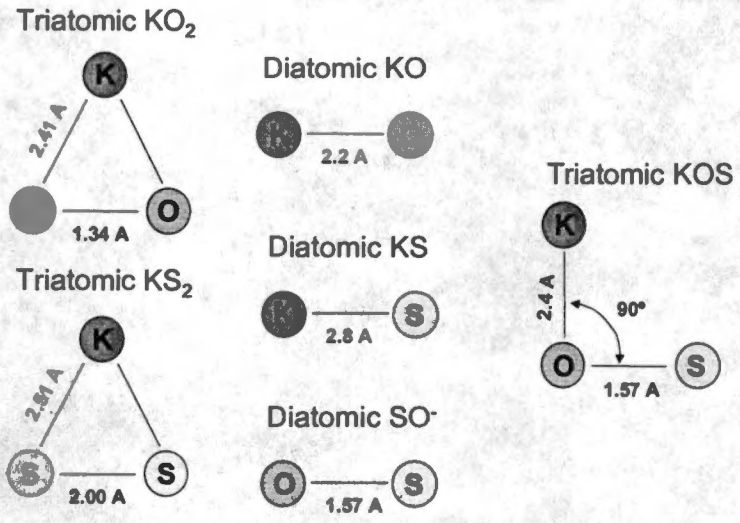

Figure 5-21 K-S-O bond comparisons (determined by analogy with NaSO).

Table 5-17 Summary of KOS thermodynamic properties and the parameters used to estimate them.

Parameter	Value	Parameter	Value
$r_{e,K\text{-}O}$ (Å)	2.4	α (degrees)	90°
$r_{e,S\text{-}O}$ (Å)	1.57	ν_1 (cm^{-1})	906
Electronic Degenerecy	2	ν_2 (cm^{-1})	307
D_0 (kcal/mole)	67.9	ν_3 (cm^{-1})	304
$\Delta_f H^0$ (kcal/mole)	-45.2		

Polyatomic species KSO_2

There are no experimental determinations for the geometry of the species KSO_2. Goumri et al [104] performed *ab initio* calculations to determine the KSO_2 geometry. The species $NaSO_2$ has been experimentally investigated [105] and found to have the sodium atom equally distant from each oxygen atom and the sulfur atom bound to the oxygen atoms as in SO^-_2 [106]. The sodium atom was not in the plane of the SO^-_2 adduct. The geometry of the $NaSO_2$ molecule was found to correlate well with the geometry of Na_2SO_4. The geometry of Goumri, et al [104] is shown in Figure 5-22 compared to the geometry of K_2SO_4.

Vibrational frequencies are reported by Goumri, et al [104]. The computed frequencies compare well with those of SO^-_2 [106]and KO_2. Goumri, et al [104] derived the bond disssociation energy D_0(K-SO_2) from their rate measurements using two approximate methods. Their value, 49.7 kcal/mole, was used to calculate $\Delta_f H^0_{,KSO_2}$ as was done for the other molecules

$$\Delta_f H^0\Big|_{KSO_2} = \Delta_f H^0\Big|_{K(v)} + \Delta_f H^0\Big|_{SO_2(v)} - D_0\left(K - SO_2\right) \qquad (5.44).$$

These are shown in Table 5-18 along with the other parameters used to calculate the thermodynamic properties.

5.5.2 Transport Properties

As discussed in section 5.3.2, a simple model was used to compute molecular transport properties for these molecules. Thus, transport properties for K/S

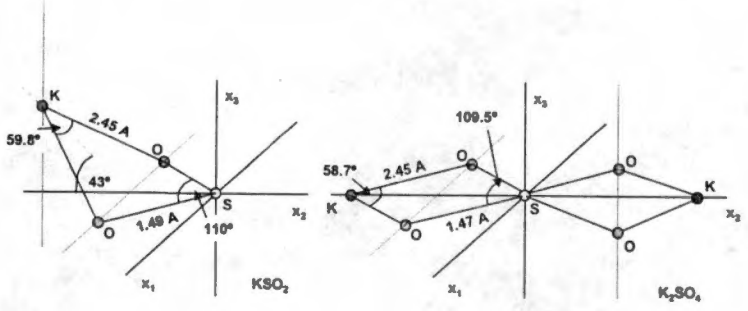

Figure 5-22 Comparison of KSO_2 and K_2SO_4.

Table 5-18 Summary of KSO_2 thermodynamic properties and the parameters used to estimate them.

Parameter	Value		Parameter	Value
$r_{e,K\text{-}O}$ (Å)	2.45		ν_1 (cm^{-1})	1042
$r_{e,S\text{-}O}$ (Å)	1.495		ν_2 (cm^{-1})	985
α (degrees)	100°		ν_3 (cm^{-1})	496
β (degrees)	59.8°		ν_4 (cm^{-1})	308
δ (degrees)	43°		ν_5 (cm^{-1})	300
Electronic Degenerecy	2		ν_6 (cm^{-1})	190
D_0 (kcal/mole)	49.7		$\Delta_f H^0$ (kcal/mole)	-98.45

molecules were only crudely estimated. The parameters for each of the K/O/S/H species molecule were set equal to the corresponding K/O/H analog. In the case of KSO_2, the transport properties were set equal to the properties for SO_2. For the atmospheric pressure flames under investigation, the results will not be

sensitive to these values. The values used for these calculations are summarized in Table 5-19.

5.5.3 Modeling Results - Flames with Sulfur

Reactions between the potassium species (K, KO, KO_2, KOH), K/S species (KS, KOS, KS_2, KSH, KSO_2), and flame species (H, O, OH, H_2, O_2, H_2O, HO_2) and the third-body species [M] were considered. As was the case for the potassium oxidation mechanism, a modified version of the algorithm of Indritz, et al [84] was used to determine the possible reactions between the K/O, K/S and the flame species. The initial pass yielded 418 reactions. Eliminating endothermic reactions, reduced the list to 95 reactions. Limiting the number bonds created and formed reduced the list to 42 reactions. These reactions are tabulated in Table 5-20. The procedure for estimating the rates of these reactions is identical to that used in the case of the potassium oxidation mechanism. In this case, the reactions from the K/O mechanism were used as analogs for the K/S reactions where possible. Otherwise, gas kinetic rates were assigned to bimolecular reactions.

Table 5-19 Transport properties for K/O/S/H species.

Species	Collision Diameter $\sigma(Å)$	Well Depth ε/k_B (K)	Dipole Moment μ ($10^{-8}cm^{3/2}erg^{1/2}$)	Polarizability $\alpha(Å)$
KS	3.812	383	0	1
KS_2	4.69	1213	0	1
KSH	4.52	1213	0	1
KOS	4.69	1213	0	1
KSO_2	4.29	252	0	1

Table 5-20 Reactions proposed for potassium/sulfur interactions.

Reaction Number	Reaction	Rate Estimate
45	$K + S + M \Leftrightarrow KS + M$	$K + O_2 + M \Leftrightarrow KO_2 + M$
46	$K + SH + M \Leftrightarrow KSH + M$	$K + OH + M \Leftrightarrow KOH + M$
47	$K + SO + M \Leftrightarrow KOS + M$	$K + O_2 + M \Leftrightarrow KO_2 + M$
48	$K + SO_2 + M \Leftrightarrow KSO_2 + M$	$K + O_2 + M \Leftrightarrow KO_2 + M$
49	$K + S_2 + M \Leftrightarrow KS_2 + M$	$K + O_2 + M \Leftrightarrow KO_2 + M$
50	$KOS + OH \Leftrightarrow KOH + SO$	$KO_2 + OH \Leftrightarrow KOH + O_2$
51	$KOH + S \Leftrightarrow KOS + H$	$KOH + O \Leftrightarrow KO_2 + H$
52	$KSO_2 + O \Leftrightarrow KO + SO_2$	Gas Kinetic
53	$KSO_2 + OH \Leftrightarrow KOH + SO_2$	Gas Kinetic
54	$KSO_2 + O_2 \Leftrightarrow KO_2 + SO_2$	Gas Kinetic
55	$KS + H \Leftrightarrow K + SH$	$KO + H \Leftrightarrow K + OH$
56	$KS + OH \Leftrightarrow KOH + S$	$KO + OH \Leftrightarrow KOH + O$
57	$KSH + H \Leftrightarrow K + H_2S$	$KOH + H \Leftrightarrow K + H_2O$
58	$KSH + OH \Leftrightarrow KOH + SH$	Gas Kinetic
59	$KS + S \Leftrightarrow K + S_2$	$KO + O \Leftrightarrow K + O_2$
60	$KS_2 + OH \Leftrightarrow KOH + S_2$	$KO_2 + OH \Leftrightarrow KOH + O_2$
61	$KSO_2 + SO \Leftrightarrow KOS + SO_2$	Gas Kinetic
62	$KS_2 + SO \Leftrightarrow KOS + S_2$	Gas Kinetic
63	$KSH + SO \Leftrightarrow KOS + SH$	$KOH + O_2 \Leftrightarrow KO_2 + OH$
64	$KS + SO \Leftrightarrow KOS + S$	$KO + O_2 \Leftrightarrow KO_2 + O$
65	$KSO_2 + S \Leftrightarrow KS + SO_2$	Gas Kinetic
66	$KS_2 + SO_2 \Leftrightarrow KSO_2 + S_2$	Gas Kinetic
67	$KSO_2 + SH \Leftrightarrow KSH + SO_2$	Gas Kinetic
68	$KS_2 + H \Leftrightarrow KS + SH$	$KO_2 + H \Leftrightarrow KO + OH$
69	$KS_2 + S \Leftrightarrow KS + S_2$	$KO_2 + O \Leftrightarrow KO + O_2$
70	$KS_2 + SH \Leftrightarrow KSH + S_2$	$KO_2 + OH \Leftrightarrow KOH + O_2$
71	$KO_2 + S \Leftrightarrow KS + O_2$	$KO_2 + O \Leftrightarrow KO + O_2$
72	$KO_2 + SH \Leftrightarrow KSH + O_2$	$KO_2 + OH \Leftrightarrow KOH + O_2$
73	$KO + S \Leftrightarrow K + SO$	$KO + O \Leftrightarrow K + O_2$
74	$KO + SO \Leftrightarrow K + SO_2$	Gas Kinetic
75	$KS + O \Leftrightarrow K + SO$	$KO + O \Leftrightarrow K + O_2$
76	$KS + O \Leftrightarrow KO + S$	$SH + O \Leftrightarrow OH + S$
77	$KS + SH \Leftrightarrow KSH + S$	$KO + OH \Leftrightarrow KOH + O$
78	$KS_2 + O \Leftrightarrow KO + S_2$	$KO_2 + O \Leftrightarrow KO + O_2$
79	$KS_2 + O_2 \Leftrightarrow KO_2 + S_2$	Gas Kinetic
80	$KSH + H \Leftrightarrow KS + H_2$	$KOH + H \Leftrightarrow KO + H_2$
81	$KSH + O \Leftrightarrow KO + SH$	$KOH + O \Leftrightarrow KO + OH$
82	$KSH + O \Leftrightarrow KS + OH$	$KOH + O \Leftrightarrow KO + OH$
83	$KSH + OH \Leftrightarrow KS + H_2O$	$KOH + OH \Leftrightarrow KO + H_2O$
84	$KSH + SH \Leftrightarrow KS + H_2S$	$KOH + OH \Leftrightarrow KO + H_2O$
85	$KOS + O \Leftrightarrow K + SO_2$	Gas Kinetic
86	$KOS + O \Leftrightarrow KO + SO$	$KO_2 + O \Leftrightarrow KO + O_2$

This list of reactions includes all of the K/S analogs of the Na/S reactions of Schofield and Steinberg [37]. However, there are sixteen additional reactions included in Table 5-20 with no analog in Schofield's and Steinberg's [37] mechanism. Each of these is reasonable and was therefore included in the screening process. The brute force screening approach was used for these reactions just as was done for the K/O mechanism development reported in Section 5.3.4. While a handful of reactions did emerge as controlling potassium decay, the calculated profiles are not particularly sensitive to these reactions. An unambiguous determination of the major pathways connecting K/S species to other K/S species could not be identified. The final rates used for the results presented in this section are shown in Table 5-21.

The comparisons of the measured and computed potassium and hydroxyl decay profiles are shown in Figures 5-23 through 5-26. Again, the potassium values are presented in a normalized form. The data are normalized to the potassium value at 0.5 mm above the burner in the flame *without sulfur*. The calculations corresponding *no-sulfur* calculation. The proposed mechanism captures the major characteristics of the various decay profiles. However, the model does not fit the data from the fuel-lean flame as well as for the fuel-lean flame without sulfur. The model under predicts the level of potassium profile and over predicts the OH profile in the fuel-lean flame. The stoichiometric flame and the two fuel-rich flames are well matched by the model.

5-21 Final Potassium/Sulfur interaction mechanism. Rate expressions are given in the form $k_j = A_j T^n j e^{(-E_{a,j}/RT)}$. For bimolecular reactions, units are (cm^3/molecule/s). For termolecular reactions, units are (cm^6/$molecule^2$/s)

Reaction Number	Reaction	A	n	E_a
45	K + S + M ⇔ KS + M	5.80E+23	-2	0
46	K + SH + M ⇔ KSH + M	1.65E+20	-1	0
47	K + SO + M ⇔ KOS + M	1.00E+23	-2	0
48	K + SO_2 +M ⇔ KSO_2 + M	7.00E+23	-2	0
49	K + S_2 +M ⇔ KS_2 + M	1.00E+23	-2	0
50	KOS + OH ⇔ KOH + SO	1.00E+11	0.5	0
51	KOH + S ⇔ KOS + H	4.00E+07	0.5	0
52	KSO_2 + O ⇔ KO + SO_2	1.00E+11	0.5	0
53	KSO_2 + OH ⇔ KOH + SO_2	2.00E+12	0.5	0
54	KSO_2 + O_2 ⇔ KO_2 + SO_2	1.00E+11	0.5	0
55	KS + H ⇔ K + SH	6.40E+10	0.5	0
56	KS + OH ⇔ KOH + S	8.21E+10	0.5	0
57	KSH + H ⇔ K + H_2S	1.00E+11	0.5	0
58	KSH + OH ⇔ KOH + SH	9.82E+12	0.5	0
59	KS + S ⇔ K + S_2	4.22E+11	0.5	0
60	KS_2 + OH ⇔ KOH + S_2	1.00E+11	0.5	0
61	KSO_2 + SO ⇔ KOS + SO_2	1.00E+13	0.5	0
62	KS_2 + SO ⇔ KOS + S_2	7.85E+12	0.5	0
63	KSH + SO ⇔ KOS + SH	7.70E+06	0.5	0
64	KS + SO ⇔ KOS + S	2.20E+08	0.5	0
65	KSO_2 + S ⇔ KS + SO_2	9.17E+11	0.5	0
66	KS_2 + SO_2 ⇔ KSO_2 + S_2	7.66E+12	0.5	0
67	KSO_2 + SH ⇔ KSH + SO_2	9.20E+12	0.5	0
68	KS_2 + H ⇔ KS + SH	1.06E+11	0.5	0
69	KS_2 + S ⇔ KS + S_2	4.00E+11	0.5	0
70	KS_2 + SH ⇔ KSH + S_2	1.00E+11	0.5	0
71	KO_2 + S ⇔ KS + O_2	4.00E+11	0.5	0
72	KO_2 + SH ⇔ KSH + O_2	1.00E+11	0.5	0
73	KO + S ⇔ K + SO	4.22E+11	0.5	0
74	KO + SO ⇔ K + SO_2	1.80E+10	0	0
75	KS + O ⇔ K + SO	8.82E+12	0.5	0
76	KS + O ⇔ KO + S	8.30E+10	0.5	0
77	KS + SH ⇔ KSH + S	8.21E+10	0.5	0
78	KS_2 + O ⇔ KO + S_2	4.00E+11	0.5	0
79	KS_2 + O_2 ⇔ KO_2 + S_2	7.93E+11	0.5	0
80	KSH + H ⇔ KS + H_2	5.60E+10	0.5	0
81	KSH + O ⇔ KO + SH	2.80E+09	0.5	0

5-21 (continued)

Reaction Number	Reaction	*A*	*n*	E_a
82	KSH + O ⇔ KS + OH	2.80E+09	0.5	0
83	KSH + OH ⇔ KS + H_2O	9.82E+11	0.5	0
84	KSH + SH ⇔ KS + H_2S	1.03E+12	0.5	0
85	KOS + O ⇔ K + SO_2	1.00E+12	0.5	0
86	KOS + O ⇔ KO + SO	4.00E+11	0.5	0

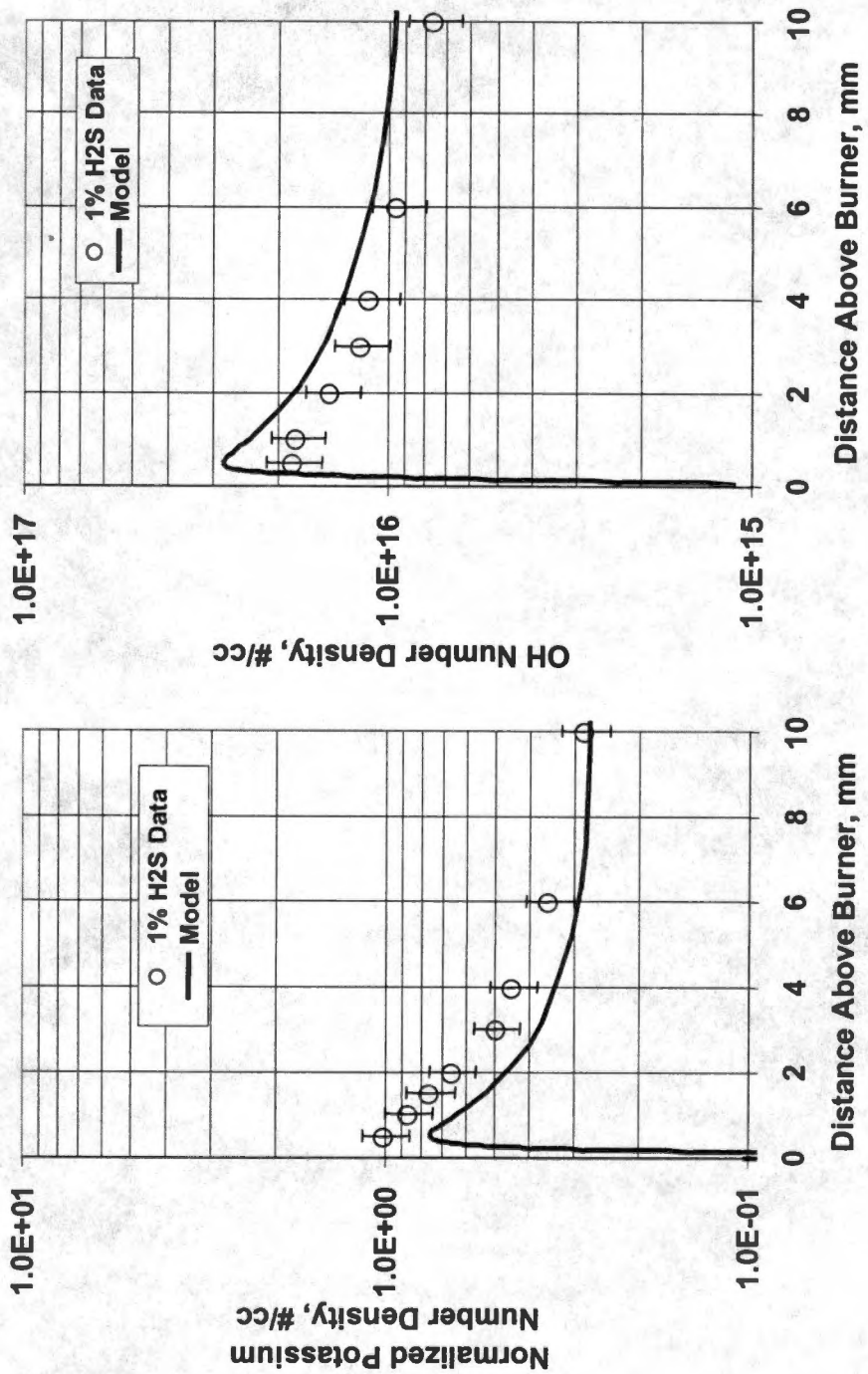

Figure 5-23 Model results for the fuel-lean (ϕ=0.85) flame - 1% added H_2S.

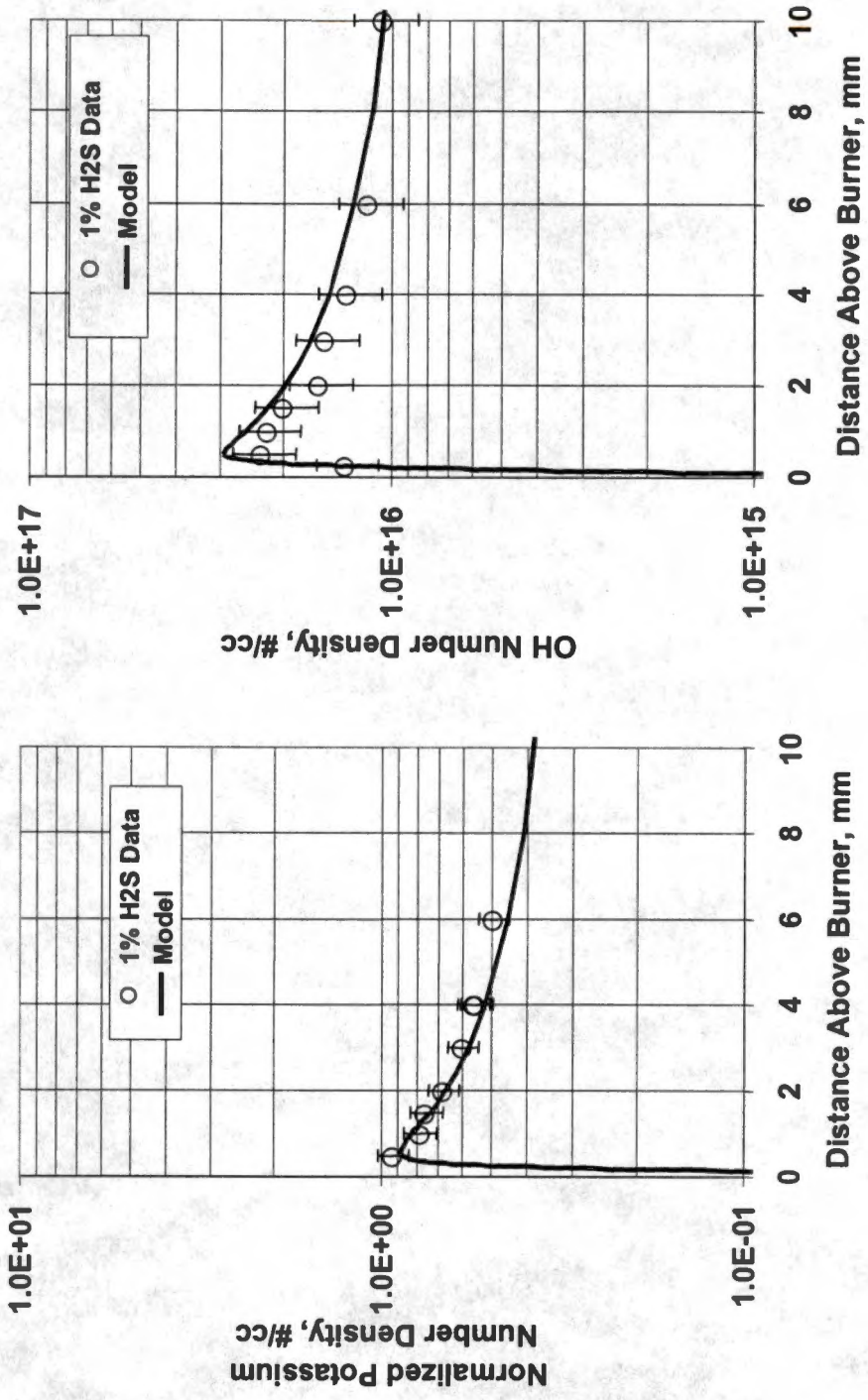

Figure 5-24 Model results for the stoichiometric flame - 1% added H_2S.

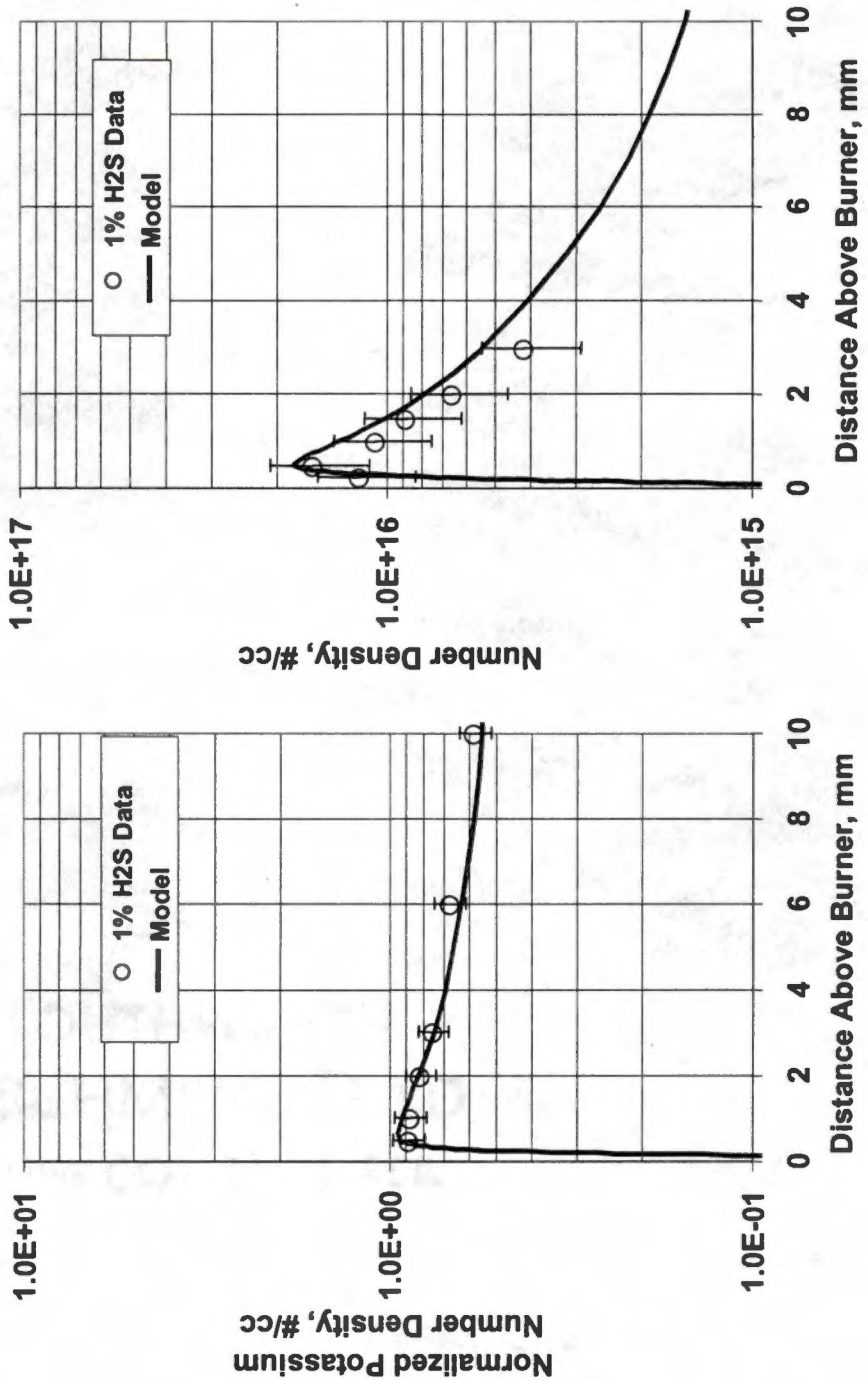

Figure 5-25 Model results for the fuel-rich (ϕ=1.2) flame - 1% added H_2S.

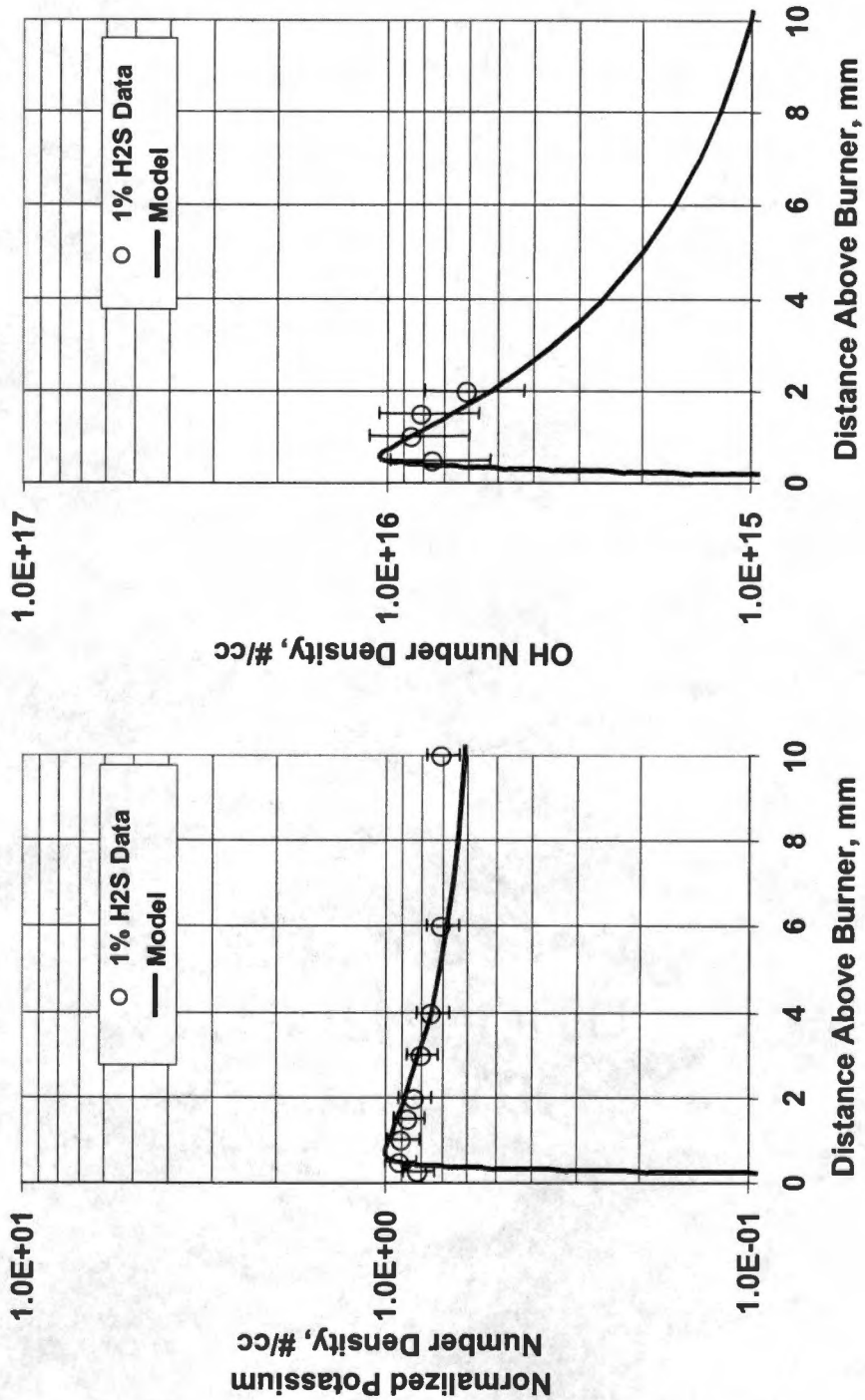

Figure 5-26 Model results for the fuel-rich (ϕ=1.3) flame - 0.75% added H_2S.

The calculated distributions of the potassium-containing species for the fuel-lean flame (ϕ=0.85) and one of the fuel-rich flames (ϕ=1.2) are shown in Figure 5-27. The trends in the oxidized potassium species follow those seen in the flames without sulfur (see Section 5.3.4). In the fuel-lean flame, the K/S species KSO_2 and KOS appear but have concentrations at least two orders of magnitude below that of atomic potassium and KOH. In the fuel-rich flame, the K/S species are more evident. KSO_2 is less than one order of magnitude below K. KOS is the are normalized to the maximum value of the potassium concentration from the next most abundant K/S species. KS, KS_2, and KSH are being formed in small amounts in the later regions of this flame (after about 4 mm).

It is useful to compare the K/O/H species of the flames with and without sulfur. For example, comparing the concentration of KOH at 4 mm above the burner from Figure 5-11 and 5-27, one finds that the concentration in the flame with sulfur is 10% greater than the concentration in the flame with no sulfur. The high KOH concentration in the fuel-lean sulfur bearing flame is due to the high calculated OH concentration. Potassium atoms are shifted towards KOH via reaction (2). As a result, the calculated atomic potassium concentration is below the measurement in the fuel-lean flame. A similar comparison for the fuel-rich flames with and without added sulfur shows similar behavior: KOH is increased with added sulfur. However in the fuel-rich case, the OH data are well matched by the calculated OH values, resulting in a good comparison between the measured and calculated relative atomic potassium concentrations.

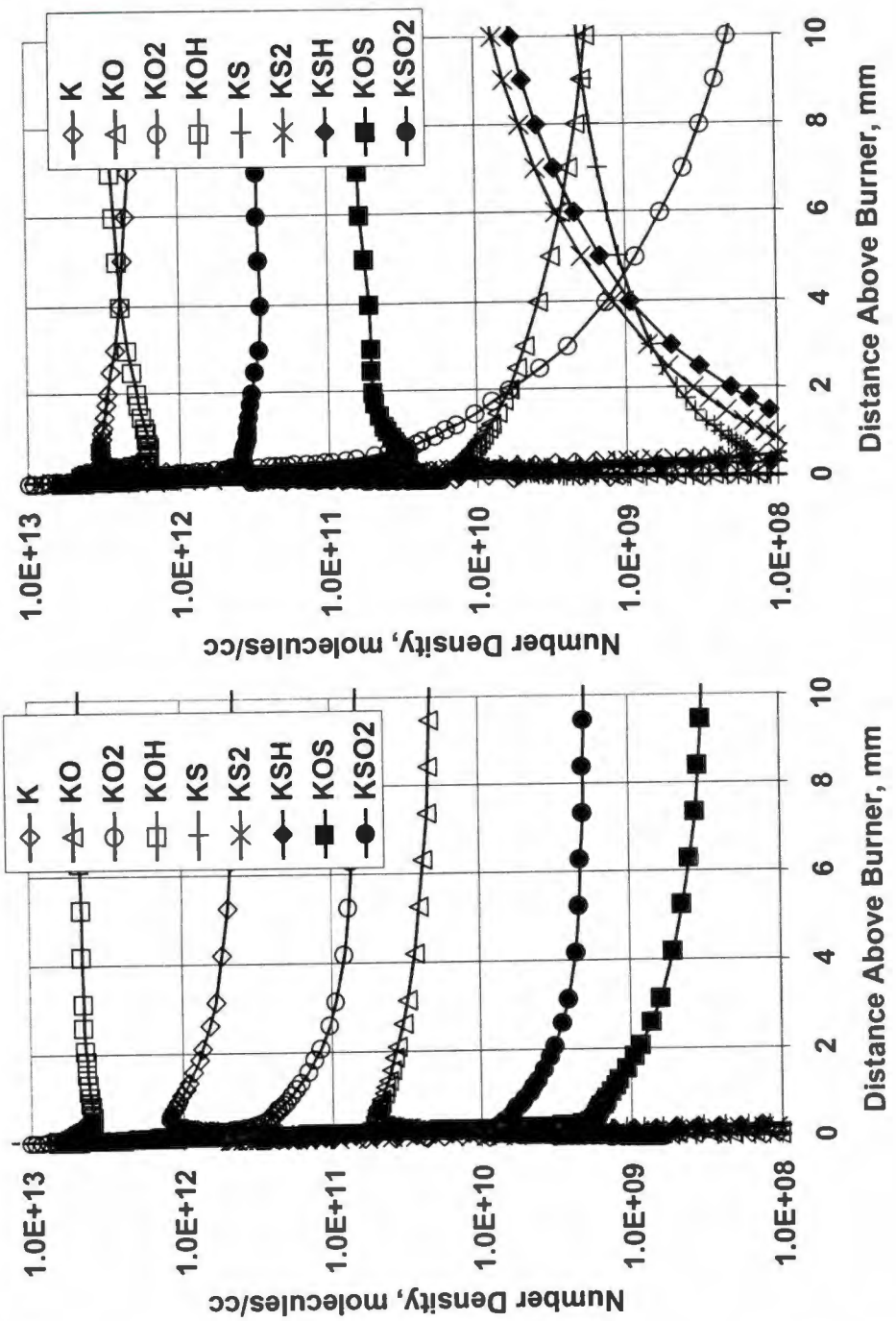

Figure 5-27 Calculated distribution of potassium species in the fuel-lean (ϕ=0.85) and fuel-rich (ϕ=1.2) flame - 1% added H_2S.

The fluxes of species through each of the active reactions of the mechanism are shown in Figure 5-28 (fuel-lean flame) and 5-29 (fuel-rich flame). Figures 5-28 and 5-29 are analogous to Figure 5-13 and 5-15 for K/O reactions. All K/O reactions are shown (1-17) while only reactions 48 and 52-54 of the K/S mechanism are shown:

$$K + SO_2 + M \Leftrightarrow KSO_2 + M \qquad (48)$$

$$KSO_2 + O \Leftrightarrow KO + SO_2 \qquad (52)$$

$$KSO_2 + OH \Leftrightarrow KOH + SO_2 \qquad (53)$$

$$KSO_2 + O_2 \Leftrightarrow KO_2 + SO_2 \qquad (54)$$

Other reactions exhibit negligible production. In both cases it appears that the addition of sulfur provides a secondary path between K and KOH. The termolecular reaction (48) consumes K to produce KSO_2. Reaction of KSO_2 with the flame radicals, O, OH, O_2, produces KO, KOH, and KO_2, respectively. In particular, (53) has a flux comparable to that of (48) and seems to be the preferred path. This situation is similar to the mechanism invoked to describe H-atom scavenging due to sulfur. Reaction (48) is the potassium analog of reaction (34) while reaction (53) is the analog reaction (37) :

$$K + SO_2 + M \Leftrightarrow KSO_2 + M \qquad (48)$$

$$H + SO_2 + M \Leftrightarrow HSO_2 + M \qquad (34)$$

$$KSO_2 + OH \Leftrightarrow KOH + SO_2 \qquad (53)$$

$$OH + HSO_2 \Leftrightarrow H_2O + SO_2 \qquad (37)$$

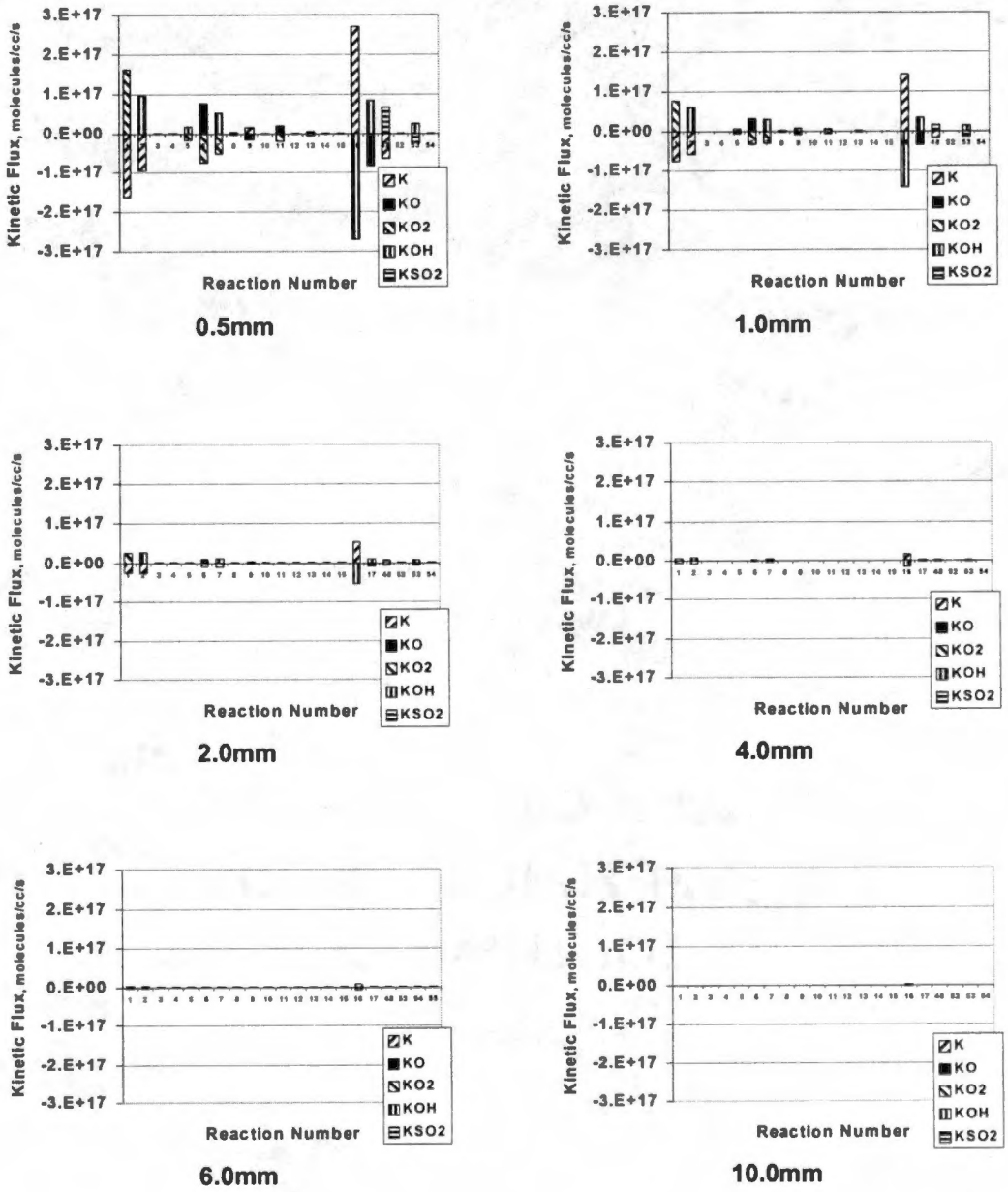

Figure 5-28 Production rates for potassium reactions - fuel-lean (ϕ=0.85) flame, 1% added H_2S.

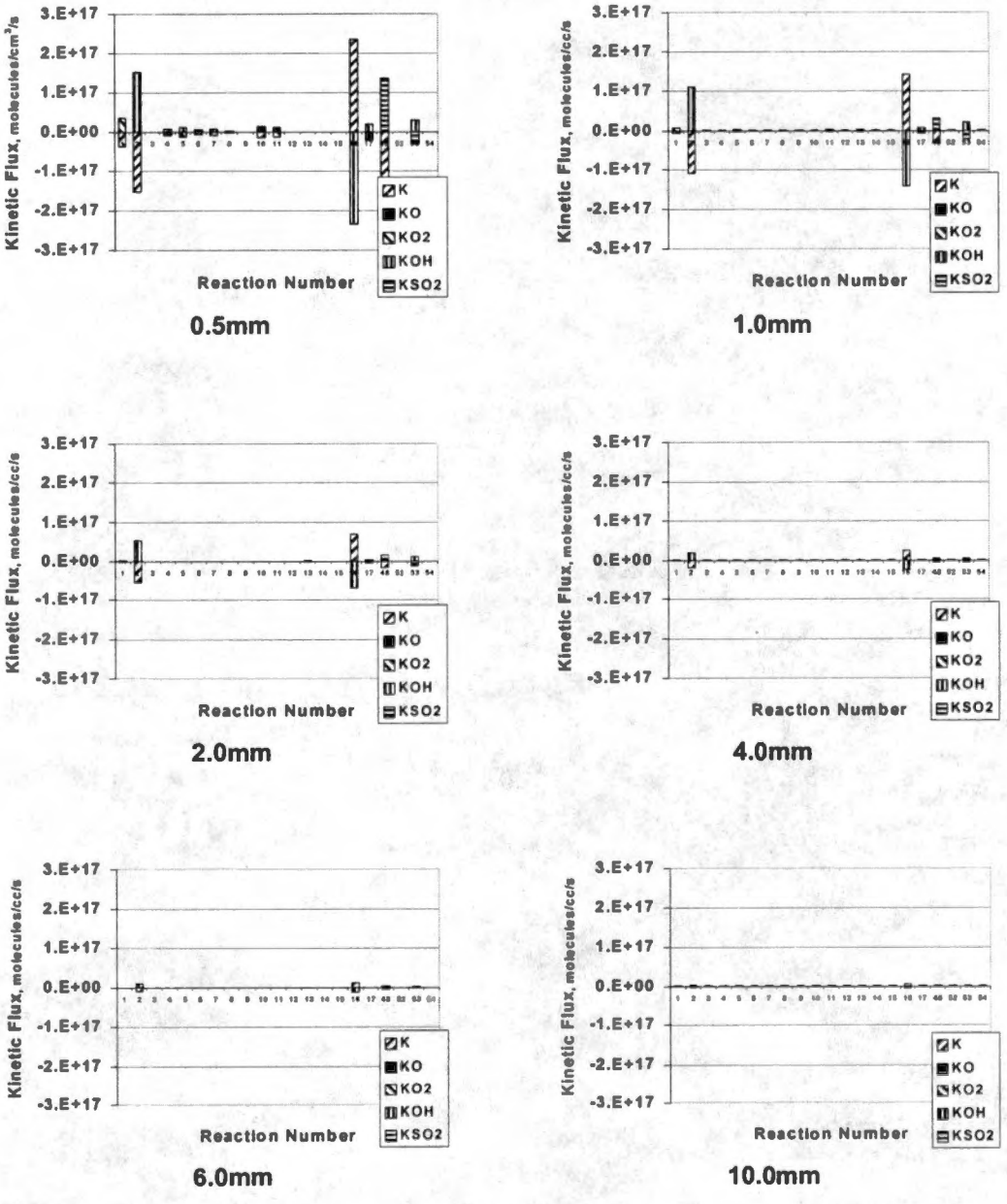

Figure 5-29 Production rates for potassium reactions - fuel-rich (ϕ=1.2) flame, 1% added H_2S.

The rates for the termolecular reactions are crudely estimated. Some guidance for the rate of reaction (48) is provided by the rate determination offered by Goumri, et al [104]. Based on that measurement, reaction (48) is expected to be faster than reaction (1), which is true for the rate specified in this mechanism.

The sensitivity coefficients bear out this analysis. The sensitivity coefficients are shown in Figures 5-30 and 5-31 for the K/O reactions, H/S/O reactions (34) and (37), and reactions (48) and (53) of the K/S mechanism. [K] decay is sensitive to only reactions (48) and (53) of the proposed K/S mechanism. In both cases, [K] is much more sensitive to the rates of the K/O reactions and the H/S/O reactions than the K/S reactions. That is, the [K] decay profile is most sensitive to the perturbation of the flame radical populations caused by the addition of sulfur. This explains the inability of the model to capture the [K] level in the fuel-lean flame. Since the H/S/O mechanism does not capture the OH decay in the fuel-lean flame, the potassium oxidation mechanism is not able to model the observed [K] decay.

The major kinetic pathways are shown in Figure 5-32. This figure is a modification of Figure 5-12, showing the primary K/S pathway. This conclusion is somewhat different than that of Schofield and Steinberg [37]. In Schofield's modeling of fuel-rich and fuel-lean $H_2/O_2/N_2$ flames with Na and sulfur added, he reported that NaOS was the predominant Na/S species in his fuel-rich flame. $NaSO_2$ was comparable to the other Na/S species. In Schofield's and Steinberg's

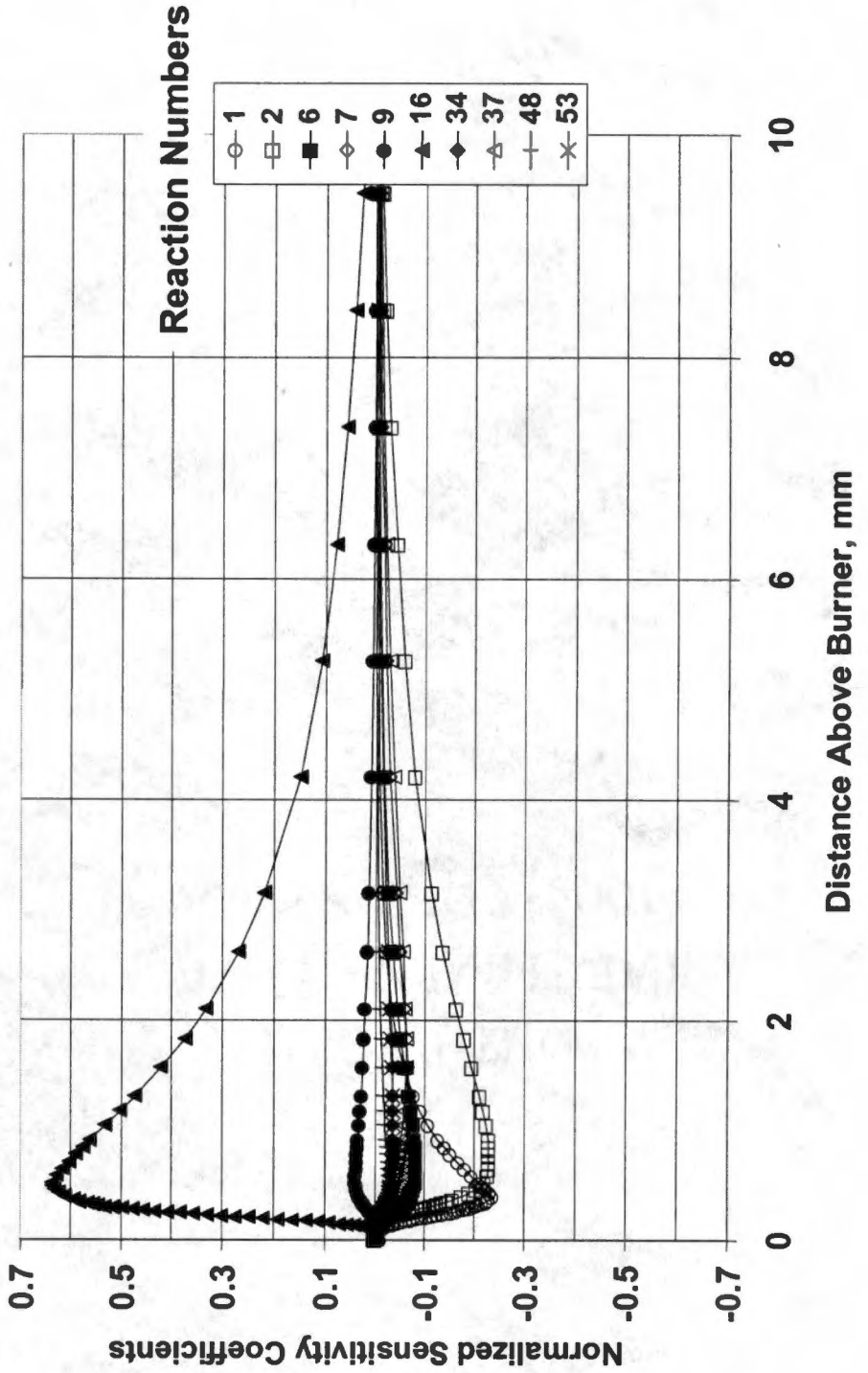

Figure 5-30 Normalized sensitivity coefficients for potassium reactions - fuel-lean (ϕ=0.85) flame, 1% added H_2S.

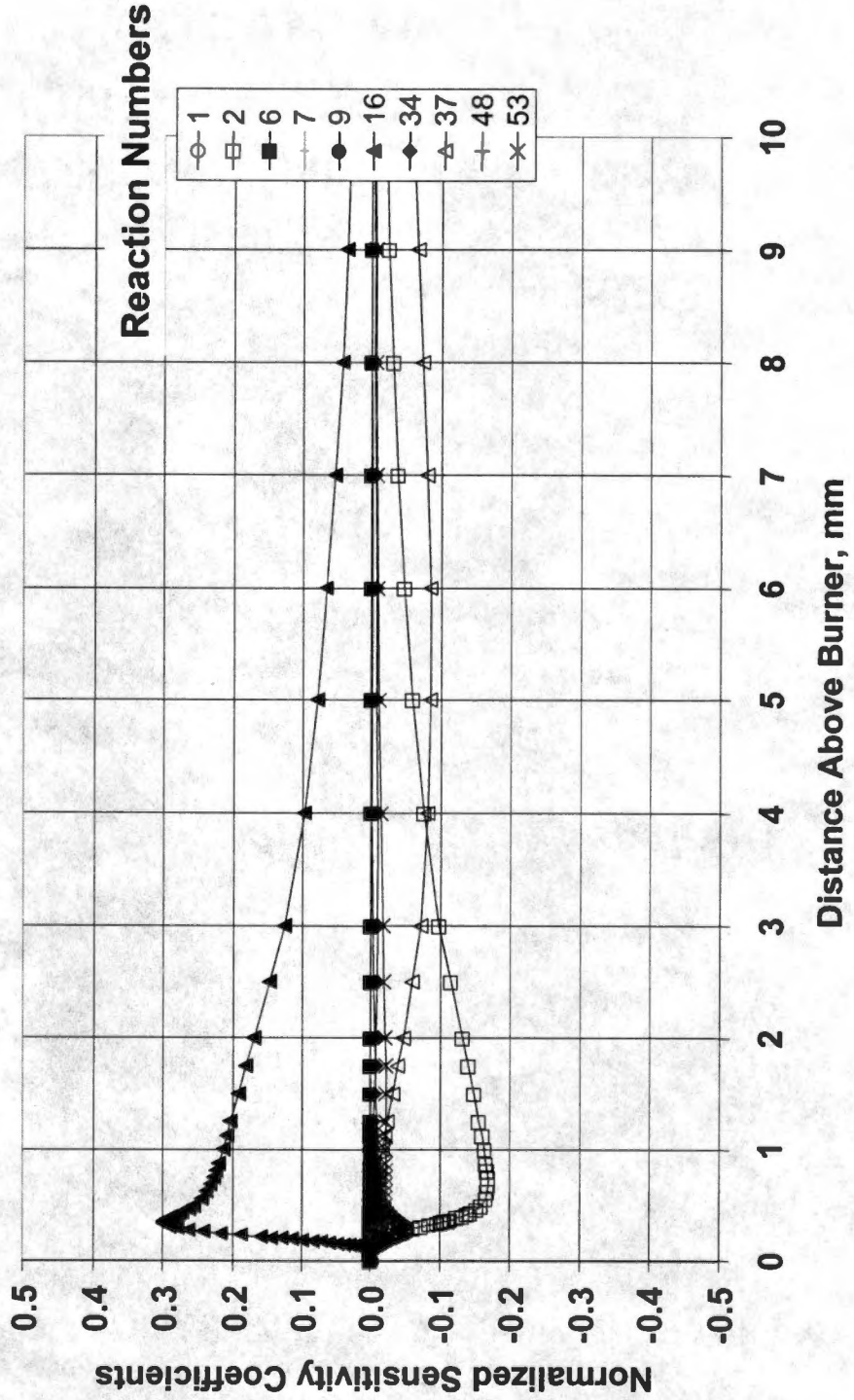

Figure 5-31 Normalized sensitivity coefficients for potassium reactions - fuel-rich (ϕ=1.2) flame, 1% added H_2S.

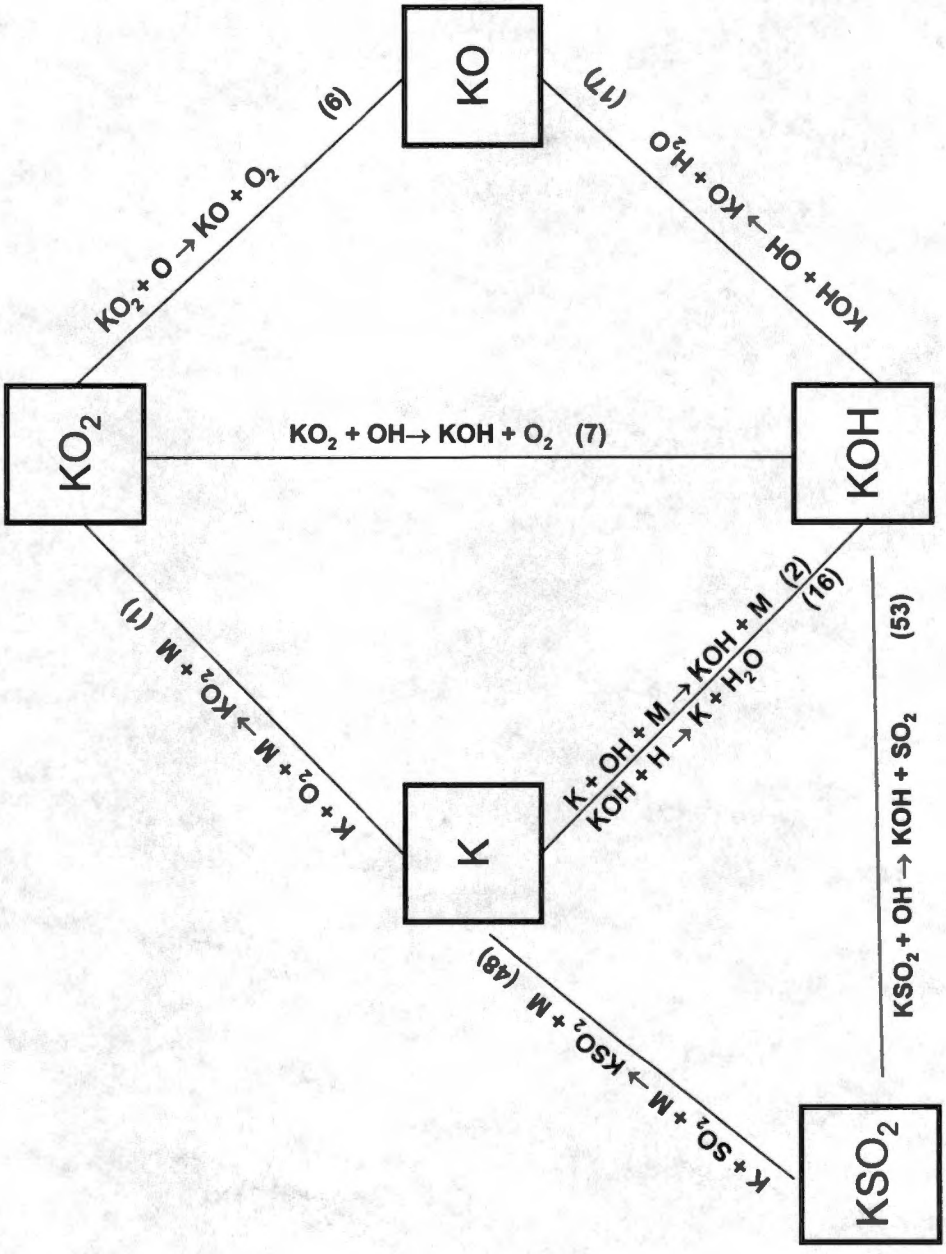

Figure 5-32 Potassium kinetics modified by sulfur.

analysis, the dissociation energy of $NaSO_2$ was fixed by their fuel-lean flame data, while the dissociation energy of NaOS was taken from preliminary calculations by Jinn and Schaefer (unpublished, prior to [102], see [37]). The actual published value of D_0(Na-SO) was about 5 kcal/mole below that used by Schofield and Steinberg [37]. The value of D_0(K-SO) used in this work is only a crude estimate. However, the KSO dissociation energy was greater than that assumed for NaSO by Schofield and Steinberg (indicating a more stable molecule). In this work, the dissociation energy of KSO_2 was fixed by the data of Goumri, et al [104]. That D_0(Na-SO) is less than D_0(K-SO) seems to favor KSO. It is possible that Schofield's and Stienberg's results are skewed by their high estimate (compared to [102]) of D_0(Na-SO). However, there can be no verification of these results until proper determinations of the relevant bond energies become available. At present, the K/S chemical interaction mechanism developed here is appropriate for application to the engineering at hand.

6.0 Secondary Combustor Modeling

6.1 Approach

The flow in the secondary combustor of the CFFF is a very complex turbulent, multijet, recirculating flow, and cannot be simply modeled. Foote [2] has provided an experimental description of this flowfield. However, the important features of the ignition behavior of the secondary combustor can be characterized using a simple flow model. The secondary combustor gas mixture is designed to ignite spontaneously in normal facility operation. The occurrence of spontaneous ignition depends on a balance of the speed of induction reactions, the rate of external energy extraction (heat loss), and residence time. The rate of the induction reactions is a function of temperature and the population of chain-branching species. The rate of energy extraction and the time available for combustion are properties of the combustion device. As described in Section 2, the anomalous shifts in the combustor behavior must have resulted from a shift in the balance of these factors. There was no reason to expect a difference in either residence time or secondary combustor cooling rate between the LMF4 and LMF5 test series. So, the concentration of this research has been focused on possible perturbations to the induction reactions in particular, to the loss of radical species involved in the induction process.

The kinetic modeling and reaction mechanism results presented in Section 5 indicate that the K/S coupling is not strong. In the flames, sulfur binds a small fraction of the total potassium as KSO_2, but KSO_2 is quickly recycled to the

hydroxide (KOH). Most of the potassium remains as free atoms or as the hydroxide. Additionally, the presence of sulfur may represent a more significant flame inhibitor than the potassium species [5]. In the face of these facts, it seems unlikely that the removal of K-atoms by sulfur will influence the flammability of the secondary combustor mixture.

The influence of temperature on spontaneous ignition can be addressed in a straightforward manner. There are two aspects of the presence of chain-branching radical species to consider. First, chain-branching species (e.g. H, OH, O) could be produced in the induction zone by the induction reactions. Secondly, chain-branchers could be provided to the reactants during the induction phase by a fluid mechanical mechanism. For example, mechanisms such as diffusion or bulk mixing of reaction products with reactants will occur in all combustors. The ignition problem was not thought likely to be related to the fluid mechanical influences because neither diffusion nor mixing intensity was expected to change between the test series LMF4 and LMF5.

By this reasoning, only the kinetic aspects of the induction problem needed to be considered to understand the differences between secondary combustor operation during LMF4 and LMF5. A 'plug-flow reactor' model is well suited for this kind of problem. A plug flow reactor is an idealization of a chemically reacting gas stream. In a plug-flow reactor, the gas stream is assumed to be inviscid, and (quasi) one-dimensional with negligible species diffusion. The evolution of the

flow parameters and species are coupled. Thus, rapid chemical heat release due to chemical reaction will influence flow parameters and externally imposed changes to flow parameters will influence the rate of chemical reaction. The secondary combustor was idealized as a constant pressure combustor with external heat extraction fed by perfectly mixed reactants.

The LSENS [[107, 108] plug-flow reactor model was used to produce all the results in this Section. In Section 6.2, the plug-flow reactor model and solution procedure is described. The plug-flow reactor model used the mechanism derived in Section 5. Primary flow compositions consistent with the products of combustion of Eastern and Western coals were used to define the input gas stream. These calculations and results are described in the Section 6.3.

6.2 LSENS Description

The Lewis General Chemical Kinetics and Sensitivity Analysis code (LSENS) [106, 107] was used as the flow model for these calculations. LSENS includes various flow models with coupled chemical kinetics. Only the plug-flow reactor model is discussed here. Under the assumptions previously stated, the governing equations become:

Mass Conservation: $\dot{M} = \rho u_z A$ (6.1)

Momentum Conservation: $\frac{u_z^2}{2}+\frac{P}{\rho}=const$ (6.2)

Energy Conservation: $\frac{c_p}{RT}\frac{dT}{dt}+\sum_{k=1}^{K}\frac{d\sigma_k}{dt}_k\frac{h_k}{RT}-\frac{\sigma_m}{RT}\frac{dp}{dt}+\frac{\dot{Q}/\dot{M}}{RT}=0$

(6.3)

State Equation: $\rho=\frac{P\overline{W}}{RT}$ (6.4)

Symbols are repeated from the equations given in Section 5.1. Additional symbols include:

σ_i - moles of species i per mass of mixture

Q - rate of external heat addition or heat loss

These equations differ from those presented in Section 5.1. First, diffusion has been neglected. Second, the possibility of imposed pressure variations and external heat losses has been retained. Finally, the governing equations are written with time as the independent variable. The space dimension is then a dependent variable. Solutions are found in the time domain and then mapped into the space domain using the local velocity. The process is described in [107]. The species conservation equation is implicit, because the only process allowed for generation or destruction of a chemical species is chemical reaction. The required initial conditions are assignment of initial species concentrations,

temperature, pressure, and velocity. (The use of other gas dynamic dependent variables is possible; e.g. density can replace pressure).

These equations form a set of time-dependant ordinary differential equations

$$\frac{d\bar{y}}{dt} = f(\bar{y}) \qquad (6.5)$$

These equations are solved using a backward difference scheme with a Newton iteration for the corrector iteration [107,108] with variable step size. Analytical Jacobians are used for the Newton iteration. Jacobians are used multiple times, but are recomputed after no more than twenty steps.

LSENS requires thermodynamic properties in the same form as those provided for PREMIX (see Section 5.1). For standard bimolecular and termolecular reactions, LSENS and PREMIX include identical formulations and therefore require identical inputs. However, LSENS cannot use termolecular rates in the Lindemann form [54] or its variants.

6.3 Plug Flow Model Results

Before the plug flow model of the secondary combustor is discussed, it is useful to review the actual secondary combustor operation. It may be useful to refer to Section 2.1. The primary CFFF combustor burned K_2CO_3-seeded coal and fuel oil with oxygen-enriched air to produce a fuel-rich high temperature (2500K-3300K) sulfur- and potassium-laden plasma. After flowing through an MHD

channel simulator duct, a diffuser and a radiant furnace, the gas cooled and condensates (ash, slag, etc.) were removed from the gas stream. Where it entered the secondary combustor, the gas temperature was typically in the range of 1500K to 1700K. Heated air for completing the combustion of the primary exhaust gases was injected into and mixed with the hot primary exhaust gas in the secondary combustor. If the mixture temperature was high enough, the induction reactions proceeded at a pace that overcame the effects of dilution by jet mixing, and external heat losses, and the gas stream ignited and burned. This is where the idealized secondary combustor model begins.

The parametric modeling effort is reported in this section. Primary gas temperature and K_2/S ratio were varied to probe the general behavior of the secondary combustor ignition problem. These parametric studies were done for typical Eastern and Western coal compositions (see section 2.1). Finally, specific comparisons were made of the combustion behavior of fuel-rich combustion product gas streams resulting from Eastern and Western coals in cases that are typical of LMF4 and LMF5 test conditions.

The approach taken here was to begin the plug-flow model calculations in the secondary combustor just downstream of the air injection station. Simply put, the air is assumed to mix instantaneously with the primary exhaust stream, and the resulting bulk flow temperature was taken to be the unreacted mixture-averaged gas temperature. The model calculates the time-evolution of species

concentrations and temperature from this point, which corresponds to the evolution of the flow as it passes on downstream in the facility flow train. If the temperature rises substantially, the result is presumed to represent ignition in the secondary combustor.

The primary combustor inflows are shown in Figure 6-1. The primary gas stream was modeled as an equilibrium mixture of these inflows, with the ash components removed from the coal. The total flows of fuels and oxidizers were taken from actual test points (Eastern coal case - LMF4-R [11], Western coal case - LMF5-H [12]). Calculations of the flow of the carbonate seed and the relative quantities of fuel and oxidizer, as well as their components are described in Appendix G. Note here that the nominal K_2/S ratios (1.0 for Eastern and 4.0 Western coals) were different although the amount of potassium added was the same. The K_2/S ratios differed because the quantities of sulfur were different for each of the coals.

Primary inflow compositions for the secondary combustor were established at bulk inlet temperatures ranging from 1150 K to 1300 K and K_2/S values ranging from 0 to 1.5 for Eastern coal and 0 to 5 for Western coal. Slag and ash components were not considered in the calculations. Virtually all the potassium survives the de-slagging or slag rejection process in the radiant furnace [6]. The primary stream was assumed to be in equilibrium and the species distribution was computed using the CEC program [108]. At the lower end of the

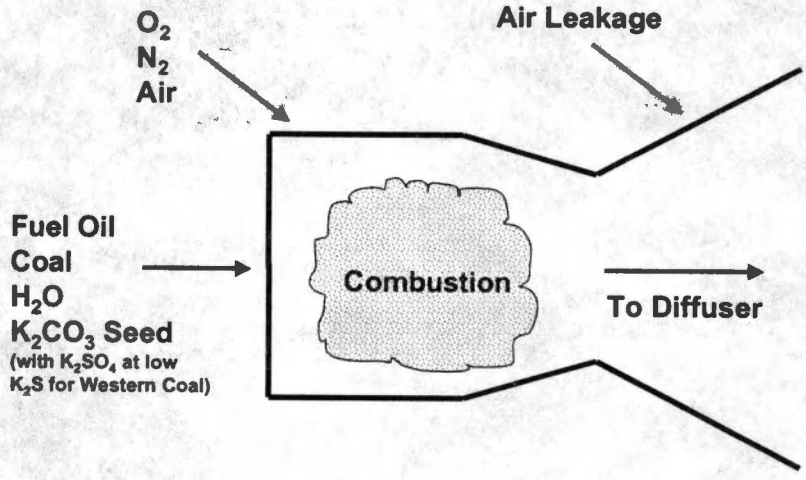

Figure 6-1 Primary combustor inflow schematic.

temperature range, condensed phase species are possible. As stated, condensed-phase species were eliminated from consideration in these calculations. Since equilibrium calculations indicate that a significant fraction of the total potassium would exist in a condensed form, this procedure maximizes the quantity of potassium in the vapor phase. However, this potassium would be released if the stream were to ignite. No vapor phase K_2 components are included in the thermodynamic database of the equilibrium program, although K_2-vapor species were considered (e.g. K_2SO_4 - [6]). Given the high level of K_2CO_3 addition in the primary stream, this omission is a possible weakness in these calculations.

The results of the equilibrium calculations with the state defined by assigned values for temperature and pressure are displayed in Figures 6-2 through 6-5. The distribution of H/S/O species for eastern coal with $K_2/S=1.0$ is shown in Figure 6-2. H_2S is the most abundant sulfur species at all temperatures. As temperature increases, sulfur is shifted toward SO_2. The results for Western coal, Figure 6-3, are similar. Because of the relatively low level of sulfur in Western coal, the levels of all sulfur-containing species are shifted downward. Potassium species distributions for Eastern and Western coals, Figures 6-4 and 6-5, respectively, show that KOH is the most abundant potassium species in all cases. In eastern coal, KSH is the second most abundant potassium species to be found, followed by atomic potassium. In western coal, atomic potassium is favored over KSH at temperatures above 1200 K.

For Eastern and Western coal, the presence of KSH changes the H/S/O species distribution, as seen in Figure 6-6 and 6-7. In both cases, H_2S is converted to KSH at equilibrium. As will be shown kinetically and discussed later, this changes the ignition behavior for low K_2/S ratios.

These species mixtures were used to represent the primary gas stream composition in subsequent calculations. Heated secondary combustor air was assumed to instantaneously mix with the primary gas stream. The secondary air flow rate was taken from actual values for LMF4-R and LMF5-H. The secondary air initial temperature was assumed to be approximately 600 K. The computation

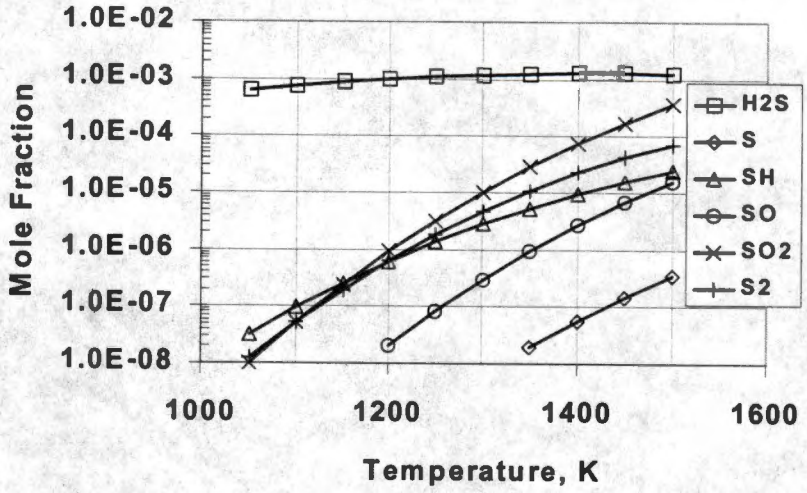

Figure 6-2 Equilibrium distribution of sulfur species with temperature in Eastern coal, $K_2/S=1.0$.

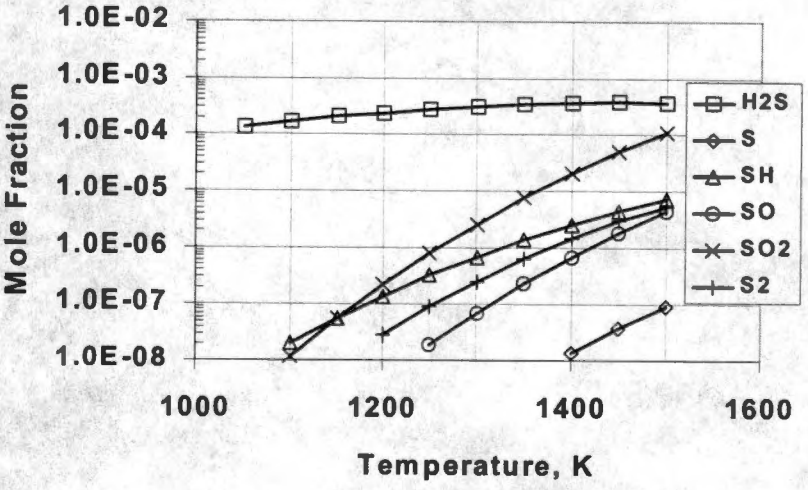

Figure 6-3 Equilibrium distribution of sulfur species with temperature in Western coal, $K_2/S=4.0$.

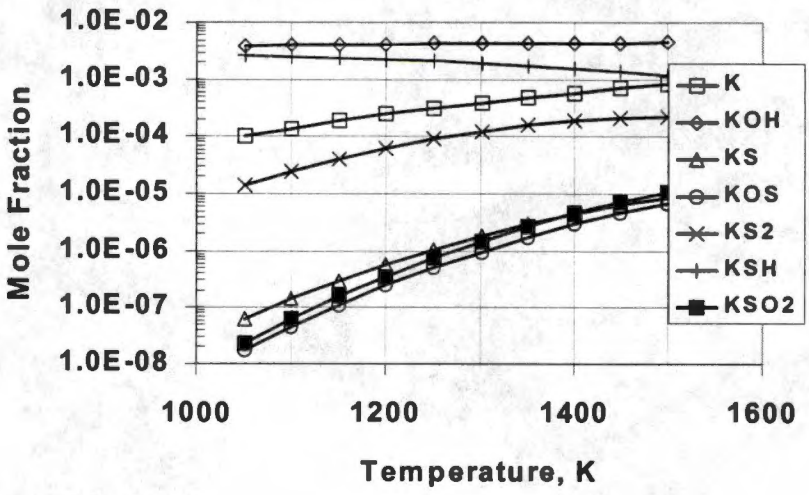

Figure 6-4 Equilibrium distribution of potassium species with temperature in Eastern coal, $K_2/S=1.0$.

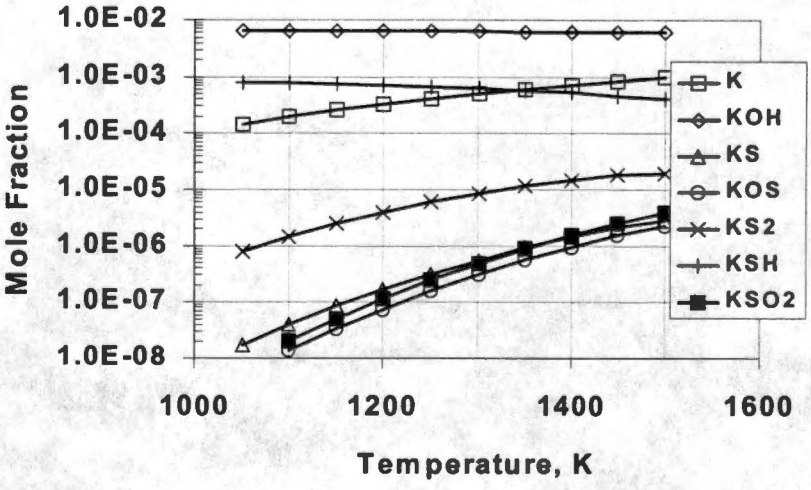

Figure 6-5 Equilibrium distribution of potassium species with temperature in Western coal, $K_2/S=4.0$.

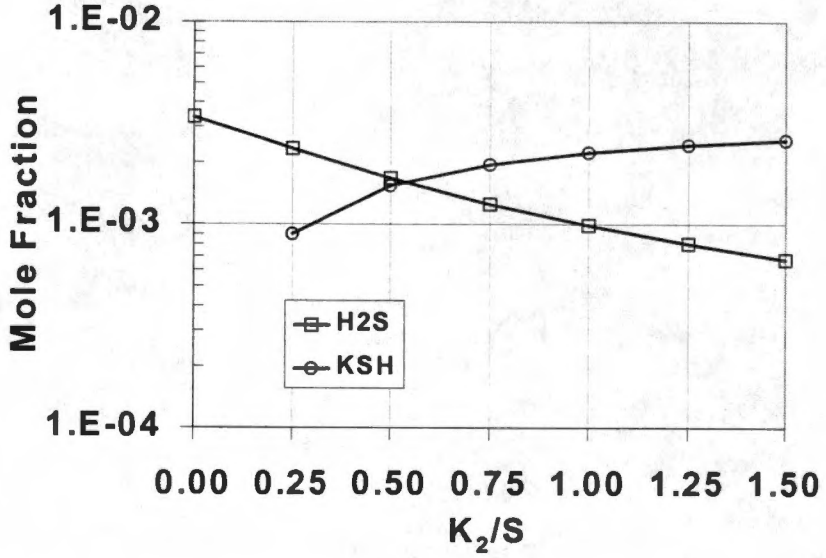

Figure 6-6 Equilibrium shift of sulfur from H_2S to KSH, Eastern coal, $T_{Primary}$=1200K.

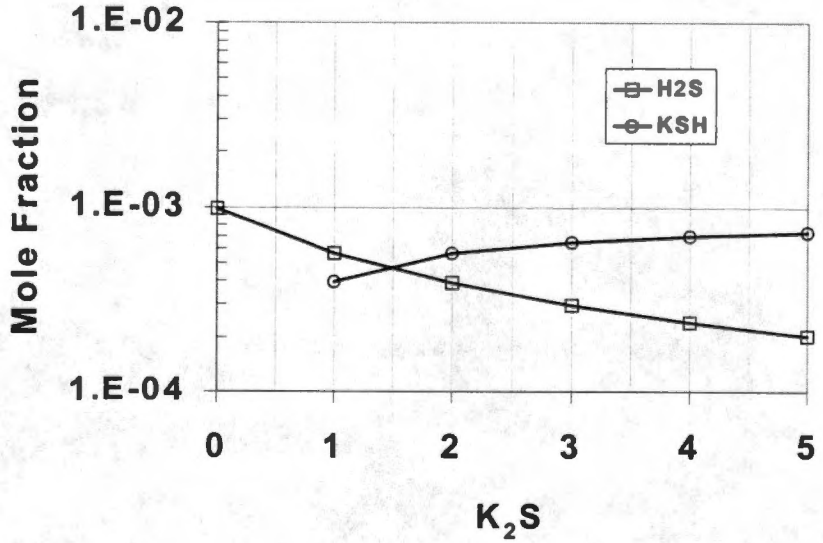

Figure 6-7 Equilibrium shift of sulfur from H_2S to KSH, Western coal, $T_{Primary}$=1200K.

of the final mixture composition and temperature are described in Appendix G. This mixture was used as the starting condition for the LSENS plug-flow reactor calculations.

The final required input was the external heat extraction. Gas temperature variation along the CFFF flow path has been recorded for various tests. These data represent the bulk rate of heat extraction from the flow path. In the region of the secondary combustor, the bulk heat loss resulted in a temperature decrease rate of about 600 K/s. This was converted, with the bulk mass flow rate, into a heat loss rate per unit length of about 200 W/cm. This value was used in all plug-flow reactor calculations.

The plug-flow model was executed in the constant-pressure mode. The independent variable for integration was specified to be distance. The program does all calculations in the time domain, but distance can be specified as an independent variable so that a length scale is added to the results. The evolution of the solution was obtained up to 500 cm (about 16 ft) from the starting point, that is, 500 cm downstream of the point of injection of the secondary air.

Calculated results for Eastern coal with $T_{Primary}$=1150 K are shown in Figure 6-8. A series of plug-flow reactor temperature profiles are plotted together. Each profile corresponds to a different primary combustor K_2/S ratio. With no potassium, the mixture ignites almost immediately at this temperature level.

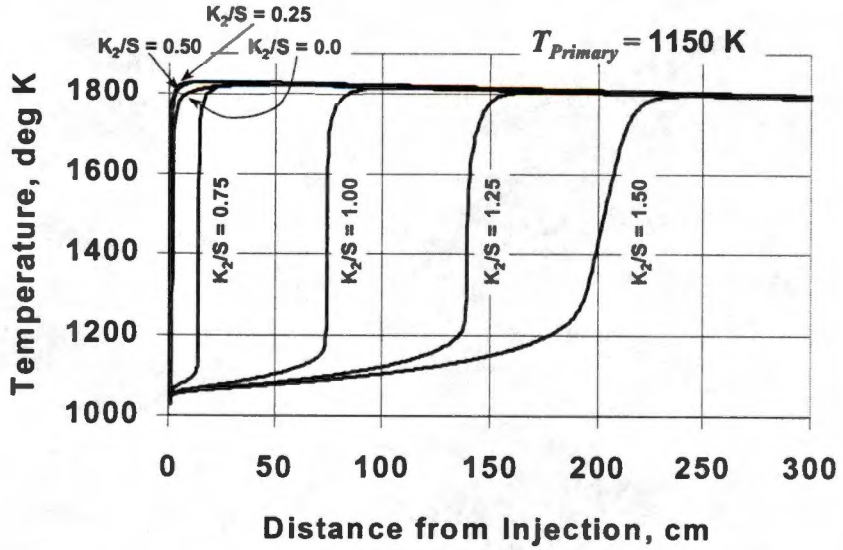

Figure 6-8 Ignition temperature histories for Eastern coal, $T_{Primary}$=1150 K.

Ignition delay is not indicated until K_2/S=0.75. Further increases in K_2/S cause correspondingly increased ignition delays. Note that at low K_2/S levels, the ignition delay is slightly *decreased*, that is, the mixture ignites faster then when K_2/S is zero. This effect will be discussed in more detail later.

The same calculations using $T_{Primary}$ =1100 K indicates that ignition is significantly delayed when the K_2/S ratio is as low as 0.75. Calculations at 1200 K show that all mixtures ignite within 100 cm of injection of secondary air.

The plug-flow calculations for Western coal are shown in Figure 6-9. The temperature profiles in this figure show that, qualitatively, potassium has the

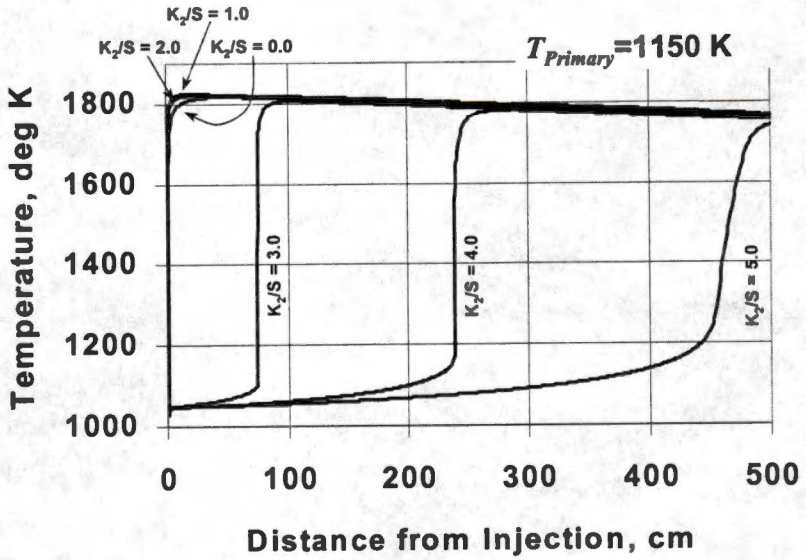

Figure 6-9 Ignition temperature histories for Western coal, $T_{Primary}$=1150 K.

same affect on ignition in the secondary combustor for both Eastern and Western coals. For cases of low K_2/S, ignition occurs within 100 cm of the injection point. At higher levels of K_2/S, ignition is significantly delayed. At 1100 K, ignition occurs only for K_2/S less than 3. At 1200 K, ignition occurs within 100 cm for all K_2/S levels.

The comparison of these two sets of calculations indicates that the characteristics of the ignition process of the secondary combustor mixture for Eastern coal and Western coal are not drastically different. Note that the Eastern coal case with K_2/S=1.0 and the Western coal case with K_2/S=4.0 have about the same quantity of potassium carbonate seed (by mass, K_2/S=1 for Eastern coal is

identical to $K_2/S=3.5$ for Western coal). The temperature profiles at fixed K_2/S ratio but for various initial stream temperatures are shown in Figures 6-10 and 6-11 (Eastern and Western coal, respectively). From Figure 6-10, it is clear that the primary stream temperature must be at least 1150 K for rapid ignition of the gas mixture. In that case ignition occurs about 80 cm downstream of the injection of secondary air. The Western coal calculations are shown in Figure 6-11. The primary stream temperature must be at least 1200 K to ignite the gas mixture within 100 cm of the injection point. The results of these calculations indicate that, at the nominal K_2S level, Western coal is more difficult to ignite in the secondary combustor than Eastern coal.

The results for Western coal are consistent with the LMF5 experiments. Recall that the LMF5 experiments indicate that ignition and secondary combustion occurred whenever $T_{Primary}$ was greater than about 1200 K and the K_2/S ratio was less than 3. From the results shown in Figure 6-9 and 6-11, it is seen that the model produces long ignition delays when the temperature is less than 1200 K and the K_2/S ratio is greater than about 2. The model and full-scale facility operation and experiment produced consistent results.

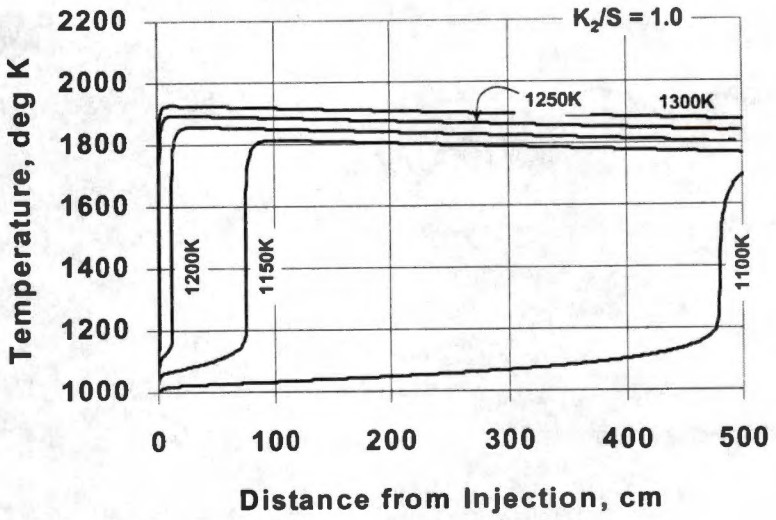

Figure 6-10 Ignition of the secondary combustor, Eastern Coal with $K_2/S = 1.0$.

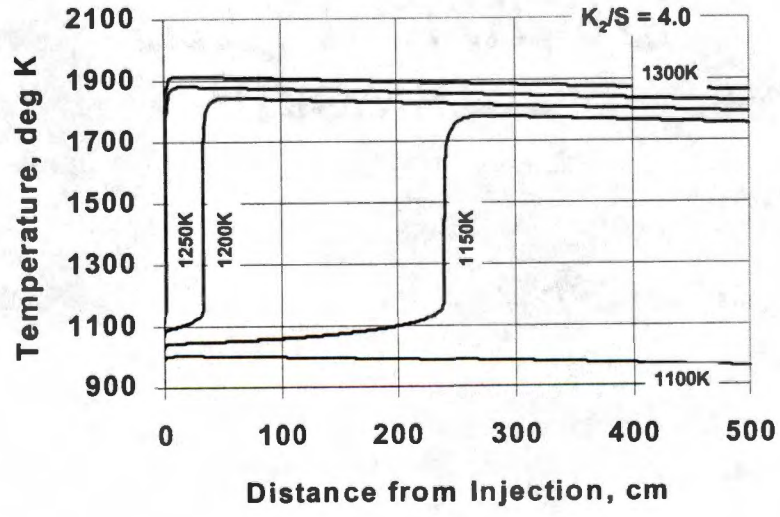

Figure 6-11 Ignition of the secondary combustor, Western Coal with $K_2/S = 4.0$.

The K/S interactions are not the primary cause of the observed ignition delays. The scale on Figure 6-8 is expanded and presented in Figure 6-12 (Eastern coal) and Figure 6-9 is expanded and presented in Figure 6-13 (Western coal). Two observations may be made. First, ignition with no potassium is only slightly slower for Eastern coal than for Western coal. This difference is probably due to slight differences in initial mixture temperature, stoichiometry, and carbon-to-hydrogen ratio. Second, addition of small amounts of potassium were found to *decreases* ignition time, as noted above. Similar results were obtained for Western coal (Figure 6-13). This result is counter to the original hypothesis and requires further examination.

By examining the species production rates for various times prior to ignition in each of these cases, the productive reactions are revealed. The S/H/O reaction production rates are shown in Figure 6-14. The addition of potassium greatly accelerates the conversion of SH to SO through reaction with O_2. This is caused by an increase in the production of SH through reaction (72) and mediated by reaction (84),

$$KO_2 + SH \Leftrightarrow KSH + O_2 \qquad (72)$$

$$KSH + SH \Leftrightarrow KS + H_2S \qquad (84).$$

Reaction (72) is the analog of (7), which also fast in the K/O mechanism. Reaction (84) is the analog of reaction (17). The production of H/S and K/S reactions is shown in Figures 6-14 a and b. Reaction (72) is producing SH, while

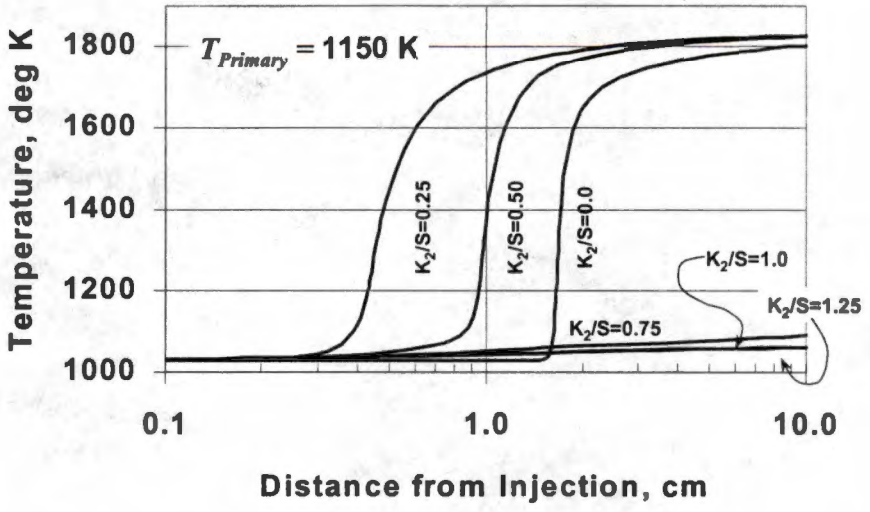

Figure 6-12 Detail of ignition temperature history for Eastern coal.

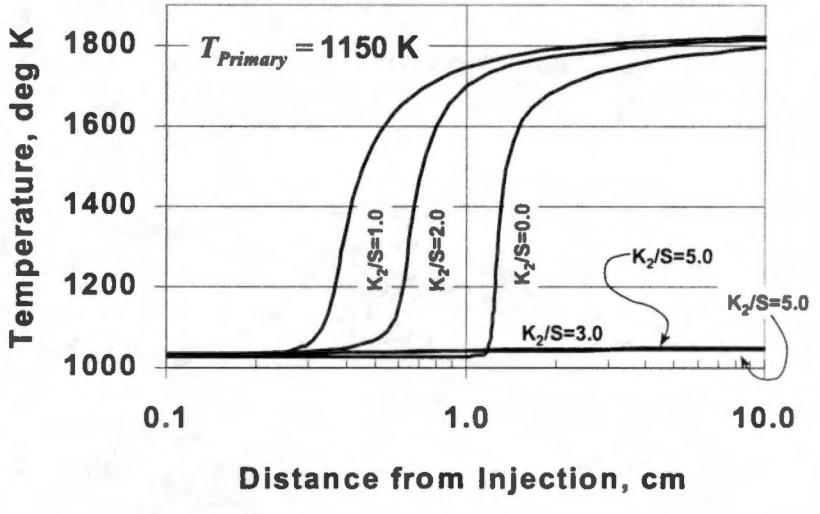

Figure 6-13 Detail of ignition temperature history of Western coal.

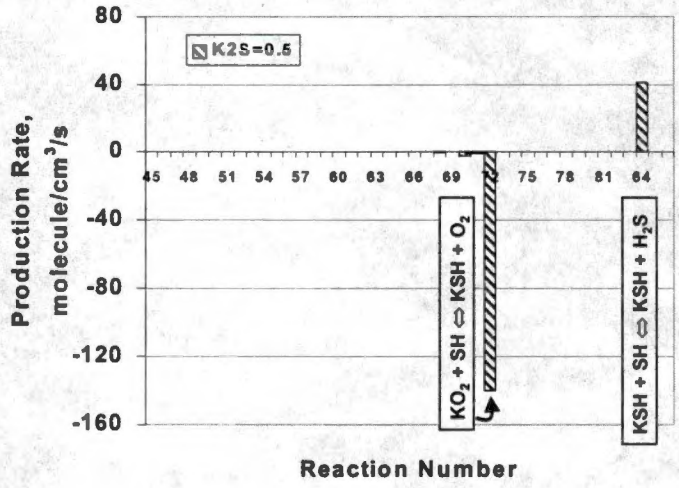

b. K/S reactions

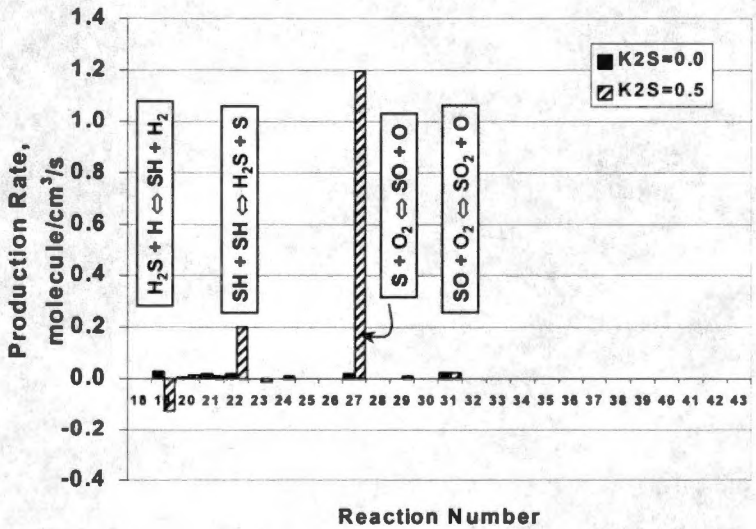

b. Sulfur reactions

Figure 6-14 Production rates for K/S/H/O and S/H/O reactions prior to ignition. Eastern coal with $T_{Primary}$ = 1150K.

reaction (84) is consuming SH. However, the production of SH is increased. This reaction proceeds swiftly due to the abundance of KSH in the flow. The sulfur reactions, Figure 6-14b, show the result of the increased SH production. Reaction (19) consumes SH and produces H_2S. Reaction (22) consumes SH and produces S. The abundance of S drives reaction (27) to produce SO_2 through reaction (31).

$$H_2S + H \Leftrightarrow SH + H_2 \qquad (19)$$

$$SH + SH \Leftrightarrow H_2S + S \qquad (22)$$

$$S + O_2 \Leftrightarrow SO + O \qquad (27)$$

$$SO + O_2 \Leftrightarrow SO_2 + O \qquad (31)$$

The equilibrium calculations discussed above show that KSH is highly favored at the primary flow temperatures. This compound binds a significant portion of the sulfur present, reducing the concentration of the otherwise favored H_2S. The sulfur oxidation/reduction mechanism, discussed in Section 5, is modified as shown in Figure 6-15. Without potassium/sulfur species, H_2S is converted to SO_2 along the path indicated. However, in the presence of potassium, and especially KSH, the path is modified as indicated in Figure 6-15. The additional channels due to K/S species accelerate the consumption of H_2S for very low levels of potassium seeding.

The more significant increase in ignition time observed with higher levels of potassium is due, for a fixed initial temperature, to the potassium inhibition

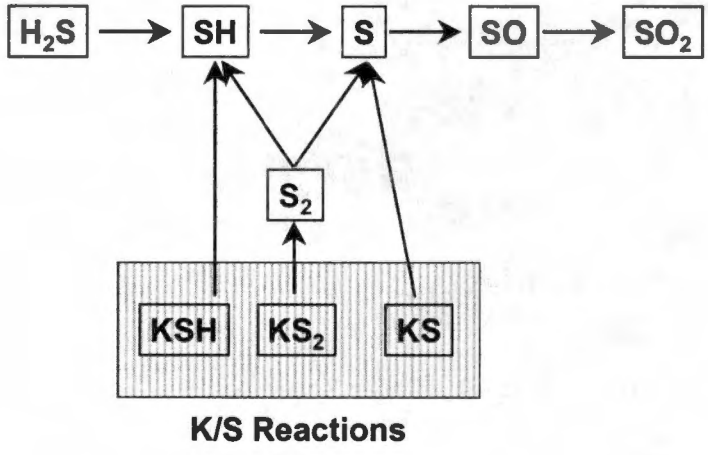

Figure 6-15 Modification to the mechanism for the oxidation of H_2S.

mechanism, reactions (1) through (17), rather than K/S interactions, reactions (45) through (86). The K/S interaction described above is primarily responsible for the small temperature changes prior to ignition (or at the end of the calculation) through changes in the mixture thermal properties, particularly mixture specific heat. However, this interaction is progressively offset by the effects of increased potassium in the K/O cycle. Plug flow calculations with K/O reactions only and no K/S species show trends similar to the trends described here. That is, when K_2/S levels are increased, ignition times are increased. Differences that do exist are probably due to the action of the K/S reactions prior to ignition.

K/O interactions control the ignition behavior of the flow in the secondary combustor. K/S interactions have only a minor effect. The differences in the secondary combustor ignition with Eastern and Western coals, then, are not explained by K/S interactions. To explain the difference, several points are noted:

1. The heat of combustion for typical Eastern coal is higher than for Western coal.
2. The seed injection method for LMF5 injected a significant quantity of water in the stream.
3. The experiments varying K_2/S conducted during LMF5 were never conducted during LMF4. Further, there is no evidence that secondary combustor ignition was ever attempted at $T_{Primary}$ less than about 1250 K during LMF4.

Because of the first two points, $T_{Primary}$ would always be greater during LMF4 than during LMF5 for the same fuel flow rate and stoichiometry. By the third point, it is seen that inhibition of the secondary combustor flame indicated by the model would not have been observed during LMF4 since no attempt was made to ignite the stream at a temperature below about 1200 K. Thus it seems that the observed differences in combustion inhibition can be attributed primarily to differences in $T_{Primary}$.

7.0 Final Conclusions

In this work, an analysis of the secondary combustor ignition behavior was performed to explain the observed results in two different test of the CFFF, one for Eastern coal and one for Western coal. Experiments were conducted in methane flames with added potassium and sulfur to determine the kinetics of the interactions of potassium and sulfur species. As a results of this work, a new potassium oxidation mechanism has been developed, thermodynamic properties of several K/S species have been estimated, and a mechanism describing the kinetic interaction of potassium and sulfur has been developed. These developments were used in a plug flow model of the secondary combustor to explain the observed secondary combustor ignition characteristics.

The potassium oxidation mechanism developed herein is a modification and extension of the model discussed by Slack, et al [20] and Hynes, et al [18]. Several discrepancies in the literature were uncovered and appropriate corrections made. Uncertainties remain in the thermodynamic properties of potassium superoxide, KO_2. Additionally, uncertainties remain in the rates of reactions (1) and (2):

$$K + O_2 + M \Rightarrow KO_2 + M \qquad (1)$$

$$K + OH + M \Rightarrow KOH + M \qquad (2).$$

Direct measurements of these rates have been made, but relative third body efficiencies are only approximately determined. Because of the cyclic nature of the potassium oxidation mechanism, changes to these rates will be offset by

adjustments to the rates of the simple bimolecular reactions in the cycle. Thus, unique determinations of the rates of the numerous bimolecular reaction rates is not possible based on the flame data.

Structures, vibrational parameters and bond energies were estimated for potassium and sulfur compounds (KS, KSO, KSH, KS_2, KSO_2) so that thermodynamic properties could be determined. Of the five species, only two have been observed (KS, KSO_2) experimentally and the sodium analog of KOS (NaOS) has been identified computationally. The molecular properties of species KS_2 and KSH are almost certainly analogous to those of KO_2 and KOH.

A mechanism consisting of 42 K/S reactions was constructed (Appendix A) and used to fit the experimentally measured decay profiles OH and atomic potassium in flames of methane, oxygen and nitrogen. H/S, K/O, and H/O reaction analogs were used to estimate the reaction rates for the 42 K/S reactions. No independent determinations of these reaction rates have been made. K/S interactions were not found to be significant in the fuel-lean and stoichiometric flames, but were required to match the data in the fuel-rich flames. In the fuel-rich flames, the reactions:

$$K + SO_2 + M \Rightarrow KSO_2 + M \qquad (48)$$

$$KSO_2 + OH \Rightarrow KOH + SO_2 \qquad (53)$$

were found to provide an efficient alternate path between K and KOH. A good match to the fuel-lean flame data could not be achieved due to the inability of the H/S/O radical scavenging chemistry to reproduce the OH decay profile.

The K/S mechanism developed herein was applied in a simple plug flow kinetic model of the secondary combustor flowfield. The model reproduced the ignition behavior from the LMF5 series of test with Western coal. That is, a K_2/S ratio greater than 3 or primary gas stream temperature less than 1200 K prevented ignition in the secondary combustor. Similar behavior was predicted for the LMF4-like test conditions using Eastern coal. Due to differences in the properties of astern and Western coals and differences in the test facility for LMF4 and LMF5, the secondary combustor inlet temperatures at nominal test point for LMF5 was about 200 F below that of a nominal test point for LMF4. Therefore, it was concluded that the K/O interactions were primarily responsible for the observed combustion inhibition in LMF5 tests. Since the LMF4 test series did not include an attempt to ignite the secondary combustor at temperatures below 1250K, flame inhibition would not be observed, as indicated by the model.

REFERENCES

Section 1

1. Attig, R.C., J.C. Chapman, N.R. Johanson, "Status of Proof-of-Concept Testing at the Coal-Fired Flow Facility", *Proceedings of the 31st Symposium on the Engineering Aspects of Magentohydrodynamics*, pp II.5.1 – II.5.11, Whitefish, MT June 29 – July 1, 1993.
2. Foote, J.P., "A Cold Flow Model Study of Turbulent Mixing in a Secondary Combustor", Master Thesis, The University of Tennessee, 1982.
3. Friedman, R. and Levy, J.B., "Inhibition of Opposed-Jet Methane-Air Diffusion Flames. The Effects of Alkali Metal Vapours and Organic Halides", *Combustion and Flame*, **7**, 195 (1963).
4. Webster, P, Walsh, A. D., "The Effect of Sulfur Dioxide on the Second Pressure Limit of Explosion of Hydrogen-Oxygen Mixtures", *Tenth Symposium (International) on Combustion*, 462, (1965).
5. Lewis, P., Piper, L., Wilemski, G., Kemp, N., and Conin, J., "Final Report: Analytical Studies of the Effects of Potassium and Sulfur on MHD Emissions", PSI-TR-143 (1978).

Section 2

6. Li, J., "Modeling Potassium-Sulfur Interactions across Secondary Combustor in a Coal-Fired Magentohydrodynamics (MHD) System", DOE/ET/10815-172 (1992).
7. "MHD Program Plan FY 1990", U.S. Department of Energy, DOE/FE-0168P, October 1989.

8. "University of Tennessee Space Institute Design Report: Secondary Combustor and Ash/Seed Hopper for the Low Mass Flow Coal Fired Flow Facility", DR-2.3.3-79-01, Kulesza, P., W. Power, R.C. Attig, N. Johanson, March 1979.
9. "Illinois No. 6 Coal 2000 Hour Proof-of-Concept Report", Edited by R.C. Attig, September 23, 1994.
10. "Final Report – Proof of Concept Test of the Magnetohydrodynamic Steam-Bottoming System at the DOE Coal-Fired Flow Facility" Edited by R.C. Attig, DOE/PC/95231-6, October 9, 1996.
11. "Express Data Report – LMF4 R", The University of Tennessee Space Institute, August 16, 1989.
12. "Express Data Report – LMF5 H", The University of Tennessee Space Institute, April 20, 1993.
13. James, C.G., and Sugden, T.M., "Photometric Investigation of Alkali Metals in Hydrogen Flame Gases. I. A General Survey of the use of Resonance Radiation in the Measurement of Atomic Concentrations", *Proceedings of the Royal Society (London)*, **A227**, 312 (1955).
14. Kaskan, W.E., "The Reaction of Alkali Atoms in Lean Flames", *Tenth Symposium (International) on Combustion*, 41, (1965).
15. Carabetta, R., and Kaskan, W.E., "The Oxidation of Sodium, Potassium, and Cesium in Flames", *Journal of Physical Chemistry*, **72** (7), 2483 (1968).
16. Jensen, D.E., Jones, G.A., and Mace, C.H., "Flame Inhibition by Potassium", *Chemical Society, Faraday Transactions I*, **75**, 2377 (1979).

17. Jensen, D.E., "Alkali-Metal Compounds in Oxygen-Rich Flames", *Chemical Society, Faraday Transactions*, **78**, 2835 (1982).

18. Hynes, A.J., Steinberg, M., and Schofield, K., "The Chemical Kinetics and Thermodynamics of Sodium Species in Oxygen-Rich Flames", *Journal of Chemical Physics*, **80** (6), 2585 (1984).

19. Steinberg, M., Schofield, K., "The High Temperature Chemistry and Thermodynamics of Alkali Metals (Lithium, Sodium, and Potassium) in Oxygen Rich Flames", Paper 3A-042 presented at the *Fall Joint Meeting of the Western States and Japanese Sections of the Combustion Institute* (1987).

20. Slack, M., Cox, J.W., Grillo, A., and Ryan, R., "Potassium Kinetics in Heavily Seeded Atmospheric Pressure Laminar Methane Flames", *Combustion and Flame*, **77**, 311 (1989).

21. McAndrew, R., and Wheeler, R., "The Recombination of Atomic Hydrogen in Propane Flame Gases", *Journal of Physical Chemistry*, ***66***, 229 (1962).

22. Fenimore, C.P., and Jones, G.W., "Sulfur in the Burnt Gas of Hydrogen-Oxygen Flames", *Journal of Physical Chemistry*, **69** (10), 3593, (1965).

23. Kallend, A.S., "Influence of SO_2 on Chemiluminescence and Atom Recombination in Hydrogen Flames", *Transactions of the Faraday Society*, **63**, 2442 (1967).

24. Halstead, C.J. and Jenkins, D.R., "Sulphur-Dioxide-Catalyzed Recombination of Radicals in Premixed Fuel-Rich Hydrogen+Oxygen+Nitrogen Flames", *Transactions of the Faraday Society*, **63**, 3013 (1969).

25. Durie, R.A., Johnson, G.M., and Smith, M.Y., "The Effect of Sulfur Dioxide on Hydrogen-Atom Recombination in the Burnt Gas of Premixed Fuel-Rich Propane-Oxygen-Nitrogen Flames", *Combustion and Flame*, **17**, 197 (1971).

26. Kallend, A.S., "Kinetics of the Sulfur Dioxide Catalyzed Recombination of Radical in Hydrogen Flames", *Combustion and Flame*, **19**, 227 (1972).

27. Muller III, C.H., Schofield, K., Steinberg, M., and Broida, H.P., "Sulfur Chemistry in Flames", *Seventeenth Symposium (International) on Combustion*, 867 (1978).

28. Kramlich, J.C., Malte, P.C., and Grosshandler, W.L., "The Reaction of Fuel-Sulfur in Hydrocarbon Combustion", *Eighteenth Symposium (International) on Combustion*. 151 (1981).

29. Smith, O.I., Wang, S., Tseregounis, S., and Westbrook, C.K., "The Sulfur Catalyzed Recombination of Atomic Oxygen in a $CO/O_2/Ar$ Flame", *Combustion Science and Technology*, **30**, 241 (1983).

30. Tseregounis, S.I., Smith, O.I., "An Experimental Investigation of Fuel Sulfur-Fuel Nitrogen Interactions in Low-Pressure Premixed Flames", *Twentieth Symposium (International) on Combustion,* 761 (1984).

31. Wendt, J.O.L., Wootan, E.C., and Corley, T.L., "Postflame Behavior of Nitrogenous Species in the Presence of Fuel Sulfur. I. Rich, Moist, $CO/Ar/O_2$ Flames", *Combustion and Flame*, **49**, 261 (1983).

32. Zachariah, M.R., and Smith, O.I., "Experimental and Numerical Studies of the Sulfur Chemistry in $H_2/O_2/SO_2$ Flames", *Combustion and Flame*, **69**, 125 (1987).

33. Pauwels, J.F., Carlier, M., Devolder, P., Sochet, L.R., "The Influence of Hydrogen Sulfide on the Combustion of Methanol in a Stoichiometric Premixed Flame. Experimental and Numerical Studies", *Combustion Science and Technology*, **86**, 237 (1992).

34. Glarborg, P., Kubel, D., and Dam-Johansen, K., "Impact of SO_2 and NO on CO Oxidation under Post-Flame Conditions", *International Journal of Chemical Kinetics*, **28**, 773 (1996).

35. Fenimore, C.P., "Two Modes of Interaction of NaOH and SO_2 in Gases from Fuel-Lean H_2-Air Flames", *Fourteenth Symposium (International) on Combustion*, 955 (1973).

36. Durie, R.A., Johnson, G.M., and Smith, M.Y., "Gas Phase Reactions of Sodium Species with Sulfur Species in Hydrocarbon Flames", *Fifteenth Symposium (International) on Combustion*, 1123 (1975).

37. Schofield, K., and Steinberg, M., "Sodium/Sulfur Chemical Behavior in Fuel-Rich and –Lean Flames", *Journal of Physical Chemistry*, **96**, 715 (1992).

Section 3

38. *Combustion Chemistry*, Gardiner, W.C., Ed., pp. 197-346, Springer-Verlag, New York (1984).

39. Bilger, R.W., Starner, S.H., and Kee, R.J., "In Reduced Mechanisms for Methane-Air Combustion in Nonpremixed Flames", *Combustion and Flame*, **80**, 135 (1990).

40. Padley, P.J. and Sugden, T.M., "Photometric Investigations of Alkali Metals in Hydrogen Flame Gases. IV. Thermal and Chemiluminescent Effects

Produced by Free Radicals", *Proceedings of the Royal Society, A*, **248**, 248 (1958).

41. Alkamade, C. Th. J., Hollander, Tj., Snelleman, W., and Zeegers, P.J. Th., *Metal Vapours in Flames*, A. Whitney & Co., Ltd., Exeter (1982).
42. Lucht, R.P., Peterson, R.C., and Laurendeau, N.M., "Fundementals of Absorption Spectroscopy for Selected Diatomic Flame Radicals", PURDU-CL-78-06 (1978).
43. Annino, R., and Driver, R., *Scientific and Engineering Applications With Personal Computers*, pp. 379-285, John Wiley & Sons Inc., New York (1986).
44. Mavrodineanu, R., and Boiteux, H., *Flame Spectroscopy*, John Wiley & Sons Inc., New York (1965).
45. Rabinovich, S., *Measurement Error: Theory and Practice*, American Institute of Physics, Woodbury, New York (1995).
46. Hornkohl, J., Personal Communication (1999).
47. Cattolica, R.J., "OH Radical Nonequilibrium in Methane-Air Flat Flames", *Combustion and Flame*. **44**, 43 (1982).
48. Schmidt , S.C, and Malte, P.C., "Spectroscopic Absorptance Measurements of OH in High-Intensity Continuous Hydrogen/Air and Methane/Air Combustion", *Journal of Quantitative Spectroscopy*. **16**, 963 (1976).
49. Winkleman, B.C., "Gas Temperature Measurements of Fluctuating Coal Fired MHD Plasmas Using Modified Line Reversal", PhD. Dissertation, University of Tennessee (1992).

Section 4

50. Lucht, K.C., and Muller, F. J., "Simultaneous Determination of Temperature and OH-Concentration in Flames Using High-Resolution Laser-Absorption Spectroscopy", *Journal Quantitative Spectroscopy and Radiative Transfer*, **17**, 403 (1977).

Section 5

51. Kee, R.J., Grcar, J.F., Smooke, M.D., and Miller, J.A., "A FORTRAN program for Modeling Steady Laminar One-Dimensional Premixed Flames", SAND85-8240 (1993).
52. Kee, R.J., Rupley, F.M., and Miller, J.A., "Chemkin-II: A FORTRAN Chemical Kinetics Package for the Analysis of Gas Phase Chemical Kinetics", SAND89-8009B (1989).
53. Kee, R.J., Dixon-Lewis, G., Warnatz, J., Coltrin, M.E., and Miller, J.A., "A Fortran Computer Code Package for the Evaluation of Gas-Phase Multicornponent Transport Properties", SAND86-8246 (1992).
54. Gardiner, W.C., *Rates and mechanisms of Chemical Reactions*, W.A. Benjamin, Inc., pp 111-149 (1972).
55. Troe,J., "Theory of Thermal Unimolecular Reactions at Low Pressures. II. Strong Collision Rate Constants. Applications", *Journal of Chemical Physics*, **66** (11), 4758 (1977).
56. Jensen, D.E., and Jones, G.E., "Kinetics of Flame Inhibition by Sodium", *Journal of the Chemical Society, Faraday Transactions I*, **72**, 2843 (1982).

57. Husain, D., and Plane, J.M.C., "Kinetic Investigation of the Third-Order Rate Processes between K + O_2 + M by Time-Resolved Atomic Resonance Absorption Spectroscopy", *Journal of the Chemical Society, Faraday Transactions 2*, **78**, 1175 (1982).

58. Husain, D., and Plane, J.M.C., "Kinetic Investigation of the Third-order Rate Processes between Na + O_2 + M by Time-resolved Atomic Resonance Absorption Spectroscopy", *Journal of the Chemical Society, Faraday Transactions 2*, **78**, 163 (1982).

59. McEwan, M.J., and Phillips, L.F., "Dissociation Energy of NaO_2*", *Transactions of the Faraday*, **62**, 1717 (1966).

60. Patrick, R., and Golden, D.M., "Termolecular Reactions of Alkali Metal Atoms with O_2 and OH", *International Journal of Chemical Kinetics*, **16**, 1567 (1984).

61. Schofield, K., Personal Communication (1999).

62. Husain, D., Plane, J.M.C., and Xiang, C.C., "A Direct Kinetic Study of the reaction K + OH + He $\rightarrow$ KOH + He by Time-Resolved Molecular Resonance-Fluorescence Spectroscopy, OH($A^2\Sigma^+$-$X^2\Pi$), Coupled with Steady Atomic Fluorescence Spectroscopy, K(5^2P_J-$4^2S_{1/2}$)", *Journal of the Chemical Society, Faraday Transactions 2.* **80**, 1465 (1984).

63. Husain, D., Lee, Y.H., and Marshall, P., "Temperature Dependence of the Absolute Third-Order Rate Constant for the Reaction between K + O_2 + N_2 over the Range 680-1010K Studied by Time-Resolved Atomic Resonance Absorption Spectroscopy", *Combustion and Flame*, **68**, 143 (1987).

64. Plane, J.M.C., Rajasekhar, B., and Bartolotti, L., "Kinetic Study of the Reaction K + O_2 + M (M=N_2, He) form 250 to 1103K", *Journal of Physical Chemistry*, **94**, 4161 (1990).

65. McBride, B.J., and Gordon, S., "Computer Program for Calculating and Fitting Thermodynamic Functions", NASA RP1271 (1992).

66. Ehlert, T.C., "Mass Spectrometric Investigations of the Oxides of Potassium", *High Temperature Science*, **9**, 237 (1972).

67. Farber, M., Srivastava, R.D., "Mass-Spectrometric Determination of the Thermodynamic Data for Potassium Compounds and Several Other Species Occurring in MHD Combustion Systems", *High Temperatures-High Pressures*, **20**, 119 (1988).

68. Woodward, J.R., Hayden, J.S., and Gole, J.L., "Formation and Characterization of a Low-Lying Electronic State of the Alkali Monoxides LiO...CsO in the Red and Near Infrared", *Chemical Physics*, **134**, 395 (1989).

69. Lamoreaux, R.H. and Hilderbrand, D. L., "High Temperature Vaporization Behavior of Oxides. I. Alkali Metal Binary Oxides", *Journal Physical Chemistry Reference Data*, **13** (1), 151 (1984).

70. Chase, Jr., M.W., Davies, C.A., Downey, Jr., J.R., Frurip, D.J., McDonald, R.A., and Syverud, A.N.,"JANAF Thermochemical Tables. Third Edition, Part II, Cr-Zr." *Journal of Physical Chemistry Reference Data*, **14**, Supplement No. 1 (1985).

71. Lee, E.P.F., Weight, T.G., and Dyke, J.M., "Calculated Dissociation Energies of the Alkali Metal Monoxides NaO and KO", *Molecular Physics*, **77** (3), (1992).

72. Schofield, K, "The Flame Chemistry of Alkali and Alkaline Earth Metals", in *Gas Phase metals Reactions*, A. Fontijn, ed., Elsevier Science Publishers, The Netherlands (1992).

73. Alberty, R.A. *Physical Chemistry*, John Wiley & Sons, New York (1987).

74. Andrews, A., "Matrix Reactions of K and Rb Atoms with Oxygen Molecules", *Journal of Chemical Physics*, **24** (11), (1971).

75. Smardzewski, R.R., Andrews, L., "Raman Spectra of the Products of Na and K Atom Argon Matrix Reactions with O_2 Molecules", *Journal Chemical Physics*, **47** (3), (1972).

76. Partridge, H., Bauschlicher, Jr., C.W., Sodupe, M., and Langhoff, S.R., "Theoretical Determination of the Alkali-Metal Superoxide Bond Energies", *Chemical Physics Letters*, **195** (2,3), (1992)

77. Trembaly, B., Manceron, L., Roy, P., LeQu`er`e, A., and Roy, D., "Vibrational Spectra and Structure of the KO_2 Complex in Solid Argon. A Far-Infrared Study.", *Chemical Physics Letters*, **228**, (1994).

78. Lee, E.P.F., and Wright, T., " A Study of the X^2A_2 State of KO_2 Using Ab Initio and Density Functional Theory: The Equilibrium Geometry and Vibrational Frequencies", *Journal of Physical Chemistry A*, **102**, (1998).

79. Gurvich, L.V., Bergman, G.A., Gorokov, L.N., Iorish, V.S., Leonidov, V. Ya., and Yungman, V.S., "Thermodynamic Properties of Alkali Metal Hydroxides.

Part I. Lithium and Sodium Hydroxides", *Journal Physical and Chemical Reference Data*, **25** (4), 1211 (1996).

80. Gurvich, L.V., Bergman, G.A., Gorokov, L.N., Iorish, V.S., Leonidov, V. Ya., and Yungman, V.S., "Thermodynamic properties of alkali metal hydroxides. Part II. Potassium, Rubidium, and Cesium", *Journal Physical and Chemical Reference Data*, **26** (4), 1031 (1997).
81. Warnatz, J., Bockhorn, H., Moser, A., Wenz, W.H., "Experimental Investigation and Computational Simulation Acetylene-Oxygen Flames from Near Stoichiometric to Sooting Conditions", *Eighteenth Symposium (International) on Combustion*, 197 (1982).
82. Bowman, C.T., Hanson, R.K., Davidson, D.F., Gardiner, Jr. W.C., Lissianski, V., Smith, G.P., Golden, D.M., Frenklach, M., and Goldenberg, M., http://www.me.berkeley.edu/gri_mech/
83. Baulch, D.L., Cobos, C.J., Cox, R.A., Frank, P., Hayman, G., Just, Th., Kerr, J.A., Murrells, T., Pilling, J., Troe, J., Walker, R.W., and Warnatz, J., "Evaluated Rate Data for Combustion Modeling. Supplement 1", *Journal Physical and Chemical Reference Data*, **23** (6), 847 (1994).
84. Indritz, D., Maday, M., Sheinson, and Shaub, W., "Construction of Large Reaction Mechanisms", *NRL Report 8498*, (1981).
85. *Combustion Chemistry*, Gardiner, W.C. Ed., pp. 128-138, Springer-Verlag, New York (1984).
86. Vincenti, W.G., and Kruger, C.H., *Introduction to Physical Gas Dynamics*, pp. 210-216, Krieger Publishing, Malabar (1982).

87. Wheeler, R., "On Radical Recombination Rates in SO_2-Doped Flames", *Journal of Physical Chemistry*, **72** (9), 3359 (1968).

88. Binns, D., and Marshall, P., "An *ab initio* Study of the Reaction of Atomic Hydrogen with Sulfur Dioxide", *Journal of Chemical Physics*, **95** (7), 4940 (1991).

89. Laasko, D., Smith, C.E., Goumri, A., Rocha, J., R., Marshall, P., "Theoretical Studies of the RSOO, ROSO, RSO2, and HOOS (R=H,CH3) Radicals", *Chemical Physics Letters*, **227** 377 (1994).

90. Laasko, D., Smith, C.E., Goumri, A., Rocha, J.-D.R., Marshall, P., "Erratum: Theoretical Studies of the RSOO, ROSO, RSO2, and HOOS (R=H,CH3) Radicals", *Chemical Physics Letters*, **231** 123 (1994).

91. Goumri, A., Rocha, J.R., Laasko, D., Smith, C.E., Marshall, P., "Characterization of the Reaction Pathways on the Potential Energy Surfaces for H + SO_2 and HS + O_2", *To be published* (1999).

92. Atkinson, R., Baulch, D.L., Cox, R.A., Hampson, Jr., R.F., Kerr, J.A., Rossi, M.J., and Troe, J., "Evaluated Kinetic and Photochemical Data for Atmospheric Chemistry: Supplement VI", *Journal of Physical and Chemical Reference Data*", **26** (6) 1329 (1997).

93. Astholz, D.C., Glanzer, K., and Troe, J., "The spin forbidden dissociation-recombination reaction $SO_3 \Leftrightarrow SO_2 + O$", *Journal of Chemical Physics*, **70** (5), 2409 (1979).

94. Herzberg, G., *Spectra of Diatomic Molecules*, D. Van Nostrand Company, Inc, Second Edition, Eighth Printing, Eq. (VIII,2), pg. 457 (1963).

95. Alberty, R.A. *Physical Chemistry*, John Wiley & Sons, p. 246, New York (1987).

96. Partridge, H., Langhoff, S.R., and Bauschlicher, C.W., "Theoretical Study of the Alkali and Alkaline-Earth Monosulfides", *Journal of Chemical Physics*, **88** (10), 6431 (1988).

97. Moran, S., and Ellison, G.B., "Photoelectron Spectroscopy of Sulfur Ions", *Journal of Physical Chemistry*, **92**, 1794 (1988).

98. Heinemann, C., Koch, W., Lindner, G.G., and Reinen, D., "Electronic Spectrum of S_2^-, The Electron Affinity of S_2, and the Binding Energies of Neutral and Anionic S_3 Clusters", *Physical Review A*, **52**, 1024 (1995).

99. Herzberg, G., *Infrared and Raman Spectra*, D. Van Nostrand Company, Inc., Eq. (VIII,2), pg. 169 (1945).

100. Gruebele, M., Polak, M., and Saykally, R.J., "Velocity Modulation Laser Spectroscopy of Negative Ions: The Infrared Spectrum of Hydrosulfide (SH^-)", *Journal of Chemical Physics*, **86**, 1698 (1987).

101. Herzberg, G., *Infrared and Raman Spectra*, D. Van Nostrand Company, Inc., 1945, Eq. (VIII,2), pg. 173

102. Jin, S., and Schaefer III, F., "NaSO $\rightarrow$ NaOS Potential Energy Hypersurface", *Journal of Chemical Physics*, **93** (3) 1799 (1990).

103. Polak, M.L., Fiala, B.L., Ervin, K.M., and Lineberger, W.C., "Ultraviolet Photoelectron Spectrum of SO^{-*}", *Journal of Chemical Physics*, **94**(10) 6926 (1991).

104. Goumri, A., Laasko, D., Rocha, J.R., Francis, E., and Marshall, P., "Investigation of the Gas-Phase Kinetics of the Reaction K + SO_2 + Ar", *Journal of Physical Chemistry*, **97**, 5295 (1993).

105. Adrian, F.J., Cochran, E.I., and Bowers, V.A., "ESR Spectra and Structures of $NaSO_2$ and NaO_2", *Journal of Chemical Physics*, **59**(1) 56 (1973).

106. Nimlos, M., and Ellison, G.B., "Photoelectron Spectroscopy of SO_2^-, S_3^-, and S_2O^-", *Journal of Physical Chemistry*, **90**, 2574 (1986).

Section 6

107. Radhakrishnan, K., "LSENS- A General Chemical Kinetics and Sensitivity Analysis Code for Homogeneous Gas-Phase Reactions. I. Theory and Numerical Solution Procedures", NASA RP-1328, (1994).

108. Radhakrishnan, K., and Bittker, D., "LSENS- A General Chemical Kinetics and Sensitivity Analysis Code for Homogeneous Gas-Phase Reactions. I. Code Description and Usage", NASA RP-1329, (1994).

109. McBride, B.J., and Gordon, S., "Computer Program for Calculation of Complex Chemical Equilibrium Compositions and Applications. II. Users Manual and Program Description", NASA RP-1311 (1996).

APPENDICES

Appendix A

Table A-1 Summary of reactions used in kinetic calculations. Rate expressions are given in the form $k_i = A_i T^{\beta_i} e^{(-E_{a,i}/RT)}$. For bimolecular reactions, units are (cm^3/mole/s). For termolecular reactions, units are (cm^6/$mole^2$/s). Activation Energy, E_a is cal/mole. ⇒ means one-way reaction, ⇔ means reversible reaction with reverse rate specified by the equilibrium constant.

Number	Reaction	A	β	E_a	Ref.
1	$K + O_2 + M \Leftrightarrow KO_2 + M$	7.25E+23	-2.00	712	[64]
2	$K + OH + M \Leftrightarrow KOH + M$	4.64E+21	-1.28	0	[62]
3	$K + HO_2 \Leftrightarrow KO_2 + H$	1.00E+10	0.5	0	*Est.*
4	$K + HO_2 \Leftrightarrow KOH + O$	6.13E+11	0.5	0	*Est.*
5	$KO_2 + H \Leftrightarrow KOH + O$	1.00E+11	0.5	0	*Est.*
6	$KO_2 + O \Leftrightarrow KO + O_2$	4.00E+11	0.5	0	*Est.*
7	$KO_2 + OH \Leftrightarrow KOH + O_2$	1.00E+11	0.5	0	*Est.*
8	$KO + H \Leftrightarrow K + OH$	6.40E+10	0.5	0	*Est.*
9	$KO + O \Leftrightarrow K + O_2$	4.22E+11	0.5	0	*Est.*
10	$K + HO_2 \Leftrightarrow KO + H$	9.66E+11	0.5	0	*Est.*
11	$KO_2 + H \Leftrightarrow KO + OH$	1.06E+11	0.5	0	*Est.*
12	$KO + OH \Leftrightarrow KOH + O$	8.21E+10	0.5	0	*Est.*
13	$KO + H_2 \Leftrightarrow KOH + H$	2.24E+12	0.5	0	*Est.*
14	$KO + HO_2 \Leftrightarrow KO_2 + OH$	8.02E+11	0.5	0	*Est.*
15	$KO + HO_2 \Leftrightarrow KOH + O_2$	8.02E+12	0.5	0	*Est.*
16	$KOH + H \Leftrightarrow K + H_2O$	1.00E+11	0.5	0	*Est.*
17	$KOH + OH \Leftrightarrow KO + H_2O$	2.02E+12	0.5	0	*Est.*
18	$H_2S + M \Leftrightarrow SH + H + M$	2.00E+14	0	76600	[32]
19	$H_2S + H \Leftrightarrow SH + H_2$	1.08E+13	0	2980	[32]
20	$H_2S + O \Leftrightarrow SH + OH$	4.36E+12	0	3322	[32]
21	$OH + H_2S \Leftrightarrow H_2O + SH$	1.39E+13	0	882.6	[32]
22	$SH + SH \Leftrightarrow H_2S + S$	1.00E+14	0	1430	[32]
23	$SH + H \Leftrightarrow H_2 + S$	5.16E+14	0	2100	[32]
24	$SH + O \Leftrightarrow SO + H$	3.56E+14	0	642	[32]
25	$SH + O \Leftrightarrow S + OH$	6.31E+11	0.5	8060	[32]
26	$SH + S \Leftrightarrow S_2 + H$	1.40E+13	0	478	[32]
27	$S + O_2 \Leftrightarrow SO + O$	7.94E+10	0.5	0	[32]
28	$S + OH \Leftrightarrow SO + H$	7.20E+13	0	642	[32]

Table A-1 (continued)

Number	Reaction	A	β	E_a	Ref.
29	$S_2+O \Leftrightarrow SO+S$	6.30E+11	0.5	0	[32]
30	$S+S+M \Leftrightarrow S_2+M$	1.00E+18	-1	0	[32]
31	$SO+O_2 \Leftrightarrow SO_2+O$	3.60E+11	0	5600	[32]
32	$SO+OH \Leftrightarrow SO_2+H$	1.80E+13	0	0	[32]
33	$SO+O+M \Leftrightarrow SO_2+M$	1.20E+22	-1.8	0	[32]
34	$H+SO_2+M \Leftrightarrow HOSO+M$	7.30E+16	0	0	[32]
35	$OH+SO+M \Leftrightarrow HOSO+M$	7.00E+16	0	0	[32]
36	$H+HOSO \Leftrightarrow SO_2+H_2$	4.00E+12	0	0	[32]
37	$OH+HOSO \Leftrightarrow SO_2+H_2O$	6.80E+13	0	1772	[32]
38	$O_2+HOSO=SO_2+HO_2$	1.00E+12	0	1000	[32]
39	$SO+SO \Leftrightarrow SO_2+S$	3.30E+11	0	2250	[32]
40	$H+SO_3 \Leftrightarrow OH+SO_2$	1.81E+13	0	0	[32]
41	$S+SO_3 \Leftrightarrow SO+SO_2$	1.20E+12	0	0	[32]
42	$SO+SO_3 \Leftrightarrow SO_2+SO_2$	4.22E+12	0	0	[32]
43	$SO_2+O+M \Leftrightarrow SO_3+M$	3.99E+28	-4	5256	[32]
44	$O+SO_3 \Leftrightarrow O_2+SO_2$	4.40E+11	0	6100	[32]
45	$K+S+M \Leftrightarrow KS+M$	5.80E+23	-2	0	*Est.*
46	$K+SH+M \Leftrightarrow KSH+M$	1.65E+20	-1	0	*Est.*
47	$K+SO+M \Leftrightarrow KOS+M$	1.00E+23	-2	0	*Est.*
48	$K+SO_2+M \Leftrightarrow KSO_2+M$	7.00E+23	-2	0	*Est.*
49	$K+S_2+M \Leftrightarrow KS_2+M$	1.00E+23	-2	0	*Est.*
50	$KOS+OH \Leftrightarrow KOH+SO$	1.00E+11	0.5	0	*Est.*
51	$KOH+S \Leftrightarrow KOS+H$	4.00E+07	0.5	0	*Est.*
52	$KSO_2+O \Leftrightarrow KO+SO_2$	1.00E+11	0.5	0	*Est.*
53	$KSO_2+OH \Leftrightarrow KOH+SO_2$	2.00E+12	0.5	0	*Est.*
54	$KSO_2+O_2 \Leftrightarrow KO_2+SO_2$	1.00E+11	0.5	0	*Est.*
55	$KS+H \Leftrightarrow K+SH$	6.40E+10	0.5	0	*Est.*
56	$KS+OH \Leftrightarrow KOH+S$	8.21E+10	0.5	0	*Est.*
57	$KSH+H \Leftrightarrow K+H_2S$	1.00E+11	0.5	0	*Est.*
58	$KSH+OH \Leftrightarrow KOH+SH$	9.82E+12	0.5	0	*Est.*
59	$KS+S \Leftrightarrow K+S_2$	4.22E+11	0.5	0	*Est.*
60	$KS_2+OH \Leftrightarrow KOH+S_2$	1.00E+11	0.5	0	*Est.*
61	$KSO_2+SO \Leftrightarrow KOS+SO_2$	1.00E+13	0.5	0	*Est.*
62	$KS_2+SO \Leftrightarrow KOS+S_2$	7.85E+12	0.5	0	*Est.*
63	$KSH+SO \Leftrightarrow KOS+SH$	7.70E+06	0.5	0	*Est.*
64	$KS+SO \Leftrightarrow KOS+S$	2.20E+08	0.5	0	*Est.*
65	$KSO_2+S \Leftrightarrow KS+SO_2$	9.17E+11	0.5	0	*Est.*
66	$KS_2+SO_2 \Leftrightarrow KSO_2+S_2$	7.66E+12	0.5	0	*Est.*
67	$KSO_2+SH \Leftrightarrow KSH+SO_2$	9.20E+12	0.5	0	*Est.*
68	$KS_2+H \Leftrightarrow KS+SH$	1.06E+11	0.5	0	*Est.*

Table A-1 (continued)

Number	Reaction	A	β	E_a	
69	$KS_2+S \Leftrightarrow KS+S_2$	4.00E+11	0.5	0	*Est.*
71	$KO_2+S \Leftrightarrow KS+O_2$	4.00E+11	0.5	0	*Est.*
72	$KO_2 + SH \Leftrightarrow KSH+O_2$	1.00E+11	0.5	0	*Est.*
73	$KO+ S \Leftrightarrow K+SO$	4.22E+11	0.5	0	*Est.*
74	$KO+ SO \Leftrightarrow K+SO_2$	1.80E+10	0	0	*Est.*
75	$KS+ O \Leftrightarrow K+SO$	8.82E+12	0.5	0	*Est.*
76	$KS+ O \Leftrightarrow KO+S$	8.30E+10	0.5	0	*Est.*
77	$KS+ SH \Leftrightarrow KSH S$	8.21E+10	0.5	0	*Est.*
78	$KS_2+ O \Leftrightarrow KO+S_2$	4.00E+11	0.5	0	*Est.*
79	$KS_2+ O_2 \Leftrightarrow KO_2+S_2$	7.93E+11	0.5	0	*Est.*
80	$KSH+ H \Leftrightarrow KS+H_2$	5.60E+10	0.5	0	*Est.*
81	$KSH+ O \Leftrightarrow KO+SH$	2.80E+09	0.5	0	*Est.*
82	$KSH+ O \Leftrightarrow KS+OH$	2.80E+09	0.5	0	*Est.*
83	$KSH+ OH \Leftrightarrow KS+H_2O$	9.82E+11	0.5	0	*Est.*
84	$KSH+ SH \Leftrightarrow KS+H_2S$	1.03E+12	0.5	0	*Est.*
85	$KOS+ O \Leftrightarrow K+SO_2$	1.00E+12	0.5	0	*Est.*
86	$KOS+ O \Leftrightarrow KO+SO$	4.00E+11	0.5	0	*Est.*
87	$H_2+OH \Rightarrow H_2O+H$	1.00E+08	1.6	3330	[81]
88	$H_2O+H \Rightarrow H_2+OH$	4.60E+08	1.6	18560	[81]
89	$OH+OH \Rightarrow H_2O+O$	1.50E+09	1.1	0	[81]
90	$H_2O+O \Rightarrow OH+OH$	1.50E+10	1.1	17240	[81]
91	$H+H+M \Leftrightarrow H_2+M^1$	1.80E+18	-1.0	0	[81]
92	$H+OH+M \Leftrightarrow H_2O+M^1$	2.20E+22	-2.0	0	[81]
93	$H+O_2+M \Leftrightarrow HO_2+M^1$	2.00E+18	-0.8	0	[81]
94	$HO_2+H \Leftrightarrow OH+OH$	1.50E+14	0.0	1000	[81]
95	$HO_2+H \Leftrightarrow H_2+O_2$	2.50E+13	0.0	690	[81]
96	$HO_2+O \Leftrightarrow OH+O_2$	2.00E+13	0.0	0	[81]
97	$HO_2+OH \Leftrightarrow H_2O+O_2$	2.00E+13	0.0	0	[81]
98	$CO+OH \Leftrightarrow CO_2+H$	6.32E+06	1.5	-497	[81]
99	$CH_3+H(+M) \Leftrightarrow CH_4(+M)$	6.00E+16	-1.0	0	[81]
	Low Pressure[2]	8.00E+26	-3.0	0	[81]
100	$CH_4+H \Rightarrow CH_3+H_2$	2.20E+04	3.0	8740	[81]
101	$CH_3+H_2 \Rightarrow CH_4+H_2$	6.60E+02	3.0	7740	[81]
102	$CH_4+O \Rightarrow CH_3+OH$	1.20E+07	2.1	7630	[81]
103	$CH_3+OH \Rightarrow CH_4+O$	1.30E+05	2.1	4680	[81]
104	$CH_4+OH \Rightarrow CH_3+H_2O$	1.60E+06	2.1	2460	[81]
105	$CH_3+H_2O \Rightarrow CH_4+OH$	2.90E+05	2.1	16790	[81]
106	$CH_3+O \Leftrightarrow CH_2O+H$	8.43E+13	0.0	0	[81]
107	$CH_2O+H \Leftrightarrow HCO+H_2$	2.50E+13	0.0	3990	[81]
108	$CH_2O+O \Leftrightarrow HCO+OH$	3.50E+13	0.0	3510	[81]

Table A-1 (continued)

Number	Reaction	A	β	E_a	
109	$CH_2O+OH \Leftrightarrow HCO+H_2O$	3.00E+13	0.0	1190	[81]
110	$HCO+H \Leftrightarrow CO+H_2$	2.00E+14	0.0	0	[81]
111	$HCO+O \Leftrightarrow CO+OH$	3.00E+13	0.0	0	[81]
112	$HCO+OH \Leftrightarrow CO+H_2O$	5.00E+13	0.0	0	[81]
113	$HCO+O_2 \Leftrightarrow CO+HO_2$	3.00E+12	0.0	0	[81]
114	$HCO+M \Rightarrow CO+H+M$[1]	1.57E+14	0.0	15760	[81]
115	$H+CO+M \Rightarrow HCO+M$[1]	1.92E+14	0.0	735	[81]
116	$CH_2+H \Leftrightarrow CH+H_2$	4.00E+13	0.0	0	[81]
117	$CH_2+O \Leftrightarrow CO+H+H$	5.00E+13	0.0	0	[81]
118	$CH_2+O_2 \Leftrightarrow CO_2+H+H$	1.30E+13	0.0	1500	[81]
119	$CH+O \Leftrightarrow CO+H$	4.00E+13	0.0	0	[81]
120	$CH+O_2 \Leftrightarrow CO+OH$	2.00E+13	0.0	0	[81]

[1] Third body efficiencies relative to N_2 are $H_2 = 1.0$, $O_2 = 0.4$, $H_2O = 6.5$, $CO_2 = 1.5$, $CO = 0.75$

[2] Lindemann form of the reaction rate for pressure-dependant reactions, see Gardiner [54].

Appendix B

Flowmeter Calibration

The flowmeters were individually calibrated using a bubble flowmeter. The bubble flow meter was a secondary standard used by the UTSI chemistry lab. The bubble meter is a vertical glass tube of precisely graduated volume. To calibrate each of the rotometers, regulated gas (CH_4, O_2, or N_2) was supplied to the flowmeter. The gas leaving the flowmeter then passed through the bubble meter. The bubble meter provided a means of introducing a bubble solution into the gas stream, causing a thin film to form across the cross-section of the calibration section (the vertical tube) of the bubble meter. As the gas flows, the film propagates upward along the calibration section. The flow rate is determined by the time required for the film to sweep out the known volume of the calibration section. Calibration sections were available in three volume ranges.

The schematic for the calibration setup is shown in Figure B-1. Regulated gas was supplied to the flowmeter at the pressure to be used in the experiment. The control valve on the flowmeter was set so that the float was located at the desired graduation. Liquid bubble solution was admitted to the stream by compressing the bulb and forcing bubble solution into the gas stream. The bubble film was visually tracked into the uniform, graduated section of the bubble meter. At a pre-selected graduation, a stopwatch was started. When the bubble swept the desired volume, the stopwatch was stopped and the elapsed time recorded. For

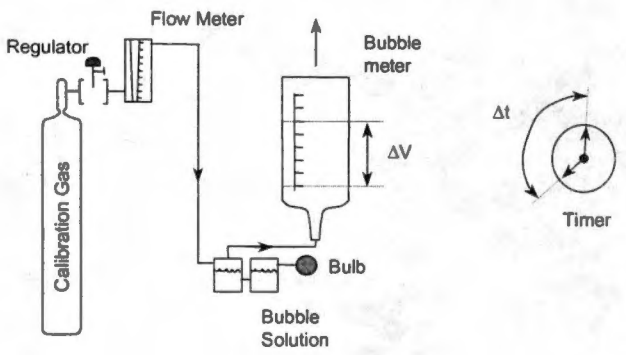

Figure B-1. Flowmeter calibration schematic.

each flow rate setting, the calibration volume was selected so that the volume would be swept in about 10 seconds. Ten or thirty samples were gathered at each calibration point. The calibration data are recorded in Tables B-1 through B-4. At the top of each table, the calibration graduations and volumes are shown. The recorded elapsed times are then tabulated for each sample. Finally, the mean and standard deviation of the elapsed time is tabulated, followed by the volumetric flow rate at ambient pressure and temperature.

Two corrections were applied to the measured flowrates:

1. Correction for Presence of Water Vapor. The bubble solution is predominately water; thus the slug of gas passing through the bubble solution

Table B-1 Calibration data for N_2 flowmeter.

Scale Position (mm)	40	50	60	80	100	120
Bubble Meter Volume (cc)	600	800	800	900	1000	1000
Sample	Time (s)	Time (s)	Time (s)	Time (s)	Time (s)	Time (s)
1	7.90	8.71	7.56	6.56	6.21	5.50
2	7.84	8.75	7.46	6.56	6.15	5.56
3	7.87	8.75	7.46	6.46	6.15	5.53
4	7.93	8.78	7.43	6.59	6.15	5.50
5	7.87	8.84	7.53	6.53	6.18	5.50
6	7.81	8.71	7.31	6.62	6.15	5.50
7	7.84	8.78	7.56	6.56	6.18	
8	7.90	8.81	7.46	6.59	6.21	
9	7.93	8.78	7.46	6.53	6.18	
10	7.84	8.78	7.50	6.59	6.09	
11		8.68	7.53	6.62	6.15	
12		8.71	7.53	6.50	6.21	
13		8.75	7.46	6.56	6.21	
14		8.78	7.50	6.59	6.03	
15		8.78	7.43	6.62	6.18	
16		8.71	7.56	6.65	6.21	
17		8.78	7.50	6.59	6.15	
18		8.81	7.43	6.59	6.09	
19		8.81	7.59	6.56	6.21	
20		8.81	7.46	6.68	6.21	
21		8.78	7.50	6.59	6.25	
22		8.78	7.53	6.65	6.21	
23		8.81	7.50	6.65	6.15	
24		8.84	7.50	6.62	6.25	
25		8.78	7.53	6.59	6.21	
26		8.78	7.53	6.62	6.15	
27		8.75	7.46	6.59	6.18	
28		8.68	7.59	6.62	6.18	
29		8.78	7.59	6.62	6.25	
30		8.75	7.50	6.59	6.18	
Mean, μ (s)	7.873	8.768	7.4983	6.5897	6.1770	5.5150
Standard Deviation, σ (s)	0.0411	0.04213	0.05943	0.04620	0.04858	0.02510
Q (lpm)	4572.6	5474.5	6401.4	8194.7	9713.5	10879.5
Q_{SLPM} (lpm)	4309.03	5158.91	6032.45	7722.32	9153.58	10252.34

Table B-2 Calibration data for O_2 flowmeter.

Scale Position (mm)	20	40	60	80	100	120	140	150
Bubble Meter Volume (cc)	300	400	600	700	800	800	800	800
Sample	Time (s)	Time (s)	Time (s)	Time (s)	Time (s)	Time (s)	Time (s)	Time (s)
1	13.84	10.84	11.71	10.81	10.21	8.96	7.96	7.25
2	13.96	10.90	11.75	10.77	10.12	9.06	7.87	7.43
3	13.84	10.84	11.81	10.81	10.18	9.03	7.87	7.28
4	13.87	10.87	11.65	10.87	10.06	9.03	7.90	7.37
5	13.90	10.81	11.68	10.81	10.18	8.96	7.81	7.31
6	13.81	10.90	11.71	10.78	10.25	9.09	7.81	7.28
7	13.84	10.90	11.68	10.87	10.21	9.06	7.90	7.31
8	13.81	10.81	11.62	10.78	10.15	9.06	7.93	7.37
9	13.93	10.81	11.68	10.75	10.12	9.06	7.87	7.37
10	13.87	10.81	11.68	10.75	10.21	9.09	8.00	7.28
11			11.68	10.84	10.15	8.96	7.81	7.37
12			11.78	10.71	10.18	8.96	7.90	7.4
13			11.81	10.68	10.25	9.09	8.00	7.28
14			11.68	10.81	10.18	9.00	7.84	7.28
15			11.68	10.9	10.15	8.96	7.96	7.37
16			11.71	10.71	10.21	9.00	7.90	7.34
17			11.62	10.71	10.21	8.93	7.81	7.34
18			11.65	10.87	10.09	9.03	7.90	7.46
19			11.81	10.84	10.15	9.03	7.90	7.28
20			11.78	10.78	10.21	9.03	7.96	7.31
21			11.71	10.78	10.15	8.96	7.93	7.34
22			11.75	10.78	10.25	9.09	7.90	7.31
23			11.75	10.81	10.21	9.00	7.84	7.28
24			11.68	10.75	10.15	9.00	7.90	7.34
25			11.65	10.78	10.18	8.93	7.96	7.37
26			11.71	10.75	10.25	9.03	7.87	7.4
27			11.71	10.68	10.15	9.12	7.84	7.34
28			11.71	10.78	10.25	9.03	7.93	7.37
29			11.68	10.81	10.18	8.96	7.87	7.31
30			11.81	10.78	10.28	9.06	7.90	7.43
Mean, μ (s)	13.867	10.849	11.711	10.785	10.184	9.019	7.895	7.339
Standard Deviation, σ (s)	0.0499	0.0401	0.0556	0.0553	0.0513	0.0529	0.0538	0.0531
Q (lpm)	1298.05	2212.19	3074.03	3894.30	4713.28	5322.10	6080.05	6540.40
Q_{SLPM} (lpm)	1268.93	2162.57	3005.08	3806.08	4607.56	5202.72	5943.68	6393.70

Table B-3 Calibration data for CH_4 flowmeter.

Scale Position (mm)	20	40	60	80	100	120
Bubble Meter Volume (cc)	100	200	300	300	300	400
Sample	Time (s)	Time (s)	Time (s)	Time (s)	Time (s)	Time (s)
1	13.62	15.12	16.59	12.62	10.56	12.06
2	13.53	15.53	16.43	12.59	10.50	12
3	13.50	15.59	16.50	12.65	10.37	12.09
4	13.43	15.50	16.34	12.56	10.53	12
5	13.56	15.28	16.34	12.62	10.37	12.03
6	13.40	15.28	16.31	12.78	10.43	12.03
7	13.53	15.37	16.28	12.65	10.56	12.06
8	13.59	15.12	16.25	12.62	10.50	12.09
9	13.56	15.43	16.43	12.59	10.50	12.12
10	13.56	15.25	16.50	12.56	10.62	12.09
11			16.25	12.71	10.53	12.09
12			16.25	12.59	10.50	12.09
13			16.56	12.68	10.62	12.15
14			16.62	12.62	10.46	12
15			16.40	12.53	10.62	12.03
16			16.50	12.71	10.62	12.03
17			16.31	12.62	10.46	12.09
18			16.56	12.53	10.50	12.12
19			16.46	12.80	10.53	12.09
20			16.50	12.65	10.59	12.12
21			16.62	12.62	10.59	12.03
22			16.28	12.56	10.65	12.09
23			16.34	12.62	10.68	12.15
24			16.53	12.71	10.62	12.12
25			16.43	12.56	10.65	12.12
26			16.43	12.56	10.65	12.03
27			16.50	12.50	10.65	12.18
28			16.34	12.65	10.62	12.06
29			16.28	12.68	10.59	12.03
30			16.18	12.71	10.59	12.15
Mean, μ (s)	13.528	15.347	16.410	12.628	10.555	12.078
Standard Deviation, σ (s)	0.0684	0.165	0.124	0.072	0.083	0.050
Q (lpm)	443.52	781.91	1096.87	1425.37	1705.30	1987.08
Q_{SLPM} (lpm)	431.25	760.27	1066.50	1385.91	1658.09	1932.07

Table B-4 Calibration data for H_2S (using N_2).

Scale Position (mm)	20	40	60	80	100	120	140	150
Bubble Meter Volume (cc)	10	10	20	30	40	50	60	70
Sample	Time (s)	Time (s)	Time (s)	Time (s)	Time (s)	Time (s)	Time (s)	Time (s)
1	19.18	9.21	10.78	10.46	10.15	9.93	9.93	10.53
2	19.28	9.18	10.75	10.50	10.15	10.06	9.90	10.59
3	19.37	9.12	10.71	10.43	10.12	9.90	9.87	10.59
4	19.50	9.18	10.75	10.50	10.15	10.00	9.84	10.62
5	19.46	9.12	10.75	10.43	10.15	9.90	9.75	10.56
6	19.40	9.06	10.65	10.37	10.15	9.90	9.75	10.59
7	19.50	9.21	10.81	10.50	10.12	9.96	9.84	10.56
8	19.53	9.28	10.65	10.50	10.09	9.93	9.87	10.59
9	19.40	9.15	10.68	10.43	10.18	10.00	9.78	10.65
10	19.43	9.21	10.71	10.37	10.09	9.96	9.87	10.62
11			10.68	10.50	10.12	10.00	9.81	10.56
12			10.78	10.53	10.18	10.03	9.84	10.56
13			10.62	10.53	10.12	9.93	9.87	10.59
14			10.71	10.43	10.18	9.96	9.84	10.62
15			10.59	10.37	10.15	9.90	9.87	10.53
16			10.65	10.43	10.15	9.96	9.87	10.62
17			10.68	10.40	10.15	9.93	9.84	10.65
18			10.81	10.37	10.15	9.93	9.87	10.65
19			10.62	10.43	10.09	9.93	9.87	10.62
20			10.78	10.40	10.15	9.93	9.87	10.65
21			10.71	10.50	10.12	10.03	9.81	10.62
22			10.68	10.43	10.15	9.90	9.84	10.65
23			10.59	10.43	10.18	10.03	9.90	10.62
24			10.56	10.40	10.18	9.93	9.90	10.59
25			10.62	10.40	10.18	9.93	9.90	10.59
26			10.68	10.43	10.18	10.03	9.90	10.59
27			10.65	10.46	10.12	9.90	9.87	10.65
28			10.75	10.40	10.15	10.03	9.87	10.68
29			10.59	10.40	10.21	10.00	9.93	10.71
30			10.81	10.50	10.21	9.96	9.84	10.59
Mean, μ (s)	19.405	9.172	10.693	10.441	10.149	9.9593	9.857	10.608
Standard Deviation, σ (s)	0.1079	0.0619	0.0723	0.0499	0.0319	0.0493	0.0443	0.0421
Q (lpm)	30.92	65.42	112.22	172.40	236.48	301.23	365.22	395.93
Q_{SLPM} (lpm)	29.79	63.03	108.13	166.12	227.87	29026	351.93	381.51
Q_{SLPM} (lpm) Density Corrected	27.04	57.20	98.13	150.75	206.79	263.40	319.37	346.22

becomes saturated with water vapor. The additional gas adds to the measured volumetric flowrate and must be numerically removed from the volumetric flowrate calculated.

2. Correction to Standard Conditions. The volumetric flowrate at a given scale position will depend on the ambient temperature and pressure. The utility of the calibration is increased by correcting the measured flowrate (Q) to a standard state (Q_{SLPM} – Standard liters per minute). The standard state is 1atm and 298.16K. Thus the calibration results in Q_{SLPM} v. scale position.

To correct for the presence of water vapor, the partial pressure of water (P_{v,H_2O}) as a function of temperature was taken from the table of [B-1]. The measured ambient pressure was reduced by P_{v,H_2O} before correction to standard conditions. Correction to standard conditions, including the correction for water vapor was given by the equation:

$$Q_{SLPM} = Q\frac{\left(P - P_{v,H_2O}\right)}{P_{REF}}\frac{T_{REF}}{T}. \qquad \text{(B.1)}$$

Since the H_2S meter could not be safely calibrated using H_2S, this meter was calibrated using N_2. This calibration was corrected for the difference in the densities based on the equation for rotometer flowrate given in reference [B-2]. The volumetric flowrate through a rotometer is given by

$$Q = CA\sqrt{\frac{2gV_f(\rho_f - \rho)}{A_f\rho}}, \qquad \text{(B.2)}$$

where

CA = a constant for the flowmeter

V_f = volume of the float

A_f = cross sectional area of the float

ρ_f = density of the float

ρ = density of the fluid

For any fluid, the parameters CA, V_f, A_f, and ρ_f are constant. When the flowmeter is operated with a second fluid, the ratio of volumetric flowrates when the float is at the same scale position would be

$$\frac{Q_2}{Q_1} = \sqrt{\left(\frac{\rho_f - \rho_2}{\rho_2}\right) \Big/ \left(\frac{\rho_f - \rho_1}{\rho_1}\right)}. \qquad \text{(B.3)}$$

For gases, $\rho_f >> \rho$ so this ratio is approximately.

$$\frac{Q_2}{Q_1} = \sqrt{\frac{\rho_1}{\rho_2}}. \qquad \text{(B.4)}$$

For perfect gases at the same temperature ,

$$\frac{Q_2}{Q_1} = \sqrt{\frac{W_1}{W_2}}, \qquad \text{(B.5)}$$

where W is the molecular weight. This correction was used for the H_2S calibration.

The uncertainty in the flowmeter readings was estimated from the random uncertainty of the bubble meter measurements. Uncertainty contributions from the measurement errors in ambient temperature and pressure are negligible.

The 3σ-level of uncertainty from the bubble meter readings was approximately +/-2%. The uncertainty for the H_2S meter is higher due to the density correction. This error was estimated to be +/-5%.

A second order polynomial curvefit, determined by the algorithm specified in reference [B-3], was used to fit the calibration data for each flowmeter. These curve fits were used to set the flowmeter positions during the test and to establish flowrate inputs to the kinetics model applied to the laboratory burner flame experiments. The final results for each flowmeter are shown in Figures B-2 through B-5. Note that in the case of H_2S, only the low range data (scale position 20 – 100 mm) were used to determine the curve fit coefficients.

Nebulizer Calibration

The nebulizer was calibrated using the trapping method. The trapping method was discussed by Alkamade [B-4]. Alkamade suggested seeding the salt to be nebulized with a radioactive tracer, then trapping the nebulized salt in a filter and determining the quantity of tracer trapped in the filter. In the method employed here, a disposable filter unit (0.1μm, Dalston BQ) was used to trap the liquid droplets flowing from the nebulizer. Figure B-6 shows a schematic of the process.

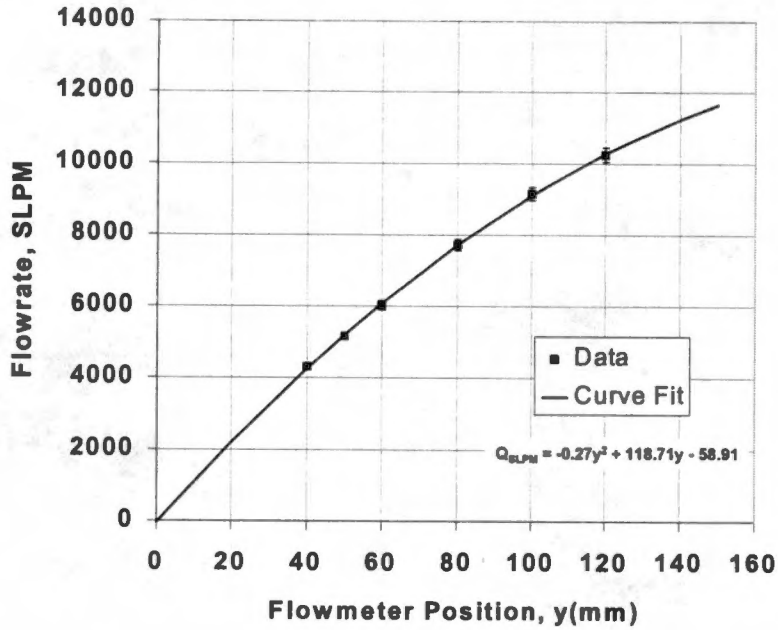

Figure B-2 N_2 calibration results.

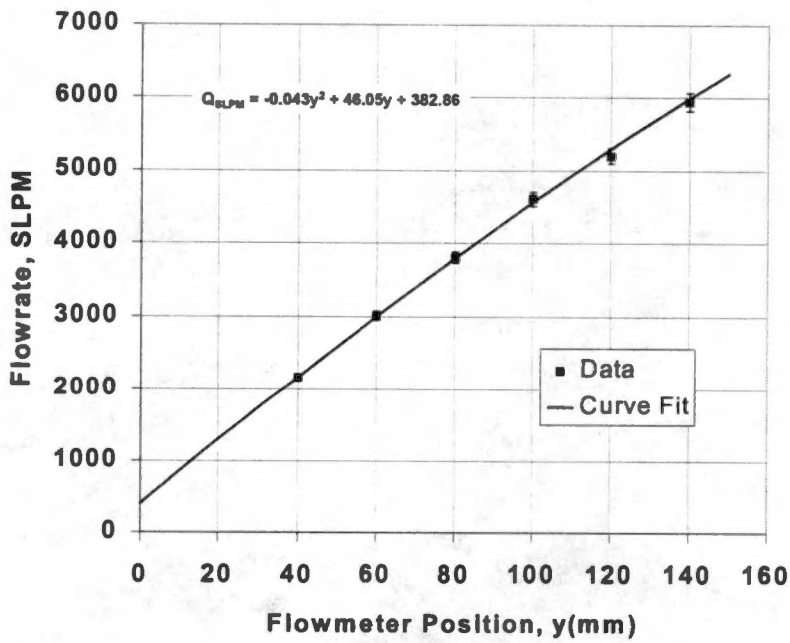

Figure B-3 O_2 calibration results.

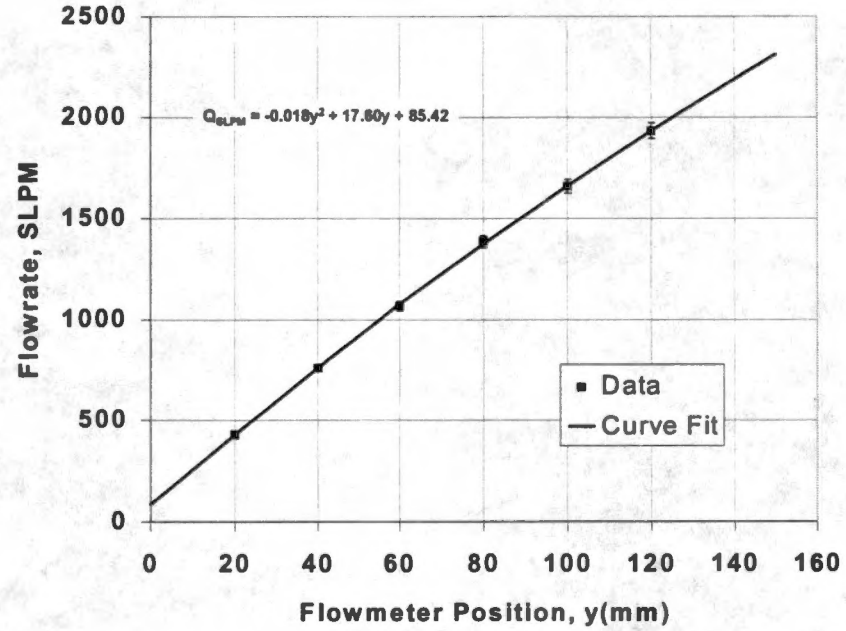

Figure B-4 CH_4 calibration results.

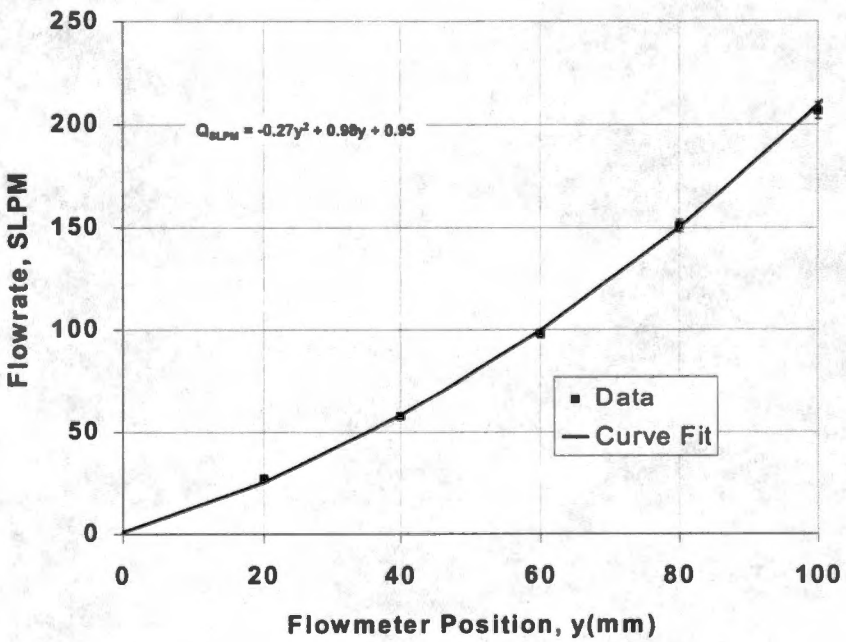

Figure B-5 H_2S calibration results.

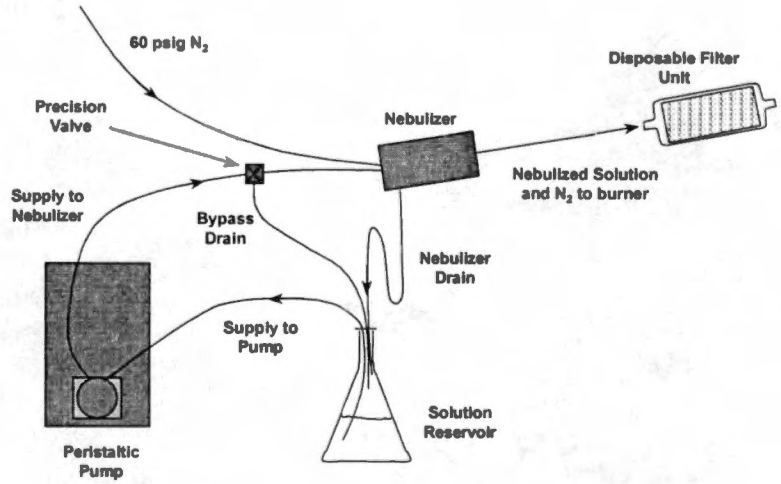

Figure B-6 Nebulizer calibration system.

The filter was measured prior to the admission of the nebulized salt and immediately after the flow was stopped. The elapsed time between the beginning and ending of the nebulized flow was approximately one minute. It was assumed that the mass loss due to the evaporation of trapped water droplets was negligible. The results of the calibration are included in Table B-5. The average of these eight samples is 2.76×10^{-4} gm/s. The standard deviation is 3.79×10^{-5} gm/s, or about 14%.

Table B-5 Nebulizer calibration results.

Initial Mass (gm)	Final Mass (gm)	Fill Time (s)	Flow Rate (gm/s)
14.1814	14.1956	61.72	2.293E-04
14.1955	14.2085	60.00	2.175E-04
14.2083	14.2253	60.00	2.822E-04
14.2252	14.2426	60.07	2.895E-04
14.2425	14.2598	60.05	2.894E-04
14.2597	14.2784	60.47	3.099E-04
14.2784	14.2974	60.67	3.142E-04

References

B-1 *CRC Handbook of Chemistry and Physics, 56th Edition*, pp. D-180, D-181, CRC Press, Cleveland, 1975.

B-2 Fischer, K., "How to predict calibration of variable-area flow meters", *Chemical Engineering*, June 1952.

B-3 Annino, R, and Driver, R. *Scientific and Engineering Applications with Personal Computers*, pp. 331-335, John Wiley and Sons, New York, 1986

B-4 Alkamade, C. Th. J., Hollander, Tj., Snelleman, W., and Zeegers, P.J. Th., *Metal Vapours in Flames*, A. Whitney & Co., Ltd., Exeter (1982).

Appendix C

Measurement Error Analysis

The procedure used to determine the error in the potassium concentration, OH concentration and MLR temperature measurements will be given in this Appendix. Note that only the errors of quantities measured in this experiment contribute to the reported uncertainty. This is because the other errors are fixed relative to this experiment. For example, the oscillator strength, f_{pq} has an associated uncertainty. However, this error is fixed in the experiment. Additionally, the value that was used for f_{pq} was that accepted by the community, having been used in numerous related publications. Hence, this error is fixed in the community and does not affect the comparison of trends.

All random error components are stated as twice the estimated standard deviation (2σ). For a normal distribution, this is nearly a 95% confidence interval. However, the errors encountered here are not identically distributed. Thus a percentage confidence interval can not be properly stated. All bias errors are assumed to be two-sided.

Potassium Concentration

As discussed in Section 3.3.2, the potassium number density (n) is not directly measured, but inferred from the measurement of integrated absorption (W), path length (l), gas temperature (T_g) and a model relating the potassium population to

these quantities, along with a variety of constant factors. Since the measured components are independent, the random uncertainty was given by

$$U_{Random} = \sqrt{\left(\frac{\partial n}{\partial T_g}\delta T_g\right)^2 + \left(\frac{\partial n}{\partial \ell}\delta \ell\right)^2 + \left(\frac{\partial n}{\partial W}\delta W\right)^2} \qquad \text{(C.1).}$$

The fixed error – or bias – is given by

$$U_{fixed} = \left|\frac{\partial n_p}{\partial T_g}\delta T_g^{Bias}\right| \qquad \text{(C.2).}$$

The total uncertainty (the random error component and the bias component) is given by

$$U_{Total} = U_{Random} + U_{Bias} \qquad \text{(C.3).}$$

The partial derivative terms, or influence coefficients, were calculated by perturbing the model relating potassium populations to the components of the measurement. For example, in the case of gas temperature:

$$\frac{\partial n}{\partial T_g} \approx \frac{\left(n^{High} - n^{Low}\right)}{\left(T_g^{High} - T_g^{Low}\right)} \qquad \text{(C.4)}$$

where T_g^{High} is 1% greater than nominal temperature, or $T_g^{High} = 1.01 * T_g^{Nominal}$ and T_g^{Low} is 1% below the nominal temperature, or $T_g^{Low} = 0.99 * T_g^{Nominal}$. The potassium populations that correspond to the perturbed temperatures with all other parameters held fixed are n^{High} and n^{Low}, respectively. Similar calculations were made for each of the other parameters. The component uncertainties; δT_g, δl, δT_g^{Bias} and δW, were determined by various means. The temperature error is composed of a random and fixed components (discussed below in the temperature measurement section). The component uncertainties tabulated in

Table 3-3 of the main body of the dissertation (repeated below as Table C-1) were used to determine the total uncertainty in the potassium number density.

The path length was measured by a steel scale with 1/32" divisions. Additionally, the uncertainty in the path length across the burner is derived from the tubes in the tube bundle arrangement. Tubes were staggered along the edge of the burner, thus, the burner width could only be know within one-half of a tube diameter, or 1/32". The path length was taken to be the measured value +/- 1/32". The path length error distribution was assumed to be uniform over a 1/32" interval. Therefore, the standard deviations was

$$\sigma = \Delta\ell / \sqrt{12} = 0.046 \text{ mm.}$$

Table C-1 Uncertainty parameters for integrated absorption - potassium

	Absorption Scan	Source Scan
δV (volt)	7.3×10^{-2}	6.9×10^{-2}
$\partial W / \partial V$ (cm^{-1}/volt)	7.3×10^{-2}	6.9×10^{-2}
$\Delta\omega$ (cm^{-1})	0.17	0.17
δW (cm^{-1})	0.0088	0.0088
δW (%)	1	1

The integrated absorption component error was determined from the statistics of the measured absorption signal. The uncertainty in the integrated absorption was derived from the uncertainty of each component of the absorption measurement, that is the individual signal measurements at each wavelength. Integrated absorption was calculated from

$$W = \sum_{i=1}^{n} (\nu_{i+1} - \nu_i) \frac{W_{i+1} + W_i}{2} \qquad \text{(C.5)}$$

where n is the number of samples in the scan across the spectral line. Here, W_i is the spectral absorption given by $(1\text{-}I_i/I_{0,i})$, and I_i and $I_{0,i}$ are the signal levels with and without the absorbing medium at wavelength i. I_i and $I_{0,i}$ were determined by multiple measurements of the detector output voltage:

$$I_i = \frac{\sum_{j=1}^{p} V_i^j}{p} \qquad \text{(C.6)}$$

$$I_{0,i} = \frac{\sum_{j=1}^{m} V_{0,i}^j}{m} \qquad \text{(C.7)},$$

where superscript j indicates the $j\text{-}th$ scan over the wavelength interval and p and m represent the number of absorption and source scans, respectively.
The random error resides in the measurement, of $V^j_{0,i}$ and V^j_i. The total integrated absorption is written in terms of the measured voltages for error propagation. Since W_{i+1} and W_i are nearly the same, one can take total integrated absorption as

$$W \approx \sum_{i=1}^{n} \Delta\nu_i W_i \qquad \text{(C.8)}.$$

When W_i is written in terms of the measured voltages, one has:

$$W \approx \sum_{i=1}^{n} \Delta\nu_i \left(1 - \frac{\sum_{j=1}^{p} V_i^j \Big/ p}{\sum_{j=1}^{m} V_{0,i}^j \Big/ m} \right) \qquad \text{(C.9)}$$

Here, there are n equally spaced points in the scan across the spectral line, p scans of the spectral line, and m scans of the source. The uncertainty due to random error in W then is

$$U_w \approx \sqrt{\sum_{i=1}^{n} \left[\sum_{j=1}^{m} \left(\frac{\partial W}{\partial V_{0,i}^j} \delta V_{0,i}^j \right)^2 + \sum_{j=1}^{p} \left(\frac{\partial W}{\partial V_i^j} \delta V_i^j \right)^2 \right]} \qquad \text{(C.10).}$$

The influence coefficients are:

$$\frac{\partial W}{\partial V_{0,i}^j} = \frac{1}{m} \frac{\sum_{j=1}^{p} V_i^j \Big/ p}{\left(\sum_{j=1}^{m} V_{0,i}^j \Big/ m \right)^2} \Delta\nu_i \qquad \text{(C.11)}$$

$$\frac{\partial W}{\partial V_i^j} = \frac{1}{p} \frac{1}{\sum_{j=1}^{m} V_{0,i}^j \Big/ m} \Delta\nu_i \qquad \text{(C.12).}$$

The errors, $\delta V^j{}_i$ and $\delta V^j{}_{0,i}$, are practically constant for all points as are the influence coefficients. Therefore, the random uncertainty is approximately given by

$$U_w \approx \sqrt{nm \left(\frac{\partial W}{\partial V_0'} \delta V_0' \right)^2 + np \left(\frac{\partial W}{\partial V'} \delta V' \right)^2} \qquad \text{(C.13)}$$

where $V^j{}_i$ and $V^j{}_{0,i}$ are the constant errors. The influence coefficients become:

$$\frac{\partial W}{\partial V_0'} = \frac{1}{m}\frac{V'}{\left(V_0'\right)^2}\Delta\nu \qquad \text{(C.14)}$$

$$\frac{\partial W}{\partial V'} = -\frac{1}{p}\frac{1}{V'}\Delta\nu \qquad \text{(C.15)}$$

Figure C-1 shows the data from three spectral scans of the source lamp. The source lamp output was essentially constant in this wavelength interval. The statistics of this set of voltage measurements are representative of the statistics of the parameters in the uncertainty relationships. A histogram of these data points is shown in Figure C-2. A normal distribution using the mean and variance of this sample is superimposed on the histogram. The histogram compares well with the normal distribution. The parameters V' and V'_0 were set equal to the mean in the calculation of the influence coefficients. This procedure slightly over estimates $\partial W/\partial V'_0$ and under estimates $\partial W/\partial V'$. The component errors, $\delta V'$ and $\delta V'_0$, were set equal to twice the standard deviation of the sample of voltage readings from the three scans. Table C-2 shows the values and the results of the computation of δW.

The combination of these errors yields a total uncertainty on the potassium number density of about 5% of the derived population. A conservative statement of the error is 10% of the derived population.

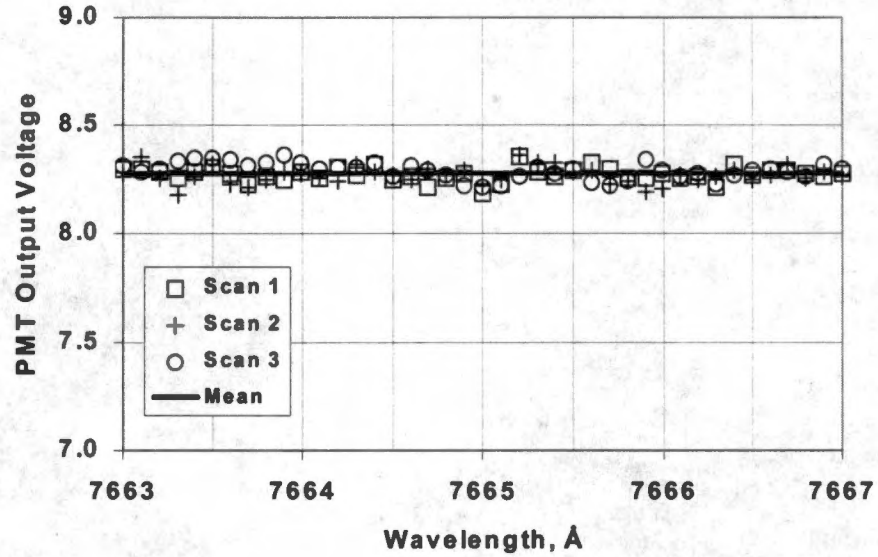

Figure C-1 Signal statistics for potassium absorption measurement.

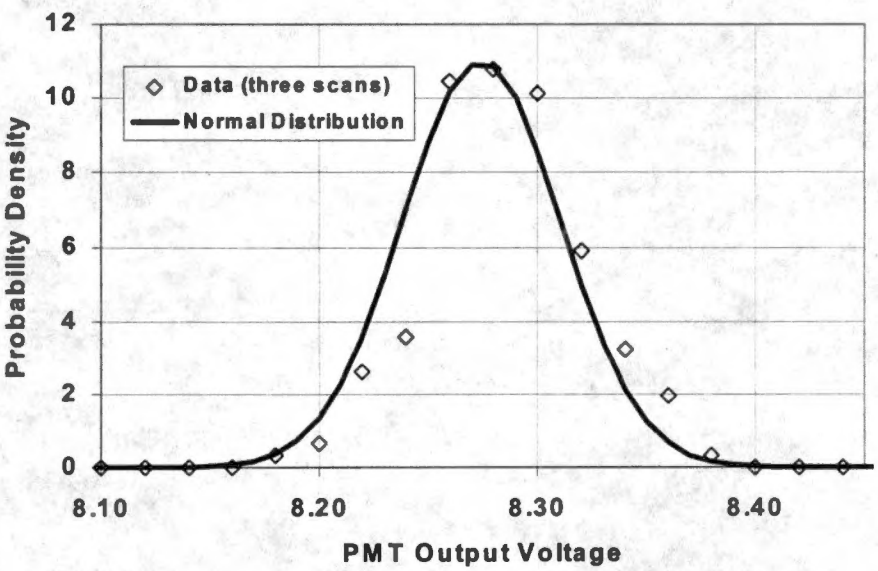

Figure C-2 Histogram for potassium absorption measurement.

Table C-2 Estimated component errors.

Parameter	Random Uncertainty	Bias Uncertainty
Temperature, δT (K)	17	35
Path Length, $\delta \ell$ (cm)	0.046	0.0
Integral Absorption, δW (cm^{-1})	0.009	0.0
Total Error, δn_p ($atoms/cm^3$)	3.4%	1.3%

OH Concentration

Random errors for the OH absorption data were assessed in the same way as those for the potassium absorption data. In addition, a bias error in the absorption measurement must be include in the determination of [OH] uncertainty. The source of the bias is discussed in Appendix D. The random error components of the population measurement are included in the following equation:

$$U_{random} = \sqrt{\left(\frac{\partial n}{\partial T_g}\delta T_g\right)^2 + \left(\frac{\partial n}{\partial \ell}\delta \ell\right)^2 + \left(\frac{\partial n}{\partial W}\delta W\right)^2 + \left(\frac{\partial n}{\partial \eta}\delta \eta\right)^2} \qquad \text{(C.16)}$$

where η is the required voltage shift (defined in Appendix D). The uncertainty that results from the bias error is

$$U_{Bias} = \left|\frac{\partial n_p}{\partial T_g}\delta T_g^{Bias}\right| + \left|\frac{\partial n_p}{\partial W}\delta W^{Bias}\right| \qquad \text{(C.17)}$$

The total error is then

$$U_{Total} = U_{Random} + U_{Bias}. \qquad \text{(C.18)}$$

The determinations of random component errors for temperature and path length are identical to that discussed previously for potassium. The random error in the integrated absorption is similar to that for potassium. However, the data statistics and component errors are different. In the case of the OH distribution, the I_0 shifting procedure introduced additional component errors. Following the development given for the potassium measurement, the integrated absorption is:

$$W = \sum_1^n (\nu_{i+1} - \nu_i)\frac{W_{i+1} + W_i}{2}. \qquad \text{(C.19)}$$

In this case, the modification for the shift in the source scan requires:

$$I_i = \frac{\sum_{j=1}^{p} V_i^j}{p}, \qquad \text{(C.20)}$$

$$I_{0,i} = \sum_{j=1}^{m} V_{0,i}^j \Big/ m - \eta, \qquad \text{(C.21)}$$

where η is the required shift. In addition, the grating ghost requires an additional correction. Applying the ghosting correction and approximating the sum as was previously done:

$$W \approx \alpha \sum_{i=1}^{n} \Delta\nu_i W_i. \qquad \text{(C.22)}$$

Now, the integrated absorption is:

$$W \approx \alpha \sum_{i=1}^{n} \Delta\nu_i \left[1 - \frac{\sum_{j=1}^{p} V_i^j \Big/ p}{\sum_{j=1}^{m} V_{0,i}^j \Big/ m - \eta} \right], \qquad \text{(C.23)}$$

and the uncertainty expression becomes:

$$U_W \approx \sqrt{\sum_{i=1}^{n} \left[\sum_{j=1}^{m} \left(\frac{\partial W}{\partial V_{0,i}^j} \delta V_{0,i}^j \right)^2 + \sum_{j=1}^{p} \left(\frac{\partial W}{\partial V_i^j} \delta V_i^j \right)^2 \right] + \left(\frac{\partial W}{\partial \eta} \delta\eta \right)^2}. \qquad \text{(C.24)}$$

Influence coefficients become:

$$\frac{\partial W}{\partial V_{0,i}^j} = \frac{\alpha}{m} \frac{\sum_{j=1}^{p} V_i^j \Big/ p}{\left(\sum_{j=1}^{m} V_{0,i}^j \Big/ m - \eta \right)^2} \Delta\nu_i \qquad \text{(C.25)}$$

$$\frac{\partial W}{\partial V_i^j} = -\frac{\alpha}{p} \frac{1}{\sum_{j=1}^{m} V_{0,i}^j \Big/ m - \eta} \Delta\nu_i \qquad \text{(C.26)}$$

$$\frac{\partial W}{\partial \eta} = W - 1 \qquad \text{(C.27)}$$

$V^j_{0,i}$, and V^j_i are as described above. For the voltage measurements, the error components and influence coefficients are nearly equal, so the uncertainty expression simplifies to:

$$U_W \approx \sqrt{nm \left(\frac{\partial W}{\partial V_0'} \delta V_0' \right)^2 + np \left(\frac{\partial W}{\partial V'} \delta V' \right)^2 + \left(\frac{\partial W}{\partial \eta} \delta\eta \right)^2}, \qquad \text{(C.28)}$$

where V'_0 and V' are defined as in the case for potassium.

The error components of the voltage measurement were derived from a measurement of the source lamp. Five source lamp scans are displayed in Figure C-3, along with the sample mean. (The OD spectral feature has been removed from the scan, otherwise the lamp output is essentially constant. See Appendix D for details.) The parameters V' and V'_0 were set equal to the mean of this set of voltage measurements. The parameters $\delta V'$ and $\delta V'_0$ were set equal to twice the sample standard deviation. As in the case of potassium absorption data, the voltage measurement is nearly normally distributed (Figure C-4).

The random error component for the source shift, $\delta\eta$, was estimated to be uniformly distributed about the accepted value (see Appendix D) over a 0.03 volt interval. The error range for this parameter is shown in Figure C-5 compared to the mean square error results of the fitting routine. The component errors are summarized in Table C-3.

There are two sources of bias error in these measurements. The temperature measurement included a bias error due to the bias in the source temperature measurement. The integrated absorption error includes a bias error due to properties of the measuring instrument. The source of these errors:

1. I_0 bias due to grating "ghosts"
2. I_0 corrections to remove the spectral emission feature on the source lamp
3. I_0 corrections to account for source beam obscuration are discussed in Appendix D.

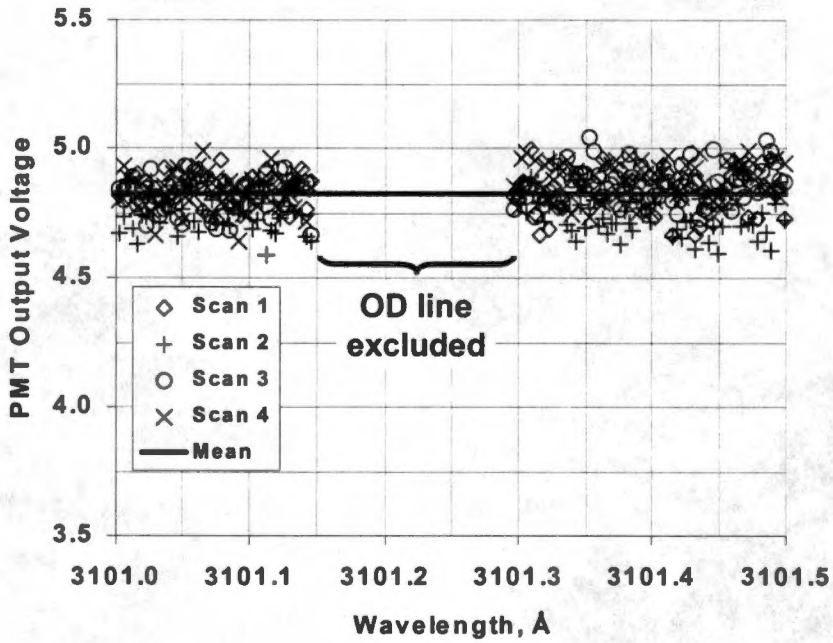

Figure C-3 Signal statistics for OH absorption measurement.

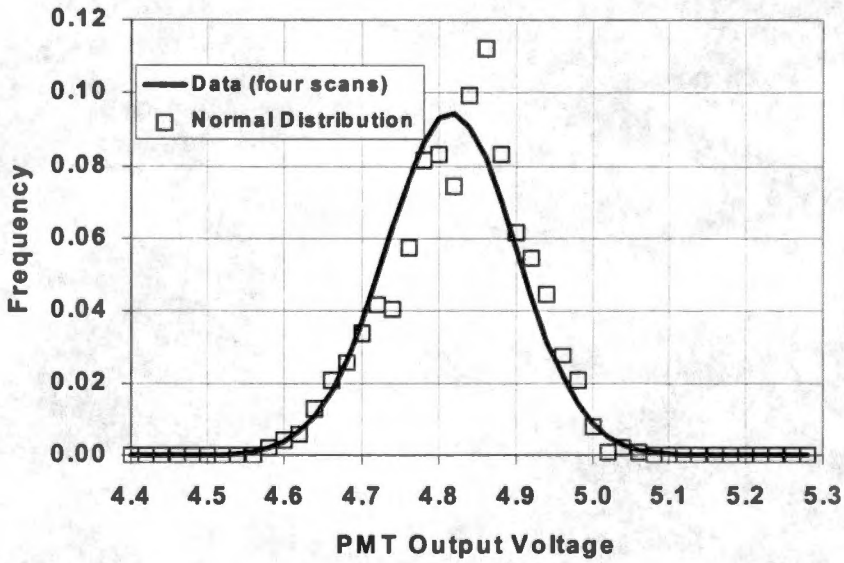

Figure C-4 Histogram for OH absorption measurement.

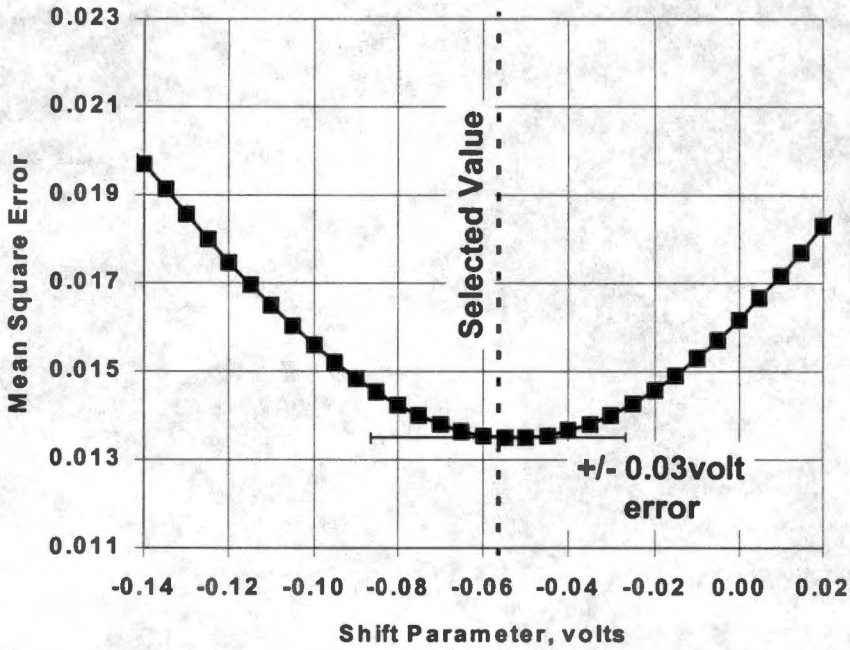

Figure C-5 Estimate of $\delta\eta$.

Table C-3 Uncertainty parameters for integrated absorption - OH

	Absorption Scan	Source Scan
δV (volt)	0.17	0.17
$\partial W/\partial V$ (cm^{-1}/volt)	-1.62×10^{-3}	1.65×10^{-3}
$\delta\eta$ (volt)	--	0.00173
$\partial W/\partial\eta$ (cm^{-1}/volt)	--	-0.68
$\Delta\omega$ (cm^{-1})	0.035	0.035
δW (cm^{-1})	0.0114	0.0114
δW (%)	3.6	3.6

The temperature bias is discussed in the next section. The bias due to the instrument correction was assumed to be equal to the value of the correction. For the nominal level of integrated absorption of 0.38cm^{-1}, the bias was assumed to be 0.025 cm^{-1}. This fixed value was assumed for all measurements.

A summary of error components is shown in Table C-4. The total error is about 18%. An error specification of 20% is conservative.

Modified Line Reversal Temperature Measurement Errors

Just as for the other measurements, gas temperature is not directly measured, but is inferred from other measurements and a model. Thus the error analysis must propagate the error of each of the component measurements in a consistent way. The measured gas temperature, T_g, is a function of the lamp temperature, the flame radiance (irradiance) measurements and the geometric

Table C-4 Error components for OH absorption data.

Parameter	Random Uncertainty	Bias Uncertainty
Temperature, δT (K)	17	35
Path Length, δl (cm)	0.046	0
Integral Absorption, δW	0.0114	0.025
Total Uncertainty	5.6%	12.0%

factors. The uncertainty due to random error is given by the following equation:

$$U_{Random} = \sqrt{\left(\frac{\partial T_g}{\partial T_s}\delta T_s\right)^2 + \left(\frac{\partial T_g}{\partial \eta_{foc}}\delta \eta_{foc}\right)^2 + \left(\frac{\partial T_g}{\partial R_s}\delta R_s\right)^2 + \left(\frac{\partial T_g}{\partial R_f}\delta R_f\right)^2 + \left(\frac{\partial T_g}{\partial R_{s+f}}\delta R_{s+f}\right)^2},$$

(C.29)

where η_{foc} relates geometric properties of the MLR optical train, R_s is the source radiance, R_f is the flame radiance, and R_{s+f} is the combined source and flame radiance. Bias error for this measurement is computed from:

$$U_{Bias} = \left|\frac{\partial T_g}{\partial T_s}\delta T_s^{Bias}\right| \qquad \text{(C.30)}$$

and the total error is:

$$U_{Total} = U_{Random} + U_{Bias}. \qquad \text{(C.31)}$$

The source temperature random error component was determined from the statistics of the source temperature measurements. As discussed in Appendix D, the source temperature was taken to be the mean of ten independent measurements of the lamp brightness temperature at a fixed current setting. The standard deviation of this data set provides an estimate of δT_s. This data set is shown in Table C-5 for the 12.5 amp current setting. There is a possible bias error of about 35 K in the tungsten strip lamp source. This bias is discussed in Appendix D.

Table C-5 Brightness temperature statistics.

Sample	Temperature (deg K)
1	1822
2	1829
3	1828
4	1829
5	1828
6	1833
7	1827
8	1830
9	1826
10	1821
μ (deg K)	1827.3
σ (deg K)	3.6
δT_s (deg K)	8

The optical factor, η_{foc} was also an inferred quantity, its value depending on the measurement in Table C-6. The expression for the uncertainty in η_{foc} is given by

$$U_{\eta_{foc}} = \sqrt{\left(\frac{\partial \eta_{foc}}{\partial p_1}\delta p_1\right)^2 + \left(\frac{\partial \eta_{foc}}{\partial q_1}\delta q_1\right)^2 + \left(\frac{\partial \eta_{foc}}{\partial p_2}\delta p_2\right)^2 + \left(\frac{\partial \eta_{foc}}{\partial d_2}\delta d_2\right)^2 + \left(\frac{\partial \eta_{foc}}{\partial r_{s_1}}\delta r_{s_1}\right)^2 + \left(\frac{\partial \eta_{foc}}{\partial \tau_s}\delta \tau_s\right)^2} \quad \text{(C.32)}$$

Except for the optical transmissivity, each of the parameters is a length or radius measurement. The error components are tabulated in Table C-6. The error in the length measurements was assumed to be uniformly distributed over an interval of 0.794 mm (1/32"). The error in the diameter measurements was assumed to be uniformly distributed over an interval of 0.025 mm (0.001"). The focal length, F_1, of the source lens was taken as the nominal value for the lens. The error is assumed to be uniformly distributed over an interval of (0.25").

Table C-6 Error components for MLR optical train.

	δ(parameter)	Influence Coefficient	Result
p_1 (mm)	0.46	-0.005	--
q_1 (mm)	0.46	-0.002	--
p_2 (mm)	0.46	2.2×10^{-4}	--
d_2 (mm)	0.46	-2.2×10^{-4}	--
r_{s_2}(mm)	0.015	1.5×10^{-5}	--
F_1 (mm)	3.77	0.013	--
τ_s (-)	0.01	0.787	--
$\delta\eta$ (volts)	--	--	0.051
$\delta\eta$ (%)	--	--	6.6

Transmissivity measurement was based in the ratio of two radiance values. The error in the transmissivity measurement was based on the 2σ error in the radiance values discussed above. The influence coefficients were computed numerically from 1% perturbations in the parameters. The resulting 2σ uncertainty in η_{foc} is 0.05 or about 7%.

The error for the radiance components were taken from the signal statistics, similar to that demonstrated for [K] and [OH] above. That is, the standard deviation of a set of voltage readings from a spectral scan of the source was used as the estimates of δR_s, δR_{s+f}, and δR_f. Influence coefficients were computed numerically from 1% perturbations of the model parameters.

The error components are summarized in Table C-7. When all these errors are

Table C-7 Estimated component errors.

Parameter	Random Uncertainty (2σ)	Bias Uncertainty
Source Temperature, δT (K)	8	+/-35
Optical Correction, $\delta\eta_{foc}$	0.05	0
Source Radiance, δR_s (volts)	0.004	0
Flame Radiance, δR_f (volts)	0.004	0
Total Radiance, δR_{s+f} (volts)	0.004	0
Total Uncertainty (deg K)	17	35

propagated through the above equations, the total uncertainty in the flame gas temperature is found to be 17 K random error with 35 K bias. The total temperature uncertainty is about 60 K.

Appendix D

OH Data Reduction

Densities of atomic and molecular species in gas mixtures can be inferred by measuring the absorption of light by the gas mixture. An absorption measurement is made by illuminating an absorbing medium with a beam of radiation at an energy (frequency) coincident with that of some appropriately chosen energy transition for an atom or molecule of interest. The situation is illustrated in Figure D-1. The *general* development of the relationship between the measured absorption and species population is given in this section. This development closely follows that of Lucht, et al [42] and is repeated from Section 3.2 for completeness.

The quantities $I_{0,\nu}$ and I_ν represent the spectral radiation flux entering and leaving the absorption volume, respectively. Radiation-absorbing species in the volume will reduce the intensity I_ν below the incident intensity $I_{0,\nu}$. By considering

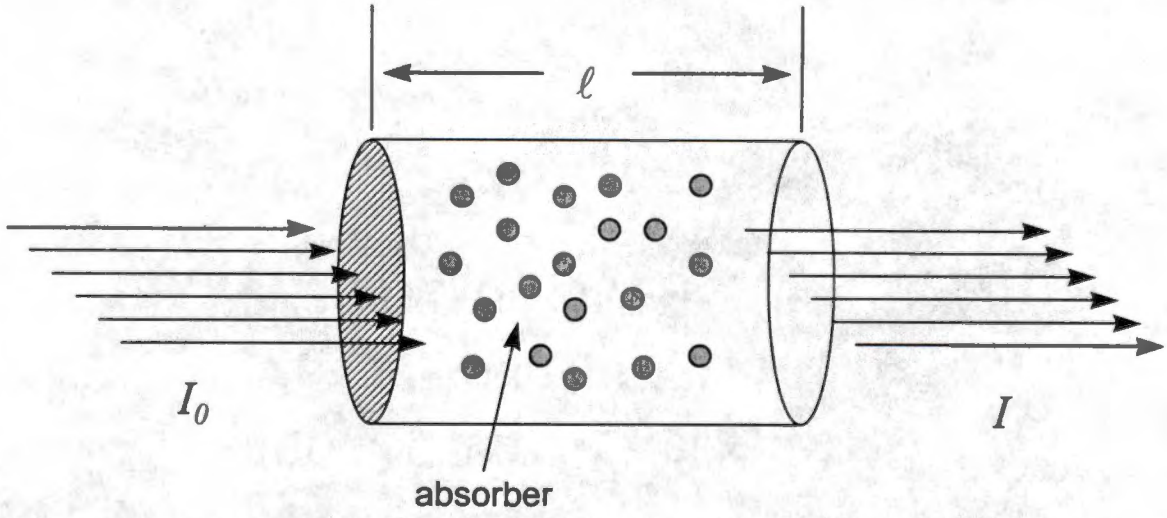

Figure D-1 Schematic of absorption measurement (After Alkemade [41]).

an infinitesimal volume of absorbing gas, and defining the spectral absorption coefficient, κ_ν, the relationship between the percentage of radiation absorbed and the path length, l, through the uniform absorbing medium is found as follows:

$$I_{\nu,x+\Delta x} - I_{\nu,x} = -I_{\nu,x}\kappa_\nu \Delta x \qquad \text{(D.1)}$$

$$\lim_{\Delta x \to 0}\left(\frac{I_{\nu,x+\Delta x} - I_{\nu,x}}{I_{\nu,x}} = -\kappa_\nu \Delta x\right) \qquad \text{(D.2)}$$

$$\int_{I_\nu(x)=I_\nu(0)}^{I_\nu(x)=I_\nu(\ell)} \frac{dI_\nu}{I_\nu} = -\int_{x=0}^{x=\ell} \kappa_\nu dx \qquad \text{(D.3)}$$

$$\ln\left(\frac{I_\nu(\ell)}{I_\nu(0)}\right) = -\kappa_\nu \ell \qquad \text{(D.4)}$$

$$\frac{I_\nu(\ell)}{I_\nu(0)} = e^{-\kappa_\nu \ell} \qquad \text{(D.5)}$$

This expression is commonly known as Lambert-Beer's law and serves to relate the measured absorption to the number density of the absorbing species through the spectral absorption coefficient, $\kappa_\nu(n_p, T_{gas})$. The spectral transmission is defined as:

$$T(\nu) = \frac{I_\nu}{I_{\nu,0}} \qquad \text{(D.6)}$$

and the spectral absorption is:

$$A(\nu) = 1 - T(\nu) \qquad \text{(D.7)}$$

The total absorption is the quantity:

$$A = \int_{\nu-\Delta\nu}^{\nu+\Delta\nu} A(\nu)d\nu = \int_{\nu-\Delta\nu}^{\nu+\Delta\nu} (1 - e^{-\kappa_\nu \ell})d\nu\,. \qquad \text{(D.8)}$$

It is related, through the absorption coefficient, to the number density and is the quantity sought in the absorption measurement.

For the case at hand, continuum light sources were used for the absorption measurements. When the source radiation is observed with a spectrometer, the quantity, $\bar{I}_\nu$ is measured. $\bar{I}_\nu$ is the convolution of the instrument response and the incident radiation:

$$\bar{I}_\nu = \int_{\nu_1}^{\nu_2} I(\nu')g(\nu-\nu')d\nu' \qquad \text{(D.9)}$$

and $g(\nu-\nu')$ is the so-called 'slit function' that represents the modification of the incident radiation by the spectrometer. For good spectrometers, the slit function is approximately gaussian. The effect of the slit function is to disperse the incident radiation spectrally. Thus, a delta function is observed as a gaussian and other peaked functions are similarly dispersed. The quantity, $\bar{I}_{\nu,0}$ is the measured radiation without the absorbing medium.

In the experiments described here, the measured quantity is:

$$W = \int_{\nu-\Delta\nu}^{\nu+\Delta\nu} \left[1 - \frac{\int_{\nu_1}^{\nu_2} I_\nu(\nu')g(\nu-\nu')d\nu'}{\int_{\nu_1}^{\nu_2} I_{0,\nu}(\nu')g(\nu-\nu')d\nu'} \right] d\nu \qquad \text{(D.10)}$$

or

$$W = \int_{\nu-\Delta\nu}^{\nu+\Delta\nu} \left[1 - \frac{\bar{I}_\nu}{\bar{I}_{0,\nu}} \right] d\nu \qquad \text{(D.11)}$$

Two specific deviations from the requirements of this derivation were encountered in the acquisition of the OH absorption data. First, the grating in the spectrometer was very densely ruled and, as a result, the slit function, $g(\nu-\nu')$, included spectral features known as "ghosts". Secondly, the recorded source spectrum, $\bar{I}_{\nu,0}$, was at times compromised by either physical occlusion, spectral occlusion, or temporal variation. This Appendix deals with corrections made to the OH absorption data.

I_0 Spectral Feature

The spectral character of the deuterium lamp used for the OH absorption measurement is shown in Figure D-2. This scan is the average of five individual scans. Note that there is a prominent feature at 310.122nm. This feature is due to emission from the OD molecule. Evidently, the deuterium source was compromised and atmospheric oxygen was admitted. This fact contributed to the weakness, unsteadiness and short life of the lamp. The feature was identified based on the line atlas for OD provided by Hornkohl, [D-2]. It is unfortunate that this spectral feature correlated with the OH $P_1(5)$ line observed in these experiments. However, it allowed for accurate spectral registration of the I_0 scans and the absorption scans.

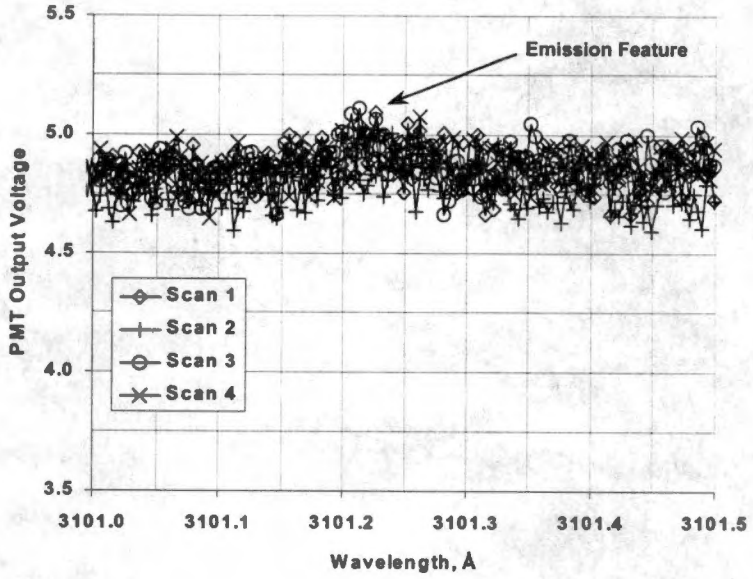

Figure D-2 Emission feature in $\bar{I}_{0,\nu}$ scan of deuterium lamp.

Effects of Slit Function - Absorption

The experimental slit function, $g_{exp}(\nu)$, of the spectrometer used to monitor OH concentration was determined by observing the narrow emission from a mercury pen ray. The Hg emission at 312.567nm was scanned prior to each experimental session. This line is sufficiently close to the observed OH transition (310.123 nm) that differences in resolution due to grating blaze were not significant.

A typical scan is displayed in Figure D-3. The scan has been normalized so that the integral is unity, as is required of a slit function. The slit function is predominately gaussian-like, however extraneous features, called ghosts, were evident. These 'ghosts' are often found with densely-ruled gratings. Additionally,

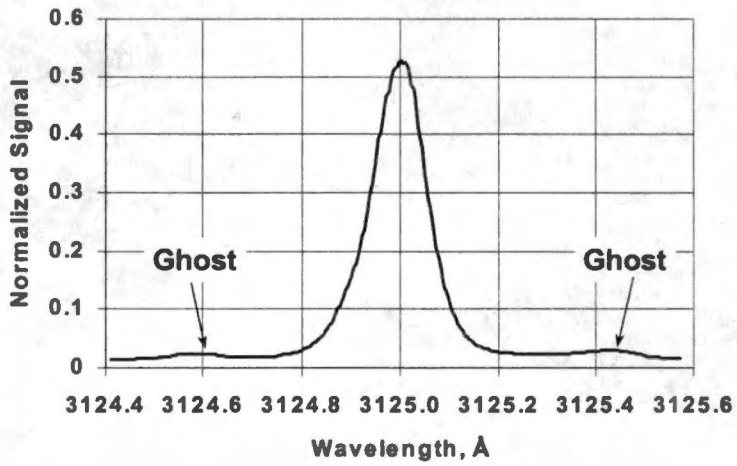

Figure D-3 Normalized scan of Hg emission line (312.567nm) to determine slit function shape.

note that the full wings of the slit function have not been recorded. It is unknown how rapidly these wings decay. However, the offset does decay to zero away from the line center. Scattered light may contribute to this offset, but it is not believed to constitute the majority of the offset. It must be shown that a proper experimental determination of absorption is allowed with this slit function.

To demonstrate the accuracy of the measured absorption analytically, expressions for the terms $\bar{I}_\nu$, g, etc. are needed. For this demonstration, theoretical expressions will be used to determine $\bar{I}_\nu$ and $\bar{I}_{0,\nu}$ but the measured slit function was used to represent g. The experimental source spectrum, $\bar{I}_{0,\nu}$ was taken as a constant value with a weak emission feature added to simulate the presence of the OD feature observed in the lamp spectrum. The emission feature is a Voight-broadened line profile scaled to match the OD feature seen in

the data. The absorption profile is the theoretical line profile (using nominal values for n_{OH}, T, and path length).

A theoretical representation of a physical line profile (that is, not modified by the observing instrument), is shown as the heavy line in Figure D-4. The conditions for this profile are indicted in the figure. The convolution of this profile with the slit function shown in Figure D-3 is also shown in Figure D-4. Each of these profiles was integrated across the entire line (wing-towing) to provide the results for total integrated absorption indicated in the figure. The integrated absorption for the two profiles differs by much less than 1%. This is more than adequate for the purpose at hand.

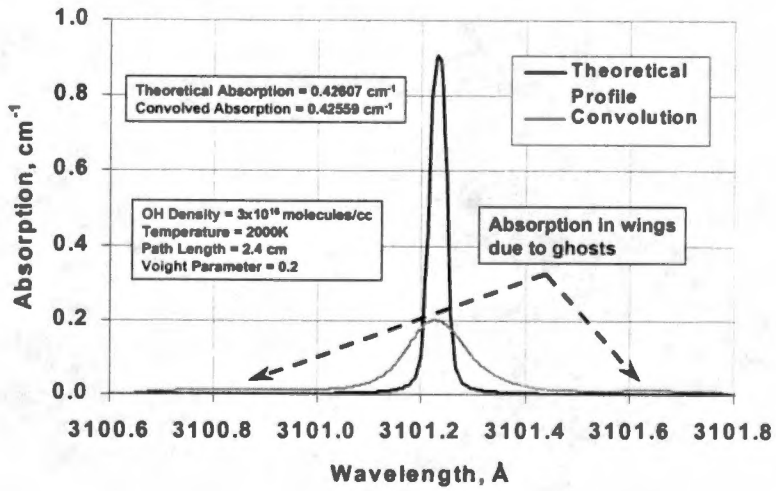

Figure D-4 Theoretical and convolved absorption profiles.

Determination of the $\bar{I}_0$ Correction

Because of the low intensity of the lamp and the requirement for high spectral resolution, the OH data were acquired with low signal-to-noise ratio (SNR). Multiple scans (five scans in most cases) were acquired and averaged to increase SNR. This data acquisition procedure was very time (and gas) consuming. The compromised lamp envelope compounded this problem. Thus $\bar{I}_0$ scans were made only at the beginning and end of an experimental session. This precluded tracking variations in $\bar{I}_0$ due to either fluctuations in time or due to obscuration by the burner (scans made at positions between 0.5 mm and 1.5 mm).

A method to correct the data in a consistent way was devised. The previously described slit function defines the spectral shape of any sufficiently narrow spectral source. Thus, all narrow spectral shapes will appear identically when viewed by this instrument. This fact was employed to shift the $\bar{I}_0$ scan relative to the absorption scan to account for the effects noted above. Essentially, the $\bar{I}_0$ scan was shifted vertically until the measured absorption profile best matched (in a least-squares sense) the measured slit function. This procedure is illustrated in Figure D-5.

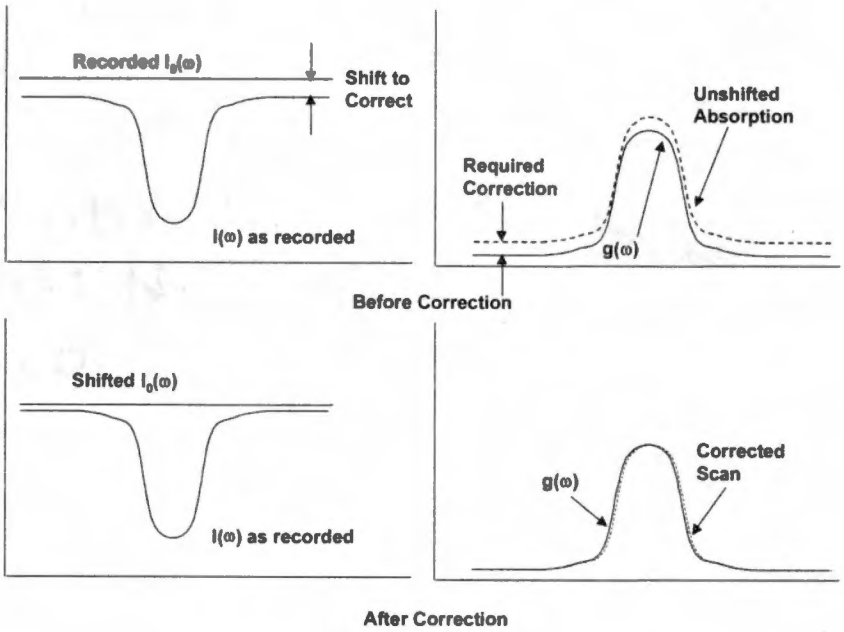

Figure D-5 $\bar{I}_{0,\nu}$ correction procedure.

This procedure was accomplished by first correlating the averaged absorption scan and the slit function and then scaling the slit function so that the peak of the absorption scan and the slit function had the same value. The residual of the difference between the two profiles was computed as follows:

$$r = \sum_{i=1}^{n} (a_i - g_i)^2 \qquad \text{(D.12)}$$

where r is the residual and a and g are the absorption and slit function scans, respectively. A Newton iteration was used to determine shift corrections for the $\bar{I}_0$ scans. Usually, the best fit was determined within five iterations. $\bar{I}_0$ corrections were typically less than 2% of the nominal $\bar{I}_0$ value for cases where burner obscuration caused the shift and less than 1% for other cases.

An example of the results of the procedure is shown in Figure D-6. This particular scan was obtained for the stoichiometric flame with no sulfur, at a height of 1mm above the burner surface. Figure D-6a shows the result of a slit function fit. The fit is quite good, verifying the assertion that the narrow OH line would be observed with the shape of the slit function. Figure D-6b shows the difference between the slit function and the final line profile. The structure observed in the residual is symmetric, consistent with expectations: the profile is too low at the peak and two high on the sides.

Total Absorption Correction

The spectral scan width for this experiment was restricted in a way that appeared to capture the entire OH absorption line. However, due to the very broad slit function, especially the slit function ghosts, the experimental spectral scan width did not adequately capture the entire absorption profile. Two corrections for this omission has been developed and applied to the data. The first is associated with

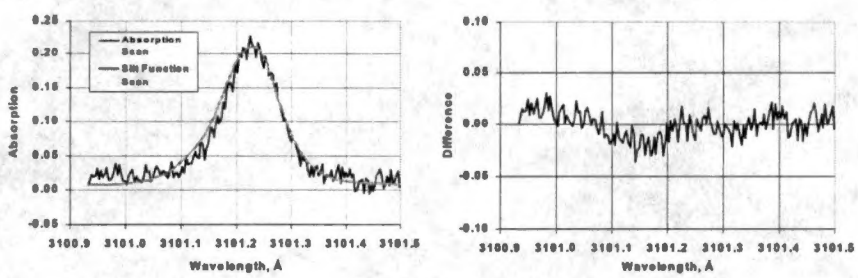

a. b.

Figure D-6 Examples of OH absorption data correction procedure. 5a. Absorption scan fit to slit function. 5b. Fit residual.

the slit function as recorded – the maximum correction. The second is associated with a slit function that has been corrected with the assumption that the recorded slit function is contaminated with stray light – the minimum correction.

The procedure to develop these corrections was similar to the previously described procedure for correcting for source intensity variations. Using the experimental values for the path length and temperature and nominal values for n_{OH}, several theoretical line profiles were calculated. These profiles were integrated to provide the theoretical integrated absorption ($A_{theoretical}$). These absorption profiles were then convolved with the two (maximum and minimum) slit functions to produce representations of the experimental values of integrated absorption ($A_{convolved}$) that correspond to theoretical absorption. The factor that relates the true and measured absorption has the form

$$A_{true} = (1 - \frac{A_{convolved}}{A_{theoretical}}) A_{measured} \qquad \text{(D.13)}$$

Then, the correction, C, to be applied to the measured integrated absorption ($A_{measured}$) is

$$C = (1 - \frac{A_{convolved}}{A_{theoretical}}) \qquad \text{(D.14)}$$

This correction has been developed based on several different values of number densities at experimental temperatures for the measured slit function and the resulting correction is shown in Figure D-7. The measured slit function contains

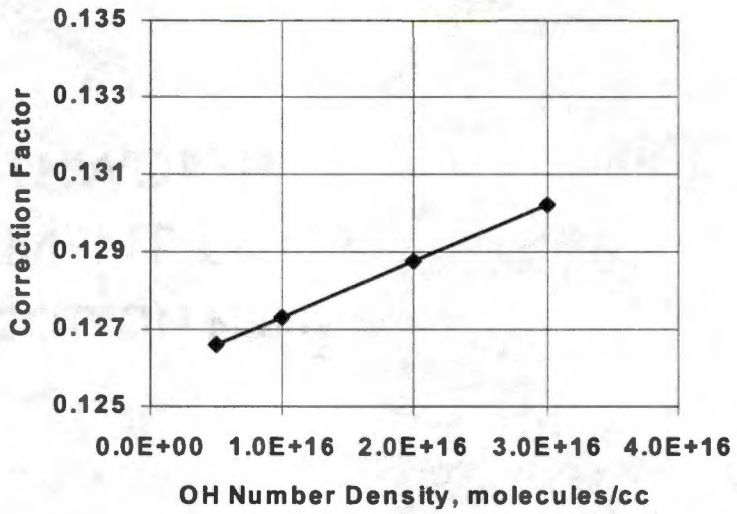

Figure D-7 Maximum correction for limited spectral scan.

a bias that is most likely related to the actual width of the slit function. However, it could be caused by stray light scattered within the spectrometer. If this were the case, the actual slit function would be represented by the measured slit function with the bias removed. The bias has a slight increase with wavelength, so a linear correction was made. This slit function is shown in Figure D-8. Figure D-9 shows the resulting absorption correction.

The maximum correction is approximately 13% while the minimum correction is approximately 6%. These values were applied to the measured OH absorption data prior to the curve-of-growth calculations.

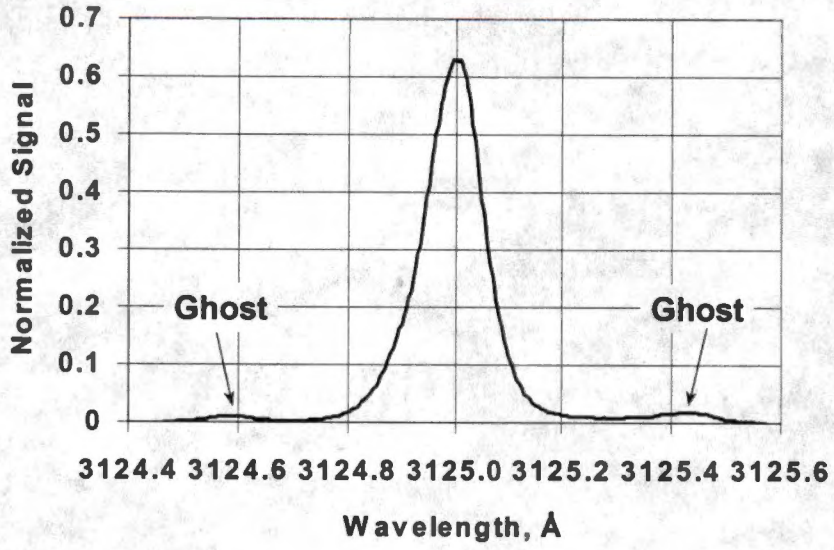

Figure D-8 Slit function corrected for scattered light.

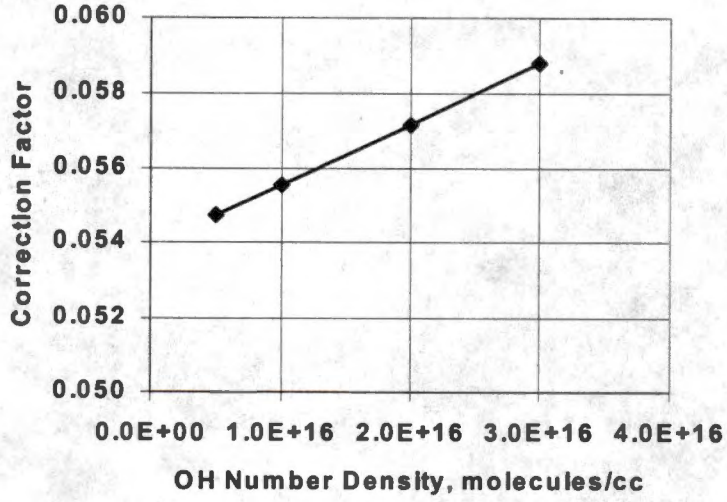

Figure D-9 Minimum correction for limited spectral scan.

Reference:

D-1 Alkamade, C. Th. J., Hollander, Tj., Snelleman, W., and Zeegers, P.J., Th., *Metal Vapours in Flames*, A. Whitney & Co., Ltd., Exter (1982).

D-2 Hornkohl, private communication (1999).

Appendix E

Calibration of Tungsten Strip Lamp

Determination of the source temperature is critical for the MLR gas temperature measurement. The lamp source temperature, or brightness temperature is the temperature that a black body would have to produce the same emissive power. For these experiments, the brightness temperature was measured using on optical pyrometer. This device was calibrated to determine the brightness temperature at 653 nm, $T_{s,653nm}$. To determine the brightness temperature at 765 nm (required for the potassium line reversal measurement), a Planck correction was applied to $T_{s,653nm}$. The calibration and correction are described in this section.

A Leeds & Northrup model 8632-C optical pyrometer was used for these measurements. To determine the brightness temperature of an object, the object (in this case the filament of a tungsten strip lamp) is viewed with the optical pyrometer. The radiation from the object is filtered so that only light at 653 nm enters the pyrometer. The brightness of the image of the object is compared to an internal reference source. Three internal sources are available to increase the calibration range of the instrument. The intensity of the reference source is adjusted until the reference source is judged to be as bright the object. The adjustment of the reference source is calibrated in degrees C. When the brightness of the internal source and the object match, the brightness temperature (at 653 nm) is read from the scale.

While the lamp was operated at a constant power (12.51 amps) for the MLR measurements, calibrations for these experiments were performed at many lamp currents. The lamp current was established at the desired value. Ten samples from the optical pyrometer were made at each lamp current. The samples were averaged and are displayed in Figure E-1. Three calibrations are shown. The first calibration was made early in the experimental program. The pyrometer was in the "High" setting. The next two were made just prior to the experiments. The pyrometer was set in the temperature range appropriate to the anticipated brightness temperature.

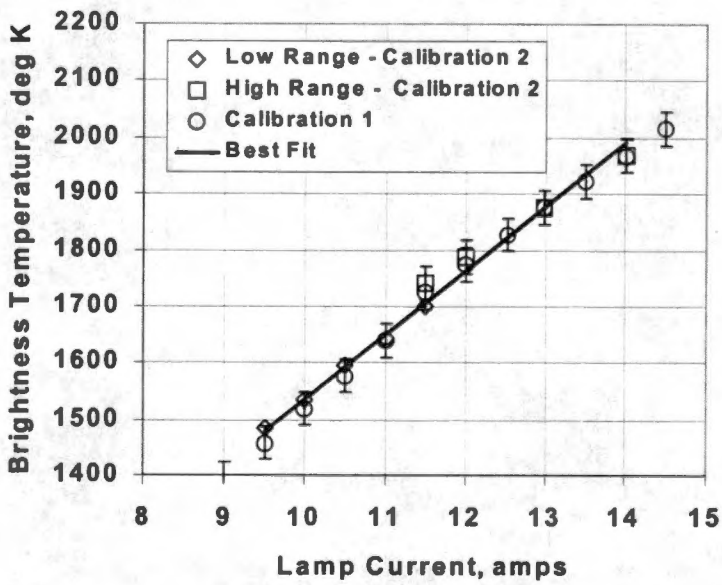

Figure E-1 Results of brightness temperature calibration.

The average of the ten pyrometer samples at 12.51 amps is 1821° C (2094 K) with a standard deviation of <4 K. A least-squares linear fit to the data from calibration 2 is also shown in Figure E-1. Comparing the best-fit line to the data, it is evident that there is a difference between the data recorded from the "low-range" setting and the data recorded on the "high-range" setting. This difference is treated as a 35 K bias in the uncertainty calculations.

The lamp brightness temperature at 765 nm was determined from the measured value at 653 nm by comparing the response of the spectrometer to a calibrated lamp at the two wavelengths. To develop this method, consider that the spectrometer response to illumination is given as:

$$V(\lambda_1) = cS(\lambda_1)I(\lambda_1) \qquad \text{(E.1)}$$

where

c = a calibration constant

$S(\lambda_1)$ = the relative response of the spectrometer at λ_1

$I(\lambda_1)$ = the spectral radiant flux density at λ_1

and

$$I(\lambda_1) = \varepsilon(\lambda_1)I_b(\lambda_1) \qquad \text{(E.2)}$$

where

$\varepsilon(\lambda_1)$ = the emissivity at λ_1

$I_b(\lambda_1)$ = the black body spectral radiant flux density.

Now, if the spectrometer observes the source lamp at λ_1, the response, $V(\lambda_1)$ will be the same as if it had been illuminated by a blackbody at T_{b,λ_1}. If the spectrometer observes the source lamp at λ_2, the response, $V(\lambda_2)$ will be the same as if it had been illuminated by another blackbody at an unknown temperature, T_{b,λ_2}. Since we have

$$V(\lambda) = cS(\lambda)I(\lambda), \qquad \text{(E.3)}$$

we can ratio $V(\lambda_1)$ and $V(\lambda_2)$ and find that

$$\frac{V(\lambda_1)}{V(\lambda_2)} = \frac{S(\lambda_1)I_b(\lambda_1)}{S(\lambda_2)I_b(\lambda_2)}. \qquad \text{(E.4)}$$

Since $I_b(\lambda)$ can be related to temperature, if the ratio $S(\lambda_1)/S(\lambda_2)$ can be determined, then the unknown temperature can be determined.

The relative response of the spectrometer was determined by observing an irradiance calibrated tungsten lamp at the two wavelengths. The well known Planck expression for $I_b(\lambda)$ is

$$I_b(\lambda) = \frac{C_1}{\lambda^5\left(e^{\frac{hc}{\lambda kT}} - 1\right)}. \qquad \text{(E.5)}$$

Substituting this expression into the ratio, rearranging terms and recognizing that the temperature of the blackbody is the brightness temperature, the expression

$$T_{b,765} = hc\left[\lambda_{765}k\ln\left(\frac{V(\lambda_{653})}{V(\lambda_{765})}\frac{S(\lambda_{765})}{S(\lambda_{653})}\left(\frac{\lambda_{653}}{\lambda_{765}}\right)^5\left(e^{\frac{hc}{\lambda_{653}kT}} - 1\right) + 1\right)\right]^{-1} \qquad \text{(E.6)}$$

gives the brightness temperature of the lamp at 765 nm. The ratio $V(\lambda_{653})/V(\lambda_{765})$ was determined before each series of flame temperature measurements. Based on the above measurements and procedure, the lamp brightness temperature at 765 nm was determined to be 2043 K

Appendix F

Tabulation of Thermodynamic Properties

Tables of thermodynamic properties and curve-fit coefficients as reported by PAC91 [65] are given in this appendix. Curve fit coefficients for thermodynamic functions are given in the NASA [52] format discussed in Section 5.2 (Tables F-1 through F-9). Coefficients are specified for two temperature ranges, 0 K < T < 1000 K and 1000 K < T < 6000 K. The low-temperature coefficients are a_1 through a_7. The high-temperature coefficients are b_1 through b_7. The thermodynamic properties for each species for which properties were determined in this work are tabulated in Tables F-10 through F-18.

Table F-1 Curve fit coefficients for KO.

a_1	3.43E+00	b_1	4.40E+00
a_2	4.77E-03	b_2	1.18E-04
a_3	-8.74E-06	b_3	-5.33E-08
a_4	7.35E-09	b_4	1.06E-11
a_5	-2.34E-12	b_5	-7.71E-16
a_6	5.80E+03	b_6	5.63E+03
a_7	7.88E+00	b_7	3.35E+00

Table F-2 Curve fit coefficients for KO_2.

a_1	4.14E+00	b_1	6.21E+00
a_2	8.21E-03	b_2	8.85E-04
a_3	-1.06E-05	b_3	-3.90E-07
a_4	6.74E-09	b_4	7.62E-11
a_5	-1.71E-12	b_5	-5.48E-15
a_6	-1.56E+04	b_6	-1.60E+04
a_7	7.78E+00	b_7	-2.54E+00

Table F-3 Curve fit coefficients for KOH.

a_1	3.81E+00	b_1	5.67E+00
a_2	1.25E-02	b_2	1.20E-03
a_3	-2.41E-05	b_3	-3.29E-07
a_4	2.13E-08	b_4	4.14E-11
a_5	-6.93E-12	b_5	-1.94E-15
a_6	-2.94E+04	b_6	-2.96E+04
a_7	4.10E+00	b_7	-3.94E+00

Table F-4 Curve fit coefficients for KS.

a_1	3.84E+00	b_1	4.44E+00
a_2	3.04E-03	b_2	6.53E-05
a_3	-5.67E-06	b_3	-2.97E-08
a_4	4.84E-09	b_4	5.91E-12
a_5	-1.56E-12	b_5	-4.31E-16
a_6	1.22E+04	b_6	1.21E+04
a_7	7.51E+00	b_7	4.70E+00

Table F-5 Curve fit coefficients for KS_2.

a_1	4.68E+00	b_1	6.77E+00
a_2	1.02E-02	b_2	2.70E-04
a_3	-1.85E-05	b_3	-1.22E-07
a_4	1.55E-08	b_4	2.42E-11
a_5	-4.90E-12	b_5	-1.76E-15
a_6	-3.61E+03	b_6	-3.98E+03
a_7	7.23E+00	b_7	-2.54E+00

Table F-6 Curve fit coefficients for KSH.

a_1	5.37E+00	b_1	5.67E+00
a_2	5.25E-03	b_2	1.68E-03
a_3	-1.05E-05	b_3	-6.46E-07
a_4	1.05E-08	b_4	1.14E-10
a_5	-3.79E-12	b_5	-7.68E-15
a_6	-7.99E+03	b_6	-7.96E+03
a_7	-7.12E-01	b_7	-1.62E+00

Table F-7 Curve fit coefficients for KOS.

a_1	3.78E+00	b_1	6.40E+00
a_2	1.14E-02	b_2	6.80E-04
a_3	-1.77E-05	b_3	-3.02E-07
a_4	1.32E-08	b_4	5.93E-11
a_5	-3.85E-12	b_5	-4.28E-15
a_6	-2.28E+04	b_6	-2.33E+04
a_7	1.00E+01	b_7	-2.69E+00

Table F-8 Curve fit coefficients for KSO_2.

a_1	3.64E+00	b_1	8.56E+00
a_2	2.03E-02	b_2	1.64E-03
a_3	-2.88E-05	b_3	-7.25E-07
a_4	2.00E-08	b_4	1.42E-10
a_5	-5.48E-12	b_5	-1.02E-14
a_6	-4.99E+04	b_6	-5.10E+04
a_7	1.12E+01	b_7	-1.29E+01

Table F-9 Curve fit coefficients for HOSO.

a_1	4.53E+00	b_1	6.18E+00
a_2	8.44E-03	b_2	3.08E-03
a_3	-7.63E-06	b_3	-1.26E-06
a_4	3.35E-09	b_4	2.31E-10
a_5	-4.80E-13	b_5	-1.57E-14
a_6	-3.07E+04	b_6	-3.11E+04
a_7	6.48E+00	b_7	-1.81E+00

Table F-10 Thermodynamic properties for KO.

T DEG-K	CP J/MOL-K	H-H298 KJ/MOL	S J/MOL-K	-(G-H298)/T J/MOL-K	H KJ/MOL	DELTA H KJ/MOL	LOG K
0	-------	-9.517	-------	-------	48.442	59.870	-------
100	30.074	-6.590	201.278	267.175	51.369	59.614	-27.0101
200	33.598	-3.395	223.276	240.252	54.564	58.761	-11.5299
298.15	35.350	0.000	237.065	237.065	57.959	57.959	-6.5075
300	35.372	0.065	237.284	237.065	58.024	57.942	-6.4448
400	36.182	3.648	247.584	238.464	61.607	54.575	-3.9997
500	36.599	7.289	255.707	241.129	65.248	53.574	-2.5867
600	36.838	10.962	262.403	244.133	68.921	52.623	-1.6617
700	36.986	14.654	268.094	247.160	72.613	51.690	-1.0128
800	37.084	18.357	273.039	250.092	76.317	50.742	-0.5349
900	37.152	22.070	277.411	252.890	80.029	49.755	-0.1701
1000	37.202	25.787	281.328	255.541	83.746	48.702	0.1157
1100	37.238	29.509	284.876	258.049	87.468	47.552	0.3444
1200	37.266	33.235	288.117	260.422	91.194	46.280	0.5301
1300	37.288	36.962	291.101	262.669	94.922	44.853	0.6828
1400	37.305	40.692	293.865	264.799	98.651	43.244	0.8093
1500	37.320	44.423	296.439	266.824	102.383	41.421	0.9147
1600	37.331	48.156	298.848	268.751	106.115	39.352	1.0027
1700	37.341	51.890	301.112	270.589	109.849	37.009	1.0761
1800	37.349	55.624	303.246	272.344	113.583	34.357	1.1372
1900	37.355	59.359	305.266	274.024	117.318	31.366	1.1874
2000	37.361	63.095	307.182	275.635	121.054	28.003	1.2283
2100	37.366	66.831	309.005	277.181	124.791	24.239	1.2609
2200	37.371	70.568	310.744	278.667	128.527	20.040	1.2860
2300	37.374	74.306	312.405	280.098	132.265		
2400	37.378	78.043	313.996	281.478	136.002		
2500	37.381	81.781	315.521	282.809	139.740		
2600	37.383	85.519	316.988	284.096	143.478		
2700	37.386	89.258	318.398	285.340	147.217		
2800	37.388	92.996	319.758	286.545	150.955		
2900	37.390	96.735	321.070	287.713	154.694		
3000	37.391	100.474	322.338	288.846	158.433		
3100	37.393	104.214	323.564	289.947	162.173		
3200	37.394	107.953	324.751	291.016	165.912		
3300	37.395	111.692	325.902	292.056	169.651		
3400	37.397	115.432	327.018	293.068	173.391		
3500	37.398	119.172	328.102	294.053	177.131		
3600	37.399	122.911	329.156	295.014	180.871		
3700	37.399	126.651	330.180	295.950	184.610		
3800	37.400	130.391	331.178	296.864	188.350		
3900	37.401	134.131	332.149	297.757	192.090		
4000	37.402	137.872	333.096	298.628	195.831		
4100	37.402	141.612	334.020	299.480	199.571		
4200	37.403	145.352	334.921	300.313	203.311		
4300	37.404	149.092	335.801	301.129	207.051		
4400	37.404	152.833	336.661	301.926	210.792		
4500	37.405	156.573	337.502	302.708	214.532		
4600	37.405	160.314	338.324	303.473	218.273		
4700	37.405	164.054	339.128	304.223	222.013		
4800	37.406	167.795	339.916	304.959	225.754		
4900	37.406	171.535	340.687	305.680	229.494		
5000	37.407	175.276	341.443	306.388	233.235		
5100	37.407	179.017	342.183	307.082	236.976		
5200	37.407	182.757	342.910	307.764	240.716		
5300	37.408	186.498	343.622	308.434	244.457		
5400	37.408	190.239	344.322	309.092	248.198		
5500	37.408	193.980	345.008	309.739	251.939		
5600	37.408	197.721	345.682	310.375	255.680		
5700	37.409	201.461	346.344	311.000	259.420		
5800	37.409	205.202	346.995	311.615	263.161		
6000	37.409	212.684	348.263	312.816	270.643		

0*A CHANGE IN PHASE OF AN ASSIGNED REFERENCE ELEMENT HAS OCCURRED BETWEEN THIS TEMPERATURE AND THE PRECEDING ONE,
K -- 336.860

Table F-11 Thermodynamic properties for KO_2.

T DEG-K	CP J/MOL-K	H-H298 KJ/MOL	S J/MOL-K	-(G-H298)/T J/MOL-K	H KJ/MOL	DELTA H KJ/MOL	LOG K
0	-------	-12.149	-------	-------	-128.858	-113.090	-------
100	37.316	-8.732	230.587	317.903	-125.441	-114.307	60.8393
200	44.724	-4.580	259.066	281.966	-121.289	-115.658	30.8387
298.15	48.314	0.000	277.650	277.650	-116.710	-116.710	20.8550
300	48.368	0.089	277.949	277.651	-116.620	-116.730	20.7290
400	50.853	5.057	292.223	279.580	-111.652	-120.197	15.5686
500	52.643	10.237	303.774	283.300	-106.473	-121.190	12.4170
600	53.921	15.569	313.491	287.544	-101.141	-122.061	10.2998
700	54.838	21.009	321.876	291.863	-95.700	-122.873	8.77690
800	55.506	26.528	329.245	296.085	-90.181	-123.675	7.62730
900	56.001	32.105	335.812	300.140	-84.605	-124.500	6.72720
1000	56.376	37.724	341.733	304.009	-78.985	-125.384	6.00220
1100	56.666	43.377	347.120	307.687	-73.333	-126.358	5.40460
1200	56.893	49.055	352.061	311.181	-67.654	-127.453	4.90250
1300	57.074	54.754	356.622	314.504	-61.955	-128.701	4.47380
1400	57.221	60.469	360.857	317.665	-56.240	-130.132	4.10250
1500	57.342	66.197	364.810	320.678	-50.512	-131.780	3.77690
1600	57.441	71.937	368.514	323.553	-44.773	-133.676	3.48810
1700	57.525	77.685	371.998	326.301	-39.024	-135.852	3.22930
1800	57.595	83.441	375.289	328.932	-33.268	-138.342	2.99550
1900	57.656	89.204	378.404	331.455	-27.506	-141.177	2.78200
2000	57.707	94.972	381.363	333.877	-21.737	-144.390	2.58600
2100	57.752	100.745	384.180	336.206	-15.964	-148.013	2.40420
2200	57.791	106.522	386.867	338.448	-10.187	-152.078	2.23460
2300	57.825	112.303	389.437	340.609	-4.406		
2400	57.856	118.087	391.899	342.695	1.378		
2500	57.882	123.874	394.261	344.711	7.165		
2600	57.906	129.664	396.532	346.661	12.954		
2700	57.927	135.455	398.717	348.549	18.746		
2800	57.946	141.249	400.824	350.378	24.540		
2900	57.963	147.044	402.858	352.153	30.335		
3000	57.979	152.842	404.823	353.876	36.132		
3100	57.993	158.640	406.725	355.550	41.931		
3200	58.005	164.440	408.566	357.179	47.731		
3300	58.017	170.241	410.351	358.763	53.532		
3400	58.028	176.043	412.083	360.306	59.334		
3500	58.037	181.847	413.766	361.809	65.137		
3600	58.046	187.651	415.401	363.275	70.941		
3700	58.054	193.456	416.991	364.706	76.746		
3800	58.062	199.262	418.539	366.102	82.552		
3900	58.069	205.068	420.048	367.466	88.359		
4000	58.075	210.875	421.518	368.799	94.166		
4100	58.082	216.683	422.952	370.103	99.974		
4200	58.087	222.492	424.352	371.378	105.782		
4300	58.092	228.301	425.719	372.625	111.591		
4400	58.097	234.110	427.054	373.847	117.401		
4500	58.102	239.920	428.360	375.044	123.211		
4600	58.106	245.731	429.637	376.217	129.021		
4700	58.110	251.541	430.887	377.367	134.832		
4800	58.114	257.353	432.110	378.495	140.643		
4900	58.117	263.164	433.308	379.601	146.455		
5000	58.121	268.976	434.483	380.687	152.266		
5100	58.124	274.788	435.634	381.753	158.079		
5200	58.127	280.601	436.762	382.801	163.891		
5300	58.130	286.414	437.869	383.829	169.704		
5400	58.132	292.227	438.956	384.840	175.517		
5500	58.135	298.040	440.023	385.834	181.330		
5600	58.137	303.854	441.070	386.811	187.144		
5800	58.141	315.481	443.110	388.717	198.772		
6000	58.145	327.110	445.082	390.563	210.401		

0*A CHANGE IN PHASE OF AN ASSIGNED REFERENCE ELEMENT HAS OCCURRED BETWEEN THIS TEMPERATURE AND THE PRECEDING ONE,
K -- 336.860

Table F-12 Thermodynamic properties for KOH.

T DEG-K	CP J/MOL-K	H-H298 KJ/MOL	S J/MOL-K	-(G-H298)/T J/MOL-K	H KJ/MOL	DELTA H KJ/MOL	LOG K
0	-------	-11.674	-------	-------	-243.662	-228.000	-------
25	29.101	-10.948	150.390	588.310	-242.936		
50	29.331	-10.219	170.591	374.971	-242.207		
75	31.059	-9.468	182.747	308.987	-241.456		
100	34.162	-8.654	192.089	278.629	-240.642		
150	40.449	-6.783	207.179	252.399	-238.771		
200	44.784	-4.643	219.457	242.672	-236.631		
250	47.504	-2.331	229.765	239.089	-234.319		
298.15	49.185	0.000	238.287	238.287	-231.988	-231.988	40.9396
300	49.237	0.091	238.591	238.288	-231.897	-232.006	40.6891
350	50.386	2.583	246.273	238.893	-229.405	-234.851	34.8991
400	51.179	5.123	253.056	240.249	-226.865	-235.376	30.5130
450	51.749	7.697	259.118	242.014	-224.291	-235.858	27.0937
500	52.179	10.296	264.594	244.002	-221.692	-236.307	24.3541
600	52.805	15.547	274.166	248.254	-216.441	-237.144	20.2329
700	53.296	20.852	282.344	252.555	-211.136	-237.933	17.2790
800	53.759	26.205	289.490	256.734	-205.783	-238.708	15.0562
900	54.230	31.605	295.849	260.732	-200.383	-239.494	13.3217
1000	54.714	37.052	301.588	264.536	-194.936	-240.320	11.9295
1100	55.203	42.548	306.826	268.146	-189.440	-241.215	10.7864
1200	55.687	48.092	311.650	271.573	-183.896	-242.208	9.8300
1300	56.154	53.684	316.126	274.831	-178.304	-243.331	9.0172
1400	56.599	59.322	320.304	277.931	-172.666	-244.614	8.3171
1500	57.017	65.003	324.223	280.888	-166.985	-246.092	7.7069
1600	57.406	70.725	327.915	283.712	-161.263	-247.796	7.1695
1700	57.765	76.483	331.407	286.417	-155.505	-249.762	6.6919
1800	58.095	82.277	334.718	289.009	-149.711	-252.021	6.2638
1900	58.398	88.101	337.867	291.498	-143.887	-254.610	5.8769
2000	58.675	93.955	340.870	293.893	-138.033	-257.559	5.5251
2200	59.159	105.740	346.485	298.421	-126.248	-264.672	4.9056
2400	59.563	117.613	351.651	302.646	-114.375		
2600	59.901	129.561	356.432	306.601	-102.427		
2800	60.186	141.570	360.882	310.321	-90.418		
3000	60.427	153.632	365.043	313.832	-78.356		
3200	60.632	165.739	368.949	317.156	-66.249		
3400	60.807	177.883	372.630	320.311	-54.105		
3600	60.958	190.060	376.110	323.316	-41.928		
3800	61.088	202.265	379.410	326.182	-29.723		
4000	61.202	214.494	382.546	328.923	-17.494		
4200	61.302	226.745	385.535	331.548	-5.243		
4400	61.389	239.014	388.389	334.068	7.026		
4600	61.466	251.300	391.119	336.489	19.312		
4800	61.535	263.600	393.737	338.820	31.612		
5000	61.596	275.913	396.250	341.067	43.925		
5200	61.651	288.238	398.667	343.237	56.250		
5400	61.700	300.573	400.994	345.332	68.585		
5600	61.744	312.918	403.239	347.361	80.930		
5800	61.784	325.270	405.407	349.326	93.282		
6000	61.820	337.631	407.502	351.230	105.643		

0*A CHANGE IN PHASE OF AN ASSIGNED REFERENCE ELEMENT HAS OCCURRED BETWEEN THIS TEMPERATURE AND THE PRECEDING ONE,
K -- 336.860

Table F-13 Thermodynamic properties for KS.

T DEG-K	CP J/MOL-K	H-H298 KJ/MOL	S J/MOL-K	-(G-H298)/T J/MOL-K	H KJ/MOL	DELTA H KJ/MOL	LOG K
0	-------	-9.830	-------	-------	102.150	113.650	-------
100	31.495	-6.862	212.688	281.309	105.118	114.195	-51.0522
200	35.026	-3.506	235.809	253.339	108.474	113.317	-21.3060
298.15	36.220	0.000	250.056	250.056	111.980	111.980	-11.6102
300	36.233	0.067	250.280	250.056	112.047	111.949	-11.4890
400	36.724	3.718	260.780	251.485	115.698	105.531	-6.7201
500	36.965	7.404	269.003	254.196	119.383	102.167	-4.0034
600	37.099	11.108	275.756	257.243	123.087	99.248	-2.2490
700	37.182	14.822	281.481	260.307	126.802	96.617	-1.0304
800	37.236	18.543	286.450	263.271	130.523	94.153	-0.1402
900	37.273	22.268	290.838	266.095	134.248	91.682	0.5343
1000	37.300	25.997	294.766	268.769	137.977	89.171	1.0593
1100	37.320	29.728	298.322	271.297	141.708	86.586	1.4768
1200	37.335	33.461	301.570	273.686	145.441	83.896	1.8143
1300	37.347	37.195	304.559	275.948	149.175	81.068	2.0907
1400	37.356	40.930	307.327	278.091	152.910	78.072	2.3192
1500	37.364	44.666	309.905	280.127	156.646	74.875	2.5096
1600	37.370	48.403	312.317	282.065	160.383	71.446	2.6689
1700	37.375	52.140	314.582	283.912	164.120	67.753	2.8026
1800	37.379	55.878	316.719	285.675	167.858	63.764	2.9150
1900	37.383	59.616	318.740	287.363	171.596	59.447	3.0092
2000	37.386	63.354	320.657	288.980	175.334	54.770	3.0878
2100	37.389	67.093	322.481	290.532	179.073	49.703	3.1529
2200	37.391	70.832	324.221	292.024	182.812	44.213	3.2060
2300	37.393	74.571	325.883	293.461	186.551		
2400	37.395	78.311	327.474	294.845	190.291		
2500	37.397	82.050	329.001	296.181	194.030		
2600	37.398	85.790	330.468	297.472	197.770		
2700	37.399	89.530	331.879	298.720	201.510		
2800	37.400	93.270	333.239	299.929	205.250		
2900	37.401	97.010	334.552	301.100	208.990		
3000	37.402	100.750	335.820	302.236	212.730		
3100	37.403	104.491	337.046	303.340	216.470		
3200	37.404	108.231	338.234	304.412	220.211		
3300	37.405	111.971	339.385	305.454	223.951		
3400	37.405	115.712	340.501	306.468	227.692		
3500	37.406	119.452	341.586	307.456	231.432		
3600	37.406	123.193	342.639	308.419	235.173		
3700	37.407	126.934	343.664	309.358	238.913		
3800	37.407	130.674	344.662	310.274	242.654		
3900	37.408	134.415	345.634	311.168	246.395		
4000	37.408	138.156	346.581	312.042	250.136		
4100	37.408	141.897	347.504	312.895	253.876		
4200	37.409	145.638	348.406	313.730	257.617		
4300	37.409	149.379	349.286	314.547	261.358		
4400	37.409	153.119	350.146	315.346	265.099		
4500	37.410	156.860	350.987	316.129	268.840		
4600	37.410	160.601	351.809	316.896	272.581		
4700	37.410	164.342	352.614	317.647	276.322		
4800	37.410	168.083	353.401	318.384	280.063		
4900	37.410	171.824	354.173	319.106	283.804		
5000	37.411	175.565	354.928	319.815	287.545		
5100	37.411	179.307	355.669	320.511	291.286		
5200	37.411	183.048	356.396	321.194	295.027		
5300	37.411	186.789	357.108	321.865	298.768		
5400	37.411	190.530	357.808	322.524	302.509		
5500	37.411	194.271	358.494	323.172	306.251		
5600	37.412	198.012	359.168	323.809	309.992		
5800	37.412	205.494	360.481	325.051	317.474		
6000	37.412	212.977	361.749	326.253	324.957		

0*A CHANGE IN PHASE OF AN ASSIGNED REFERENCE ELEMENT HAS OCCURRED BETWEEN THIS TEMPERATURE AND THE PRECEDING ONE,
K -- 336.860
S -- 388.360

Table F-14 Thermodynamic properties for KS_2.

T DEG-K	CP J/MOL-K	H-H298 KJ/MOL	S J/MOL-K	-(G-H298)/T J/MOL-K	H KJ/MOL	DELTA H KJ/MOL	LOG K
0	-------	-13.280	-------	-------	-29.012	-13.100	-------
100	41.241	-9.714	248.989	346.128	-25.446	-12.647	16.4426
200	49.859	-5.100	280.622	306.124	-20.833	-13.910	13.0263
298.15	53.587	0.000	301.321	301.321	-15.732	-15.732	11.7665
300	53.633	0.099	301.653	301.322	-15.633	-15.774	11.7499
400	55.404	5.561	317.354	303.451	-10.171	-24.986	10.9369
500	56.334	11.153	329.827	307.522	-4.50	-30.380	10.2219
600	56.874	16.815	340.150	312.124	1.083	-34.921	9.6546
700	57.212	22.521	348.944	316.772	6.788	-38.907	9.1964
800	57.437	28.254	356.600	321.282	12.522	-42.563	8.8172
900	57.593	34.006	363.374	325.590	18.274	-46.207	8.4957
1000	57.707	39.771	369.448	329.677	24.039	-49.882	8.2172
1100	57.791	45.546	374.953	333.547	29.814	-53.623	7.9718
1200	57.856	51.329	379.984	337.210	35.596	-57.464	7.7523
1300	57.906	57.117	384.617	340.681	41.385	-61.437	7.5534
1400	57.947	62.910	388.910	343.974	47.177	-65.576	7.3714
1500	57.979	68.706	392.909	347.105	52.974	-69.912	7.2031
1600	58.006	74.505	396.652	350.086	58.773	-74.479	7.0461
1700	58.028	80.307	400.169	352.929	64.575	-79.307	6.8985
1800	58.047	86.111	403.486	355.647	70.378	-84.431	6.7590
1900	58.062	91.916	406.625	358.248	76.184	-89.880	6.6259
2000	58.076	97.723	409.604	360.742	81.991	-95.688	6.4985
2100	58.088	103.532	412.437	363.137	87.799	-101.886	6.3758
2200	58.098	109.341	415.140	365.440	93.608	-108.506	6.2569
2300	58.106	115.151	417.723	367.657	99.419		
2400	58.114	120.962	420.196	369.795	105.230		
2500	58.121	126.774	422.568	371.859	111.041		
2600	58.127	132.586	424.848	373.853	116.854		
2700	58.132	138.399	427.042	375.783	122.667		
2800	58.137	144.213	429.156	377.652	128.480		
2900	58.142	150.027	431.196	379.463	134.294		
3000	58.146	155.841	433.167	381.220	140.109		
3100	58.149	161.656	435.074	382.927	145.923		
3200	58.152	167.471	436.920	384.586	151.738		
3300	58.155	173.286	438.710	386.199	157.554		
3400	58.158	179.102	440.446	387.769	163.369		
3500	58.160		442.132	389.298	169.185		
3600	58.163	190.734	443.770	390.789	175.002		
3700	58.165	196.550	445.364	392.242	180.818		
3800	58.167	202.367	446.915	393.661	186.634		
3900	58.168	208.184	448.426	395.046	192.451		
4000	58.170	214.001	449.899	396.399	198.268		
4100	58.172	219.818	451.335	397.721	204.085		
4200	58.173	225.635	452.737	399.014	209.902		
4300	58.174	231.452	454.106	400.280	215.720		
4400	58.176	237.270	455.443	401.518	221.537		
4500	58.177	243.087	456.751	402.731	227.355		
4600	58.178	248.905	458.029	403.919	233.173		
4700	58.179	254.723	459.280	405.084	238.990		
4800	58.180	260.541	460.505	406.226	244.808		
4900	58.181	266.359	461.705	407.346	250.626		
5000	58.181	272.177	462.880	408.445	256.444		
5100	58.182	277.995	464.033	409.524	262.263		
5200	58.183	283.813	465.162	410.583	268.081		
5300	58.184	289.632	466.271	411.623	273.899		
5400	58.184	295.450	467.358	412.645	279.718		
5500	58.185	301.269	468.426	413.650	285.536		
5600	58.185	307.087	469.474	414.637	291.355		
5800	58.187	318.724	471.516	416.564	302.992		
6000	58.188	330.362	473.489	418.428	314.629		

0*A CHANGE IN PHASE OF AN ASSIGNED REFERENCE ELEMENT HAS OCCURRED BETWEEN THIS TEMPERATURE AND THE PRECEDING ONE,
K -- 336.860
S -- 388.360

Table F-15 Thermodynamic properties for KSH.

T DEG-K	CP J/MOL-K	H-H298 KJ/MOL	S J/MOL-K	-(G-H298)/T J/MOL-K	H KJ/MOL	DELTA H KJ/MOL	LOG K
0	-------	-12.940	-------	-------	-64.734	-49.000	----
100	41.177	-9.649	206.208	302.695	-61.443	-49.631	31.5503
200	49.670	-5.007	238.049	263.082	-56.801	-50.570	18.4942
298.15	51.950	0.000	258.386	258.386	-51.794	-51.794	14.1037
300	51.975	0.096	258.708	258.387	-51.698	-51.823	14.0480
400	52.905	5.345	273.802	260.439	-46.449	-58.094	11.6910
500	53.508	10.667	285.675	264.341	-41.127	-61.284	10.1365
600	54.091	16.047	295.481	268.737	-35.748	-63.992	9.0467
700	54.719	21.487	303.866	273.171	-30.308	-66.366	8.2366
800	55.375	26.991	311.215	277.476	-24.803	-68.523	7.6079
900	56.024	32.561	317.775	281.596	-19.233	-70.636	7.1034
1000	56.640	38.195	323.710	285.515	-13.599	-72.745	6.6875
1100	57.207	43.888	329.136	289.238	-7.906	-74.888	6.3372
1200	57.719	49.635	334.136	292.774	-2.160	-77.103	6.0366
1300	58.176	55.430	338.774	296.136	3.636	-79.430	5.7747
1400	58.582	61.268	343.101	299.338	9.474	-81.905	5.5434
1500	58.939	67.144	347.155	302.392	15.350	-84.565	5.3365
1600	59.255	73.055	350.969	305.310	21.260	-87.447	5.1494
1700	59.534	78.994	354.570	308.103	27.200	-90.584	4.9785
1800	59.780	84.960	357.980	310.780	33.166	-94.012	4.8211
1900	59.997	90.949	361.218	313.350	39.155	-97.764	4.6747
2000	60.191	96.959	364.300	315.821	45.165	-101.874	4.5367
2100	60.363	102.987	367.241	318.200	51.193	-106.375	4.4082
2200	60.516	109.031	370.053	320.493	57.237	-111.299	4.2852
2300	60.653	115.089	372.746	322.707	63.295		
2400	60.776	121.161	375.330	324.846	69.367		
2500	60.887	127.244	377.813	326.916	75.450		
2600	60.987	133.338	380.203	328.919	81.544		
2700	61.078	139.441	382.507	330.862	87.647		
2800	61.160	145.553	384.729	332.746	93.759		
2900	61.235	151.673	386.877	334.576	99.879		
3000	61.303	157.800	388.954	336.354	106.006		
3100	61.365	163.933	390.965	338.084	112.139		
3200	61.422	170.073	392.914	339.767	118.279		
3300	61.474	176.218	394.805	341.406	124.424		
3400	61.523	182.368	396.641	343.004	130.573		
3500	61.567	188.522	398.425	344.562	136.728		
3600	61.608	194.681	400.160	346.082	142.887		
3700	61.646	200.844	401.849	347.567	149.049		
3800	61.681	207.010	403.493	349.017	155.216		
3900	61.714	213.180	405.096	350.434	161.386		
4000	61.745	219.353	406.659	351.821	167.559		
4100	61.773	225.529	408.184	353.177	173.735		
4200	61.799	231.707	409.673	354.504	179.913		
4300	61.824	237.888	411.127	355.804	186.094		
4400	61.847	244.072	412.549	357.078	192.278		
4500	61.869	250.258	413.939	358.326	198.464		
4600	61.889	256.446	415.299	359.550	204.652		
4700	61.909	262.636	416.630	360.750	210.842		
4800	61.927	268.828	417.934	361.928	217.033		
4900	61.944	275.021	419.211	363.084	223.227		
5000	61.960	281.216	420.462	364.219	229.422		
5100	61.975	287.413	421.689	365.334	235.619		
5200	61.989	293.611	422.893	366.429	241.817		
5300	62.002	299.811	424.074	367.506	248.017		
5400	62.015	306.011	425.233	368.564	254.217		
5500	62.027	312.214	426.371	369.605	260.420		
5600	62.039	318.417	427.489	370.629	266.623		
5800	62.060	330.827	429.666	372.627	279.033		
6000	62.079	343.241	431.770	374.564	291.447		

0*A CHANGE IN PHASE OF AN ASSIGNED REFERENCE ELEMENT HAS OCCURRED BETWEEN THIS TEMPERATURE AND THE PRECEDING ONE,
K -- 336.860
S -- 388.360

Table F-16 Thermodynamic properties for KOS.

T DEG-K	CP J/MOL-K	H-H298 KJ/MOL	S J/MOL-K	-(G-H298)/T J/MOL-K	H KJ/MOL	DELTA H KJ/MOL	LOG K
0	-------	-12.225	-------	-------	-188.940	-173.100	-------
100	37.323	-8.808	237.495	325.573	-185.523	-173.556	96.0192
200	45.069	-4.644	266.044	289.265	-181.359	-175.082	50.5402
298.15	49.235	0.000	284.882	284.882	-176.715	-176.715	35.4279
300	49.296	0.091	285.186	284.882	-176.624	-176.750	35.2373
400	51.981	5.165	299.764	286.852	-171.550	-183.230	27.4378
500	53.714	10.456	311.563	290.652	-166.259	-186.518	22.6138
600	54.855	15.888	321.464	294.984	-160.827	-189.289	19.3430
700	55.629	21.415	329.982	299.390	-155.301	-191.735	16.9742
800	56.171	27.006	337.447	303.690	-149.709	-193.998	15.1757
900	56.562	32.644	344.087	307.816	-144.071	-196.260	13.7605
1000	56.853	38.315	350.062	311.747	-138.400	-198.560	12.6150
1100	57.074	44.012	355.492	315.481	-132.703	-200.934	11.6668
1200	57.245	49.728	360.466	319.025	-126.987	-203.416	10.8669
1300	57.381	55.460	365.053	322.392	-121.255	-206.039	10.1816
1400	57.490	61.204	369.310	325.593	-115.512	-208.834	9.5864
1500	57.579	66.957	373.279	328.641	-109.758	-211.835	9.0634
1600	57.652	72.719	376.998	331.548	-103.996	-215.074	8.5989
1700	57.714	78.487	380.495	334.326	-98.228	-218.583	8.1826
1800	57.765	84.261	383.795	336.983	-92.454	-222.395	7.8064
1900	57.809	90.040	386.919	339.530	-86.675	-226.543	7.4636
2000	57.847	95.823	389.886	341.974	-80.892	-231.058	7.1493
2100	57.879	101.609	392.709	344.323	-75.106	-235.973	6.8590
2200	57.907	107.399	395.402	346.584	-69.317	-241.319	6.5892
2300	57.932	113.191	397.977	348.763	-63.525		
2400	57.954	118.985	400.443	350.866	-57.730		
2500	57.973	124.781	402.809	352.896	-51.934		
2600	57.990	130.579	405.083	354.860	-46.136		
2700	58.005	136.379	407.272	356.761	-40.336		
2800	58.019	142.180	409.382	358.603	-34.535		
2900	58.031	147.983	411.418	360.389	-28.732		
3000	58.042	153.787	413.385	362.123	-22.929		
3100	58.052	159.591	415.289	363.808	-17.124		
3200	58.061	165.397	417.132	365.445	-11.318		
3300	58.070	171.204	418.919	367.039	-5.512		
3400	58.077	177.011	420.652	368.590	0.296		
3500	58.084	182.819	422.336	370.102	6.104		
3600	58.091	188.628	423.972	371.576	11.913		
3700	58.097	194.437	425.564	373.013	17.722		
3800	58.102	200.247	427.113	374.417	23.532		
3900	58.107	206.058	428.623	375.787	29.342		
4000	58.112	211.868	430.094	377.127	35.153		
4100	58.116	217.680	431.529	378.436	40.965		
4200	58.120	223.492	432.929	379.717	46.776		
4300	58.124	229.304	434.297	380.971	52.589		
4400	58.127	235.116	435.633	382.198	58.401		
4500	58.130	240.929	436.940	383.400	64.214		
4600	58.134	246.742	438.217	384.578	70.027		
4700	58.136	252.556	439.468	385.732	75.841		
4800	58.139	258.370	440.692	386.865	81.655		
4900	58.142	264.184	441.890	387.975	87.469		
5000	58.144	269.998	443.065	389.065	93.283		
5100	58.146	275.813	444.216	390.136	99.097		
5200	58.148	281.627	445.346	391.186	104.912		
5300	58.150	287.442	446.453	392.219	110.727		
5400	58.152	293.257	447.540	393.233	116.542		
5500	58.154	299.073	448.607	394.230	122.357		
5600	58.156	304.888	449.655	395.211	128.173		
5800	58.159	316.520	451.696	397.124	139.804		
6000	58.162	328.152	453.668	398.976	151.436		

0*A CHANGE IN PHASE OF AN ASSIGNED REFERENCE ELEMENT HAS OCCURRED BETWEEN THIS TEMPERATURE AND THE PRECEDING ONE,
K -- 336.860
S -- 388.360

Table F-17 Thermodynamic properties for KSO_2.

T DEG-K	CP J/MOL-K	H-H298 KJ/MOL	S J/MOL-K	-(G-H298)/T J/MOL-K	H KJ/MOL	DELTA H KJ/MOL	LOG K
0	-------	-14.391	-------	-------	-414.580	-394.400	-------
100	42.329	-10.809	248.832	356.925	-410.999	-396.143	208.3493
200	55.491	-5.853	282.662	311.925	-406.042	-398.331	104.6601
298.15	63.266	0.000	306.367	306.367	-400.189	-400.189	70.3431
300	63.387	0.117	306.759	306.369	-400.072	-400.225	69.9111
400	68.832	6.745	325.788	308.926	-393.445	-406.637	52.3847
500	72.571	13.827	341.575	313.922	-386.363	-409.664	41.7288
600	75.135	21.220	355.048	319.681	-378.969	-412.054	34.5758
700	76.921	28.828	366.772	325.589	-371.361	-414.046	29.4392
800	78.196	36.587	377.131	331.397	-363.602	-415.810	25.5694
900	79.129	44.456	386.398	337.003	-355.733	-417.544	22.5468
1000	79.828	52.405	394.773	342.368	-347.784	-419.297	20.1186
1100	80.363	60.416	402.407	347.484	-339.773	-421.114	18.1234
1200	80.781	68.474	409.419	352.357	-331.715	-423.029	16.4534
1300	81.113	76.569	415.898	356.999	-323.620	-425.080	15.0337
1400	81.380	84.694	421.919	361.423	-315.495	-427.301	13.8107
1500	81.599	92.844	427.542	365.646	-307.346	-429.728	12.7449
1600	81.780	101.013	432.814	369.681	-299.176	-432.395	11.8069
1700	81.931	109.199	437.777	373.542	-290.991	-435.333	10.9738
1800	82.059	117.398	442.463	377.242	-282.791	-438.580	10.2281
1900	82.167	125.610	446.903	380.793	-274.579	-442.166	9.5555
2000	82.260	133.831	451.120	384.204	-266.358	-446.126	8.9452
2100	82.341	142.061	455.136	387.487	-258.128	-450.492	8.3877
2200	82.411	150.299	458.968	390.650	-249.890	-455.296	7.8757
2300	82.473	158.543	462.632	393.700	-241.646		
2400	82.527	166.793	466.144	396.646	-233.396		
2500	82.574	175.049	469.513	399.494	-225.141		
2600	82.617	183.308	472.753	402.250	-216.881		
2700	82.655	191.572	475.872	404.919	-208.618		
2800	82.689	199.839	478.878	407.507	-200.350		
2900	82.719	208.109	481.780	410.019	-192.080		
3000	82.747	216.383	484.585	412.458	-183.807		
3100	82.772	224.659	487.299	414.828	-175.531		
3200	82.795	232.937	489.927	417.134	-167.252		
3300	82.816	241.218	492.475	419.379	-158.972		
3400	82.834	249.500	494.948	421.565	-150.689		
3500	82.852	257.784	497.349	423.696	-142.405		
3600	82.868	266.070	499.683	425.775	-134.119		
3700	82.883	274.358	501.954	427.803	-125.831		
3800	82.896	282.647	504.165	429.784	-117.542		
3900	82.909	290.937	506.318	431.719	-109.252		
4000	82.920	299.229	508.417	433.610	-100.961		
4100	82.931	307.521	510.465	435.460	-92.668		
4200	82.941	315.815	512.463	437.269	-84.375		
4300	82.950	324.109	514.415	439.041	-76.080		
4400	82.959	332.405	516.322	440.776	-67.784		
4500	82.967	340.701	518.187	442.475	-59.488		
4600	82.975	348.998	520.010	444.141	-51.191		
4700	82.982	357.296	521.795	445.774	-42.893		
4800	82.989	365.595	523.542	447.376	-34.595		
4900	82.995	373.894	525.253	448.948	-26.296		
5000	83.001	382.194	526.930	450.491	-17.996		
5100	83.006	390.494	528.574	452.006	-9.695		
5200	83.012	398.795	530.186	453.494	-1.394		
5300	83.017	407.096	531.767	454.956	6.907		
5400	83.021	415.398	533.319	456.393	15.209		
5500	83.026	423.701	534.842	457.806	23.511		
5600	83.030	432.003	536.338	459.195	31.814		
5800	83.038	448.610	539.252	461.905	48.421		
6000	83.045	465.218	542.067	464.531	65.029		

0*A CHANGE IN PHASE OF AN ASSIGNED REFERENCE ELEMENT HAS OCCURRED BETWEEN THIS TEMPERATURE AND THE PRECEDING ONE,
K -- 336.860
S -- 388.360

Table F-18 Thermodynamic properties for HOSO.

T DEG-K	CP J/MOL-K	H-H298 KJ/MOL	S J/MOL-K	-(G-H298)/T J/MOL-K	H KJ/MOL	DELTA H KJ/MOL	LOG K
0	-------	-13.853	-------	-------	-255.253	-237.927	-------
100	43.740	-9.743	234.243	331.674	-251.143	-238.908	124.6865
200	49.480	-5.070	266.402	291.753	-246.470	-240.135	62.1693
298.15	53.675	0.000	286.972	286.972	-241.400	-241.400	41.4770
300	53.746	0.099	287.304	286.973	-241.301	-241.425	41.2165
400	57.276	5.656	303.265	289.125	-235.744	-244.897	30.6714
500	60.159	11.533	316.367	293.301	-229.867	-247.477	24.2455
600	62.456	17.668	327.546	298.100	-223.732	-249.547	19.9190
700	64.310	24.009	337.318	303.019	-217.391	-251.276	16.8051
800	65.848	30.519	346.009	307.859	-210.881	-252.784	14.4545
900	67.156	37.171	353.842	312.540	-204.229	-254.226	12.6156
1000	68.286	43.945	360.977	317.033	-197.455	-255.617	11.1362
1100	69.267	50.824	367.533	321.330	-190.576	-256.969	9.9194
1200	70.118	57.794	373.597	325.436	-183.606	-258.288	8.9000
1300	70.856	64.843	379.240	329.360	-176.557	-259.584	8.0330
1400	71.493	71.962	384.515	333.113	-169.438	-260.862	7.2863
1500	72.041	79.139	389.466	336.707	-162.261	-262.132	6.6358
1600	72.511	86.367	394.131	340.151	-155.033	-263.399	6.0640
1700	72.914	93.639	398.539	343.458	-147.761	-264.668	5.5570
1800	73.258	100.948	402.717	346.635	-140.452	-265.945	5.1042
1900	73.551	108.289	406.686	349.692	-133.111	-267.233	4.6970
2000	73.801	115.657	410.465	352.637	-125.743	-268.537	4.3288
2100	74.014	123.048	414.071	355.477	-118.352	-269.858	3.9940
2200	74.195	130.459	417.519	358.219	-110.941	-271.200	3.6882
2300	74.350	137.886	420.820	360.870	-103.514	-272.564	3.4075
2400	74.481	145.328	423.987	363.434	-96.072	-273.950	3.1490
2500	74.592	152.782	427.030	365.917	-88.618	-275.364	2.9099
2600	74.687	160.246	429.958	368.325	-81.154	-276.801	2.6880
2700	74.767	167.719	432.778	370.660	-73.681	-278.266	2.4815
2800	74.835	175.199	435.498	372.927	-66.201	-279.757	2.2887
2900	74.893	182.685	438.125	375.130	-58.715	-281.275	2.1083
3000	74.941	190.177	440.665	377.273	-51.223	-282.820	1.9390
3100	74.982	197.673	443.123	379.358	-43.727	-284.391	1.7797
3200	75.017	205.173	445.504	381.388	-36.227	-285.990	1.6296
3300	75.045	212.676	447.813	383.366	-28.724	-287.615	1.4877
3400	75.069	220.182	450.054	385.294	-21.218	-289.265	1.3534
3500	75.089	227.690	452.230	387.176	-13.710	-290.940	1.2261
3600	75.105	235.200	454.346	389.012	-6.200	-292.642	1.1052
3700	75.118	242.711	456.404	390.806	1.311	-294.368	0.9900
3800	75.129	250.223	458.407	392.559	8.823	-296.119	0.8804
3900	75.137	257.737	460.359	394.272	16.337	-297.894	0.7757
4000	75.144	265.251	462.261	395.948	23.851	-299.693	0.6757
4100	75.148	272.766	464.117	397.589	31.366	-301.514	0.5799
4200	75.152	280.281	465.928	399.194	38.881	-303.360	0.4882
4300	75.154	287.796	467.696	400.767	46.396	-305.227	0.4002
4400	75.155	295.311	469.424	402.308	53.911	-307.117	0.3156
4500	75.155	302.827	471.113	403.818	61.427	-309.029	0.2344
4600	75.154	310.342	472.765	405.299	68.942	-310.963	0.1562
4700	75.153	317.857	474.381	406.752	76.457	-312.917	0.0807
4800	75.151	325.373	475.963	408.177	83.973	-314.892	0.0081
4900	75.149	332.888	477.513	409.576	91.488	-316.888	-0.0620
5000	75.146	340.402	479.031	410.950	99.002	-318.903	-0.1298
5100	75.143	347.917	480.519	412.300	106.517	-320.938	-0.1953
5200	75.139	355.431	481.978	413.626	114.031	-322.991	-0.2587
5300	75.136	362.945	483.409	414.929	121.545	-325.061	-0.3202
5400	75.132	370.458	484.814	416.210	129.058	-327.150	-0.3797
5500	75.128	377.971	486.192	417.470	136.571	-329.256	-0.4374
5600	75.124	385.484	487.546	418.709	144.084	-331.376	-0.4934
5800	75.116	400.508	490.182	421.129	159.108	-335.662	-0.6007
6000	75.107	415.530	492.728	423.473	174.130	-340.001	-0.7021

0*A CHANGE IN PHASE OF AN ASSIGNED REFERENCE ELEMENT HAS OCCURRED BETWEEN THIS TEMPERATURE AND THE PRECEDING ONE,
S -- 388.360

Appendix G

Inputs for LSENS Plug-Flow Reactor Calculations

The flow rates of the primary combustor fuels and oxidizers were taken from actual test settings of tests LMF4-R and LMF5-H in the UTSI/DOE CFFF. The potassium seed level was taken as a parameter and was specified by the K_2/S ratio. In this Appendix, the derivation of the potassium seed flow rate and the fuel and oxidizer component and overall percentages will be given.

The mass balance for the primary combustor:

$$\dot{m}_{Total} = \dot{m}_{Fuels} + \dot{m}_{Oxidizers} . \qquad \text{(G.1)}$$

Here, m_{Fuels} given by:

$$\dot{m}_{Fuels} = \dot{m}_{Coal} + \dot{m}_{H_2O}\Big|_{Coal} + \dot{m}_{FuelOil} + \dot{m}_{K_2CO_3} + \dot{m}_{H_2O}\Big|_{K_2CO_3} \qquad \text{(G.2)}$$

and $m_{Oxidizers}$ given by:

$$\dot{m}_{Oxidizers} = \dot{m}_{Air} + \dot{m}_{O_2} + \dot{m}_{N_2} \qquad \text{(G.3)}$$

where symbols are defined as follows:

m_{Coal} = mass flow rate of coal without ash components

$m_{H_2O}|_{Coal}$ = mass flow rate of water from moisture in the pulverized coal

$m_{FuelOil}$ = mass flow rate of fuel oil

$m_{K_2CO_3}$ = mass flow rate of potassium carbonate seed

$m_{H_2O}|_{K_2CO_3}$ = mass flow rate of water from seed solution

m_{Air} = mass flow rate of air

m_{O_2} = mass flow rate of oxygen

m_{N_2} = mass flow rate of nitrogen

Each of these parameters is specified except for $m_{K_2CO_3}$ and $m_{H_2O|_{K_2CO_3}}$, which were specified via the molar K_2/S ratio. The value of $m_{K_2CO_3}$ depends on the molar quantity of sulfur in the coal and fuel oil. The molar flowrate of potassium carbonate is given as follows:

$$\dot{n}_{K_2CO_3} = (K_2 / S)\dot{n}_S \qquad \text{(G.4)}$$

where n_S is the molar flowrate of sulfur in the mixture. This is given by:

$$\dot{n}_s = \frac{\dot{m}_S}{W_S} \qquad \text{(G.5)}$$

The total mass flow rate of sulfur, m_S, is determined from the sulfur content of the coal and fuel oil as follows:

$$\dot{m}_S = \dot{m}_{Coal}\alpha_{Coal} + \dot{m}_{FuelOil}\alpha_{FuelOil} \qquad \text{(G.6)}$$

where α_{Coal} and $\alpha_{FuelOil}$ are the mass fractions of sulfur in the coal and fuel oil, respectively. The compositions of the coal and fuel oil were taken from [5] and [6] in the main reference section of this dissertation. Finally, the mass flow rate of potassium carbonate seed is given by:

$$\dot{m}_{K_2CO_3} = \frac{W_{K_2CO_3}(K_2 / S)(\dot{m}_{Coal}\alpha_{Coal} + \dot{m}_{FuelOil}\alpha_{FuelOil})}{W_S}. \qquad \text{(G.7)}$$

For LMF5, the seed was injected as a solution. The solution was 47% K_2CO_3 by mass. The mass flow rates of water from the seed is then:

$$\dot{m}_{H_2O}\Big|_{K_2CO_3} = \frac{0.53\dot{m}_{K_2CO_3}}{0.47} \qquad \text{(G.8)}$$

Now, the relative percentages of the fuels and oxidizers are determined simple as follows:

$$Y_{Coal}^{Fuels} = \frac{\dot{m}_{Coal}}{\dot{m}_{Fuels}} \qquad \text{(G.9)}$$

$$Y_{FuelOil}^{Fuels} = \frac{\dot{m}_{FuelOil}}{\dot{m}_{Fuels}} \qquad \text{(G.10)}$$

$$Y_{H_2O}^{Fuels} = \frac{\dot{m}_{H_2O}\Big|_{Coal} + \dot{m}_{H_2O}\Big|_{K_2CO_3}}{\dot{m}_{Fuels}} \qquad \text{(G.11)}$$

$$Y_{K_2CO_3}^{Fuels} = \frac{\dot{m}_{K_2CO_3}}{\dot{m}_{Fuels}} \qquad \text{(G.12)}$$

$$Y_{Air}^{Oxidizers} = \frac{\dot{m}_{Air}}{\dot{m}_{Oxidizers}} \qquad \text{(G.13)}$$

$$Y_{O_2}^{Oxidizers} = \frac{\dot{m}_{O_2}}{\dot{m}_{Oxidizers}} \qquad \text{(G.14)}$$

$$Y_{N_2}^{Oxidizers} = \frac{\dot{m}_{N_2}}{\dot{m}_{Oxidizers}} \qquad \text{(G.15)}$$

The relative amounts of fuel and oxidizer are given by:

$$Y_{Oxidizers} = \frac{\dot{m}_{Oxidizers}}{\dot{m}_{Total}} \qquad \text{(G.16)}$$

$$Y_{Fuels} = \frac{\dot{m}_{Fuels}}{\dot{m}_{Total}}. \qquad \text{(G.17)}$$

The ash-free coal compositions specified in the form ($C_xH_yN_zO_q$) were used to define both fuel species, based on either 'Illinois #6' coal composition or

'Rosebud' coal composition for inclusion in the NASA CEA thermodynamic data bank. Additionally, the fuel species 'Fuel_Oil' was include in the CEA data bank. Rather than specifying stoichiometry directly, relative amounts of fuel and oxidizer were specified. Equilibrium mixtures properties of the primary combustor inputs were then calculated at specified temperatures ranging from 1100 K to 1350 K, using the NASA CEA code [109].

Vita

David Pruitt was born in Suches, Georgia on October 18, 1961. He graduated from Henry County Senior High School in McDonough, Georgia in 1978. David attended college at the Georgia Institute of Technology in Atlanta, Georgia, obtaining a Bachelor's of Science Degree in Mechanical Engineering in 1982 and a Master of Science Degree in Mechanical Engineering in 1984. He was employed by Sverdrup Technology, Inc. at the Arnold Engineering Development Center in 1984.